JPTM
Journal of Pathology and Translational Medicine

Journal of Pathology and Translational Medicine

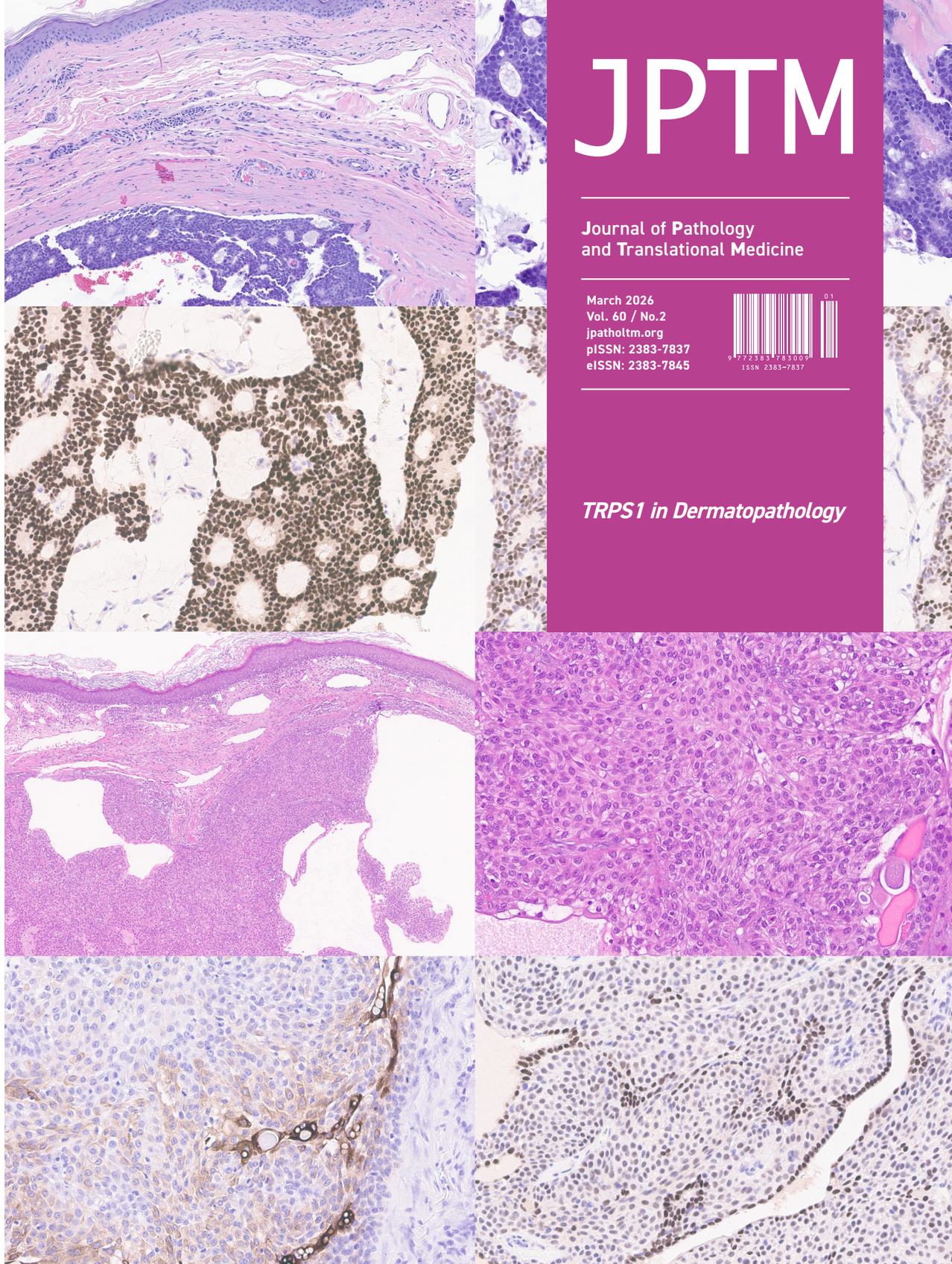

JPTM

Journal of Pathology and Translational Medicine

March 2026
Vol. 60 / No.2
jpatholtm.org
pISSN: 2383-7837
eISSN: 2383-7845

TRPS1 in Dermatopathology

Vol. 60, No.2, pp 129-283, March 2026

JPTM

jpatholtm.org
pISSN 2383-7837 · eISSN 2383-7845

Vol. 60, No.2, March 2026

Published on 15 March 2026

Aims & Scope

The Journal of Pathology and Translational Medicine is an open venue for the rapid publication of major achievements in various fields of pathology, cytopathology, and biomedical and translational research. The Journal aims to share new insights into the molecular and cellular mechanisms of human diseases and to report major advances in both experimental and clinical medicine, with a particular emphasis on translational research. The investigations of human cells and tissues using high-dimensional biology techniques such as genomics and proteomics will be given a high priority. Articles on stem cell biology are also welcome. The categories of manuscript include original articles, review and perspective articles, case studies, brief case reports, and letters to the editor.

Subscription Information

To subscribe to this journal, please contact the Korean Society of Pathologists/the Korean Society for Cytopathology. Full text PDF files are also available at the official website (https://jpatholtm.org). *Journal of Pathology and Translational Medicine* is indexed by Emerging Sources Citation Index (ESCI), PubMed, PubMed Central, Scopus, KoreaMed, KoMCI, WPRIM, Directory of Open Access Journals (DOAJ), and CrossRef. Circulation number per issue is 50.

Contact the Korean Society of Pathologists/the Korean Society for Cytopathology

Publishers: Kang, Gyeong Hoon, MD; Choi, Yoon Jung, MD
Editors-in-Chief: Jung, Chan Kwon, MD; Park, So Yeon, MD
Published by the Korean Society of Pathologists/the Korean Society for Cytopathology

Editorial Office
Suite 706, 217 Saechang-ro, Yongsan-gu, Seoul 04376, Korea
Tel: +82-2-795-3094 Fax: +82-2-790-6635 E-mail: office@jpatholtm.org
#1508 Renaissancetower, 14 Mallijae-ro, Mapo-gu, Seoul 04195, Korea
Tel: +82-2-593-6943 Fax: +82-2-593-6944 E-mail: office@jpatholtm.org

Printed by M2PI
#805, 26 Sangwon 1-gil, Seongdong-gu, Seoul 04779, Korea
Tel: +82-2-6966-4930 Fax: +82-2-6966-4945 E-mail: support@m2-pi.com

Manuscript Editing by InfoLumi Co.
210-202, 421 Pangyo-ro, Bundang-gu, Seongnam 13522, Korea
Tel: +82-70-8839-8800 E-mail: infolumi.chang@gmail.com

Front cover image: Examples of TRPS1-positive sweat gland tumors (p. 134, p. 135)

This work was supported by the Korean Federation of Science and Technology Societies Grant funded by the Korean Government (Ministry of Education).

Editorial Board

JPTM

jpatholtm.org
pISSN 2383-7837 · eISSN 2383-7845

Contents

Vol. 60, No.2, March 2026

REVIEW ARTICLES

ORIGINAL ARTICLES

JPTM

jpatholtm.org
pISSN 2383-7837 · eISSN 2383-7845

Contents

Vol. 60, No.2, March 2026

NEWSLETTER

JPTM

REVIEW ARTICLE

pISSN 2383-7837 · eISSN 2383-7845

Journal of Pathology and Translational Medicine 2026; 60: 129-143
https://doi.org/10.4132/jptm.2025.11.25

The evolving role of TRPS1 in dermatopathology: insights from the past 4 years

Mokhtar H. Abdelhammed[1], Woo Cheal Cho[2]

[1]Department of Pathology and Immunology, Baylor College of Medicine, Houston, TX, USA
[2]Department of Anatomical Pathology, The University of Texas MD Anderson Cancer Center, Houston, TX, USA

Over the past 4 years, trichorhinophalangeal syndrome type 1 (TRPS1) has rapidly gained attention among practicing pathologists, with numerous studies emerging that both support and question its diagnostic utility. Initially regarded as a highly specific marker for tumors of mammary origin, TRPS1 is now recognized to have broader expression patterns, including in a variety of cutaneous neoplasms. This is likely due to embryologic parallels between breast tissue and skin adnexal structures, an overlap that was underappreciated in early investigations. Although TRPS1 lacks absolute specificity—even among cutaneous neoplasms—it can still offer meaningful diagnostic value when interpreted alongside conventional immunohistochemical markers and within the appropriate morphologic context. Noteworthy diagnostic applications include mammary Paget disease, primary extramammary Paget disease, rare adnexal neoplasms such as endocrine mucin-producing sweat gland carcinoma and primary cutaneous NUT adnexal carcinoma, and cutaneous metastases from breast carcinoma. In this review, we present the most comprehensive and up-to-date evaluation of the utility and limitations of TRPS1 immunohistochemistry in dermatopathology. Our aim is to deepen understanding of this emerging marker and provide practical guidance on its optimal integration with established immunohistochemical panels to enhance diagnostic accuracy in routine practice.

Keywords: TRPS1; Immunohistochemistry; Cutaneous neoplasms; Cutaneous adnexal neoplasms; Cutaneous mesenchymal neoplasms; Cutaneous melanocytic neoplasms; Cutaneous metastases; Mammary Paget disease; Extramammary Paget disease; Primary cutaneous NUT adnexal carcinoma; Endocrine mucin-producing sweat gland carcinoma

INTRODUCTION

Trichorhinophalangeal syndrome type 1 (TRPS1) immunohistochemistry (IHC) has gained significant traction among surgical pathologists and cytopathologists in recent years, initially being regarded as a highly sensitive and specific marker for carcinomas of mammary origin [1]. However, the study by Ai et al. [1], which first highlighted its potential, had a significant limitation: the authors employed tissue microarrays for analysis instead of whole tissue sections. This approach failed to account for the heterogeneity of TRPS1 expression within the same tumor types, undermining the robustness of their findings. Furthermore, their analysis excluded most cutaneous neoplasms, focusing primarily on melanomas, casting doubt on their assertion that TRPS1 expression is "highly specific" for breast carcinomas [1].

Subsequent studies have challenged this claim, demonstrating that TRPS1 expression extends beyond breast neoplasms. Tumors in sites with embryological similarities to breast tissue, such as skin adnexal structures, often share similar immunoprofiles (e.g., cytokeratin [CK] 7+/GATA3+). TRPS1 expression has been notably observed in various cutaneous adnexal neoplasms, including mammary Paget diseases (MPDs) [2,3], extramammary Paget diseases (EMPDs) [2-4], endocrine mu-

Received: September 11, 2025 **Revised:** November 24, 2025 **Accepted:** November 25, 2025
Corresponding Author: Woo Cheal Cho, MD
Department of Anatomical Pathology, Section of Dermatopathology, The University of Texas MD Anderson Cancer Center, B3.4607, Unit 085, 1515 Holcombe Blvd, Houston, TX 77030-4009, USA
Tel: +1-832-785-9136, Fax: +1-713-745-0789, E-mail: WCho@mdanderson.org

cin-producing sweat gland carcinomas (EMPSGCs) [5], and numerous other cutaneous adnexal tumors [6-11].

In this review, we provide the most comprehensive and up-to-date examination of the utility and limitations of TRPS1 IHC in cutaneous neoplasms, encompassing not only adnexal tumors but also other epithelial and mesenchymal neoplasms of cutaneous origin. This knowledge will deepen our understanding of this emerging marker in dermatopathology and offer guidance on how to optimally integrate TRPS1 IHC with other established immunohistochemical markers to improve diagnostic accuracy in routine dermatopathology practice.

ANTI-TRPS1 ANTIBODIES

The successful detection of TRPS1 expression in formalin-fixed, paraffin-embedded (FFPE) tissues hinges on the selection of an optimal antibody and immunohistochemical protocol. Among the various anti-TRPS1 antibodies and clones reported in the literature, EPR16171, a rabbit monoclonal antibody, appears to be the most widely used for IHC [3,5-8,12]. However, its application varies across laboratories, with differences in antibody dilution (e.g., 1:2,000 [3,5,6,12] vs. 1:6,000 [7,8]), incubation times, antigen retrieval methods, and staining platforms.

The second most frequently employed anti-TRPS1 antibody is PA5-84587, a rabbit polyclonal antibody, used at diverse dilutions such as 1:100 [1], 1:250 [9], and 1:1,000 [4]. Another reported clone is ZR382, a rabbit monoclonal antibody used at a 1:200 dilution [13,14].

In our own experience, both monoclonal and polyclonal anti-TRPS1 antibodies have been evaluated. Notably, the monoclonal antibody EPR16171 reliably demonstrates TRPS1 expression in FFPE skin specimens. Internal controls, such as eccrine glands, consistently show strong (3+) expression intensity, supporting the reproducibility and robustness of this clone under our testing conditions.

TRPS1 EXPRESSION IN NORMAL SKIN

Understanding TRPS1 expression in the innate cellular and structural components of normal skin is crucial for identifying the types of cutaneous neoplasms that may express this marker. Neoplastic cells often retain the immunoprofile of their normal cellular counterparts as they proliferate and transform. In normal skin, TRPS1 immunoreactivity is prominently observed in various adnexal structures (Table 1), with the strongest expression (3+) found in eccrine glands (Fig. 1A), acrosyringia, matrical cells (Fig. 1B), and mesenchymal cells of the dermal papillae (Fig. 1C) [2,6]. These structures serve as ideal internal controls due to their consistent, robust TRPS1 expression. Sebocytes in sebaceous glands typically show weak-to-moderate (1+ to 2+) TRPS1 immunoreactivity, while the germinative cells of these glands are devoid of expression (Fig. 1D) [2,6]. Hair follicles exhibit variable TRPS1 expression in the outer and inner root sheaths and matrical cells, generally ranging from weak to strong intensity (1+ to 3+) (Fig. 1B) [2,6]. Arrector pili muscles also show natural TRPS1 immunoreactivity with weak-to-moderate intensity (1+ to 2+) (Fig. 1E). Notably, innate apocrine glands in normal skin do not express TRPS1 [2,6]. In contrast, anogenital mammary-like glands exhibit strong (3+) TRPS1 immunoreactivity [9].

Regarding non-adnexal epithelial components, epidermal keratinocytes in the stratum spinosum may display weak-to-moderate (1+ to 2+) TRPS1 expression [2,6]. Although this TRPS1 immunoreactivity in innate epidermal keratinocytes was initially thought to be restricted to actinically damaged skin, it was later found that the epidermis from sun-protected sites can also occasionally express TRPS1 in weak-to-moderate (1+ to 2+) intensity [2,6]. The exact frequency of TRPS1 immunoreactivity in normal epidermal keratinocytes, as well as the comparison between sun-damaged and sun-protected skin, remains largely unknown at this point. Interestingly, while weak-to-moderate TRPS1 expression may be present in the normal epidermis, basal keratinocytes, unlike those in the stratum spinosum, naturally lack TRPS1 expression [2,6].

TRPS1 EXPRESSION IN CUTANEOUS NON-ADNEXAL EPITHELIAL NEOPLASMS

Most studies investigating TRPS1 expression in cutaneous non-adnexal epithelial neoplasms have focused on malignant tumors such as squamous cell carcinomas (SCCs), basal cell carcinomas (BCCs), and Merkel cell carcinomas (MCCs) (Table 1). A recent comprehensive study analyzing TRPS1 immunoreactivity across 200 cases of various cutaneous neoplasms found that nearly all SCCs (94%) demonstrated moderate to strong TRPS1 expression, with a median H-score of 200 [6]. Interestingly, the intensity of TRPS1 expression often decreases as SCC cells invade deeper into the dermis, whereas stronger expression tends to be retained in cells near the epidermis or within

https://doi.org/10.4132/jptm.2025.11.25

Table 1. Summary of TRPS1 immunoreactivity in normal skin and various cutaneous neoplasms

Category	Type	TRPS1 expression patterns	Potential diagnostic utility and other key points
Normal skin	Eccrine glands, acrosyringia, matrical cells, mesenchymal cells of dermal papillae [2,6]	Strong (3+)	Serve as ideal internal controls
	Anogenital mammary-like glands [9]	Strong (3+)	-
	Sebocytes of sebaceous glands [2,6]	Weak-to-moderate (1+ to 2+)	-
	Outer and inner root sheaths of hair follicles [2,6]	Weak-to-strong (1+ to 3+)	-
	Epidermal keratinocytes in stratum spinosum [2,6]	Weak-to-moderate (1+ to 2+)	-
	Epidermal keratinocytes in stratum basale [2,6]	Negative	May explain the frequent absence of TRPS1 expression in basal cell carcinomas
	Apocrine glands [2,6]	Negative	-
Non-adnexal epithelial neoplasms	Squamous cell carcinoma [2,6]	Moderate-to-strong (2+ to 3+); patchy-to-diffuse	May provide potential diagnostic utility in distinguishing squamous cell carcinomas from basal cell carcinomas
	Basal cell carcinoma [5,6]	Negative (typically); only focal when present	May provide potential diagnostic utility in distinguishing basal cell carcinomas from squamous cell carcinomas
	Merkel cell carcinoma [5,6]	Negative	Helps distinguish Merkel cell carcinomas (TRPS1–/INSM1+) from endocrine mucin-producing sweat gland carcinomas (TRPS1+/INSM1+)
Adnexal neoplasms with apocrine and eccrine differentiation	Endocrine mucin-producing sweat gland carcinoma [5,6]	Strong (3+); diffuse	Helps distinguish endocrine mucin-producing sweat gland carcinomas (TRPS1+/INSM1+) from basal cell carcinomas (TRPS1–/INSM1–) and Merkel cell carcinomas (TRPS1–/INSM1+)
	Primary cutaneous NUT adnexal carcinoma [15,16]	Strong (3+); diffuse	Helps distinguish primary cutaneous NUT adnexal carcinomas (TRPS1+/SOX10+/NUT+) from basal cell carcinomas (TRPS1–/SOX10–/NUT–)
	Benign (poroma, hidradenoma, spiradenoma, cylindroma, syringoma, syringocystadenoma papilliferum)	Weak-to-strong (1+ to 3+); focal-to-diffuse	Lacks diagnostic utility in distinguishing these tumor types from their morphologic mimics
	Malignant (porocarcinoma, hidradenocarcinoma, digital papillary adenocarcinoma, squamoid eccrine ductal carcinoma) [5-7,9,10,15,16]	Weak-to-strong (1+ to 3+); focal-to-diffuse	Lacks diagnostic utility in distinguishing these tumor types from their morphologic mimics
	Primary cutaneous apocrine carcinoma [11,17]	Negative (typically)	Diffuse expression reported in one rare case with a *RARA::NPEPPS* fusion [11]
	Microcystic adnexal carcinoma [7]	Negative	-
Adnexal neoplasms with follicular differentiation	Benign (trichoepithelioma, trichoblastoma, trichilemmoma, trichofolliculoma, pilar sheath acanthoma, proliferating pilar tumor, pilomatricoma)	Weak-to-strong (1+ to 3+); focal-to-diffuse	Largely lacks diagnostic utility in distinguishing these tumor types from their morphologic mimics May be useful to highlight the papillary mesenchymal bodies of trichoepitheliomas and trichoblastomas, which exhibit strong (3+) TRPS1 expression
	Malignant (malignant proliferating trichilemmal tumor, trichilemmal carcinoma, trichoblastic carcinoma) [6,8,9]	Weak-to-strong (1+ to 3+); focal-to-diffuse	
Adnexal neoplasms with sebaceous differentiation	Sebaceous adenoma, sebaceoma, sebaceous carcinoma [6,9]	Weak-to-moderate (1+ to 2+); focal-to-diffuse	Lacks diagnostic utility in distinguishing sebaceous adenomas from sebaceous carcinomas

Continued

Table 1. Continued

Category	Type	TRPS1 expression patterns	Potential diagnostic utility and other key points
Site-specific adnexal neoplasms	Mammary Paget disease [2-4,9]	Strong (3+); diffuse	Helps distinguish mammary Paget diseases (TRPS1+/p63–/SOX10–) from melanomas in situ (TRPS1–/p63–/SOX10+) and pagetoid squamous cell carcinomas in situ (TRPS1+/p63+/SOX10–)
	Primary extramammary Paget disease arising in non-perianal cutaneous sites [2-4,9]	Strong (3+); diffuse	Helps distinguish primary extramammary Paget diseases (TRPS1+/p63–/SOX10–) from melanomas in situ (TRPS1–/p63–/SOX10+) and pagetoid squamous cell carcinomas in situ (TRPS1+/p63+/SOX10–)
			The presence of TRPS1 expression is highly sensitive (100%) and specific (100%) for primary extramammary Paget disease of non-perianal cutaneous origin and essentially rules out secondary extramammary Paget disease
	Primary extramammary Paget disease arising in the perianal region [2-4,9]	Negative (typically)	The immunoprofile (TRPS1–) mimics that of secondary extramammary Paget disease (TRPS1–), invariably requiring additional clinical workup (e.g., endoscopy, imaging studies) to completely rule out an internal malignancy
	Secondary extramammary Paget disease [2-4,9]	Negative	The lack of TRPS1 expression strongly supports a diagnosis of secondary extramammary Paget disease over primary extramammary Paget disease, except for lesions arising in the perianal region
	Hidradenoma papilliferum [13]	Strong (3+); diffuse	-
Melanocytic neoplasms	Melanoma situ and invasive melanoma [1,2]	Negative	Helps distinguish melanomas in situ (TRPS1–/SOX10+) from mammary and extramammary Paget diseases (TRPS1+/SOX10–), including mammary Paget diseases secondary to underlying triple-negative breast carcinomas, which can be positive for SOX10 (TRPS1+/SOX10+) [18,19]
Mesenchymal neoplasms	Atypical fibroxanthoma/pleomorphic dermal sarcoma, angiosarcoma, dermatofibroma, dermatofibrosarcoma protuberans, Kaposi sarcoma, leiomyoma, leiomyosarcoma, neurofibroma, malignant peripheral nerve sheath tumor [12,20]	Weak-to-strong (1+ to 3+); focal-to-diffuse	Lacks diagnostic utility in distinguishing these tumor types from their morphologic mimics
			Atypical fibroxanthomas/pleomorphic dermal sarcomas exhibit the highest median H-score of 240, while vascular neoplasms and peripheral nerve sheath tumors consistently show low median H-scores below 10 [12]
	Schwannoma [20]	Negative	-
Cutaneous metastatic carcinomas	Carcinoma of mammary origin [1,9,14]	Strong (3+); diffuse	The presence of strong and diffuse TRPS1 expression helps support a diagnosis of metastatic carcinoma of mammary origin in the appropriate morphologic and immunophenotypic (CK7+/GATA3+) context
	Carcinomas of pulmonary, gynecological, or renal origin [9,14]	Weak (1+); focal (occasionally)	-
	Carcinomas of gastrointestinal or prostatic origin [9,14]	Negative	-

TRPS1, trichorhinophalangeal syndrome type 1; INSM1, insulinoma-associated protein 1; CK, cytokeratin.

https://doi.org/10.4132/jptm.2025.11.25

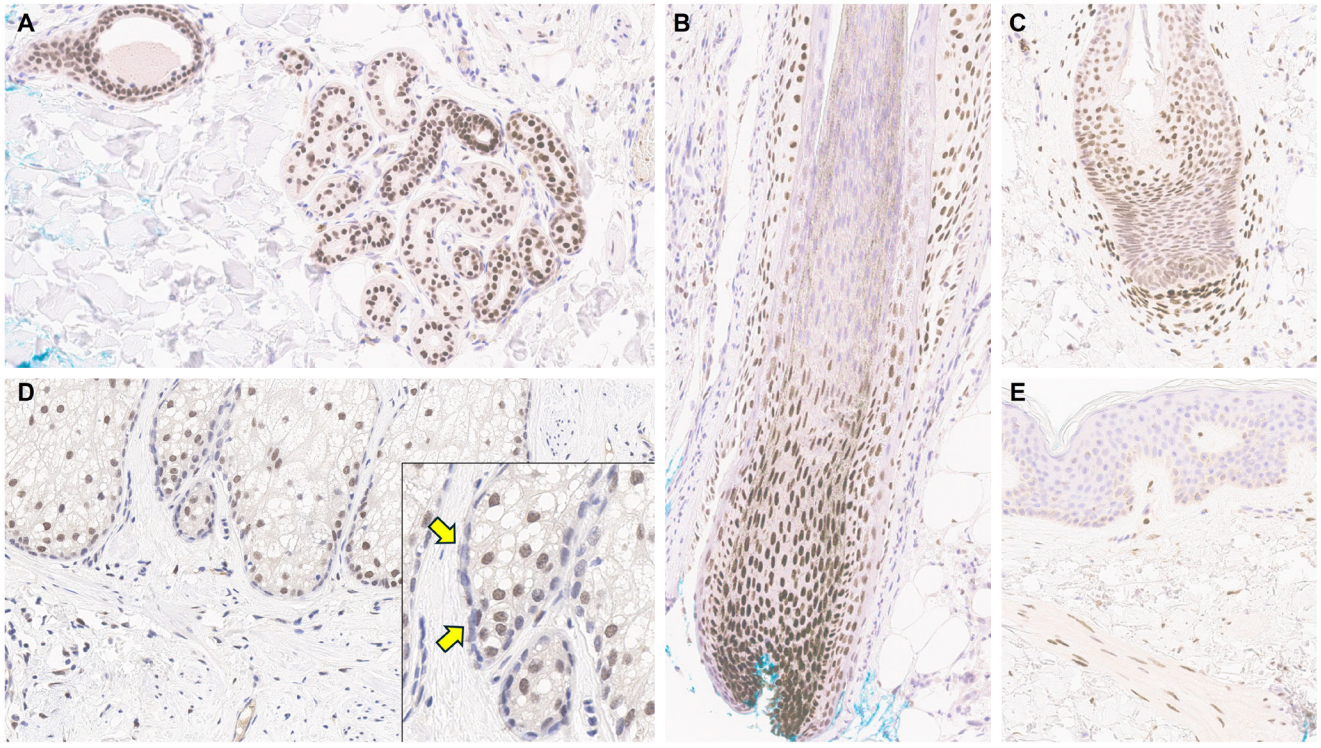

Fig. 1. Trichorhinophalangeal syndrome type 1 (TRPS1) expression in normal skin. TRPS1 is strongly expressed in eccrine glands (A), matrical cells of hair follicles (B), and mesenchymal cells of the dermal papillae (C), making these structures reliable internal positive controls. Other skin adnexal structures, such as sebaceous glands (D) and arrector pili muscles (E), typically exhibit weak-to-moderate TRPS1 immunoreactivity (1+ to 2+). Notably, while sebocytes demonstrate TRPS1 expression, the germinative cells of sebaceous glands lack immunoreactivity (D, inset, yellow arrows).

in situ components. This observation is supported by an earlier study showing diffuse and strong TRPS1 expression in 92% of SCC in situ (SCCIS) cases [2].

In contrast, the same study by Liu et al. [6] reported that the majority of BCCs (90%) either lacked TRPS1 expression entirely or showed only focal immunoreactivity, with a median H-score of 5. Given that BCCs are thought to originate from the basal layer of the interfollicular epidermis [21], the minimal TRPS1 expression may reflect the absence of TRPS1 expression in native basal keratinocytes. The difference in TRPS1 expression between SCCs and BCCs was statistically significant ($p < .001$) [6], highlighting its potential diagnostic utility in distinguishing between these entities. The authors further investigated whether squamous differentiation in BCCs might confound TRPS1-based discrimination. Even in BCCs with squamous differentiation, TRPS1 expression remained significantly more frequent in SCCs ($p < .001$) [6]. However, while these findings are statistically significant, clinical interpretation should be approached with caution, as exceptions do occur. For example, diffuse TRPS1 expression may occasionally be seen in BCCs with hamartomatous or infundibulocytic features and extensive squamous differentiation [6]. Conversely, TRPS1 expression may be nearly absent in rare cases of SCC [6,9].

Therefore, in diagnostically challenging scenarios, such as distinguishing BCCs with extensive squamous differentiation from SCCs with basaloid features, a comprehensive morphologic evaluation supplemented by an immunohistochemical panel, including TRPS1, epithelial membrane antigen, and BerEP4, may provide greater diagnostic accuracy. However, the utility of this proposed IHC panel in such cases warrants confirmation in larger, future studies.

MCCs consistently lack TRPS1 immunoreactivity, as demonstrated in prior studies [5,6]. This distinct immunophenotypic profile may be diagnostically useful in differentiating MCCs from EMPSGCs, a primary cutaneous adnexal carcinoma with neuroendocrine differentiation, which will be discussed in more detail below.

TRPS1 EXPRESSION IN CUTANEOUS ADNEXAL NEOPLASMS

Various benign and malignant cutaneous adnexal neoplasms have been shown to express TRPS1 with varying intensity and proportion [2-11,13,15,16,22], indicating that this marker is not specific to tumors of mammary origin (Table 1). However, TRPS1 generally lacks significant discriminatory power among most cutaneous adnexal neoplasms. Nonetheless, in certain diagnostic contexts, when used in combination with other immunohistochemical markers, TRPS1 may offer valuable diagnostic utility (Table 1).

TRPS1 EXPRESSION IN TUMORS WITH APOCRINE AND ECCRINE DIFFERENTIATION

Although not all tumor types that belong to this category of cutaneous adnexal neoplasms have been thoroughly investigated, published studies indicate that the majority, including poromas, hidradenomas (Fig. 2), spiradenomas, cylindromas, syringomas, mixed tumors, syringocystadenomas papilliferum, porocarcinomas, hidradenocarcinomas, digital papillary adenocarcinomas, squamoid eccrine ductal carcinomas, EMPSGCs, and primary cutaneous NUT adnexal carcinomas, express TRPS1 at least focally [5-7,9,10,15,16]. When present, TRPS1 expression in these tumors is typically weak-to-moderate (1+ to 2+), with the notable exception of EMPSGCs and primary cutaneous NUT adnexal carcinomas, which consistently demonstrate strong (3+) expression intensity [5,15,16], akin to that seen in eccrine glands, acrosyringia, or the mesenchymal cells of the dermal papillae. This consistent strong expression highlights the diagnostic utility of TRPS1 in identifying EMPSGCs and primary cutaneous NUT adnexal carcinomas.

EMPSGCs are uncommon adnexal carcinomas of sweat gland origin with neuroendocrine differentiation and are often regarded as the cutaneous analogue of solid papillary carcinoma of the breast [23,24]. Histopathologically, EMPSGCs present as nodular proliferations of basaloid cells with varied architectural patterns and frequently contain intracellular and

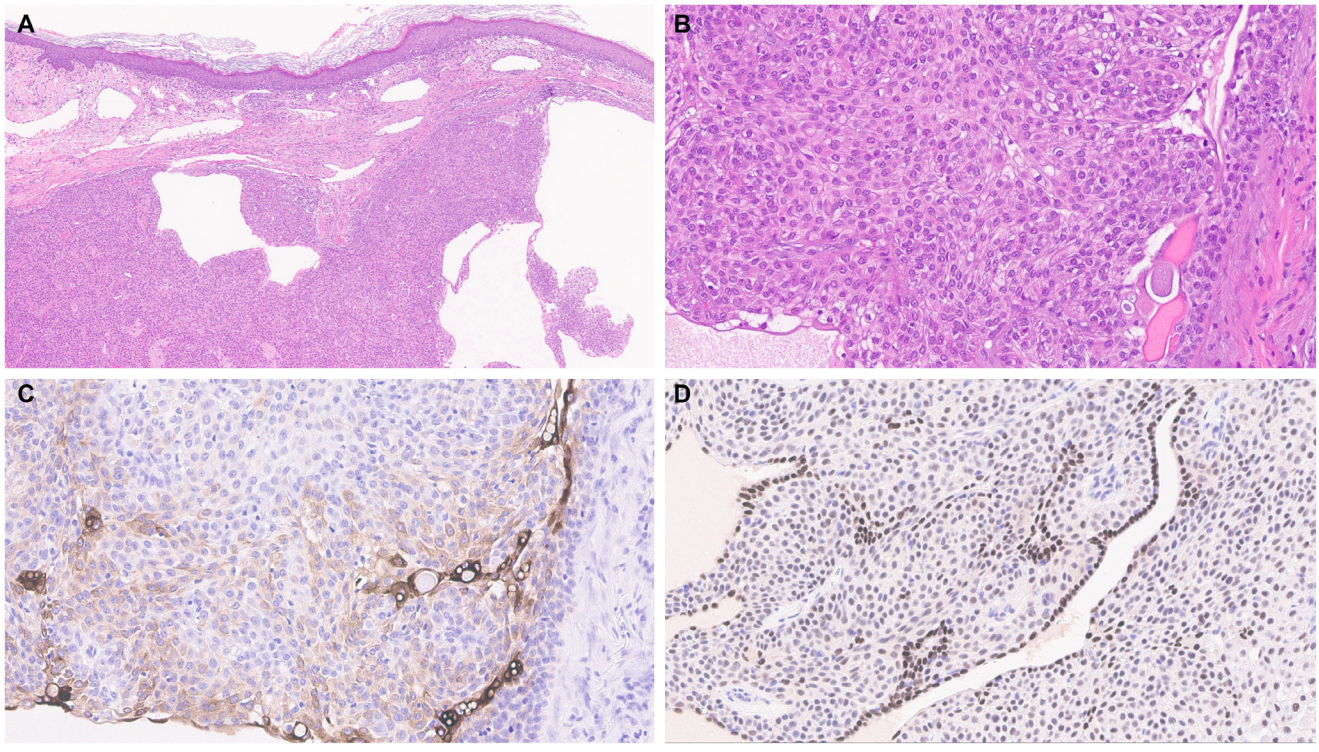

Fig. 2. Hidradenoma. A biopsy from the left chest of a 62-year-old male patient reveals a solid and cystic hidradenoma (A, B). Cytokeratin 19 highlights ductal differentiation within the tumor (C). Intriguingly, while the majority of tumor cells show weak-to-moderate trichorhinophalangeal syndrome type 1 (TRPS1) immunoreactivity (1+ to 2+), the cuboidal cells lining the ductal structures exhibit strong TRPS1 expression (D).

https://doi.org/10.4132/jptm.2025.11.25

extracellular mucin, which can mimic BCCs, especially in superficial or shallow biopsies. Immunophenotypically, their expression of neuroendocrine markers such as insulinoma-associated protein 1 (INSM1), synaptophysin, and chromogranin may also lead to confusion with MCCs, another skin malignancy with neuroendocrine differentiation, albeit more common than EMPSGCs. A recent study evaluating TRPS1 expression in EMPSGCs, BCCs, and MCCs found that all EMPSGCs demonstrated diffuse, strong TRPS1 positivity, while most BCCs and all MCCs lacked TRPS1 immunoreactivity [5]. These findings support the role of TRPS1, particularly in combination with neuroendocrine markers such as INSM1, as a valuable immunohistochemical tool for differentiating EMPSGCs (Fig. 3) from their morphologic mimics, including BCCs and MCCs. Among neuroendocrine markers, INSM1 (Fig. 3D) is especially useful in this context due to its superior sensitivity compared to others like SOX11, synaptophysin, and chromogranin [25-27].

Primary cutaneous NUT adnexal carcinomas are a rare and recently characterized entity defined by recurrent *NUTM1* or *NUTM2B* gene fusions [15,16,22,28]. These tumors typically exhibit a basaloid morphology, often resembling BCCs or other basaloid adnexal carcinomas such as porocarcinomas. Recent studies have shown that primary cutaneous NUT adnexal carcinomas consistently express TRPS1, SOX10, and NUT [15,16,28], suggesting that this unique immunoprofile can aid in distinguishing them from morphologically similar tumors such as porocarcinomas and BCCs. While porocarcinomas may express NUT in cases harboring a *YAP1::NUTM1* fusion [29,30], they typically lack SOX10 expression [31], and TRPS1 expression in poroid neoplasms is generally not diffusely or strongly positive [6,7]. BCCs are typically negative for TRPS1, SOX10, and NUT, further supporting the diagnostic utility of this panel of IHC.

Among the primary cutaneous adnexal carcinomas studied to date, microcystic adnexal carcinomas were found to lack TRPS1 expression in one study [7]. Consistent with the observation that normal apocrine glands are also TRPS1-negative, primary cutaneous apocrine carcinomas were initially believed

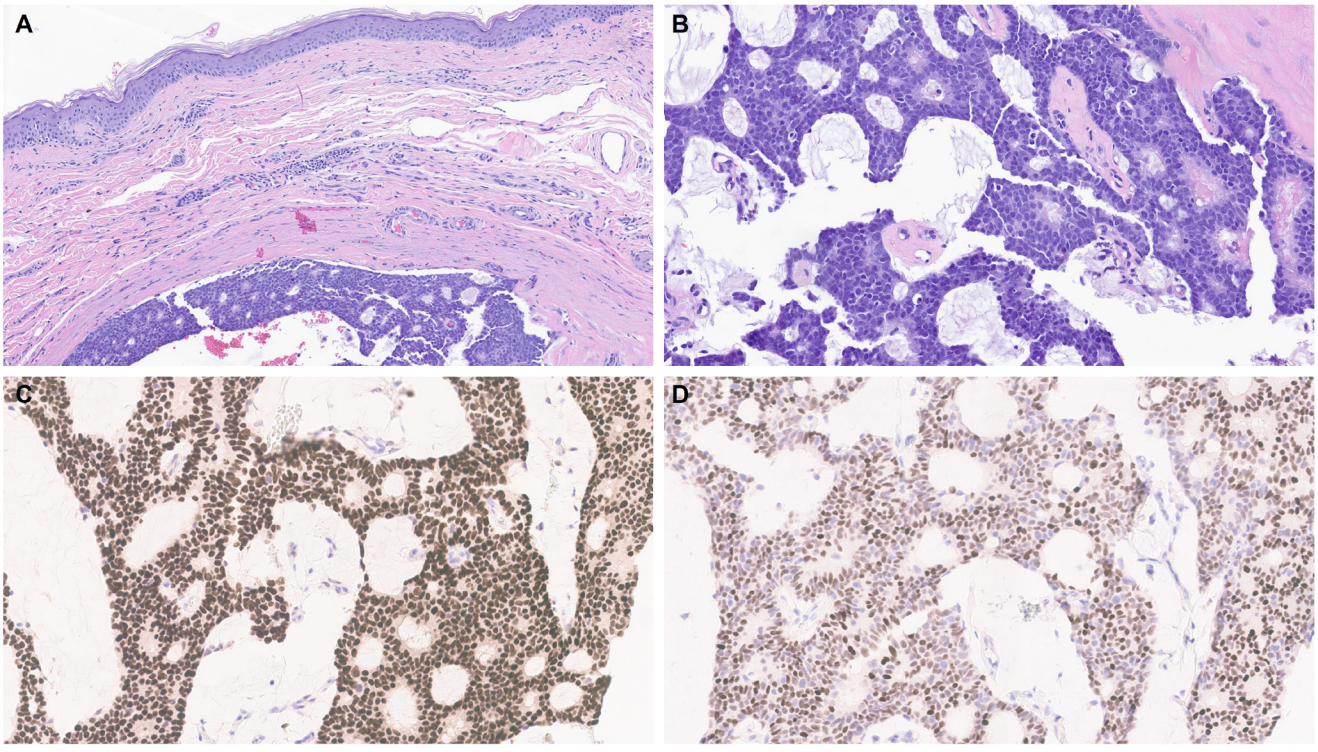

Fig. 3. Endocrine mucin-producing sweat gland carcinoma. A biopsy from the right parietal scalp of a 71-year-old female patient demonstrates an endocrine mucin-producing sweat gland carcinoma (A, B). The tumor cells are diffusely positive for trichorhinophalangeal syndrome type 1 (TRPS1) (C) and insulinoma-associated protein 1 (D). In the absence of clinical or radiologic evidence of an underlying breast carcinoma, this immunoprofile in a cutaneous tumor is diagnostic of endocrine mucin-producing sweat gland carcinoma. Notably, TRPS1 expression in this tumor is consistently strong, comparable to that seen in native eccrine glands.

to be devoid of TRPS1 expression [17]. However, a recent case report described a primary cutaneous apocrine carcinoma harboring an *RARA::NPEPPS* fusion that showed diffuse TRPS1 positivity [11]. This finding underscores the need for additional studies with larger cohorts to clarify the true frequency and diagnostic relevance of TRPS1 expression in this rare tumor type.

TRPS1 EXPRESSION IN TUMORS WITH FOLLICULAR DIFFERENTIATION

Since hair follicles inherently express TRPS1, its presence in cutaneous adnexal neoplasms of hair follicle origin or those with follicular differentiation is expected rather than incidental. Several studies have documented TRPS1 expression, at least focally and with varying intensities, in tumors such as trichoepitheliomas, trichoblastomas, trichilemmomas, trichofolliculomas, pilar sheath acanthomas, proliferating pilar tumors, pilomatricomas, malignant proliferating trichilemmal tumors, trichilemmal carcinomas, and trichoblastic carcinomas [6,8,9].

While the diagnostic value of TRPS1 in these tumors remains somewhat limited, recent work suggests it may aid in differentiating trichoepitheliomas and trichoblastomas from BCCs, their morphologic mimics [8]. Mesenchymal cells in the dermal papillae typically exhibit strong (3+) TRPS1 expression, and this pattern is also seen in the papillary mesenchymal bodies of trichoepitheliomas and trichoblastomas. In contrast, BCCs, though they may show weak TRPS1 expression in peritumoral stromal cells, lack papillary mesenchymal bodies. While further systematic validation is needed, TRPS1 could offer additional diagnostic and discriminative value for dermatopathologists when used alongside other established markers, such as CK20 (for innate Merkel cells) and PHLDA1 (a follicular stem cell marker), especially in challenging cases (e.g., small biopsy samples) [32].

TRPS1 EXPRESSION IN TUMORS WITH SEBACEOUS DIFFERENTIATION

Sebaceous adenomas, sebaceomas, and sebaceous carcinomas typically show at least focal expression of TRPS1, with weak-to-moderate (1+ to 2+) intensities, reflecting the expression pattern seen in their cell of origin, sebocytes [6,9]. Due to the lack of specificity within this tumor category, TRPS1 offers limited diagnostic utility in distinguishing sebaceous adenomas from malignant counterparts like sebaceous carcinomas.

TRPS1 EXPRESSION IN SITE-SPECIFIC ADNEXAL TUMORS

One of the earliest and most promising applications of TRPS1 IHC in dermatopathology has been its supportive role in diagnosing MPDs and EMPDs [2-4,9]. This utility is grounded in the origin of Paget cells in MPDs, which are derived from the underlying ductal carcinoma of the breast. These cells exhibit strong epidermotropism within the nipple-areolar complex. Given that TRPS1 is highly expressed in nearly all breast carcinomas, including those with a triple-negative phenotype [1], it is not surprising that Paget cells in MPDs are also TRPS1-positive (Fig. 4). A seminal study confirmed this, demonstrating consistent TRPS1 expression in all MPD cases examined (100%; 24/24) [2].

When evaluating a pagetoid intraepidermal neoplasm, such as MPD or EMPD, in the skin or nipple-areolar region, a panel of immunohistochemical studies is typically required to distinguish these entities from morphologic mimics, particularly pagetoid SCCIS and melanoma in situ (MIS). The reliable expression of TRPS1 in Paget cells is diagnostically helpful, particularly when interpreted alongside other markers such as CK7 (or Cam5.2), p63, and SOX10. For example, MPDs typically demonstrate immunoreactivity for CK7 (or Cam5.2) and TRPS1 (Fig. 4B), while lacking expression of p63 (or CK5/6) and SOX10 (or other melanocytic markers like Melan-A or HMB45). In contrast, SCCISs and MISs have distinct immunoprofiles. Although TRPS1 expression has been observed in SCCISs [2], this entity rarely involves the nipple-areolar complex. When SCCIS occurs at other anatomic sites, tumor cells are usually positive for p63 (or CK5/6) and negative for SOX10. Since low molecular weight cytokeratins such as CK7 and Cam5.2 can sometimes be expressed in SCCISs, especially those with prominent pagetoid features [33], their diagnostic utility in this context may be limited.

MISs, on the other hand, typically express SOX10 while lacking CK7 and p63 expression. Importantly, MISs are consistently negative for TRPS1 [2], making TRPS1 a particularly useful marker in challenging cases. This is especially relevant in MPD cases arising from underlying triple-negative or metaplastic breast carcinomas, which may express SOX10 [18,19]—a well-documented diagnostic pitfall. In such scenarios, the strong and diffuse expression of TRPS1 in intraepidermal pagetoid cells can support a diagnosis of MPD, even in the presence of SOX10 positivity.

https://doi.org/10.4132/jptm.2025.11.25

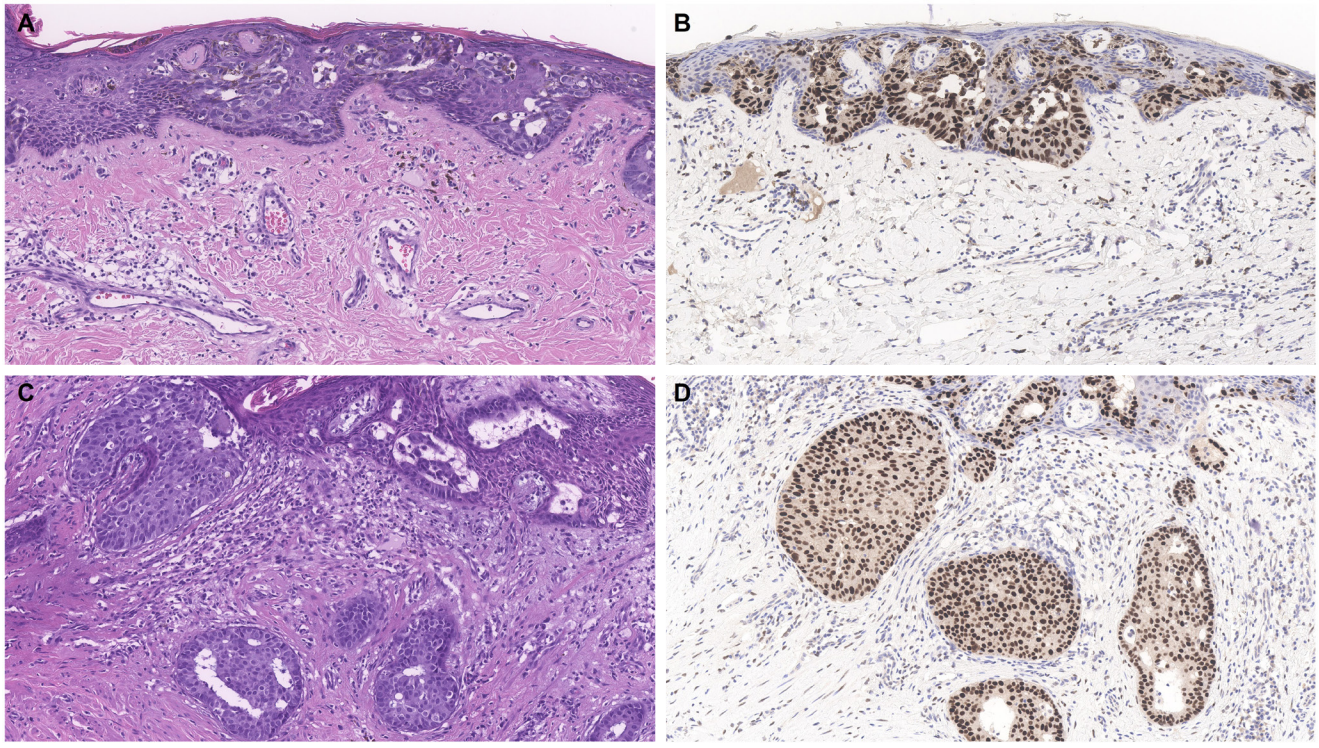

Fig. 4. Mammary Paget disease. A biopsy of the left nipple from a 62-year-old woman demonstrates mammary Paget disease predominantly involving the nipple epidermis (A). Trichorhinophalangeal syndrome type 1 (TRPS1) shows strong, diffuse positivity within the intraepidermal Paget cells (B). Focal dermal involvement is also noted (C), corresponding to an invasive component that similarly exhibits strong and diffuse TRPS1 expression (D). Given that TRPS1 is highly expressed in nearly all breast carcinomas, and that mammary Paget disease is almost always secondary to an underlying breast carcinoma, TRPS1 serves as an ideal marker for confirming the diagnosis of mammary Paget disease in this context.

Similar to MPD, recent studies have shown that the majority of EMPD cases—ranging from 88% to 100%—also exhibit strong and diffuse TRPS1 expression [2-4,9]. Three key findings have emerged from these studies [2-4,9]: (1) TRPS1 is both highly sensitive (100%) and specific (100%) for primary EMPD arising outside the perianal region, such as the groin/inguinal area and axilla (Fig. 5); (2) secondary EMPDs, which originate from underlying internal malignancies such as colorectal or urothelial carcinomas, consistently lack TRPS1 expression (Fig. 6); and (3) the majority of perianal primary EMPDs—up to 91%—also lack TRPS1 expression, mimicking the immunoprofile of secondary EMPDs.

This third observation is especially diagnostically important. Given the high rate of TRPS1 negativity in perianal primary EMPDs, thorough clinical workup, including endoscopy or imaging, is essential to conclusively exclude an associated internal malignancy. Additional markers, such as CK20 and gross cystic disease fluid protein-15 (GCDFP-15), may aid in this distinction: a CK20-negative/GCDFP-15–positive immunoprofile may support a primary origin, while CK20 positivity with GCDFP-15 negativity leans toward a secondary source [34]. However, caution is warranted, as CK20 expression is not entirely specific—approximately one-third of perianal primary EMPDs can also express CK20 [34].

A few additional tumor types fall within this category, all of which are associated with anogenital mammary-like glands. These include hidradenoma papilliferum (HP), fibroadenoma and phyllodes tumor of anogenital mammary-like glands, and adenocarcinoma of mammary gland type. HPs, believed to originate from anogenital mammary-like glands, most commonly occur in the vulva and only rarely in the perianal region. Given that native anogenital mammary-like glands demonstrate TRPS1 expression [9], it is not surprising that a recent study found consistent TRPS1 positivity in all HPs (100%; 9/9), except within intratumoral foci exhibiting oxyphilic metaplasia, which lacked expression [13].

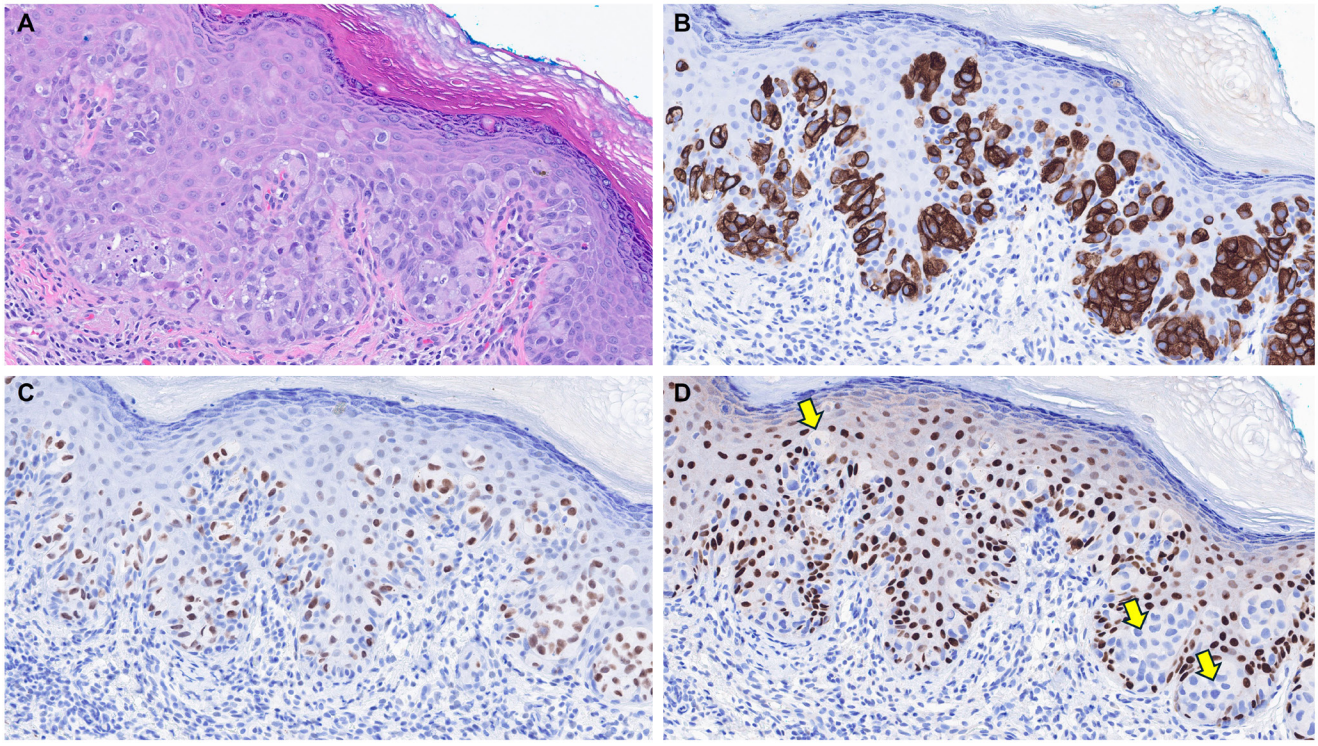

Fig. 5. Primary extramammary Paget disease. A biopsy from the right medial thigh of a 63-year-old male patient reveals a pagetoid intraepidermal neoplasm (A). The lesional cells exhibit diffuse immunoreactivity for cytokeratin 7 (B) and trichorhinophalangeal syndrome type 1 (TRPS1) (C). In contrast, these cells show a complete absence of p63 immunoreactivity (D, yellow arrows). Given that the neoplasm arises outside the perianal region, this immunoprofile is consistent with primary extramammary Paget disease.

Due to the rarity of other neoplasms in this group, data on TRPS1 expression in tumors such as adenocarcinomas of mammary gland type remain limited. However, based on the authors' limited experience, TRPS1 immunoreactivity has been observed in at least one case of adenocarcinoma of mammary gland type, although larger studies are needed to confirm and better characterize this finding.

TRPS1 EXPRESSION IN MELANOCYTIC NEOPLASMS

MISs and invasive melanomas are essentially devoid of TRPS1 expression (Table 1) [1,2]. While benign melanocytic neoplasms such as common (banal) nevi have not been well studied with regard to TRPS1 immunoreactivity, they are also likely negative for TRPS1, given that normal epidermal melanocytes do not express this marker. However, the TRPS1 expression profile in other melanocytic neoplasms, including melanocytomas such as WNT-activated deep penetrating/plexiform melanocytomas and pigmented epithelioid melanocytomas, remains largely uncharacterized.

TRPS1 EXPRESSION IN CUTANEOUS MESENCHYMAL NEOPLASMS

Limited studies have explored TRPS1 immunoreactivity in non-epithelial neoplasms (Table 1). One recent study assessed TRPS1 expression in 135 cases of various cutaneous mesenchymal neoplasms and tumors of uncertain differentiation, including atypical fibroxanthomas (AFXs) (Fig. 7A, B). TRPS1 was frequently expressed in dermatofibromas (100%; 24/24), leiomyomas (100%; 8/8), AFXs/pleomorphic dermal sarcomas (PDSs) (95%; 20/21), leiomyosarcomas (75%; 6/8), and dermatofibrosarcomas protuberans (64%; 14/22) (Fig. 7C, D) [12]. Expression was less frequent in neurofibromas (29%; 5/17), Kaposi sarcomas (25%; 2/8), and angiosarcomas (15%; 3/20), and was completely absent in perineuriomas [12]. Considering both the proportion and intensity of TRPS1 expression, AFXs/PDSs exhibited the highest median H-score of 240, whereas vascular neoplasms and peripheral nerve sheath tumors had consistently

https://doi.org/10.4132/jptm.2025.11.25

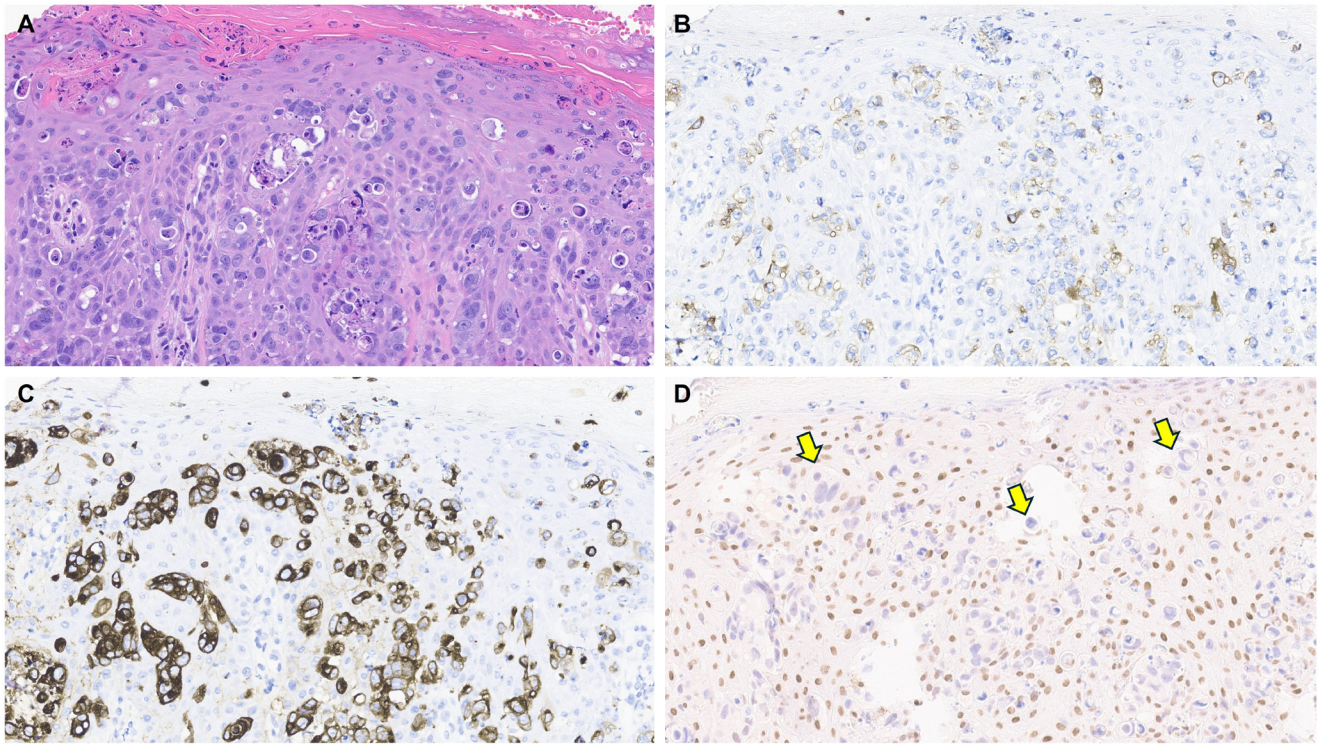

Fig. 6. Secondary extramammary Paget disease. A biopsy from the perianal skin of a 79-year-old female patient with a known rectal adenocarcinoma shows a pagetoid intraepidermal neoplasm (A). The lesional cells exhibit patchy, weak positivity for cytokeratin (CK) 7 (B) and diffuse positivity for CK20 (C). These cells are completely negative for trichorhinophalangeal syndrome type 1 (TRPS1) (D, yellow arrows). In the context of the underlying rectal adenocarcinoma, this immunoprofile is consistent with secondary extramammary Paget disease. Note that epidermal keratinocytes may occasionally be weakly immunoreactive for TRPS1 (D).

low median H-scores below 10 [12].

The morphologic differential diagnosis of AFX often includes poorly differentiated or sarcomatoid SCC, melanoma, angiosarcoma, and leiomyosarcoma. The aforementioned study also examined the potential of TRPS1 in distinguishing AFXs from these morphologic mimics. While significant differences in H-scores were observed between AFXs and angiosarcomas ($p < .001$), melanomas ($p < .001$), and leiomyosarcomas ($p = .029$), no significant difference was noted when compared to sarcomatoid SCCs, suggesting limited discriminatory value of TRPS1 in this context [12].

Another recent study highlighted that a subset of malignant peripheral nerve sheath tumors also expresses TRPS1, albeit generally with weak intensity [20]. In contrast, other benign peripheral nerve sheath tumors, such as schwannomas and neurofibromas, consistently lacked TRPS1 expression [20].

Together, these studies provide new insights into TRPS1 expression patterns in a subset of cutaneous mesenchymal neoplasms and tumors of uncertain differentiation. This extends beyond prior research primarily focused on epithelial tumors and underscores potential limitations associated with TRPS1 IHC.

Finally, TRPS1 expression is not confined to neoplastic processes in the skin. Similar to its expression in cutaneous mesenchymal neoplasms of fibroblastic, myofibroblastic, or fibrohistiocytic origin, TRPS1 is also found in non-neoplastic stromal cells like fibroblasts and myofibroblasts, particularly in wound healing and scar formation [35]. This may be linked to TRPS1's role as a key regulator in tissue regeneration. Notably, down-regulation of *TRPS1* has been shown to promote epithelial-mesenchymal transition (EMT) and metastasis in various cancer types by repressing FOXA1, a negative regulator of EMT [36].

TRPS1 EXPRESSION IN CUTANEOUS METASTATIC CARCINOMAS

Given the well-documented high frequency of TRPS1 expression in breast carcinomas [1], it is not surprising that 95%–100% of metastatic mammary carcinomas involving the

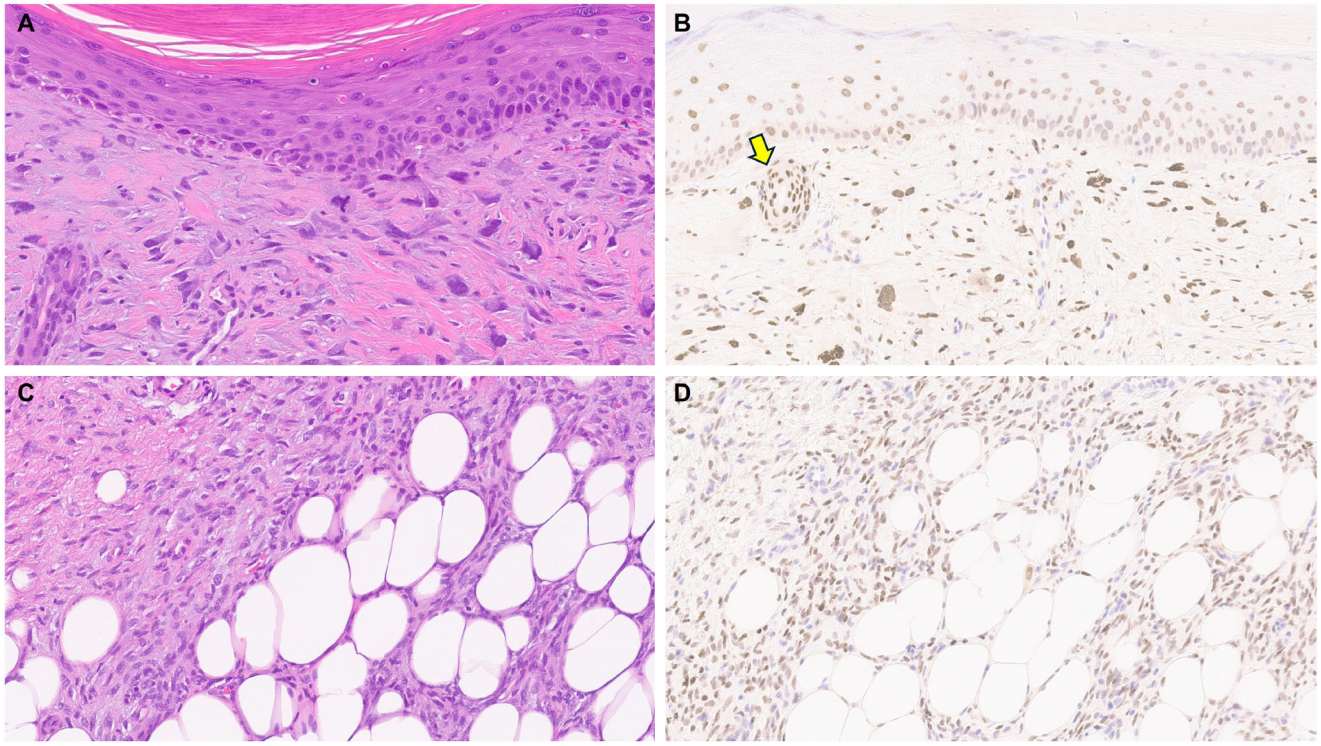

Fig. 7. Atypical fibroxanthoma and dermatofibrosarcoma protuberans. A biopsy from the left frontal scalp of a 72-year-old male patient reveals a dermal proliferation of pleomorphic spindled and epithelioid cells that are negative for cytokeratin cocktail, p40, SOX10, ERG, and desmin, but positive for CD10, consistent with atypical fibroxanthoma (A). The tumor cells exhibit diffuse and strong positivity for trichorhinophalangeal syndrome type 1 (TRPS1) (B). Notably, the intensity of TRPS1 expression in these atypical fibroxanthoma cells is similar to that in eccrine sweat ducts (yellow arrow), which serve as an internal control known to show 3+ TRPS1 immunoreactivity. A radical resection from the left groin of a 42-year-old male patient shows dermatofibrosarcoma protuberans (C), which may occasionally demonstrate TRPS1 expression (D).

skin demonstrate strong and diffuse TRPS1 immunoreactivity (Table 1) [9,14]. In contrast, only focal and weak TRPS1 immunoreactivity may occasionally be observed in metastatic carcinomas of pulmonary (particularly SCCs), gynecologic, or renal origin (Table 1) [9,14]. Notably, carcinomas originating from the gastrointestinal tract, such as colonic and gastric adenocarcinomas, or from the prostate, typically lack TRPS1 expression (Table 1) [9,14]. Therefore, in the appropriate morphologic and immunophenotypic context (e.g., CK7+/GATA3+), strong and diffuse TRPS1 expression in a suspected case of cutaneous metastasis can support a mammary origin (Fig. 8).

However, a key diagnostic limitation is that TRPS1 expression does not distinguish between a primary cutaneous adnexal carcinoma, including primary cutaneous apocrine carcinoma, and a cutaneous metastasis of breast carcinoma, as both can exhibit strong and diffuse TRPS1 positivity. In such cases, thorough clinicopathologic correlation, including imaging studies, is essential for accurate classification.

CONCLUSION

It is well recognized that the initially reported sensitivity and specificity of a new immunohistochemical marker often decline over time as its use becomes more widespread and as additional data and real-world experiences accumulate. TRPS1 IHC is no exception. Initially regarded as a highly sensitive and specific marker for breast carcinomas [1], TRPS1 has since been shown to be expressed in a broader range of cutaneous neoplasms, challenging its specificity.

As demonstrated throughout this review, TRPS1 expression is not exclusive to any single cutaneous tumor type. Nevertheless, when interpreted in conjunction with conventional markers and within the proper morphologic and immunophenotypic context, TRPS1 can offer valuable diagnostic insight. Notable

https://doi.org/10.4132/jptm.2025.11.25

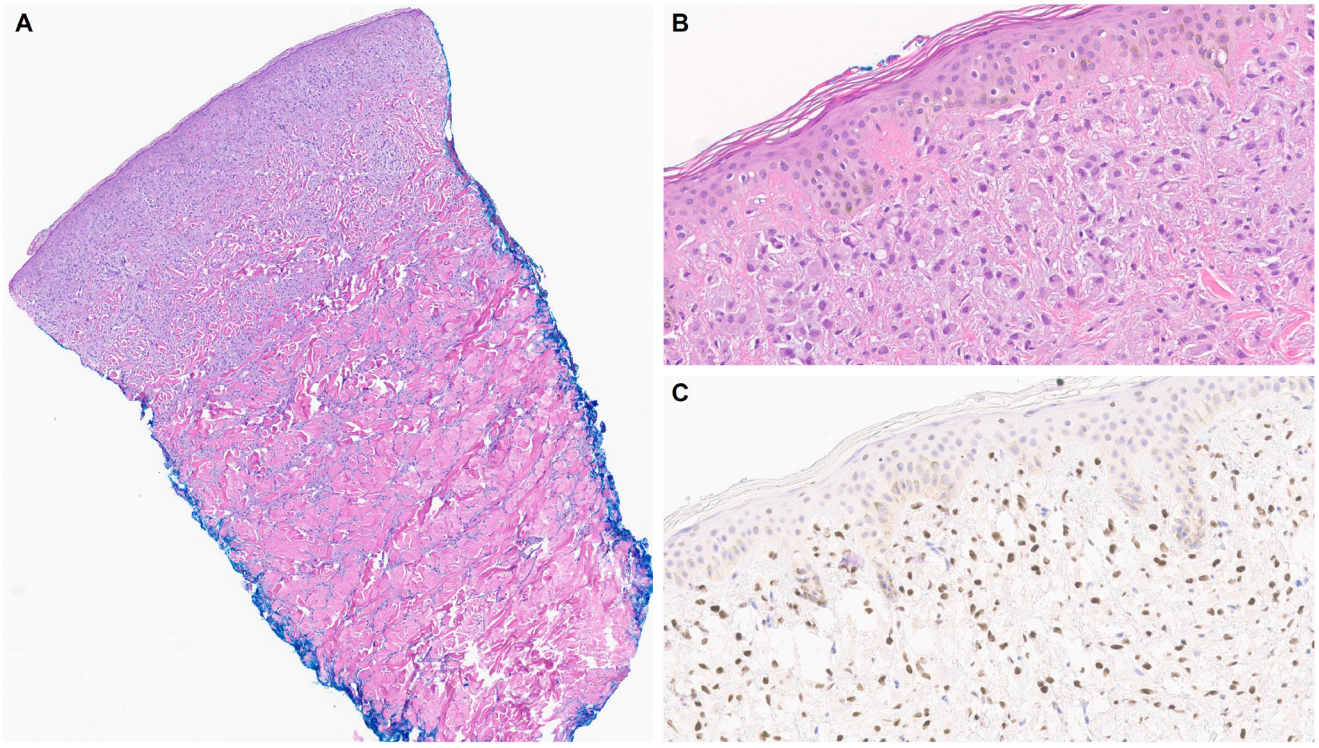

Fig. 8. Cutaneous metastasis of breast lobular carcinoma. A biopsy from the right abdomen of a 68-year-old female patient with a history of mammary lobular carcinoma reveals an infiltrating carcinoma involving the dermis, characterized by prominent histiocytoid morphology (A, B). The tumor cells show strong and diffuse nuclear positivity for trichorhinophalangeal syndrome type 1 (TRPS1) (C), supporting the diagnosis of cutaneous metastasis from the patient's known breast carcinoma.

examples include its use in diagnosing MPD (TRPS1+/CK7+/SOX10-/p63–), primary EMPD (TRPS1+/CK7+/SOX10–/p63–), primary cutaneous NUT adnexal carcinoma (TRPS1+/SOX10+/NUT+), EMPSGC (TRPS1+/INSM1+), and cutaneous metastases of mammary carcinoma (TRPS1+/CK7+/GATA3+). Although immunohistochemical studies are typically not necessary to differentiate SCCs from BCCs, the stark contrast in TRPS1 immunoreactivity (TRPS1+ in SCCs and TRPS1– in BCCs) may possibly provide additional diagnostic value.

We hope this review has provided a comprehensive and practical overview of the diagnostic utility and limitations of TRPS1 in dermatopathology. Ultimately, it is critical to emphasize that immunohistochemical findings must always be interpreted in the context of the overall morphologic features, and no single marker, regardless of its perceived sensitivity or specificity, should be used in isolation.

Ethics Statement

All procedures performed in the current review were approved by the IRB of the University of Texas MD Anderson Cancer Center (IRB#: 2022-0662) in accordance with the 1964 Helsinki declaration and its later amendments. Formal written informed consent was not required with a waiver by the appropriate IRB.

Availability of Data and Material

The data of this review are available from the corresponding author on reasonable request.

Code Availability

Not applicable.

ORCID

Mokhtar H. Abdelhammed https://orcid.org/0009-0001-9607-683X
Woo Cheal Cho https://orcid.org/0000-0001-5867-1403

Author Contributions

Conceptualization: WCC. Data curation: MHA. Formal anal-

ysis: MHA. Funding acquisition: WCC. Investigation: all authors. Methodology: WCC. Project administration: WCC. Resources: WCC. Software: N/A. Supervision: WCC. Validation: all authors. Visualization: all authors. Writing—original draft preparation: all authors. Writing—review & editing: all authors. Approval of final manuscript: all authors.

Conflicts of Interest

The authors declare that they have no potential conflicts of interest.

Funding Statement

This review was supported in part by the Institutional Start-up Funds from the University of Texas MD Anderson Cancer Center awarded to WCC.

REFERENCES

1. Ai D, Yao J, Yang F, et al. TRPS1: a highly sensitive and specific marker for breast carcinoma, especially for triple-negative breast cancer. Mod Pathol 2021; 34: 710-9.
2. Cho WC, Ding Q, Wang WL, et al. Immunohistochemical expression of TRPS1 in mammary Paget disease, extramammary Paget disease, and their close histopathologic mimics. J Cutan Pathol 2023; 50: 434-40.
3. Liu YA, Collins K, Aung PP, et al. TRPS1 expression in primary and secondary extramammary Paget diseases: an immunohistochemical analysis of 93 cases. Hum Pathol 2024; 143: 5-9.
4. Cook EE, Harrison BT, Hirsch MS. TRPS1 expression is sensitive and specific for primary extramammary Paget disease. Histopathology 2023; 83: 104-8.
5. Liu YA, Cho WC. TRPS1 expression in endocrine mucin-producing sweat gland carcinoma: diagnostic utility and pitfalls. Am J Dermatopathol 2024; 46: 133-5.
6. Liu YA, Aung PP, Wang Y, et al. TRPS1 expression in non-melanocytic cutaneous neoplasms: an immunohistochemical analysis of 200 cases. J Pathol Transl Med 2024; 58: 72-80.
7. Zengin HB, Bui CM, Rybski K, Pukhalskaya T, Yildiz B, Smoller BR. TRPS1 is differentially expressed in a variety of malignant and benign cutaneous sweat gland neoplasms. Dermatopathology (Basel) 2023; 10: 75-85.
8. Rybski KJ, Zengin HB, Smoller BR. TRPS1: a marker of follicular differentiation. Dermatopathology (Basel) 2023; 10: 173-83.
9. Taniguchi K, Goto K, Yabushita H, Yamasaki R, Ichimura K. Transcriptional repressor GATA binding 1 (TRPS1) immunoexpression in normal skin tissues and various cutaneous tumors. J Cutan Pathol 2023; 50: 1006-13.
10. Alsawas M, Muhaj FF, Aung PP, Nagarajan P, Cho WC. Syringocystadenoma papilliferum-like features in poroma: an unusual morphologic pattern of poroma or true synchronous occurrence of 2 distinct neoplasms? Am J Dermatopathol 2024; 46: 871-4.
11. Lenskaya V, Yang RK, Cho WC. Primary cutaneous apocrine carcinoma with *RARA::NPEPPS* fusion. J Cutan Pathol 2024; 51: 419-23.
12. Kim MJ, Liu YA, Wang Y, Ning J, Cho WC. TRPS1 expression is frequently seen in a subset of cutaneous mesenchymal neoplasms and tumors of uncertain differentiation: a potential diagnostic pitfall. Dermatopathology (Basel) 2024; 11: 200-8.
13. Velthof L, Van Dorpe J, Tummers P, Creytens D, Van de Vijver K. TRPS1 is consistently expressed in hidradenoma papilliferum. Int J Gynecol Pathol 2025; 44: 99-103.
14. Boulogeorgou K, Topalidis C, Koletsa T, Karayannopoulou G, Kanitakis J. Expression of TRPS1 in metastatic tumors of the skin: an immunohistochemical study of 72 cases. Dermatopathology (Basel) 2024; 11: 293-302.
15. Ibrahim E, Yang RK, Gubbiotti MA, Prieto VG, Cho WC. Primary cutaneous NUT adnexal carcinoma with *BRD4::NUTM1* fusion: a 19-year follow-up. Am J Dermatopathol 2025; 47: 731-3.
16. Goto K, Kukita Y, Hishima T, et al. Primary cutaneous NUT carcinoma: clinicopathologic and genetic study of 4 cases. Am J Surg Pathol 2024; 48: 942-52.
17. Wang J, Peng Y, Sun H, et al. TRPS1 and GATA3 expression in invasive breast carcinoma with apocrine differentiation. Arch Pathol Lab Med 2024; 148: 200-5.
18. Cimino-Mathews A, Subhawong AP, Elwood H, et al. Neural crest transcription factor Sox10 is preferentially expressed in triple-negative and metaplastic breast carcinomas. Hum Pathol 2013; 44: 959-65.
19. Rolim I, Rafael M, Robson A, Costa Rosa J. Pigmented epidermotropic breast carcinoma: a diagnostic pitfall mimicking melanoma a case report and literature review. Int J Surg Pathol 2024; 32: 386-93.
20. Lazcano R, Ingram DR, Panse G, Lazar AJ, Wang WL, Cloutier JM. Trps1 expression in MPNST is correlated with PRC2 inactivation and loss of H3K27me3. Hum Pathol 2024; 151: 105632.
21. Youssef KK, Van Keymeulen A, Lapouge G, et al. Identification of the cell lineage at the origin of basal cell carcinoma. Nat Cell Biol 2010; 12: 299-305.
22. Cazzato G, Daruish M, Fortarezza F, et al. Gene fusion-driven cutaneous adnexal neoplasms: an updated review emphasizing

https://doi.org/10.4132/jptm.2025.11.25

molecular characteristics. Am J Dermatopathol 2025; 47: 453-61.
23. Flieder A, Koerner FC, Pilch BZ, Maluf HM. Endocrine mucin-producing sweat gland carcinoma: a cutaneous neoplasm analogous to solid papillary carcinoma of breast. Am J Surg Pathol 1997; 21: 1501-6.
24. Agni M, Raven ML, Bowen RC, et al. An update on endocrine mucin-producing sweat gland carcinoma: clinicopathologic study of 63 cases and comparative analysis. Am J Surg Pathol 2020; 44: 1005-16.
25. Quattrochi B, Russell-Goldman E. Utility of insulinoma-associated protein 1 (INSM1) and mucin 2 (MUC2) immunohistochemistry in the distinction of endocrine mucin-producing sweat gland carcinoma from morphologic mimics. Am J Dermatopathol 2022; 44: 92-7.
26. Parra O, Linos K, Yan S, Lilo M, LeBlanc RE. Comparative performance of insulinoma-associated protein 1 (INSM1) and routine immunohistochemical markers of neuroendocrine differentiation in the diagnosis of endocrine mucin-producing sweat gland carcinoma. J Cutan Pathol 2021; 48: 41-6.
27. Do J, Wang Y, Aung PP, et al. INSM1: a highly sensitive marker for primary and metastatic Merkel cell carcinoma, superior to SOX11, pancytokeratin, and CK20. Hum Pathol 2025; 160: 105838.
28. Legrand M, Louveau B, Osio A, et al. Primary cutaneous NUT adnexal carcinoma: morphologic, genetic and methylation analysis of seven new cases with comparison to extracutaneous NUT carcinoma and NUTM1-rearranged porocarcinoma. Histopathology 2025; 87: 375-87.
29. Sekine S, Kiyono T, Ryo E, et al. Recurrent *YAP1-MAML2* and *YAP1-NUTM1* fusions in poroma and porocarcinoma. J Clin Invest 2019; 129: 3827-32.
30. Russell-Goldman E, Hornick JL, Hanna J. Utility of YAP1 and NUT immunohistochemistry in the diagnosis of porocarcinoma. J Cutan Pathol 2021; 48: 403-10.
31. Cassarino DS, Su A, Robbins BA, Altree-Tacha D, Ra S. SOX10 immunohistochemistry in sweat ductal/glandular neoplasms. J Cutan Pathol 2017; 44: 544-7.
32. Sellheyer K, Nelson P. Follicular stem cell marker PHLDA1 (TDAG51) is superior to cytokeratin-20 in differentiating between trichoepithelioma and basal cell carcinoma in small biopsy specimens. J Cutan Pathol 2011; 38: 542-50.
33. Clarke LE, Conway AB, Warner NM, Barnwell PN, Sceppa J, Helm KF. Expression of CK7, Cam 5.2 and Ber-Ep4 in cutaneous squamous cell carcinoma. J Cutan Pathol 2013; 40: 646-50.
34. Goldblum JR, Hart WR. Perianal Paget's disease: a histologic and immunohistochemical study of 11 cases with and without associated rectal adenocarcinoma. Am J Surg Pathol 1998; 22: 170-9.
35. Cho WC, Nagarajan P, Ding Q, Prieto VG, Torres-Cabala CA. Trichorhinophalangeal syndrome type 1-positive cells in breast dermal granulation tissues and scars: a potential diagnostic pitfall. Am J Dermatopathol 2022; 44: 964-7.
36. Huang JZ, Chen M, Zeng M, et al. Down-regulation of TRPS1 stimulates epithelial-mesenchymal transition and metastasis through repression of FOXA1. J Pathol 2016; 239: 186-96.

JPTM

REVIEW ARTICLE

pISSN 2383-7837 · eISSN 2383-7845

Journal of Pathology and Translational Medicine 2026; 60: 144-183
https://doi.org/10.4132/jptm.2026.01.09

Cutaneous soft tissue tumors in the 5th edition of the World Health Organization classification of skin tumors: key updates and new entities

Joon Hyuk Choi

Department of Pathology, Yeungnam University College of Medicine, Daegu, Korea

The 5th edition of the World Health Organization (WHO) classification of skin tumors introduces a dedicated chapter on cutaneous soft tissue tumors, providing a comprehensive, standardized reference with updated diagnostic criteria that directly inform routine dermatopathology practice and molecular diagnostics. This edition incorporates several key changes, including newly recognized entities such as *EWSR1*::*SMAD3*-rearranged fibroblastic tumor, neurotrophic tyrosine receptor kinase (NTRK)–rearranged spindle cell neoplasm, superficial CD34-positive fibroblastic tumor, and *CRTC1*::*TRIM11* cutaneous tumor. Diagnostic terminology has also been refined; for example, the term 'atypical intradermal smooth muscle neoplasm' replaces 'cutaneous leiomyosarcoma' for lesions confined to the dermis, whereas the designation leiomyosarcoma is reserved for tumors with overt subcutaneous infiltration. In addition, epithelioid fibrous histiocytoma has been reassigned to the family of tumors of uncertain differentiation. This review summarizes the key updates and newly recognized entities in the chapter on cutaneous soft tissue tumors in the 5th edition of the WHO classification of skin tumors, emphasizing their clinicopathological and molecular implications.

Keywords: World Health Organization; Classification; Soft tissue neoplasms; Diagnosis; Molecular pathology

INTRODUCTION

The 5th edition of the World Health Organization (WHO) classification of skin tumors, volume 12 of the WHO classification of tumors series, was published online in 2023 and in print in September 2025 [1]. This series is widely regarded as the gold standard for tumor diagnosis, providing an authoritative synthesis of clinical, histopathological, and molecular criteria, as well as practical diagnostic approaches. Since the publication of the 4th edition of the WHO classification of skin tumors in 2018 [2], significant advances have been made in soft tissue pathology, particularly in identifying novel molecular and genetic alterations, discovering new immunohistochemical markers, and clarifying underlying biological mechanisms [3,4]. The 5th edition incorporates these advances, thereby reflecting major progress in the understanding of soft tissue tumors.

The dedicated chapter on soft tissue tumors in the 5th edition of the WHO classification of skin tumors includes entities that are confined to the skin or characterized by distinctive cutaneous features. This chapter maintains the organizational structure of the previous edition, classifying soft tissue tumors into seven main families: (1) adipocytic tumors, (2) fibroblastic, myofibroblastic, and fibrohistiocytic tumors, (3) vascular tumors, (4) pericytic and perivascular tumors, (5) smooth muscle tumors, (6) neural tumors, and (7) tumors of uncertain differentiation (Table 1).

Cutaneous soft tissue tumors present considerable diagnostic challenges due to their diversity and overlapping histological features. The 5th edition recognizes several newly defined entities that reflect recent advances in tumor biology, molecular genetics, and diagnostic approaches [5,6]. A thorough understand-

Received: December 17, 2025 **Revised:** January 5, 2026 **Accepted:** January 8, 2026
Corresponding Author: Joon Hyuk Choi, MD, PhD
Department of Pathology, Yeungnam University College of Medicine, 170 Hyeonchung-ro, Namgu, Daegu 42415, Korea
Tel: +82-53-640-6754, Fax: +82-53-640-6769, E-mail: joonhyukchoi@ynu.ac.kr

Table 1. Soft tissue tumors that are included in the 5th edition of the WHO classification of skin tumors

- **Adipocytic tumors**
  - Benign
    - Naevus lipomatosus superficialis
    - Lipoma
    - Angiolipoma
    - Spindle cell/pleomorphic lipoma
  - *Intermediate*
    - Atypical lipomatous tumor
  - *Malignant*
    - Pleomorphic liposarcoma
- **Fibroblastic, myofibroblastic, and fibrohistiocytic tumors**
  - *Benign*
    - Fibroma of tendon sheath
    - Calcifying aponeurotic fibroma
    - Sclerotic fibroma
    - Nuchal-type fibroma
    - Gardner fibroma
    - Pleomorphic fibroma
    - Elastofibroma
    - Desmoplastic fibroblastoma
    - Fibrous papule
    - Fibroblastic connective tissue nevus
    - Fibro-osseous tumor of digits
    - Dermatofibroma (fibrous histiocytoma)
    - Superficial fibromatosis
    - Inclusion body fibromatosis
    - Plexiform fibrohistiocytic tumor
    - Superficial acral fibromyxoma
    - Cutaneous myxoma (superficial angiomyxoma)
    - Dermatomyofibroma
    - Multinucleate cell angiohistiocytoma
    - Plaque-like CD34-positive dermal fibroma
    - Nodular fasciitis
    - *EWSR1*::*SMAD3*-rearranged fibroblastic tumor
  - *Intermediate*
    - Dermatofibrosarcoma protuberans
    - Myxoinflammatory fibroblastic sarcoma
  - *Malignant*
    - Myxofibrosarcoma
- **Vascular tumors**
  - *Hemangioma*
    - Cherry hemangioma
    - Sinusoidal hemangioma
    - Microvenular hemangioma
    - Hobnail hemangioma
    - Glomeruloid hemangioma
    - Papillary hemangioma
  - *Other benign*
    - Lymphangioma (superficial lymphatic malformation)
    - Cutaneous epithelioid angiomatous nodule
    - Postradiation atypical vascular lesion
  - *Intermediate*
    - Pseudomyogenic hemangioendothelioma
    - Epithelioid hemangioendothelioma
    - Hobnail hemangioendotheliomas
    - Composite hemangioendothelioma
    - Kaposi sarcoma
  - *Malignant*
    - Cutaneous angiosarcoma
- **Pericytic and perivascular tumors**
  - *Benign*
    - Glomus tumor
    - Myopericytoma
    - Myofibroma and myofibromatosis
    - Angioleiomyoma
- **Smooth muscle tumors**
  - *Benign*
    - Smooth muscle hamartoma
    - Cutaneous leiomyomas
    - EBV-associated smooth muscle tumor
  - *Intermediate*
    - Atypical intradermal smooth muscle neoplasm
- **Neural tumors**
  - *Benign*
    - Dermal hyperneury/epithelial sheath neuroma
    - Solitary circumscribed neuroma
    - Dermal nerve sheath myxoma
    - Perineurioma
    - Neurofibroma
    - Schwannoma
    - Granular cell tumor
    - Hybrid nerve sheath tumors
  - *Malignant*
    - Malignant peripheral nerve sheath tumor
- **Tumors of uncertain differentiation**
  - *Benign*
    - Cellular neurothekeoma
    - Epithelioid fibrous histiocytoma
    - Non-neural granular cell tumor
    - PEComa
  - *Intermediate*
    - Angiomatoid fibrous histiocytoma
    - NTRK-rearranged spindle cell neoplasm
    - Atypical fibroxanthoma

(Continued to the next page)

Table 1. Continued

Spindle cell hemangioma	Superficial CD34-positive fibroblastic tumor
Epithelioid hemangioma	*Malignant*
Tufted hemangioma	Pleomorphic dermal sarcoma
Angiokeratoma	Epithelioid sarcoma
Infantile hemangioma	*CRTC1*::*TRIM11* cutaneous tumor
Congenital non-progressive hemangiomas: Rapidly involuting congenital hemangioma and non-involuting congenital hemangioma	Dermal clear cell sarcoma
Lobular capillary hemangioma	Ewing sarcoma
Poikilodermatous plaque-like hemangioma	
Acquired elastotic hemangioma	
Verrucous venous malformation	
Arteriovenous malformation	

WHO, World Health Organization; EBV, Epstein-Barr virus; PEComa, perivascular epithelioid cell tumor; NTRK, neurotrophic tyrosine receptor kinase.

ing of these updates is essential for accurate diagnosis, optimal patient management, and improved prognostication.

This review summarizes key updates to cutaneous soft tissue tumors in the 5th edition of the WHO classification, highlighting newly recognized entities and tumors incorporated from other WHO volumes, along with their clinical, histological, and molecular features, and recent advances in tumor pathogenesis and immunohistochemistry (IHC). It is intended to serve as a practical reference for practicing pathologists, with particular emphasis on updated diagnostic criteria and newly introduced molecular correlates.

The updates in the 5th edition of the WHO classification of skin tumors are summarized as follows: newly recognized tumor entities and tumors incorporated from other WHO volumes (Table 2); newly identified molecular genetic alterations and immunohistochemical markers (Table 3); tumors with revised terminology (Table 4); and tumors reassigned to different families (Table 5).

ADIPOCYTIC TUMORS

Key updates

In the 5th WHO classification, nevus lipomatosus superficialis is defined as a benign cutaneous hamartoma characterized by dermal ectopic adipose tissue rather than as a developmental anomaly [7]. It is classified into two subtypes: classic and solitary. Additionally, among conventional lipomas, osteolipoma and chondrolipoma are recognized as distinct subtypes, defined by osseous and cartilaginous metaplasia, respectively [8]. In contrast, previously described subtypes, including fibrolipoma, myxolipoma, angiomyxolipoma, sclerotic lipoma, and chondroid lipoma, have been removed from the current WHO classification [9]. Cellular angiolipoma is defined as a subtype with a predominant vascular component and a sparse adipocytic component [10,11]. Spindle cell lipoma (SCL) and pleomorphic lipoma (PL) represent a morphological spectrum of the same benign adipocytic neoplasm [12], sharing *RB1* deletion at chromosome 13q14, supporting their close biological relationship. Recognized morphologic patterns include fat-poor, myxoid, and pseudoangiomatous variants of SCL/PL (Fig. 1A, B).

Atypical lipomatous tumor (ALT) is defined as an adipocytic neoplasm of borderline malignancy characterized by focal nuclear atypia and *MDM2* and/or *CDK4* amplification [13]. Primary cutaneous or subcutaneous ALTs are exceedingly rare [14,15]. Mature heterologous elements, such as osseous or myogenic tissue, may occasionally be present; this does not indicate dedifferentiation [16,17]. The terms ALT and well-differentiated liposarcoma (WDLPS) are synonymous, as they describe morphologically and genetically identical neoplasms. However, the term 'WDLPS' should be avoided for superficial tumors because these lesions typically exhibit less aggressive behavior. Pleomorphic liposarcoma (PLPS) is a high-grade, pleomorphic spindle cell sarcoma containing variable numbers of pleomorphic lipoblasts without components of WDLPS or other differentiation (Fig. 2A, B) [18]. An epithelioid subtype of PLPS, characterized by epithelioid cytomorphology, has been recognized as a distinct subtype [19]. The absence of *MDM2* amplification is a key diagnostic criterion distinguishing PLPS from ALT and dedifferentiated liposarcoma.

https://doi.org/10.4132/jptm.2026.01.09

https://doi.org/10.4132/jptm.2026.01.09

Table 2. Newly recognized tumor entities and selected tumors newly incorporated from other volumes in the 5th edition of the WHO classification of skin tumors

Tumor family	Biological potential	Tumor type	Clinical features	Histological features	Immunohistochemistry	Molecular features
Fibroblastic, myofibroblastic, and fibrohistiocytic tumors	Benign	Fibrous papule	Middle-aged adults; sporadic in most cases; multiple early childhood lesions in tuberous sclerosis; nose, central face	Dome-shaped lesion, with dilated dermal blood vessels; spindle-shaped or stellate fibroblasts; fibrotic or collagenized stroma	CD34 (+); factor XIIIa (+)	Germline mutations in *TSC1* or *TSC2* (tuberous sclerosis-associated cases)
	Benign	Fibroblastic connective tissue nevus	Young age (median, 10 years); slight female predominance; trunk, head and neck, limbs	Bland spindle-shaped and ovoid cells arranged in short, intersecting fascicles; entrapped and preserved skin appendages	CD34 (+); SMA (+)	*KHDRBS1*::*NTRK3* (1 case)
	Benign	Fibro-osseous tumor of digit	Young adults; rapidly growing; subcutaneous tissues of the proximal phalanx (fingers and toes)	Spindle cells are arranged randomly or in short intersecting fascicles; unmineralized woven bone; vascular or myxoid stroma	SMA (+) in myofibroblasts; SATB2 (+) in osteoblast	*USP6* rearrangement
	Benign	Inclusion body fibromatosis	Most cases <3 years; ~30% present at birth; dorsal/dorsolateral distal or middle phalanges of 2nd–4th digits (hands and feet)	Spindled cells with bland nuclei and light eosinophilic cytoplasm; a rounded, pale pink, intracytoplasmic inclusion	SMA (+); calponin (+); desmin (+); inclusions: calponin-1 (+), caldesmon (+)	-
	Benign	Multinucleate cell angiohistiocytoma	Middle-aged adults; solitary or multiple; dorsal hands, fingers, lower extremities, trunk, back, rarely head and neck	Triad of multinucleated and angulated stromal cells, dermal fibrosis parallel to the epidermis, and increased small-caliber vessels	CD68 (±); factor XIIIa (+)	-
	Benign	*EWSR1*::*SMAD3*-rearranged fibroblastic tumor	Wide age range (1–68 years; median, 39 years); female predominance; acral sites, most commonly the hands and feet	Hyalinized acellular center with peripheral zones composed of intersecting fascicles of fibroblastic spindle cells; calcification	ERG (+); CD34 (–); SMA (–)	*EWSR1*::*SMAD3*
Vascular tumors	Benign	Papillary hemangioma	Adult men; exclusively head and neck	Dilated, thin-walled dermal vascular channels with numerous luminal papillary projections; intracytoplasmic eosinophilic globules	CD31 (+); CD34 (+); ERG (+)	-
	Benign	Poikilodermatous plaque-like hemangioma	Elderly men; lower extremities; usually solitary, rarely multiple plaques	Band-like proliferation of small vessels in the superficial dermis; no grenz zone; loss or reduction of elastic fibers	CD31 (+); CD34 (+); ERG (+)	-
	Benign	Acquired elastotic hemangioma	Middle-aged to elderly adults; slight female predominance; forearm, lateral neck; associated with chronic sun damage	Band-like proliferation of capillaries surrounded by pericytes; arranged parallel to the reticular dermis, in a background of solar elastosis	CD31 (+); CD34 (+); ERG (+)	-
	Intermediate	Hobnail hemangioendothelioma	PILA: infant, proximal extremities, buttock, or thigh; RHE: children or young adults, distal extremities	Hobnail endothelial cells, PILA: poorly defined slit-like or dilated lymphatic channels; RHE: infiltrative, branching vascular channels	Endothelial markers (CD31, ERG, FLI1) (+); lymphatic endothelial markers (podoplanin [D2-40], VEGFR3, PROX1) (+); loss of YAP1 C-terminus expression[a]; synaptophysin (±)[b]	PILA: unknown; RHE: *YAP1* rearrangements, most commonly *YAP1*::*MAML2* (subset)

(Continued to the next page)

Table 2. Continued

Tumor family	Biological potential	Tumor type	Clinical features	Histological features	Immunohistochemistry	Molecular features
Pericytic and perivascular tumors	Benign	Myofibroma and myofibromatosis	Most cases are in children; sporadic or familial; skin or subcutaneous tissue of the head and neck, upper extremities, trunk	Biphasic pattern of small primitive rounded cells and plump spindled myoid cells; hemangiopericytoma-like vessels	SMA (+); caldesmon (±); desmin (–)	Germline *PDGFRB* and *NOTCH3* mutations (familial); somatic *PDGFRB* mutations (sporadic); *SRF* rearrangement (cellular cases)
Smooth muscle tumors	Benign	Smooth muscle hamartoma	Broad age spectrum; usually solitary; rare multiple or familial; trunk, extremities, head and neck, external genitalia	Haphazardly arranged bundles of mature smooth muscle in the dermis, often near pilosebaceous units	SMA (+); desmin (+); caldesmon (+)	*ACTB* mutations (subset)
	Intermediate	EBV-associated smooth muscle tumor	Wide age distribution; immunosuppressed patients; CNS, liver, lung, subcutaneous tissues of the limbs and trunk	Interlacing fascicles of spindled myoid cells; admixture of smaller rounded cells; intratumoral lymphocytes	SMA (+); desmin (+); caldesmon (+); EBER in situ hybridization (+)	*MYC* overexpression (subset)
Neural tumors	Benign	Dermal hyperneury/epithelial sheath neuroma	Syndromic cases in children; sporadic cases usually present in older adults; female predominance; lips, eyelid, tongue, trunk	Dermal hyperneury: enlarged, prominent dermal neural fibers; epithelial sheath neuroma: enlarged nerve fibers ensheathed by squamous epithelium	S100 protein (+); neurofilament (+); CD57 (+) in nerve fibers; CKs in perineural epithelial sheaths	-
	Benign	Hybrid nerve sheath tumors	Any age (peak in young adults); wide anatomic sites; HSP is sporadic; HSN is associated with NF1 and NF2; HNP is associated with NF1	HSP: admixture of Schwann and perineurial cells; HSN: schwannomatous nodules or Schwann cell bundles within neurofibroma; HNP: plexiform neurofibroma with areas of perineurial differentiation	S100 protein (+) and SOX10 (+) in Schwann cells; EMA (+), claudin-1 (+), and GLUT1 (+) in perineurial cells; CD34 (+) in fibroblasts	*VGLL3* rearrangements (most HSPs)
Tumors of uncertain differentiation	Benign	Epithelioid fibrous histiocytoma	Young to middle-aged adults; female predominance; extremities, trunk, head and neck	Exophytic lesions with adnexal collarette; uniform epithelioid cells with abundant eosinophilic to amphophilic cytoplasm	ALK (+) (~90%); EMA (+) (65%); CD30 (±)	*ALK* rearrangements (~90%); *PRKC* rearrangements (rare)
	Benign	PEComa	Wide age (15–81 years); peak incidence in middle age; female predominance; extremities (lower limbs), trunk, head and neck	Epithelioid cells with granular, eosinophilic to clear cytoplasm; nested or trabecular architecture; perivascular growth; rare malignant features (mitotic activity, necrosis, and pleomorphism)	Melanocytic markers (HMB-45, melan-A [MART1], MITF) (+); smooth muscle markers (SMA, desmin, caldesmon) (+)	Frequent deletion of 16p; loss of heterozygosity at *TSC2*; *TP53* mutations (63% of *TSC2*-mutated tumors)
	Intermediate	Angiomatoid fibrous histiocytoma	Wide age range; peak in the first two decades of life; extremities, trunk, head and neck	Fascicles or sheets of ovoid and spindled cells; pseudoangiomatoid spaces; peripheral cuff of lymphoplasmacytic cells	SOX9 (+); desmin (+) (~50%); EMA (±); CD99 (±); CD68 (±)	*EWSR1*::*CREB1* (most frequent); *EWSR1*::*ATF1*, *FUS*::*ATF1* (rare)
	Intermediate	NTRK-rearranged spindle cell neoplasm	Any age, most commonly pediatric; no sex predilection; extremities, trunk, head and neck	Haphazardly arranged spindled cells; infiltrative growth within fat resembling lipofibromatosis; distinctive stromal and perivascular keloidal collagen	CD34 (+); S100 protein (+); pan-TRK (+); SMA (±); SOX10 (–)	*NTRK1* rearrangements: *LMNA*::*NTRK1*, *TPR*::*NTRK1*, or *TPM3*::*NTRK1*; others: *NTRK2*, *NTRK3* rearrangements

(Continued to the next page)

https://doi.org/10.4132/jptm.2026.01.09

Table 2. Continued

Tumor family	Biological potential	Tumor type	Clinical features	Histological features	Immunohistochemistry	Molecular features
	Intermediate	Superficial CD34-positive fibroblastic tumor	Middle-aged adults; slight male predominance; lower extremities (especially thigh), arm, buttock, shoulder, vulva	Spindle and pleomorphic cells with abundant, granular to glassy cytoplasm; marked nuclear pleomorphism; low mitotic activity	CD34 (+); PRDM10 (+); CADM3 (SynCAM3) (+); CKs (+) (~70%)	*PRDM10* rearrangement (~60%)
	Malignant	*CRTC1*::*TRIM11* cutaneous tumor	Broad age range (median, 44 years); extremities, trunk, head; oral and nasal mucosa (rare); slow-growing, skin-colored nodule; generally no pigment	Dermal-based, circumscribed; epithelioid to fusiform cells with vesicular nuclei, prominent nucleoli, and pale cytoplasm; intersecting fascicles;	Melanocytic markers (SOX10, S100 protein, melan-A [MART1]) (+)[c]; TRIM11 (+); Pan-TRK (+) (~60%)	*CRTC1*::*TRIM11*

WHO, World Health Organization; SMA, smooth muscle actin; SATB2, special AT-rich sequence-binding protein 2; ERG, ETS-related gene; PILA, papillary intralymphatic angioendothelioma; RHE, retiform hemangioendothelioma; FLI1, Friend leukemia virus integration 1; VEGFR3, vascular endothelial growth factor receptor 3; PROX1, prospero homeobox 1; YAP1 C-terminus, yes-associated protein 1 C-terminus; EBV, Epstein-Barr virus; CNS, central nervous system; EBER, Epstein-Barr virus-encoded small RNAs; CK, cytokeratin; HSP, hybrid schwannoma/perineurioma; HSN, hybrid schwannoma/neurofibroma; NF1, neurofibromatosis type 1; NF2, neurofibromatosis type 2; HNP, hybrid neurofibroma/perineurioma; SOX10, SRY-box transcription factor 10; EMA, epithelial membrane antigen; GLUT1, glucose transporter 1; ALK, anaplastic lymphoma kinase; PEComa, perivascular epithelioid cell tumor; HMB-45, human melanoma black 45; MART1, melanoma antigen recognized by T cells 1; MITF, microphthalmia-associated transcription factor; SOX9, SRY-box transcription factor 9; NTRK, neurotrophic tyrosine receptor kinase; pan-TRK, pan-tropomyosin receptor kinase; PRDM10, PR domain–containing protein 10; CADM3, cell adhesion molecule 3; SynCAM3, synaptic cell adhesion molecule 3; TRIM11, tripartite motif–containing 11; +, positive staining; ±, variable staining; –, negative staining.

[a]Loss of expression of YAP1 C-terminus is seen in subsets of RHE with *YAP1* rearrangements; [b]Limited synaptophysin expression may be seen in PILA and RHE; [c]All tumors show diffuse SOX10 expression, whereas diffuse S100 protein staining is present in only about 50% of cases and melan-A (MART1) and HMB-45 are expressed only focally.

Table 3. Newly identified molecular genetic alterations and immunohistochemical markers in selected cutaneous soft tissue tumors

Tumor category	Tumor type	Molecular genetic alterations	Immunohistochemistry
Adipocytic tumors	Naevus lipomatosus superficialis	Deletion of 2p24 (1 case)	-
	Lipoma	Chromosome 12q13-15 rearrangements involving *HMGA2*; chromosome 16p21 rearrangements involving *HMGA1*	HMGA2 (+)
	Angiolipoma	Mutations in *PRKD2* and *PIK3CA*	-
	Spindle cell/pleomorphic lipoma	Partial or complete loss of chromosome 13q14 (RB1 locus) and/or 16q deletions	Loss of RB1 expression; CD34 (+)
	Atypical lipomatous tumor	Amplification of *MDM2*, *CDK4*, *TSPAN31* (*SAS*), *HMGA2*, and *CPM* at 12q13-q15 region	MDM2 (+); CDK4 (+)
	Pleomorphic liposarcoma	Frequent loss of *TP53*, *RB1*, and *NF1*; frequent gain in 1p21, 1q21-q22, 5p13-p15, and 7q22	-
Fibroblastic, myofibroblastic, and fibrohistiocytic tumors	Fibroma of tendon sheath	USP6 fusion with various partners (*PKM*, *RCC1*, *ASPN*, *COL1A1*, *COL3A1*, *MYH9*, *MIR22HG*, *CTNNB1*, *SPARC*, *CAP1*, *EMP1*, *CYTOR*, *NR1D1*, *RAB1A*, and *TNC*)	-
	Calcifying aponeurotic fibroma	*FN1*::*EGF*	EGF overexpression
	Sclerotic fibroma	Loss of *PTEN* (Cowden syndrome)	CD34 (+); loss of PTEN expression (Cowden syndrome)
	Nuchal-type fibroma	*APC* mutations (a few cases); *MUTYH* mutation (1 case)	May show β-catenin nuclear expression
	Gardner fibroma	Germline *APC* mutations (FAP-associated tumors)	CD34 (+); β-catenin nuclear expression (FAP-associated tumors)
	Pleomorphic fibroma	*RB1* deletion; germline mutations in *TP53* (Li-Fraumeni syndrome)	Loss of RB1 expression; CD34 (+)

(Continued to the next page)

Table 3. Continued

Tumor category	Tumor type	Molecular genetic alterations	Immunohistochemistry
	Elastofibroma	Copy gains (Xq); alterations to chromosome 1; t(8;12)(q22;q24.3); t(2;19) and t(X;1) rearrangements (some cases)	-
	Desmoplastic fibroblastoma	t(2;11)(q31;q12); t(11;17)(q12;p11.2)	FOSL1 overexpression
	Dermatofibroma (fibrous histiocytoma)	Recurrent gene fusions involving *PKC* isoforms (*PRKCA*, *PRKCB*, and *PRKCD*) with various membrane-associated partners (*LAMTOR1*, *PDPN*, *CD63*, and *KIRREL* family genes) (minority of cases)	SMA (+); desmin (+) (~30%); CD34 (+) (5%)
	Superficial fibromatosis	Lack of *CTNNB1* and *APC* mutations	β-catenin nuclear expression (rare cases); SMA (±); desmin (±)
	Plexiform fibrohistiocytic tumor	46,X,del(X)(q13)[3]/46,XX[23], 46,XY,t(4;15)(q21;q15), and 46,XY,-6,-8,del(4)(q25q31),del(20)(q11.2) with additional der (8)(p22) (1 case)	SMA (+) in myofibroblasts; CD68 (+) in histiocytes
	Superficial acral fibromyxoma	*RB1* deletions	Loss of RB1 expression; CD34 (+); CD99 (+); nestin (+)
	Cutaneous myxoma (superficial angiomyxoma)	*PRKAR1A* mutations (45%–65% of Carney complex); *MYH8* mutations	Loss of PRKAR1A expression; SMA (+)
	Nodular fasciitis	*USP6* rearrangements (~90%); *MYH9*::*USP6* (>65%); *PPP6R3*::*USP6* and *CALD1*::*USP6* (malignant cases); *EIF5A*::*USP6* (dermal nodular fasciitis with atypical mitosis)	SMA (+)
	Dermatofibrosarcoma protuberans	*COL1A1*::*PDGFB* (>90%); *PDGFD* rearrangements with *COL6A3*, *EMILIN2*, or *TNC* (<5%)	CD34 (+)
	Myxoinflammatory fibroblastic sarcoma	*VGLL3* amplification (>50%); *TGFBR3*::*MGEA5* (13%); *BRAF* fusions or amplifications	Cyclin D1 (+); factor XIIIa (+); podoplanin (D2-40) (+); CD10 (+); CD34 (±); CD163 (±); PRAME (±); CKs (±); CD68 (±); SMA (±)
	Myxofibrosarcoma	Frequent 5p gains with coamplification of *TRIO*, *RICTOR*, *SKP2*, and *AMACR* (associated with higher grade); inactivating mutations in *TP53* (46%), *RB1* (18%), and/or *CDKN2A/2B* (16%)	SMA (±); CD34 (±)
Vascular tumors	Cherry hemangioma	Frequent somatic mutations of *GNA14*, *GNA11*, and *GNAQ*; rare somatic mutations in *HRAS* and *KRAS*	-
	Spindle cell hemangioma	*IDH1* p.R132C hotspot mutations (sporadic lesions and Maffucci syndrome); frequent somatic alterations in 2p22.3, 2q24.3, and 14q11.2 (Maffucci syndrome)	Endothelial markers (CD31, CD34, ERG) (+) in endothelial cells; SMA (±) and/or desmin (±) in spindle cells
	Epithelioid hemangioma	*FOS* or *FOSB* gene rearrangements	Endothelial markers (CD31, CD34, ERG) (+) in endothelial cells; FOSB (+) (*FOSB*-rearranged cases); SMA-positive pericytes
	Infantile hemangioma	No identified genetic abnormalities	GLUT1 (+)
	Congenital non-progressive hemangioma: RICH and NICH	Somatic activating mutations in *GNAQ* and *GNA11* (RICH and NICH)	GLUT1 (–)
	Lobular capillary hemangioma	RAS-family and *BRAF* mutations (mainly c.1799T>A p.V600E)	-
	Verrucous venous malformation	Somatic missense mutation in *MAP3K3* (some cases)	GLUT1 (±)[a]
	Arteriovenous malformation	Germline *RASA1* mutations (hereditary CM-AVM syndrome)	GLUT1 (–)
	Lymphangioma (superficial lymphatic malformation)	Mutations in *FLT4* (families with Milroy disease); mutations in *PROX1* and *FOXC2*	Lymphatic endothelial markers (podoplanin [D2-40], LYVE1, PROX1) (+); endothelial markers (CD31, ERG) (+)

(Continued to the next page)

https://doi.org/10.4132/jptm.2026.01.09

https://doi.org/10.4132/jptm.2026.01.09

Table 3. Continued

Tumor category	Tumor type	Molecular genetic alterations	Immunohistochemistry
	Postradiation atypical vascular lesion	Mutations in *HRAS* and *TERT* (rare cases)	Endothelial markers (CD31, CD34, ERG) (+); lymphatic endothelial markers (podoplanin [D2-40], LYVE1, PROX1) (+)
	Pseudomyogenic hemangioendothelioma	FOSB rearrangement, including *SERPINE1*::*FOSB*, *ACTB*::*FOSB*, *WWTR1*::*FOSB*, *CLTC*::*FOSB*, and *EGFL7*::*FOSB* (more aggressive)	CKs (+); FLI1 (+); ERG (+); FOSB (+); CD31 (+) (~50%); SMA (+) (~30%); CD34 (–)
	Epithelioid hemangioendothelioma	*WWTR1*::*CAMTA1* (>90%); *YAP1*::*TFE3* (rare subtype)	CAMTA1 (+) in EHE with *WWTR1*::*CAMTA1* fusion; TFE3 (+) and loss of YAP1 C-terminus expression in EHE with *YAP1*::*TFE3* fusion
	Composite hemangioendothelioma	*YAP1*::*MAML2* (~27%); *PTBP1*::*MAML2* (3 cases of neuroendocrine CHE); *EPC1*::*PCH2* (1 case of neuroendocrine CHE)	Loss of YAP1 C-terminus expression in CHE with *YAP1*::*MAML2* fusions; synaptophysin (+) in neuroendocrine CHE
	Kaposi sarcoma	Gain at 11q13 with *FGF3* and *FGF4* amplification; Y chromosome loss (early lesions); copy-number changes involving chromosomes 16, 17, 21, X, and Y (late lesions)	KSHV/HHV8-associated protein LANA-1 (+); CD31 (+); CD34 (+); ERG (+); podoplanin (D2-40) (+)
	Cutaneous angiosarcoma	Mutations in *KDR*, *PTPRB*, and *PLCG1* (~40%); *MYC* amplification in >90% of radiation- and lymphedema-associated angiosarcoma;*CIC* alterations (younger patients)	MYC (+)[b] and frequent loss of H3K27me3 expression in radiation-induced angiosarcoma; CKs (+) and EMA (+) in epithelioid angiosarcoma
Pericytic and perivascular tumors	Glomus tumor	Mutations in *GLMN* (familial); MIR143 and NOTCH genes (*NOTCH1*, *NOTCH2*, or *NOTCH3*) rearrangements (sporadic); *BRAF* p.V600E mutations (rare malignant tumors)	SMA (+); caldesmon (+); collagen IV (+); RGS5 (+)
	Myopericytoma	*BRAF* mutations (15%)	SMA (+); caldesmon (+); MSA (+)
	Angioleiomyoma	Monosomy of chromosome 13; loss of 6p, 21q, and 13q; *NOTCH* gene fusions (very small subset)	SMA (+); calponin (+); caldesmon (+); desmin (±); RGS5 (+)
Smooth muscle tumors	Cutaneous leiomyomas	Germline mutations in *FH* (HLRCC-associated tumors)	SMA (+); desmin (+); caldesmon (+); FH (–) and 2SC (+) in HLRCC-associated tumors
Neural tumors	Perineurioma	Deletion of 22q12, monosomies, and mutations in NF2; deletion of 17q11 (soft tissue subtype); 10q24 rearrangement (sclerosing subtype); loss of 13q and small deletions of chromosomes 3, 6, and 9 (malignant perineurioma)	EMA (+); collagen IV (+); laminin (+); claudin-1 (+); GLUT1 (+); CD34 (+) (~60%)
	Neurofibroma	Mutations in *NF1* gene (multiple or plexiform and diffuse subtypes); loss of *CDKN2A* (*ANNUBP*)	S100 protein (+); SOX 10 (+); CD34 (+) in perineurial fibroblasts; peripherin (+) in thin axons
	Schwannoma	*NF2* mutations with complete or partial loss of chromosome 22; alterations in *ARID1A/ARID1B* (~29%), *TSC1/TSC2* (~15%), or *SH3PXD2A*::*HTRA1* (~10%); germline mutations in *NF2*, *LZTR1*, *SMARCB1*, and *DGCR8* (associated with schwannoma susceptibility)	S100 protein (+); SOX10 (+); EMA (+) in perineurial capsule
	Granular cell tumor	Loss-of-function mutations in *ATP6AP1* and *ATP6AP2* (~72%)	S100 protein (+); SOX10 (+); CD68 (+); inhibin (±); calretinin (±); TFE3 (±); MITF (±)
	Malignant peripheral nerve sheath tumor	Mutations in *NF1*, *CDKN2A/CDKN2B*, and PRC2 core components (*EED* or *SUZ12*); complete loss of PRC2 activity and H3K27me3 expression (~80% of high-grade MPNSTs); *SMARCB1* inactivation (~75% of epithelioid subtype)	S100 protein (+) (<50%); SOX10 (+) (<70%); GFAP (+) (<20%–30%); loss of H3K27me3 expression[c]

(Continued to the next page)

Table 3. Continued

Tumor category	Tumor type	Molecular genetic alterations	Immunohistochemistry
Tumors of uncertain differentiation	Non-neural granular cell tumor	*ALK* rearrangements (60%)	CD68 (+); CD63 (NKI/C3) (+); ALK (+) (subset)
	Atypical fibroxanthoma	UV-radiation signature mutations in *TP53*; 9p and 13q deletions; *TERT* mutations	CD10 (+); CD68 (±); CD163 (±)
	Pleomorphic dermal sarcoma	Mutations in *TP53*, NOTCH family genes, and *TERT* promoter; alterations in *CDKN2A* and *CDKN2B*	CD10 (+); CD99 (+); PDGFRB (±); SMA (±); CD31 (±)
	Epithelioid sarcoma	Monoallelic or biallelic *SMARCB1* deletion	Loss of SMARCB1 (INI1); CKs (+); EMA (+); CD34 (+) (>50%); ERG (+) (40%–67%)
	Dermal clear cell sarcoma	*EWSR1*::*ATF1* (70%–90%); *EWSR1*::*CREB1* (~5%)	S100 protein (+); SOX10 (+); PMEL (gp100) (+); TYRP1 (gp75) (+); melan-A (MART1) (+); MITF (+); PRAME (±)[d]
	Ewing sarcoma	*EWSR1*::*FLI1* (~85%); *EWSR1*::*ERG* (5%–10%); EWSR1::FEV (rare); *EWSR1*::*ETV1* (rare); *FUS*::*ERG* (rare)	CD99 (+); NKX2.2 (+); FLI1 (+) and ERG (+)[e]

HMGA2, high mobility group AT-hook 2; RB1, retinoblastoma 1; MDM2, mouse double minute 2; CDK4, cyclin-dependent kinase 4; EGF, epidermal growth factor; PTEN, phosphatase and tensin homolog; FAP, familial adenomatous polyposis; FOSL1, FOS-like antigen 1; SMA, smooth muscle actin; PRKAR1A, protein kinase cAMP-dependent regulatory subunit type I alpha; PRAME, preferentially expressed antigen in melanoma; CK, cytokeratin; ERG, ETS-related gene; FOSB, FBJ murine osteosarcoma viral oncogene homolog B; GLUT1, glucose transporter 1; RICH, rapidly involuting congenital hemangioma; NICH, non-involuting congenital hemangioma; CM-AVM, capillary malformation–arteriovenous malformation; LYVE1, lymphatic vessel endothelial hyaluronan receptor 1; PROX1, prospero homeobox 1; FLI1, Friend leukemia virus integration 1; CAMTA1, calmodulin-binding transcription activator 1; EHE, epithelioid hemangioendothelioma; TFE3, transcription factor E3; YAP1 C-terminus, yes-associated protein 1 C-terminus; CHE, composite hemangioendothelioma; KSHV, Kaposi sarcoma-associated herpesvirus; HHV8, human herpesvirus 8; LANA-1, latency-associated nuclear antigen-1; MYC, MYC proto-oncogene; H3K27me3, histone H3 lysine 27 trimethylation; EMA, epithelial membrane antigen; RGS5, regulator of G-protein signaling 5; MSA, muscle-specific actin; HLRCC, hereditary leiomyomatosis and renal cell carcinoma; FH, fumarate hydratase; 2SC, 2-succinylcysteine; ANNUBP, atypical neurofibromatous neoplasm of uncertain biological potential; SOX10, SRY-box transcription factor 10; MITF, microphthalmia-associated transcription factor; PRC2, polycomb repressive complex 2; GFAP, glial fibrillary acidic protein; ALK, anaplastic lymphoma kinase; NOTCH, neurogenic locus notch homolog; PDGFRB, platelet-derived growth factor receptor beta; SMARCB1, SWI/SNF related, matrix associated, actin-dependent regulator of chromatin, subfamily B, member 1; INI1, integrase interactor 1; PMEL, premelanosome protein; TYRP1, tyrosinase-related protein 1; MART1, melanoma antigen recognized by T cells 1; NKX2.2, NK2 homeobox 2; +, positive staining; ±, variable staining; –, negative staining.
[a]Focal and weak endothelial GLUT1 positivity may be seen; [b]Radiation- and lymphedema-associated angiosarcomas are almost always positive for MYC but may occasionally be negative; [c]Complete loss of H3K27me3 expression occurs more frequently in high-grade and radiation-induced MPNSTs than in low-grade MPNSTs; [d]PRAME expression is usually absent or only focal; [e]FLI1 and ERG are often expressed in cases with the corresponding translocation.

Table 4. Soft tissue tumors with terminology changes in the 5th WHO classification of skin tumors

Tumor family	4th edition WHO classification of skin tumors and 5th edition WHO classification of soft tissue tumors	5th edition WHO classification of skin tumors
Fibroblastic, myofibroblastic, and fibrohistiocytic tumors	Collagenous fibroma	Desmoplastic fibroblastoma
	Acral fibromyxoma	Superficial acral fibromyxoma
	EWSR1-SMAD3–positive fibroblastic tumor (emerging)	*EWSR1*::*SMAD3*-rearranged fibroblastic tumor
Vascular tumors	Atypical vascular lesion	Postradiation atypical vascular lesion
	Retiform hemangioendothelioma	Hobnail hemangioendothelioma
Smooth muscle tumors	Cutaneous leiomyosarcoma (atypical smooth muscle tumor)	Atypical intradermal smooth muscle neoplasm
Tumors of uncertain differentiation	Primitive non-neural granular cell tumor	Non-neural granular cell tumor
	NTRK-rearranged spindle cell neoplasm (emerging)	NTRK-rearranged spindle cell neoplasm

WHO, World Health Organization; NTRK, neurotrophic tyrosine receptor kinase.

https://doi.org/10.4132/jptm.2026.01.09

Table 5. Selected soft tissue tumors whose tumor family has been changed in the 5th edition of the WHO classification of skin tumors

Tumor type	4th WHO classification of skin tumors and 5th WHO classification of soft tissue tumors	5th WHO classification of skin tumors
Epithelioid fibrous histiocytoma	Fibroblastic, myofibroblastic, and fibrohistiocytic tumors	Tumors of uncertain differentiation
Myofibroma and myofibromatosis	Fibroblastic, myofibroblastic, and fibrohistiocytic tumors	Pericytic and perivascular tumors
Superficial CD34-positive fibroblastic tumor	Fibroblastic, myofibroblastic, and fibrohistiocytic tumors	Tumors of uncertain differentiation
Myxofibrosarcoma	Tumors of uncertain differentiation	Fibroblastic, myofibroblastic, and fibrohistiocytic tumors

WHO, World Health Organization.

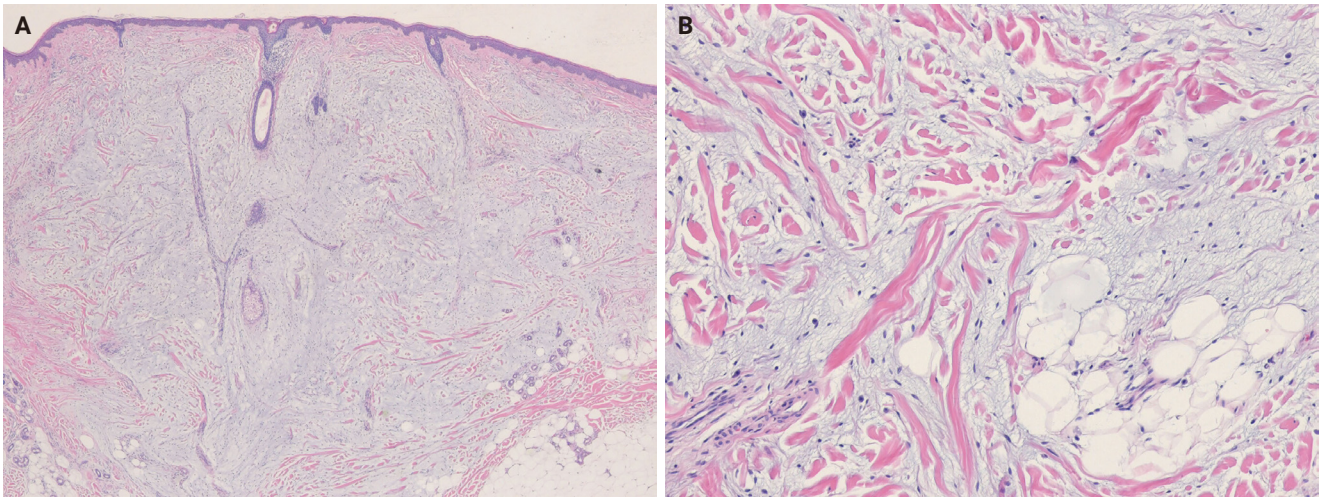

Fig. 1. Dermal myxoid spindle cell lipoma. (A) An unencapsulated, infiltrative tumor is present in the dermis. (B) The tumor is composed of bland, short spindle cells, mature adipocytes, and ropy collagen bundles in a prominent myxoid stroma.

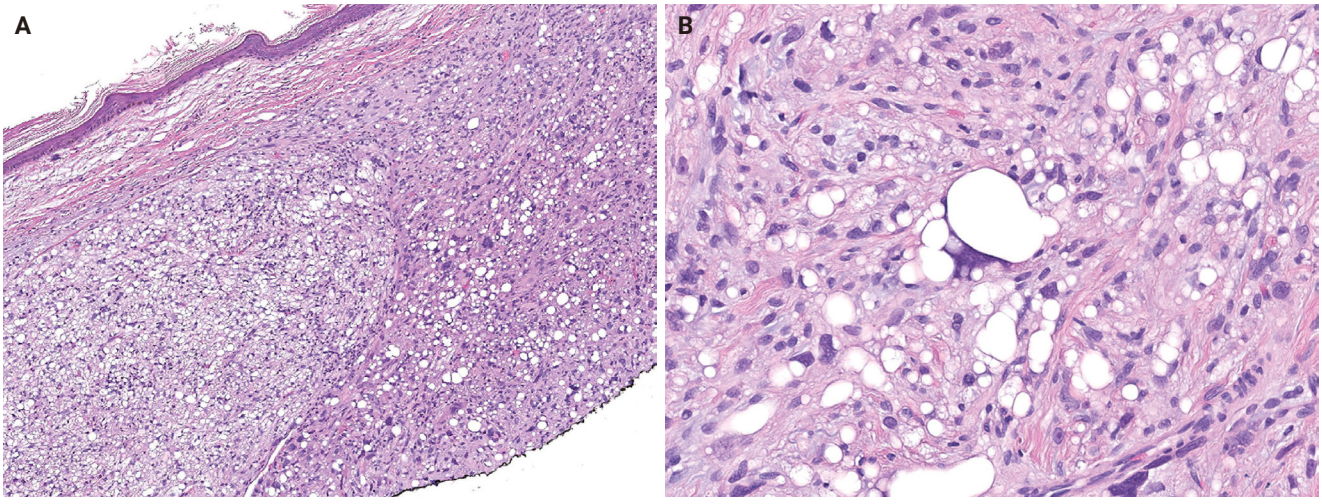

Fig. 2. Dermal pleomorphic liposarcoma. (A) The tumor is composed of an undifferentiated spindle cell sarcoma containing numerous pleomorphic lipoblasts. (B) Pleomorphic lipoblasts have lipid droplets indenting the pleomorphic, hyperchromatic nuclei. Signet-ring lipoblasts are also present. Reprinted from Patel and Folpe. Pleomorphic liposarcoma. In: WHO Classification of Tumours Editorial Board, ed. WHO classification of tumours: skin tumours. 5th ed. [18], with permission from IARC Press.

FIBROBLASTIC, MYOFIBROBLASTIC, AND FIBROHISTIOCYTIC TUMORS

Key updates

The fibroblastic, myofibroblastic, and fibrohistiocytic tumor family has been expanded in the 5th WHO classification to include several newly described entities, such as fibrous papule, fibroblastic connective tissue nevus (FCTN), fibro-osseous tumor of digits (FOTD), inclusion body fibromatosis (IBF), multinucleate cell angiohistiocytoma (MCA), and *EWSR1*::*SMAD3*-rearranged fibroblastic tumor (ESRFT). Epithelioid fibrous histiocytoma (EFH), previously classified as a subtype of dermatofibroma (fibrous histiocytoma), is now recognized as a distinct entity characterized by anaplastic lymphoma kinase (ALK) overexpression due to *ALK* rearrangement and reassigned to the family of tumors of uncertain differentiation. Myxofibrosarcoma, previously placed in the family of tumors of uncertain differentiation, has been reclassified within the fibroblastic, myofibroblastic, and fibrohistiocytic tumor family. The fibroblastic tumor previously designated as *EWSR1*::*SMAD3*-positive (emerging) is now formally recognized as an ESRFT.

Additionally, the 5th WHO classification identifies recurrent *USP6* gene rearrangements with multiple fusion partners, including *PKM*, *RCC1*, *ASPN*, *COL1A1*, *COL3A1*, *MYH9*, *MIR22HG*, *CTNNB1*, *SPARC*, *CAP1*, *EMP1*, *CYTOR*, *NR1D1*, *RAB1A*, and *TNC*, in fibroma of tendon sheath [20,21], supporting the concept that some cases represent a tenosynovial variant of nodular fasciitis [22]. Calcifying aponeurotic fibroma (CAF) harbors a recurrent *FN1*::*EGF* fusion, leading to aberrant epidermal growth factor (EGF) expression [23]. This fusion has also been identified in a subset of lipofibromatosis-like tumors, which may represent CAF variants lacking calcification [24]. Patients younger than 5 years are at higher risk of local recurrence [25]. In sclerotic fibroma, loss of phosphatase and tensin homolog (PTEN) expression on IHC may suggest Cowden syndrome [26]. Multiple pleomorphic fibromas in young patients may indicate an underlying genetic cancer syndrome, such as Li-Fraumeni syndrome associated with *TP53* germline mutations [27].

In the 5th edition, dermatofibroma (fibrous histiocytoma) is formally classified into five subtypes—classic, cellular, aneurysmal, atypical, and deep fibrous histiocytoma—each with distinct clinical and pathological features (Fig. 3A, B) [28]. Recurrent gene fusions involving *PKC* isoforms (*PRKCA*, *PRKCB*, and *PRKCD*) and various genes encoding membrane-associated proteins (*LAMTOR1*, *PDPN*, *CD63*, and *KIRREL* family genes) have been identified in a subset of these tumors [29-31]. Superficial fibromatosis is defined as a nodular, locally recurrent fibroblastic/myofibroblastic proliferation that includes palmar, plantar, and penile subtypes [32]. Although superficial fibromatosis involves activation of the WNT/β-catenin signaling pathway, it lacks the *CTNNB1* and *APC* mutations characteristic of desmoid fibromatosis [33]. Plexiform fibrohistiocytic tumor exhibits diverse cytogenetic alterations, including 46,X,del(X)(q13)[3]/46,XX[23]; 46,XY,t(4;15)(q21;q15); and 46,XY,-6,-8,del(4)

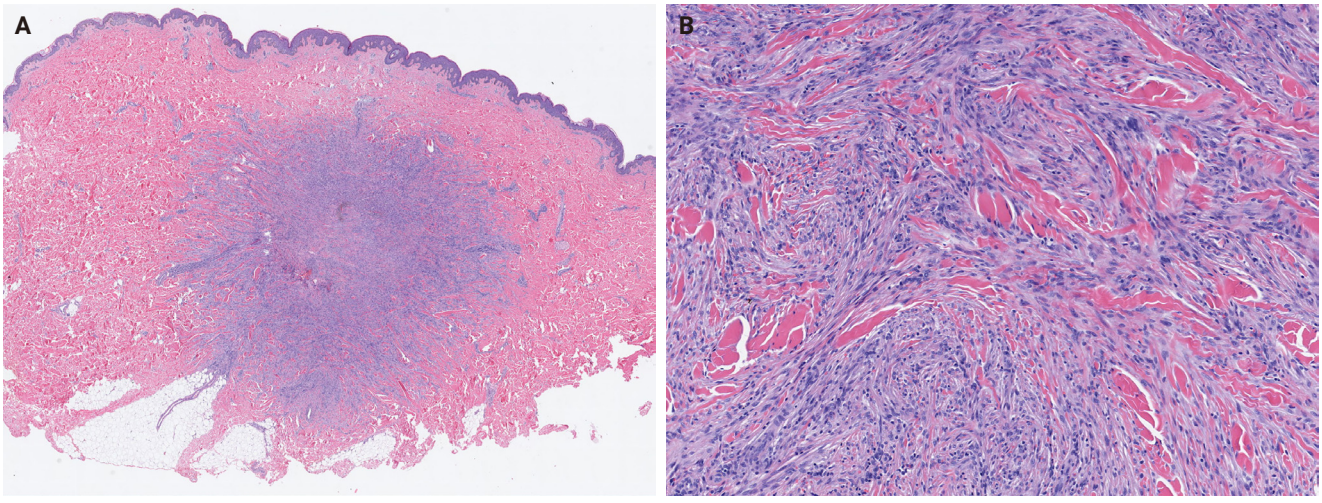

Fig. 3. Cellular dermatofibroma (fibrous histiocytoma). (A) Scanning magnification shows a dermal tumor with lateral borders interdigitating with the adjacent dermis. The overlying epidermis shows acanthosis. (B) The tumor is highly cellular and composed of spindle cells arranged in a storiform pattern. Hyalinized collagen fibers are present.

https://doi.org/10.4132/jptm.2026.01.09

(q25q31),del(20)(q11.2) with additional der(8)(p22) [34-36].

In cutaneous myxoma (superficial angiomyxoma), approximately 45%–65% of Carney complex-associated cases harbor *PRKAR1A* mutations [37,38], while alternative genetic pathways, including *MYH8* mutations, have also been identified [39]. Nodular fasciitis shows *USP6* rearrangements in approximately 90% of cases, with *MYH9*::*USP6* accounting for >65% of these [40]. Atypical or malignant nodular fasciitis cases harboring *PPP6R3*::*USP6* or *CALD1*::*USP6* fusions have rarely been reported [41,42]. An *EIF5A*::*USP6* fusion has also been identified in dermal nodular fasciitis of the forearm with atypical mitoses [43]. In dermatofibrosarcoma protuberans (DFSP), *COL1A1*::*PDGFB* remains the hallmark translocation, while alternative *PDGFD* rearrangements involving *COL6A3*, *EMILIN2*, or *TNC* have also been described [44-46]. Genomic gains of *COL1A1*::*PDGFB* and alterations in the mechanistic target of rapamycin (mTOR) pathway have been associated with fibrosarcomatous transformation [46,47]. The subtypes of DFSP have been standardized to include classic DFSP, giant cell fibroblastoma, myxoid DFSP, pigmented DFSP, myoid DFSP, plaque-like DFSP, DFSP with fibrosarcomatous transformation, and other morphological patterns (granular cell, sclerosing, and atrophic types) (Fig. 4A, B) [48].

In myxoinflammatory fibroblastic sarcoma (MIFS), *VGLL3* amplification at 3p11-p12 occurs in >50% of cases, resulting in a supernumerary ring chromosome [49]. Histologically, MIFS is characterized by atypical fibroblastic cells with macronucleoli and a mixed inflammatory infiltrate in variably myxoid and hyalinized stroma (Fig. 5A, B) [50]. A t(1;10) translocation involving *MGEA5* (*OAG*) (10q24) and *TGFBR3* (1p22) is present in approximately 13% of cases and has also been identified in pure hemosiderotic fibrolipomatous tumors (HFLTs), hybrid MIFS-HFLT lesions, and pleomorphic hyalinizing angiectatic tumors [51-53]. *BRAF* fusions or amplifications have also been identified [54]. Myxofibrosarcomas exhibit frequent chromosomal rearrangements and copy-number alterations, even in low-grade tumors, with increasing genomic complexity in recurrent tumors showing histological progression [55-58]. Myxofibrosarcomas are characterized by somatic copy-number alterations, with several oncogenes—*TRIO*, *RICTOR*, *SKP2*, and *AMACR*—located on 5p, which is frequently gained, often co-amplified, and associated with higher histological grade [59-61]. Alterations in tumor suppressor genes, including *TP53* (46%), *RB1* (18%), and *CDKN2A*/*CDKN2B* (16%), occur more frequently than oncogene amplifications involving *CDK6*, *CCND1*, or *MDM2* [61].

Fibrous papule

Fibrous papule is a benign lesion of presumed fibroblastic origin that most commonly arises on the nose or central face [62]. It predominantly affects middle-aged adults [63]. Clinically, it presents as a solitary, sporadic, dome-shaped, sessile papule. The presence of multiple (syndromic) fibrous papules is associated with tuberous sclerosis and, less commonly, with Birt-Hogg-Dubé syndrome or multiple endocrine neoplasia type 1 [64,65].

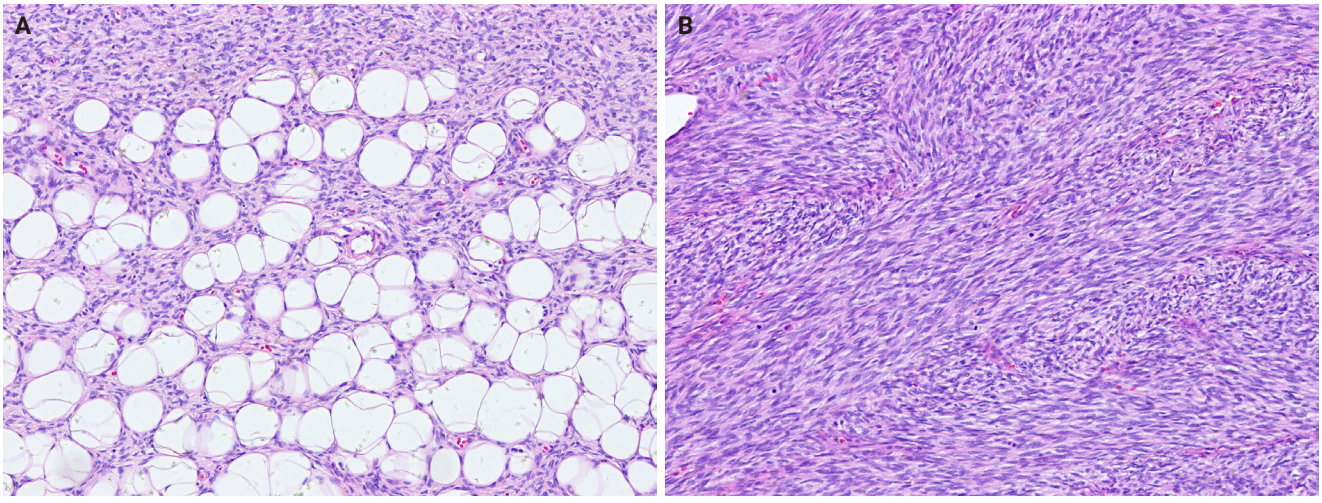

Fig. 4. Dermatofibrosarcoma protuberans with fibrosarcomatous transformation. (A) Uniform spindle-shaped tumor cells infiltrate the subcutaneous fat in a honeycomb pattern, consistent with conventional dermatofibrosarcoma protuberans. (B) Areas of fibrosarcomatous transformation show increased cellularity, a fascicular growth pattern, and frequent mitotic figures.

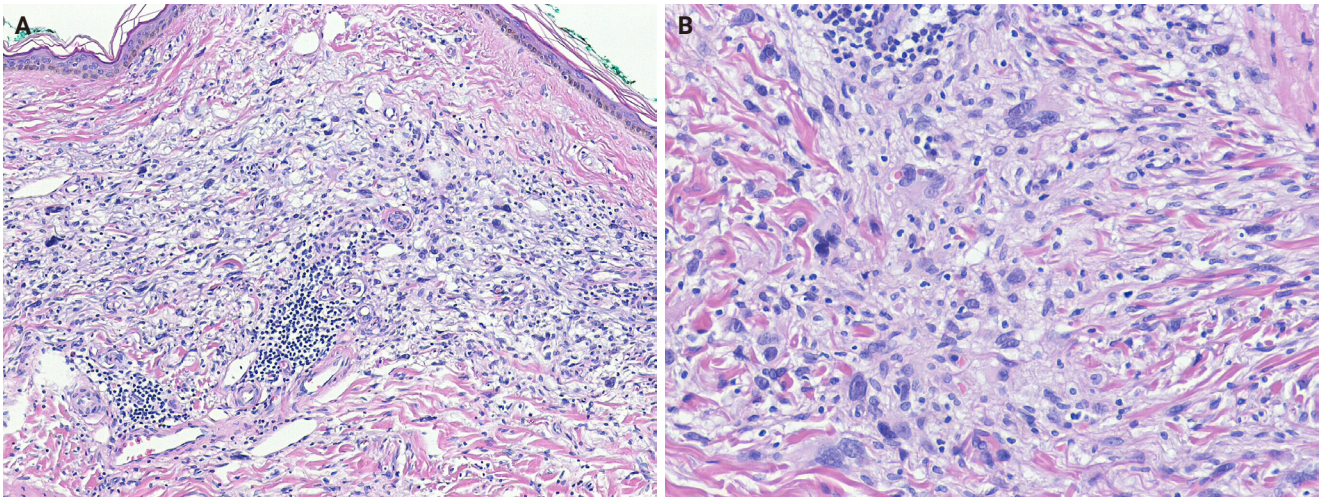

Fig. 5. Myxoinflammatory fibroblastic sarcoma. (A) The tumor shows an ill-defined dermal lesion composed of pleomorphic tumor cells admixed with inflammatory cells in a myxoid stroma. (B) Pleomorphic multinucleated giant cells with prominent nucleoli are present.

In tuberous sclerosis, multiple fibrous papules are associated with germline mutations in *TSC1* or *TSC2*, leading to activation of the mTOR pathway. A similar mTOR-related mechanism has also been proposed for sporadic fibrous papules [66].

Fibrous papules are well-circumscribed papular lesions with a tan to white cut surface. Histologically, they are dome-shaped and composed of dilated dermal blood vessels, surrounded by fibrotic or collagenized stroma containing spindle-shaped or stellate fibroblasts [67]. The overlying epidermis may exhibit melanocytic hyperplasia [68]. Histological subtypes include hypercellular, pigmented, pleomorphic, clear cell, granular cell, epithelioid, and inflammatory variants.

Fibroblastic connective tissue nevus

FCTN is a benign, dermal mesenchymal lesion of the fibroblastic/myofibroblastic lineage, characterized by short, intersecting fascicles of bland spindle cells [69]. Lesions commonly occur on the trunk, head and neck, or extremities [70-72]. FCTN shows a slight female predominance and typically affects children and young individuals (median age, 10 years). Congenital cases have been reported, often presenting as large, infiltrated plaques on the trunk [73,74]. Clinically, FCTN usually manifests as a solitary, slowly growing, painless plaque or nodule, although rare presentations include agminate lesions [75,76], atrophic plaques [77], or exophytic tumors. A single case harboring the *KHDRBS1*::*NTRK3* gene fusion has been reported [73].

Histologically, FCTN is a poorly circumscribed, dermal-based lesion localized primarily in the reticular dermis and often extending into the superficial subcutis. It comprises bland, spindle-shaped to ovoid cells arranged in short, intersecting fascicles, with preserved adnexal structures. Cellularity varies, mitotic figures are rare or absent, and a storiform pattern may occasionally be observed. Epidermal papillomatosis and ectopic dermal adipose tissue are frequently present [70]. Elastic fibers often decrease. Immunohistochemically, tumor cells express CD34 and smooth muscle actin (SMA), supporting fibroblastic/myofibroblastic differentiation [71].

Fibro-osseous tumor of digits

FOTD is a localized, self-limiting benign neoplasm that arises in the soft tissue of the digits [78]. It most commonly occurs around the proximal phalanx of the fingers and, less frequently, the toes [79-81]. FOTD occurs over a wide age range, with a predilection for young adults [79,80]. Clinically, it presents as a rapidly growing mass that may be painful and demonstrates irregular calcifications on imaging. Over time, the lesion hardens and becomes well-circumscribed [82]. Molecular studies have identified *USP6* fusion genes in FOTD [80,83], a feature shared with nodular fasciitis, which shows overlapping morphology.

Histologically, FOTD shows nodular fasciitis-like areas with variable stages of bone formation. The lesion is hypercellular and composed of randomly arranged or short, intersecting fascicles of spindle cells with plump, fusiform nuclei containing fine chromatin, conspicuous nucleoli, and moderate amounts of eosinophilic cytoplasm. Mitoses are frequent but typical. The stroma is richly vascular and variably myxoid, containing fibrin,

https://doi.org/10.4132/jptm.2026.01.09

extravasated erythrocytes, scattered lymphocytes, and osteoclast-like giant cells. Spindle cells gradually blend into ill-defined trabeculae and sheets of unmineralized woven bone, which are rimmed by prominent osteoblasts with amphophilic cytoplasm and contain large osteocytes [82,84].

Inclusion body fibromatosis

IBF is a benign myofibroblastic tumor characterized by eosinophilic intracytoplasmic inclusions and a propensity for local recurrence [85]. It is subclassified into classic (digital) and non-classic (extradigital) subtypes. Classic IBF accounts for approximately 2% of pediatric fibroblastic tumors [86], with >80% of cases diagnosed before the age of three and approximately 30% present at birth [87]. There is no sex predilection. Rare adult cases have been reported [88]. Classic IBFs typically arise on the dorsal or dorsolateral aspects of the distal or middle phalanges of the second to fourth digits, less frequently the fifth digit, and usually spare the first digit [89]. Non-classic IBF involves the extremities, tongue, and breast [90]. Clinically, classic IBFs present as asymptomatic, dome-shaped or polypoid nodules, typically <20 mm in diameter [89]. They may occur synchronously or metachronously, occasionally involving multiple digits [91]; concurrent finger and toe involvement is rare. In contrast, non-classic IBFs usually present as a solitary mass or nodule.

Histologically, IBF comprises spindle cells with lightly eosinophilic cytoplasm and elongated, bland nuclei, exhibiting low mitotic activity. These cells form whorls, short interlacing fascicles, or storiform patterns within the collagenous dermis, often oriented perpendicularly to the epidermis and encircling adnexal structures, with occasional extension into deeper tissues [91]. Rounded, pale pink, intracytoplasmic inclusions (1.5–24 μm) are highlighted by trichrome (red), phosphotungstic acid–hematoxylin (dark purple), and Movat's stains (pink) [89]. Immunohistochemically, tumor cells express vimentin, muscle actins (displaying peripheral 'tram-track' pattern), calponin, desmin, and CD99 [92]. The inclusions are positive for calponin-1 [93] and occasionally for caldesmon [89].

Multinucleate cell angiohistiocytoma

MCA is a benign, acquired lesion of fibrohistiocytic and vascular lineage [94]. It most commonly occurs on the dorsal surfaces of the hands, fingers, lower extremities, trunk, and back [95], with head and neck involvement being uncommon. Clinically, MCA typically presents in middle-aged adults as solitary or multiple smooth, erythematous papules or nodules. Some studies have reported a female predominance [96], whereas others have observed no significant sex difference [97]. The pathogenesis remains uncertain; proposed mechanisms include fibroblast proliferation, estrogen receptor α overexpression, and mast cell involvement [98,99].

Histologically, MCA exhibits a characteristic triad: multinucleated stromal cells, parallel stromal fibrosis, and proliferation of small-caliber vessels. Multinucleated stromal cells are usually angulated or stellate, with elongated cytoplasmic processes, and are often sparse, detectable only in deeper sections [97]. Stromal fibrosis runs parallel to the epidermis, and the papillary and reticular dermis contain numerous thick-walled vessels with prominent endothelial cells. Immunohistochemically, multinucleated cells variably express CD68 and factor XIIIa, but are usually negative for CD163, CD34, and factor VIII [97,100]. Endothelial markers, including CD31, CD34, ETS-related gene (ERG), and factor VIII, highlight vascular proliferation.

EWSR1::*SMAD3*-rearranged fibroblastic tumor

ESRFT is a rare, distinctive benign fibroblastic neoplasm [101]. Most cases arise in the acral region, particularly the hands and feet [102], although the lower extremity is the most common non-acral site. Clinically, ESRFT presents as a small, painless, superficial nodule, typically measuring 10–20 mm in diameter. It affects a wide age range (1–68 years; median age, 39 years) and shows a female predominance (male-to-female ratio, 1:4) [103]. Molecularly, ESRFT is characterized by an *EWSR1*::*SMAD3* gene fusion, typically involving exon 7 of *EWSR1* and exon 5 or 6 of *SMAD3*. SMAD family member 3 (SMAD3) functions as a key signal transducer in the TGF-β/SMAD pathway and is essential for fibroblast-mediated extracellular matrix synthesis, thereby supporting the fibroblastic differentiation of this tumor.

Histologically, ESRFTs are typically well-circumscribed, although focal infiltration into the subcutaneous fat may be observed. In adults, the tumor frequently exhibits a hyalinized, acellular central zone resembling collagen rosettes. This zone is surrounded by peripheral areas composed of intersecting fascicles of spindle-shaped fibroblastic cells embedded in a collagenous to variably myxoid stroma (Fig. 6A). Approximately half of the cases lack this zonation pattern. Tumor cells are cytologically bland, with no nuclear pleomorphism, hyperchromasia, prominent nucleoli, or increased mitotic activity. Myopericytomatous growth is rare, and focal stippled dystrophic calcification may be present [102,103]. Immunohistochemically, tumor cells demonstrate strong, diffuse nuclear ERG expression, whereas SMA and

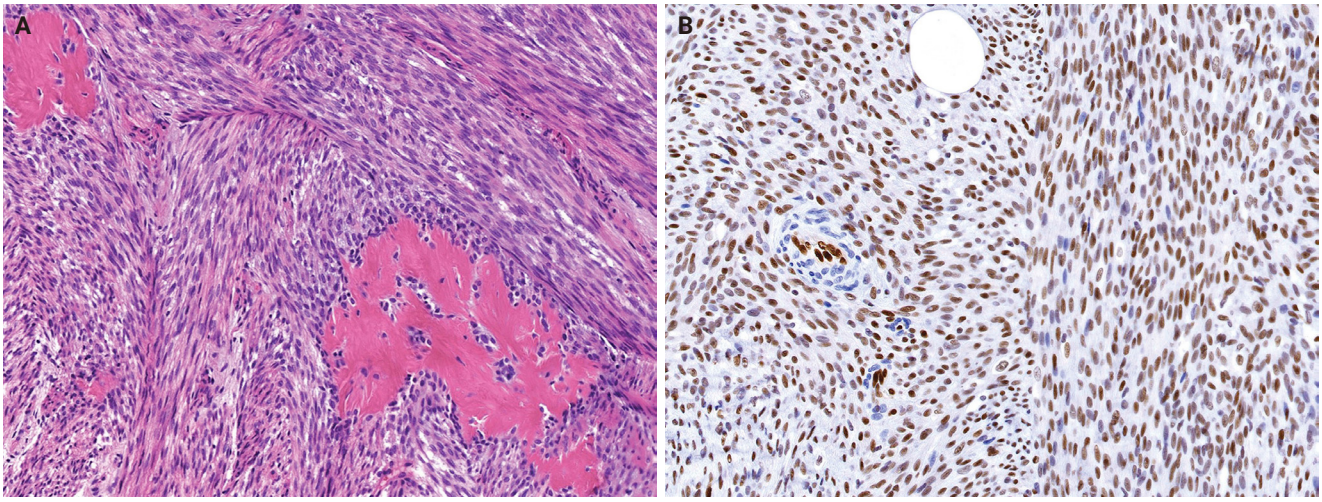

Fig. 6. *EWSR1*::*SMAD3*-rearranged fibroblastic tumor. (A) The tumor is composed of intersecting fascicles of fibroblastic spindle cells with a hyalinized collagenous stroma. (B) The tumor cells show diffuse nuclear immunoreactivity for ERG. Reprinted from Suurmeijer et al. *EWSR1*::*SMAD3*-rearranged fibroblastic tumour. In: WHO Classification of Tumours Editorial Board, ed. WHO classification of tumours: skin tumours. 5th ed. [101], with permission from IARC Press.

CD34 are negative (Fig. 6B).

VASCULAR TUMORS

Key updates

In the 5th WHO classification, hemangiomas and other benign vascular tumors are grouped separately. Newly described entities in the vascular tumor family include papillary hemangioma, poikilodermatous plaque-like hemangioma (PPLH), acquired elastotic hemangioma (AEH), verrucous venous malformation, and hobnail hemangioendothelioma (HHE). Tufted hemangioma, a benign cutaneous vascular tumor sometimes associated with Kasabach-Merritt syndrome, is now generally considered part of the Kaposiform hemangioendothelioma (KHE) spectrum [104,105], and KHE has been removed from this volume. The term 'postradiation atypical vascular lesion' replaces the previous designation 'atypical vascular lesion', highlighting its association with prior radiation exposure and distinguishing it from radiation-induced angiosarcoma [106]. Additionally, papillary intralymphatic angioendothelioma (PILA) and retiform hemangioendothelioma (RHE) are now unified under the designation of HHE [107].

In cherry hemangioma, somatic mutations in *HRAS* and *KRAS* have been identified in a small subset of cases [108]. The 5th edition also describes frequent somatic mutations in *GNA14*, *GNA11*, and *GNAQ* [109,110]. In glomeruloid hemangioma, elevated serum vascular endothelial growth factor levels suggest a potential role in lesion development [111]. In epithelioid hemangioma (EH), *FOS* or *FOSB* gene rearrangements are commonly present in bone and soft tissue EHs, although these are rare in cutaneous EH [112]. Epithelioid endothelial cells usually express FBJ murine osteosarcoma viral oncogene homolog B (FOSB) via IHC [113]. Arteriovenous malformations are now recognized as vascular malformations rather than neoplasms; terms such as arteriovenous hemangioma, cirsoid aneurysm, and acral arteriovenous tumor are no longer recommended [114].

Pseudomyogenic hemangioendothelioma (PHE) is characterized by recurrent *FOSB* rearrangements, with various fusion partners such as *SERPINE1*::*FOSB*, *ACTB*::*FOSB*, *WWTR1*::*FOSB*, *CLTC*::*FOSB*, and *EGFL7*::*FOSB* [115-120], resulting in overexpression of FOSB and constitutive transcriptional activity [120]. Fusion partner type may influence clinical features: tumors with *ACTB*::*FOSB* fusions are often solitary, whereas those with *EGFL7*::*FOSB* tend to be more aggressive [120]. Histologically, PHE is characterized by fascicles or sheets of spindled to epithelioid cells with vesicular nuclei and eosinophilic cytoplasm and showing expression of ERG and cytokeratin (AE1/AE3) (Fig. 7A, B). In epithelioid hemangioendothelioma (EHE), >90% of cases harbor *WWTR1*::*CAMTA1* fusion resulting from t(1;3)(p36;q25) translocation [121,122], whereas a minor subset exhibits a *YAP1*::*TFE3* fusion [123,124]. Nuclear expression of

https://doi.org/10.4132/jptm.2026.01.09

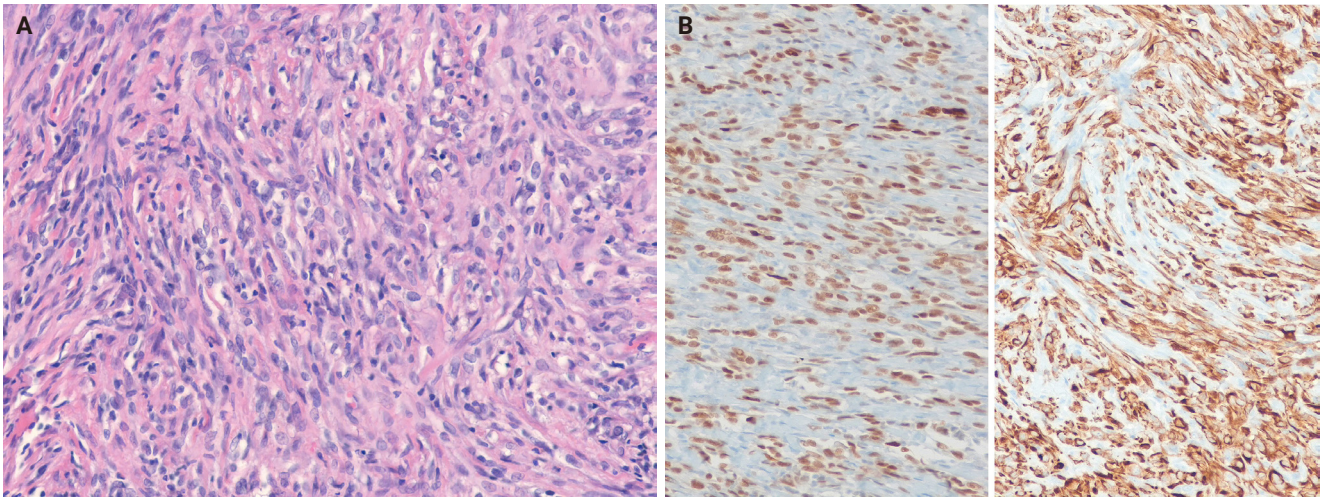

Fig. 7. Pseudomyogenic hemangioendothelioma. (A) The tumor is composed of fascicles of spindled to epithelioid tumor cells. (B) The tumor cells show diffuse immunoreactivity for ERG (left) and cytokeratin (AE1/AE3) (right).

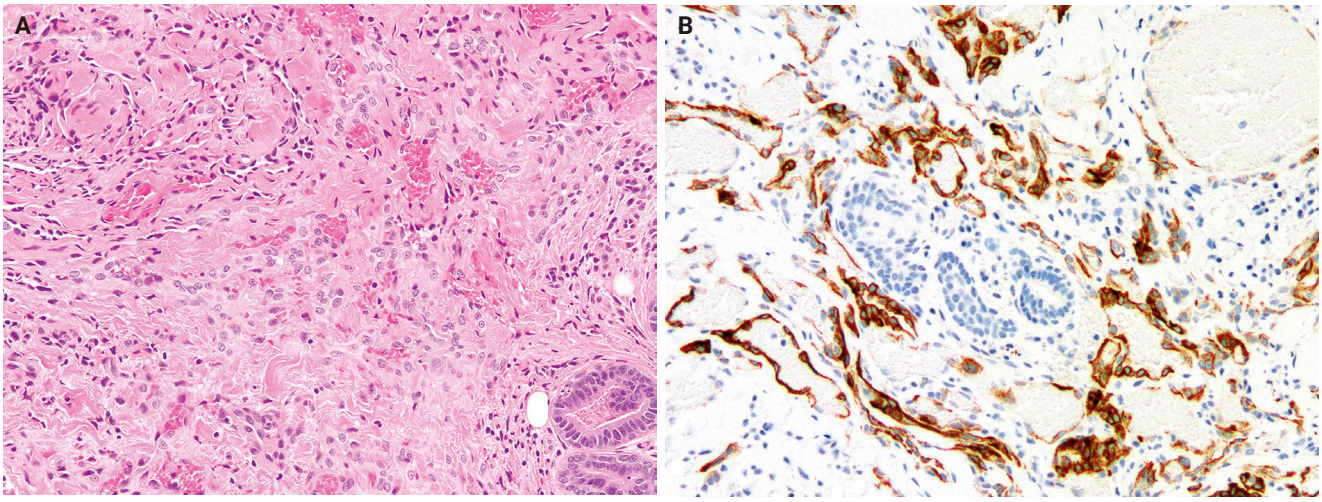

Fig. 8. Neuroendocrine composite hemangioendothelioma. (A) The tumor is composed of epithelioid endothelial cells adjacent to slit-like vascular channels lined by hobnailed cells. (B) The tumor cells are positive for synaptophysin. Reprinted from Hornick et al. Composite haemangioendothelioma. In: WHO Classification of Tumours Editorial Board, ed. WHO classification of tumours: skin tumours. 5th ed. [126], with permission from IARC Press.

calmodulin-binding transcription activator 1 (CAMTA1) serves as a surrogate marker for *WWTR1*::*CAMTA1* fusion, and nuclear transcription factor E3 (TFE3) positivity indicates *YAP1*::*TFE3* fusion. Additionally, the loss of expression of the C-terminus of yes-associated protein 1 (YAP1) is specific to tumors with *YAP1*::*TFE3* fusions [125]. In composite hemangioendothelioma (CHE), approximately 27% of tumors harbor *YAP1*::*MAML2* fusions [126,127]. Neuroendocrine CHE is recognized as a distinct subtype characterized by a mixture of retiform hemangioendothelioma-like and EHE-like areas, together with a striking nested component, and by expression of neuroendocrine markers, most commonly synaptophysin (Fig. 8A, B) [126,128]. Subsets of neuroendocrine CHEs harbor *PTBP1*::*MAML2* and *EPC1*::*PCH2* fusions [128,129], and CHEs with *YAP1*::*MAML2* fusions show loss of YAP1 C-terminus expression [125].

Kaposi sarcoma (KS) is classified into four clinical subtypes: classic, endemic African, acquired immunodeficiency syndrome–associated, and iatrogenic [130]. Genomic profiling

reveals recurrent 11q13 gains with amplification of *FGF4* and *FGF3* (*INT2*) [131]. Early-stage KS shows clonal loss of the Y chromosome, whereas late (nodular) lesions accumulate copy-number alterations on chromosomes 16, 17, 21, X, and Y [132]. Cutaneous angiosarcoma demonstrates expanded genetic heterogeneity (Fig. 9A, B) [133]. Tumors arising in the head, neck, face, and scalp frequently exhibit ultraviolet (UV) radiation-associated mutation signature and high tumor mutation burden, which may have implications for immuno-oncology-based therapy [134]. *MYC* amplifications are nearly universal in secondary angiosarcoma (post-radiation or lymphedema-associated) but occur in <10% of primary tumors [135-137]. The most common recurrent mutations involve *KDR*, *PTPRB*, and *PLCG1* (approximately 40%) [138,139], whereas mutations in *RAS*, *PIK3CA*, *TP53*, *FLT4*, and *TIE1* are less frequent [140,141]. Additionally, a *CIC*-altered subset occurs in younger patients and is associated with poorer disease-free survival [142].

Papillary hemangioma

Papillary hemangioma is a distinctive benign vascular proliferation characterized by dilated vascular channels containing prominent intraluminal papillary projections [143]. It occurs almost exclusively in the head and neck region and predominantly affects adult men [144,145]. Clinically, it presents as a solitary, long-standing, bluish-red papule, measuring up to 11 mm in diameter.

Histologically, papillary hemangioma demonstrates widely dilated, thin-walled vascular channels in the dermis, containing numerous intraluminal papillary projections. These papillary structures comprise capillary-sized vessels lined by plump endothelial cells and surrounded by pericytes. Endothelial cells often contain intracytoplasmic eosinophilic globules (so-called 'thanatosomes'), corresponding to dilated lysosomes containing fat vacuoles and cellular debris. Immunohistochemically, endothelial cells are positive for CD31, CD34, and ERG, but negative for lymphatic markers such as podoplanin (D2-40).

Poikilodermatous plaque-like hemangioma

PPLH is an acquired benign vascular proliferation characterized by a band-like pattern of small blood vessels in the superficial dermis [146]. Almost all lesions arise on the lower extremities [147,148], predominantly affecting older men. Clinically, PPLH presents as slowly growing, asymptomatic, erythematous to violaceous, scaly plaques, measuring 20–70 mm in diameter, often exhibiting poikilodermatous changes. Lesions are usually solitary but may be multiple. The course is indolent, and lesions tend to persist despite treatment.

Histologically, PPLH demonstrates a band-like proliferation of small-caliber blood vessels lined by bland endothelial cells within the papillary and superficial reticular dermis. The affected area shows loss or marked reduction of elastic fibers, and a grenz zone is absent. Variable degrees of hyperkeratosis, acanthosis, and mild perivascular lymphocytic infiltration are also commonly observed.

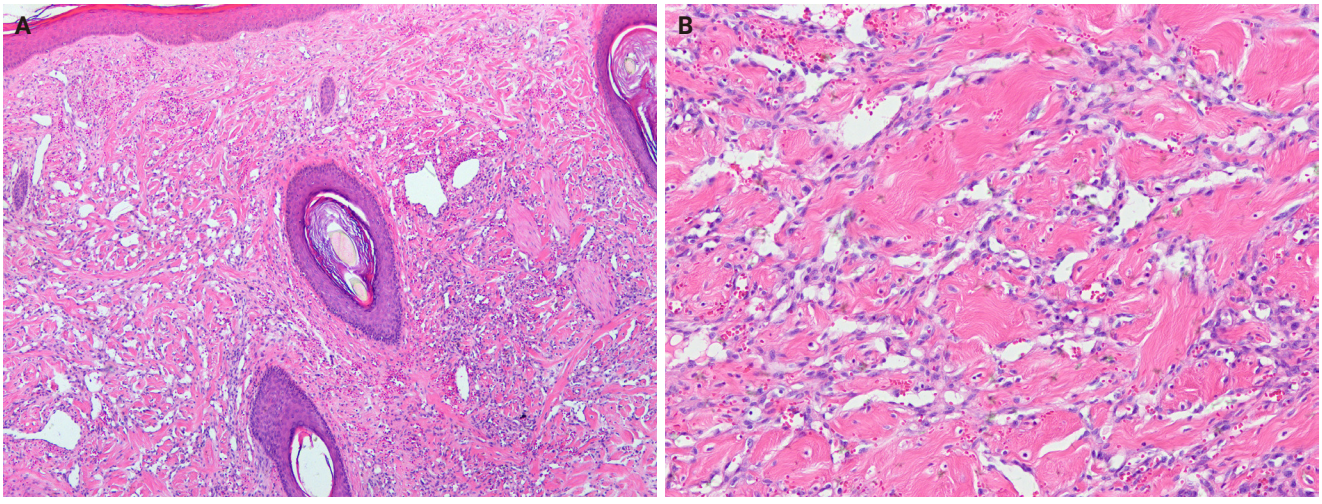

Fig. 9. Cutaneous angiosarcoma. (A) The tumor shows numerous infiltrative vascular channels dissecting between dermal collagen bundles. (B) These anastomosing vascular channels are lined by atypical endothelial cells, with focal endothelial multilayering.

https://doi.org/10.4132/jptm.2026.01.09

Acquired elastotic hemangioma

AEH is a rare, benign vascular proliferation characterized by a superficial, band-like arrangement of small blood vessels in sun-exposed skin [149]. It is typically associated with solar elastosis. AEH predominantly occurs on the forearms or lateral neck and presents as an asymptomatic papule or plaque, primarily affecting middle-aged to elderly adults, with a slight female predominance [150,151]. Multiple lesions are rare, and chronic sun damage is considered the primary etiologic factor.

Histologically, AEH exhibits a band-like proliferation of capillary-sized vessels, each surrounded by a layer of pericytes and oriented parallel to the epidermis within the upper reticular dermis. These vessels are set against a background of prominent solar elastosis.

Hobnail hemangioendotheliomas

PILA and RHE are uncommon, rarely metastasizing vascular neoplasms—both feature hobnail endothelial proliferations with a lymphatic endothelial phenotype [107]. PILA typically arises in the proximal extremities, particularly the buttock and thigh [152-154], whereas RHE predominantly occurs in the distal extremities, especially the lower leg [155,156]. Fewer than 50 cases of PILA and RHE have been reported [152,155,156]. PILA predominantly affects infants, with a slight female predominance, whereas RHE occurs in children or young adults, with no sex predilection. The etiology remains uncertain; some RHE cases are associated with prior radiotherapy [155], lymphedema [155,157], or cystic lymphangioma [158]. A subset of RHE harbors *YAP1* rearrangements, most often *YAP1*::*MAML2* fusions [127].

Histologically, PILA and RHE are morphologically similar, composed of darkly staining hobnail or columnar endothelial cells. PILA exhibits poorly defined proliferation of slit-like or dilated lymphatic channels, occasionally associated with cavernous lymphatic malformation. In contrast, RHE exhibits infiltrative growth of elongated, branching vascular channels resembling the rete testis. Shared features include hyaline fibrosis, intraluminal papillary tufts lined by hobnail endothelial cells—more conspicuous in PILA—and a lymphocytic infiltrate. Immunohistochemically, hobnail endothelial cells of PILA and RHE express pan-endothelial markers (CD31, ERG, Friend leukemia virus integration 1 [FLI1], and CD34) and lymphatic markers (podoplanin [D2-40], vascular endothelial growth factor receptor 3 [VEGFR3], and prospero homeobox 1 [PROX1]) [158,159]. Tumors harboring *YAP1* rearrangements show loss of YAP1 C-terminal expression [151]. Focal synaptophysin expression and shared *YAP1*::*MAML2* fusions support a pathogenetic link between HHE and CHE.

PERICYTIC AND PERIVASCULAR TUMORS

Key updates

No major revisions or newly recognized entities have been added to this family in the 5th edition. Myofibroma and myofibromatosis, previously categorized among fibroblastic, myofibroblastic, and fibrohistiocytic tumors, have been reclassified as pericytic and perivascular tumors. In glomus tumor, sporadic tumors often show rearrangements involving *MIR143* and *NOTCH* genes [160-162], whereas *BRAF* p.V600E mutations have been reported in rare malignant cases [163,164]. Demonstration of *MIR143*::*NOTCH1*, *MIR143*::*NOTCH2*, or *MIR143*::*NOTCH3* fusions can aid in diagnosis [161,162].

The 5th edition includes newly recognized multicentric and intravascular subtypes of myopericytoma [165]. Pericytoma-like neoplasms harboring recently identified gene fusions, such as *ACTB*::*GLI* and *SRF*::*RELA*, are likely unrelated to myopericytoma [166,167]. Angioleiomyomas exhibit cytogenetic abnormalities, including monosomy of chromosome 13 and losses of 6p, 21q, and 13q [168,169]; rare cases harbor *NOTCH* gene fusions [161,162]. In addition to solid, venous, and cavernous subtypes, hybrid subtypes have also been described. Similar to glomus tumors and myopericytomas, angioleiomyomas demonstrate diffuse immunoreactivity for the pericytic marker regulator of G-protein signaling 5 [170].

Myofibroma and myofibromatosis

Myofibroma and myofibromatosis are benign mesenchymal neoplasms of presumed myofibroblastic lineage, presenting as solitary, multicentric, or generalized lesions [171]. Solitary lesions most commonly involve the skin or subcutaneous tissue of the head and neck, upper extremities, or trunk. However, deep lesions involving muscles and bones are uncommon [172]. Multicentric lesions share a similar distribution, whereas generalized lesions involve visceral organs. Solitary lesions predominantly affect males, while multicentric lesions occur mainly in females. Myofibroma accounts for approximately 12% of pediatric soft tissue lesions, with 90% of cases occurring in children and 65% presenting before age 2. Molecularly, familial myofibromatosis exhibits germline *PDGFRB* mutations (approximately 89%) and

NOTCH3 mutations (approximately 11%), whereas sporadic solitary lesions frequently harbor somatic *PDGFRB* mutations [173,174]. *PDGFRB* mutation types differ between familial and sporadic myofibromatosis cases, and *SRF* rearrangements have been reported in highly cellular tumors [175].

Histologically, myofibroma shows a biphasic growth pattern comprising alternating bundles of primitive, small, darkly staining, rounded cells and plump, spindle-shaped mesenchymal cells (Fig. 10A, B). Tumors are richly vascularized, with numerous thin-walled, hemangiopericytoma-like vessels and mature eosinophilic myoid cells, often accompanied by myointimal nodular proliferations ('vascular balls'). Foci of calcification and ischemic-type necrosis may be present, and mitotic activity is typically low. Immunohistochemically, tumor cells are diffusely positive for SMA, while caldesmon is negative or focally positive, and desmin is generally negative.

SMOOTH MUSCLE TUMORS

Key updates

No major revisions or newly recognized entities have been added to this family in the 5th WHO classification. Smooth muscle hamartoma (SMH) and Epstein-Barr virus–associated smooth muscle tumor (EBV-SMT) are newly included in the family of smooth muscle tumors. In the 5th edition, dermal-confined lesions previously termed 'cutaneous leiomyosarcoma' are designated as 'atypical intradermal smooth muscle neoplasm', whereas the term 'cutaneous leiomyosarcoma' is reserved for tumors with overt subcutaneous fat infiltration (Fig. 11A, B) [176]. Prognosis is excellent; no metastases have been reported in the largest series to date, comprising 84 cases of completely excised dermal-confined tumors [177]. Although data remain limited, dermal tumors with minimal subcutaneous extension have a low risk of recurrence or metastasis. Histological grading does not provide prognostic value.

Smooth muscle hamartoma

SMH is a benign dermal lesion composed of haphazardly arranged smooth muscle bundles [178]. It most commonly occurs on the trunk or extremities, with less frequent involvement of the head, neck, and genital regions [179]. A positive pseudo-Darier sign is observed in up to 80% of congenital cases. Most congenital SMHs are solitary, although rare multiple, familial, or diffuse forms have been reported [180]. Diffuse congenital SMHs may be associated with Michelin tire baby syndrome [181], and combined lesions with congenital or blue nevi have also been reported [182,183]. SMH exhibits a slight male predominance, and congenital cases are uncommon, with an estimated incidence of 1 in 2,600 births [182]. Molecularly, a subset of congenital SMHs harbors postzygotic *ACTB* mutations, also identified in Becker nevi, suggesting a shared biological basis between these lesions [183].

Histologically, SMH exhibits haphazard bundles of mature smooth muscle within the dermis, often adjacent to pilosebaceous units [184]. Cytological atypia, pleomorphism, and mitotic activity are absent. Focal retraction artifacts may be present

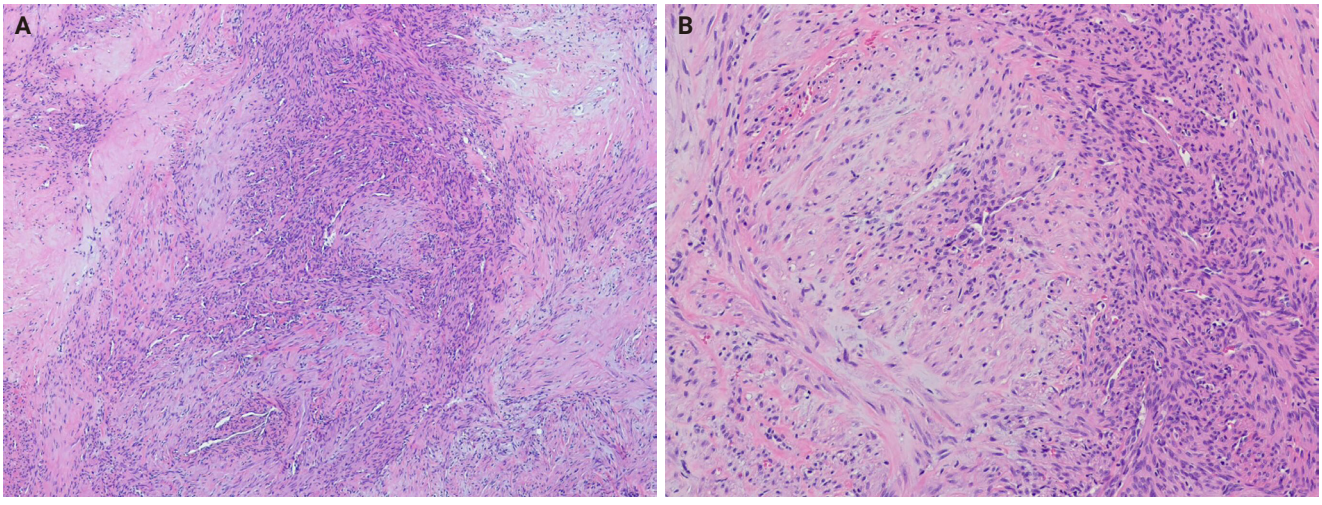

Fig. 10. Myofibroma. (A) The tumor shows a characteristic biphasic growth pattern with ill-defined nodules of myoid cells and intervening hypercellular areas. (B) Eosinophilic spindled myoid cells and smaller ovoid cells are present around pericytoma-like vessels.

https://doi.org/10.4132/jptm.2026.01.09

around smooth muscle bundles. Lesional cells express smooth muscle markers. The overlying epidermis frequently demonstrates hyperkeratosis, acanthosis, and basal hyperpigmentation, resembling features of a Becker nevus.

EBV-associated smooth muscle tumor

EBV-SMT is a rare EBV-driven smooth muscle neoplasm that develops in immunosuppressed patients [185]. The central nervous system is the most commonly affected, followed by the liver, lungs, and subcutaneous tissues of the trunk and extremities [186-189]. EBV-SMT occurs in approximately 1%–5% of immunosuppressed individuals [189], affecting a wide age range, most often adults, with a slight female predominance [190]. Tumorigenesis is driven by EBV type 2 infection in the context of a congenital immunodeficiency disorder, post-transplant immunosuppression, or human immunodeficiency virus infection [189,191]. EBV infects vascular smooth muscle progenitor cells via CD21 receptor-mediated entry or through EBV-infected lymphocytes [192,193]. Aberrant activation of the mTOR/AKT signaling pathway and *MYC* overexpression contribute to pathogenesis [193,194]. Multiple lesions typically represent independent clonal proliferations rather than metastases [186]. Prognosis is generally favorable and depends more on immune status than on tumor morphology [186,189].

Histologically, EBV-SMTs are well-circumscribed lesions composed of interlacing fascicles of spindle-shaped myoid cells within a collagenous stroma, irrespective of anatomical site [195,196]. A variable admixture of smaller rounded cells and intratumoral lymphocytes is typically present, and focal myxoid change may be observed. Mitotic activity is generally low, although rare tumors exhibit leiomyosarcoma-like features, including nuclear atypia, necrosis, and increased mitotic activity [190,191]. Immunohistochemically, tumor cells express smooth muscle markers, including SMA, muscle-specific actin, desmin, and caldesmon. EBV infection can be confirmed by in situ hybridization test for Epstein-Barr virus-encoded small RNA.

NEURAL TUMORS

Key updates

In the 5th edition, dermal hyperneury (DHN)/epithelial sheath neuroma (ESN) and hybrid nerve sheath tumor have been newly described within the neural tumors family. In solitary circumscribed neuroma (SCN), the plexiform subtype has been newly recognized as part of the SCN spectrum [197]. Dermal nerve sheath myxoma (DNSM) is now defined as a benign peripheral nerve sheath tumor (Fig. 12A, B) [198]. Pathological and molecular evidence supports its Schwann cell origin [198-201]. Gene expression profiling of DNSM aligns with dermal schwannoma, whereas cellular neurothekeoma exhibits molecular similarities to cellular dermatofibroma (fibrous histiocytoma) [201].

Three subtypes of perineurioma are recognized: reticular, sclerosing, and malignant [202]. Perineuriomas share pathogenetic features with schwannomas and meningiomas, including 22q12 deletion, monosomies, and *NF2* mutations [203-205]. Soft tissue perineuriomas commonly exhibit a 17q11 deletion

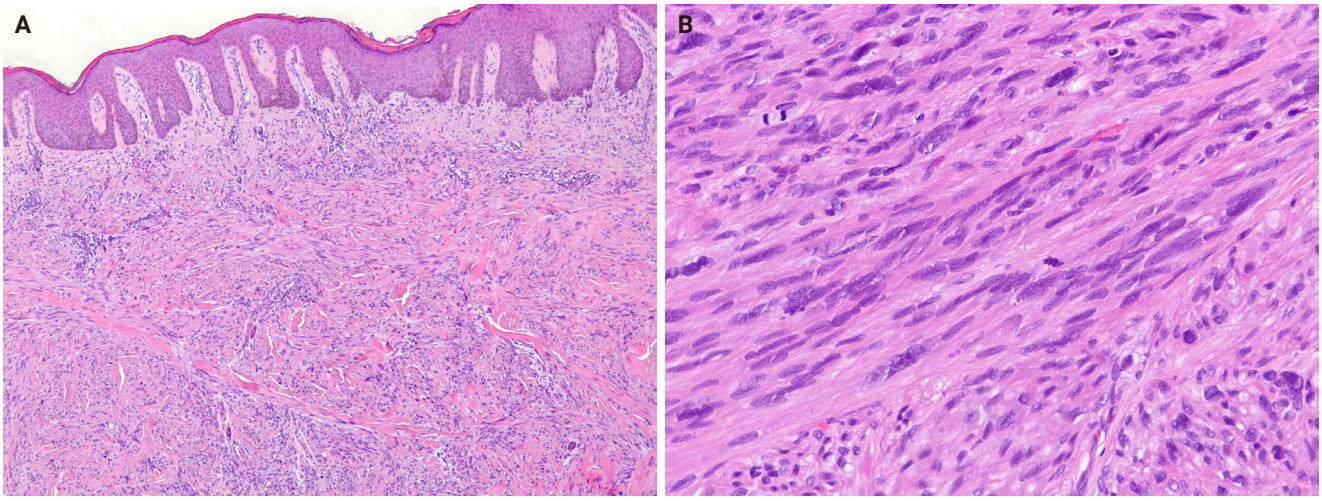

Fig. 11. Atypical intradermal smooth muscle neoplasm. (A) The tumor is composed of infiltrative spindle cells within the dermis. (B) The tumor cells show elongated, blunt-ended nuclei and brightly eosinophilic cytoplasm. Moderate nuclear atypia and mitotic figures are present.

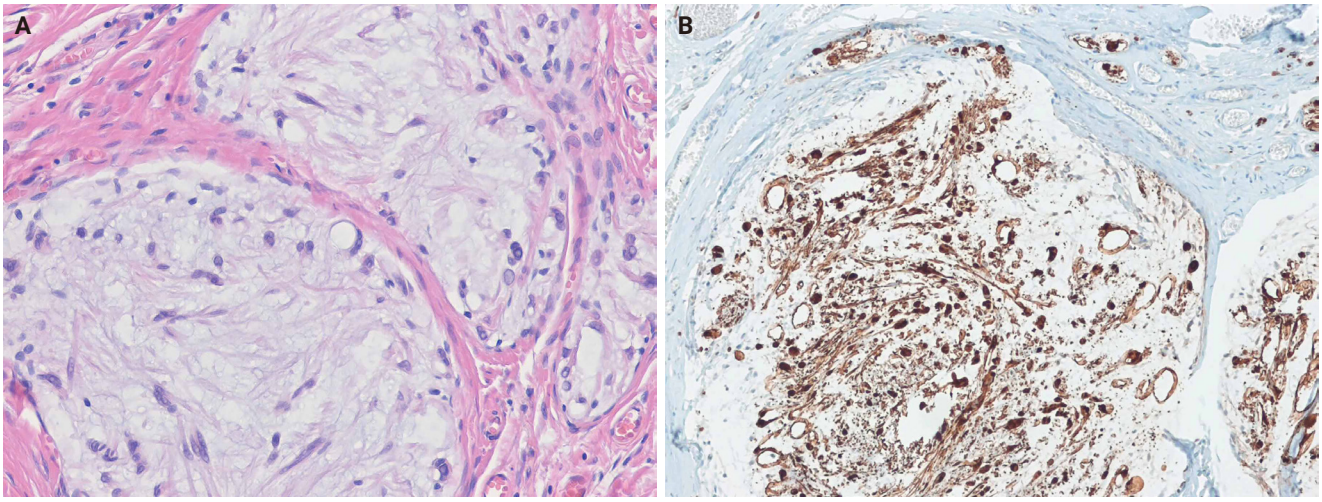

Fig. 12. Dermal nerve sheath myxoma. (A) The tumor shows a multinodular growth pattern separated by fibrous septa, with spindle, stellate, and ring-shaped tumor cells in prominent myxoid stroma. (B) The tumor cells are positive for S100 protein.

involving the *NF1* locus. The sclerosing subtype demonstrates a distinctive 10q24 rearrangement [206]. Malignant perineuriomas are associated with loss of chromosome 13q and small deletions on chromosomes 3, 6, and 9 [205,207].

Neurofibroma formally recognizes melanotic neurofibroma as a distinct subtype [208]. Multiple tumors, particularly plexiform and diffuse subtypes, are strongly associated with neurofibromatosis type 1 (NF1) and type 2 (NF2). Genotype–phenotype correlations have been established in NF1 [209]. Loss of *CDKN2A* at chromosome 9p21.3 may contribute to the development of atypical neurofibromatous tumor of uncertain biological potential [210]. Schwannoma is classified into six subtypes: plexiform, epithelioid, ancient schwannoma, cellular, microcystic/reticular, and neuroblastoma-like [211].

Granular cell tumor (GCT) is a benign neuroectodermal tumor derived from Schwann cells [212]. Loss-of-function mutations in *ATP6AP1* and *ATP6AP2*, which are mutually exclusive, occur in approximately 70% of cases [213] and are considered pathognomonic of GCT. Malignant GCT is characterized by overt malignant features, including increased cellularity, prominent spindling, a high nuclear-to-cytoplasmic ratio, marked pleomorphism, elevated mitotic activity (including atypical figures), necrosis, and a high Ki-67 proliferation index [214-216].

Cutaneous malignant peripheral nerve sheath tumor (MPNST) is rare [217]. Unlike deep MPNSTs, cutaneous MPNSTs are less frequently associated with NF1. Conventional deep-seated MPNSTs harbor inactivating mutations in *NF1*, *CDKN2A*/*CDKN2B*, and polycomb repressive complex 2 (PRC2) core components (*EED* or *SUZ12*), resulting in complete loss of PRC2 function [218-220]. Approximately 80% of high-grade MPNSTs show PRC2 inactivation, with loss of histone H3 lysine 27 trimethylation (H3K27me3) expression. The loss of H3K27me3 is a valuable diagnostic marker for these tumors [221,222]. In contrast, epithelioid MPNSTs represent a molecularly distinct subtype, characterized by *SMARCB1* inactivation in approximately 75% of cases [223]. Mutations in *NF1*, *CDKN2A*/*CDKN2B*, or PRC2 are uncommon in this subtype [218,224].

Dermal hyperneury/epithelial sheath neuroma

DHN is a form of small nerve hypertrophy characterized by large, prominent dermal nerve fibers [225]. ESN shows similar histological features, with mature squamous epithelium surrounding the perineurium. DHN/ESN is classified into syndromic and sporadic subtypes. Sporadic DHN shows a slight predilection for the trunk [226], whereas ESN most commonly arises on the back [227]. Sporadic lesions typically present in the seventh decade of life, whereas syndromic mucocutaneous neural proliferations may occur in patients as young as 5 years [228]. Mucocutaneous neural proliferations have been described in multiple endocrine neoplasia type 2B (MEN2B) [229], MEN2A [230], NF2 [231], and Cowden disease [232]. ESN occurs exclusively as a sporadic lesion. Pathogenesis may involve PTEN- and rearranged during transfection (RET)–mediated signaling pathways, particularly in syndromic cases [233].

Histologically, both DHN and ESN demonstrate aggregated neural tissue with enlarged nerve fibers located within the

https://doi.org/10.4132/jptm.2026.01.09

dermis or at the dermal-subcutaneous junction. Morphology is consistent between syndromic and sporadic cases. Nerve bundles are typically 1.5–4 times larger than normal and may exhibit mild neuroma-like disorganization. Occasionally, perineurial lymphoplasmacytic or histiocytic inflammation and intraneural mucin deposition are observed. ESN exhibits mature squamous epithelium forming an epithelial sheath around enlarged nerve fibers. Subcutaneous extension is rare [234].

Hybrid nerve sheath tumors

Hybrid nerve sheath tumors are rare benign peripheral nerve sheath tumors that exhibit combined features of two or more conventional types, most commonly schwannoma, neurofibroma, or perineurioma [235]. They occur across a wide anatomical range, most frequently in the dermis or subcutaneous tissue [236,237]. The most common subtype is hybrid schwannoma/perineurioma, which predominantly arises in the fingers [238]. Hybrid schwannoma/perineurioma usually occurs sporadically, whereas hybrid neurofibroma/schwannoma exhibits a striking association with NF1 and NF2 [239]. A high prevalence of hybrid schwannoma/neurofibroma morphology was found in tumors from patients with schwannomatosis (71%) [239,240]. Hybrid neurofibroma/perineurioma has also been reported in association with NF1 [241,242]. Most hybrid schwannoma/perineuriomas harbor *VGLL3* gene rearrangements, supporting their classification as a distinct pathological entity rather than a simple histological overlap [243].

Histologically, a hybrid schwannoma/perineurioma exhibits an intimate admixture of alternating Schwann cells and perineurial cells. Schwann cells have wavy, tapering nuclei and eosinophilic cytoplasm, whereas perineurial cells have slender nuclei and delicate, elongated cytoplasmic processes. The Schwann cell component is usually predominant and may exhibit degenerative nuclear atypia ('ancient change'), while mitoses are rare. Hybrid neurofibroma/schwannoma is characterized by schwannomatous nodules or bundles of Schwann cells within an otherwise typical neurofibroma. The neurofibromatous areas contain a mixture of fibroblasts, Schwann cells, and perineurial cells [242,244]. Hybrid neurofibroma/perineurioma shows plexiform neurofibroma with foci of perineurial differentiation, which are often subtle and require IHC for confirmation. Immunohistochemically, Schwann cells are positive for S100 protein and SRY-box transcription factor 10 (SOX10), whereas perineurial cells express epithelial membrane antigen (EMA), claudin-1, and GLUT1, and fibroblasts are positive for CD34.

TUMORS OF UNCERTAIN DIFFERENTIATION

Key updates

The 5th edition introduces several newly described entities in the family of tumors of uncertain differentiation, including perivascular epithelioid cell tumor (PEComa), angiomatoid fibrous histiocytoma (AFH), neurotrophic tyrosine receptor kinase (NTRK)–rearranged spindle cell neoplasm (NRSCN), superficial CD34-positive fibroblastic tumor (SCFT), and *CRTC1*::*TRIM11* cutaneous tumor (CTCT). The SCFT, previously classified as a fibroblastic and myofibroblastic tumor in the 5th edition of the WHO classification of soft tissue tumors, has also been reclassified as a tumor of uncertain differentiation.

Cellular neurothekeoma is a benign cutaneous neoplasm of uncertain histogenesis, distinct from nerve sheath myxoma (previously called myxoid neurothekeoma) [245]. The most consistently expressed markers include CD63 (NKI/C3) [246,247], neuron-specific enolase [248], protein gene product 9.5 (PGP9.5) [249], and S100 calcium-binding protein A6 (S100A6) [250]. The 5th edition expands the immunoprofile to include keratinocyte basal antigen 62 (KBA.62) and preferentially expressed antigen in melanoma (PRAME) [251,252]. Non-neural granular cell tumor is a rare, low-grade neoplasm of mesenchymal cells of unknown lineage, characterized by prominent cytoplasmic granularity [253]. *ALK* rearrangements have been reported in 60% of cases in a small series [254]. Atypical fibroxanthoma is defined as a dermally confined, low-grade neoplasm of uncertain histogenesis [255]. Genomic alterations include deletions at 9p and 13q, *TERT* mutations, and a variety of abnormalities similar to pleomorphic dermal sarcoma (PDS) [256-258]. Morphologic patterns include spindle cell, clear cell, granular cell, keloidal, myxoid, sclerotic, and pigmented forms [259-261].

PDS is a rare tumor affecting older adults with chronically UV radiation-exposed skin [262]. It is characterized by a high UV-related mutation burden, including mutations in *TP53*, NOTCH family genes, the *TERT* promoter, and alterations in *CDKN2A* and *CDKN2B* [256,258]. This mutation profile parallels that of cutaneous squamous cell carcinoma. Immunohistochemically, PDS commonly expresses CD10, CD99, and platelet-derived growth factor receptor beta (PDGFRB).

Epithelioid sarcoma (ES) is a malignant soft tissue tumor that exhibits hybrid mesenchymal and epithelial morphology and immunophenotypes [263]. Loss of nuclear SMARCB1 (INI1)

expression is characteristic of ES; however, a subset retains SMARCB1 (INI1) and instead shows aberrant expression of other SWI/SNF complex components, including SMARCA4 (BRG1), SMARCC1 (BAF155), and SMARCC2 (BAF170) [264]. Genomic analyses have revealed complex copy-number aberrations and a relatively high mutational burden [265].

Dermal clear cell sarcoma (CCS) is a malignant neoplasm of uncertain histogenesis with melanocytic differentiation, defined by *EWSR1*::*ATF1* or *EWSR1*::*CREB1* gene fusion [266]. Approximately 70%–90% of CCSs harbor an *EWSR1*::*ATF1* fusion resulting from t(12;22)(q13;q12). Identification of *EWSR1* rearrangement and/or confirmation of these fusions aids diagnosis, particularly in distinguishing CCS from malignant melanoma. In contrast to malignant melanomas, PRAME expression in CCS is typically absent or limited to focal areas [267,268].

Ewing sarcoma is a small round cell sarcoma defined by gene fusions involving a FUS-EWSR1-TAF15 (FET) family gene, most commonly *EWSR1*, and an erythroblast transformation-specific (ETS) family transcription factor [269]. All cases harbor *FET*::*ETS* fusions, which constitute the defining molecular hallmark. The tumorigenesis of cutaneous Ewing sarcoma is driven by oncogenic transcription factors encoded by chimeric *FET*::*ETS* fusion genes, most frequently *EWSR1*::*FLI1* (>95%), and, less commonly, *EWSR1*::*ERG* [270-272].

Epithelioid fibrous histiocytoma

EFH is a distinctive, benign cutaneous neoplasm composed of epithelioid cells [273]. It most commonly arises in the lower extremities and, less frequently, in the upper extremities, trunk, or head and neck [274,275]. EFH typically occurs in young to middle-aged adults (median age, 40 years), with a female predominance. Molecularly, approximately 90% of EFHs harbor *ALK* rearrangements, while a small subset shows mutually exclusive *PRKC* gene fusions [276,277]. *SQSTM1* and *VCL* are the most common *ALK* fusion partners, whereas *DCTN1*, *ETV6*, *PPFIBP1*, *SPECC1L*, *TPM3*, *PRKAR2A*, *MLPH*, *CLTC*, and *EML4* represent rare fusion partners [278-281].

Histologically, EFH is typically well-circumscribed, and exophytic lesions often exhibit an adnexal collarette (Fig. 13A). The tumor consists of uniform epithelioid cells with vesicular nuclei, small nucleoli, and pale eosinophilic or amphophilic cytoplasm (Fig. 13B). Binucleated forms are frequently observed. Thin-walled vessels are common, often with perivascular accentuation of tumor cells. Morphological variants include chondroblastoma-like pericellular calcification [279,282] and spindle cell-predominant forms [283,284]. Immunohistochemically, ALK is overexpressed in approximately 90% of cases [285], with D5F3 or 5A4 clones demonstrating higher sensitivity than the ALK1 clone [276,286]. EMA is positive in approximately 65% of cases [286], and CD30 expression may also be present.

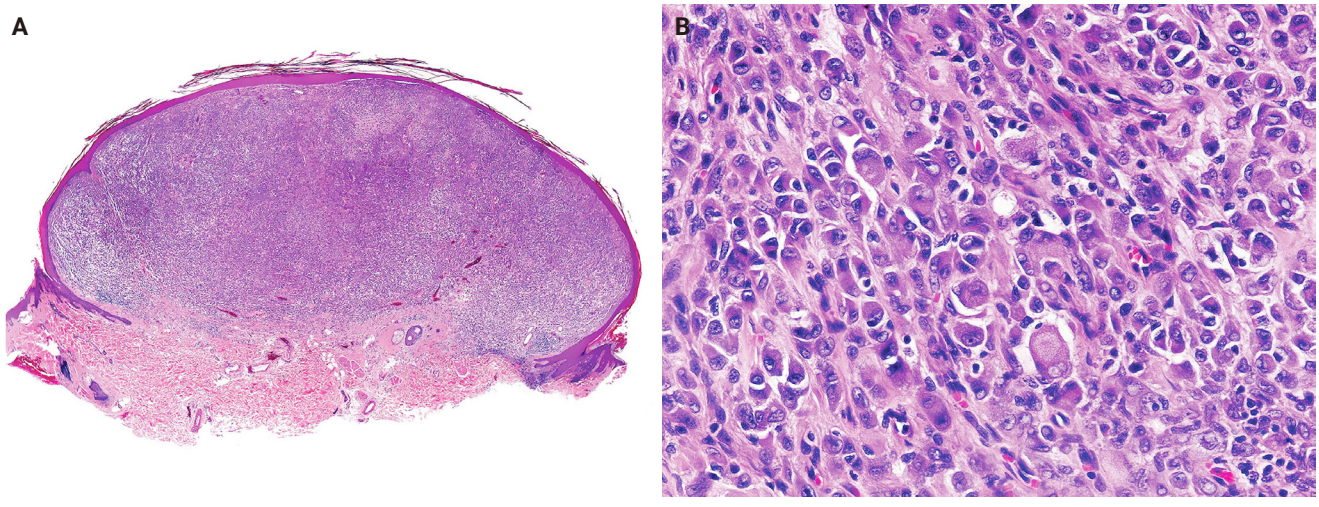

Fig. 13. Epithelioid fibrous histiocytoma. (A) Scanning magnification shows a well-circumscribed, dome-shaped dermal tumor with an adnexal collarette. (B) The tumor is composed of epithelioid cells with round to oval vesicular nuclei, small nucleoli, and abundant eosinophilic or amphophilic cytoplasm. Reprinted from Requena and Hornick. Epithelioid fibrous histiocytoma. In: WHO Classification of Tumours Editorial Board, ed. WHO classification of tumours: skin tumours. 5th ed. [273], with permission from IARC Press.

https://doi.org/10.4132/jptm.2026.01.09

PEComa

PEComas are mesenchymal neoplasms composed of distinctive perivascular epithelioid cells that coexpress melanocytic and smooth muscle markers [287]. Cutaneous PEComas are rare and most commonly involve the lower extremities, with less frequent occurrence on the trunk, head, or neck [288-290]. They affect individuals across a wide age range (15–81 years), with a peak incidence in middle age, and show a female predominance [288,289]. Most cases are sporadic; however, fibroma-like cutaneous PEComa associated with tuberous sclerosis has been reported [291]. Molecularly, deletion of 16p involving the *TSC2* gene is frequent, and loss of heterozygosity at the *TSC2* locus is seen in both sporadic and syndromic tumors [292]. *TP53* mutations occur in approximately 63% of *TSC2*-mutated PEComas [293].

Histologically, PEComa is composed of epithelioid cells with granular, pale eosinophilic, or clear cytoplasm and round nuclei with small nucleoli (Fig. 14A, B). Most PEComas exhibit a nested or trabecular architecture with a distinctive perivascular growth pattern. Mixed epithelioid-spindle cell morphology and scattered multinucleated cells may occur; however, mitoses are generally rare. Most reported cases of cutaneous PEComa lack malignant features, such as marked pleomorphism, high mitotic activity, and necrosis [292-296]. Malignant primary cutaneous PEComas are exceedingly rare [290,297]. Currently, cutaneous angiomyolipomas are classified as hamartomatous or lipomatous neoplasms with smooth muscle elements, rather than true PEComas. Immunohistochemically, PEComas coexpress melanocytic markers (e.g., human melanoma black 45 [HMB-45], melan-A (MART1), microphthalmia-associated transcription factor [MITF]) and muscle markers (e.g., SMA, desmin, caldesmon) [298,299].

Angiomatoid fibrous histiocytoma

AFH is a rare soft tissue neoplasm of intermediate malignant potential and uncertain differentiation [300]. It accounts for approximately 0.3% of all soft tissue tumors. It typically presents as a dermal or subcutaneous lesion, most commonly in the extremities, followed by the trunk, head, and neck regions. Approximately two-thirds of cases arise in sites where lymph nodes are normally present [301]. AFH affects a wide age range, but most commonly presents in the first two decades of life [302-304] and shows no sex predilection. Molecularly, the characteristic alteration is t(2;22)(q33;q12), resulting in an *EWSR1*::*CREB1* fusion, followed by t(12;22)(q12;q12), resulting in an *EWSR1*::*ATF1* fusion [305,306]. Rare cases harbor *FUS*::*ATF1* fusion [307,308].

Histologically, AFH consists of fascicles or sheets of oval to spindle-shaped cells with bland vesicular nuclei and prominent pseudoangiomatous blood-filled spaces. The tumor is characterized by a fibrous pseudocapsule with hemosiderin deposition and a pericapsular rim of lymphoplasmacytic infiltrates containing germinal centers, which may mimic a metastatic lymph node. Mitotic figures are usually infrequent, although atypical mitoses and pleomorphic cells may be present [309,310].

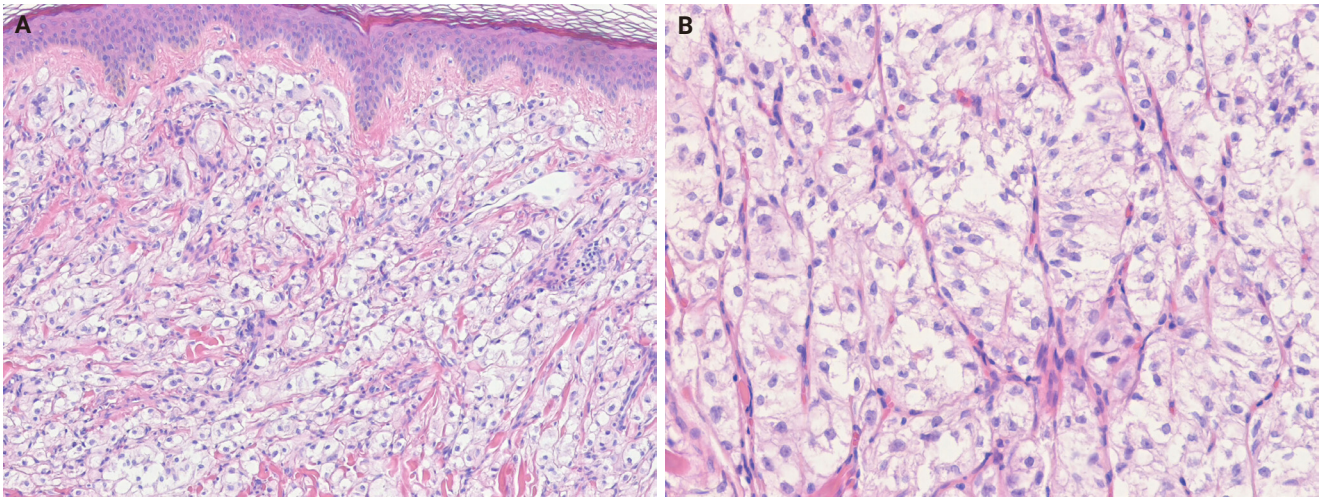

Fig. 14. Perivascular epithelioid cell tumor. (A) The tumor shows dermal epithelioid cells arranged in a trabecular and nested growth pattern. (B) The tumor cells display round to oval nuclei with fine chromatin and abundant clear to pale eosinophilic cytoplasm, with a delicate capillary network surrounding the tumor nests.

Two histological subtypes have been described: a small round cell subtype resembling undifferentiated round cell sarcoma [301,311] and a myxoid subtype [312,313]. Immunohistochemically, most AFHs express SRY-box transcription factor 9 (SOX9) [314], and approximately 50% are positive for desmin. EMA, CD99, and CD68 demonstrate variable immunoreactivity [301]. The Ki-67 proliferation index is typically low [313].

NTRK-rearranged spindle cell neoplasm

NRSCN is a recently recognized molecularly defined spindle cell tumor characterized by activating NTRK or other kinase fusions [315]. These tumors typically arise in the deep dermis and subcutis of the extremities, trunk, and head and neck area [316-318]. Although most cases occur in children and young adults, the age range is wide (0–77 years; median age, 19 years), with no sex predilection [318,319]. Oncogenesis is driven by mitogen-activated protein kinase pathway activation via kinase fusions, most commonly involving *LMNA*::*NTRK1*, *TPR*::*NTRK1*, or *TPM3*::*NTRK1* fusions [315,316]. Alternative rearrangements involving *NTRK2*, *NTRK3*, *RAF1*, *BRAF*, *RET*, *MET*, *ROS1*, or *ALK* have also been reported [318]. NRSCNs are locally infiltrative and prone to local recurrence after incomplete excision. However, metastasis is rare, and the prognostic relevance of histologic grade remains uncertain [318,319].

Histologically, NRSCNs exhibit a broad morphological spectrum. Superficial lesions often show a lipofibromatosis-like pattern, characterized by fibrous septa and spindle cells with ovoid to tapering nuclei and indistinct cytoplasm extending through the adipose tissue (Fig. 15A). Some tumors may be more cellular, with spindled to ovoid cells arranged in fascicles or dispersed loosely in a myxoid stroma. Tumors commonly exhibit hybrid patterns, with highly cellular areas devoid of entrapped adipose tissue admixed with adipose-rich regions. Additionally, lymphocytic infiltrates, staghorn-like vessels, perivascular hyalinization, and stromal collagen bands may also be present. High-grade features such as marked atypia, high mitotic activity, or necrosis are infrequently observed [318,319]. Immunohistochemically, NRSCNs typically coexpress CD34 and S100 protein, with occasional SMA positivity. Tumors with activating NTRK fusions show diffuse pan–tropomyosin receptor kinase (pan-TRK) expression (Fig. 15B) [319,320], but the immunoprofile may be non-specific [316,318]. Therefore, molecular testing is necessary for a definitive diagnosis and for selecting targeted therapy.

Superficial CD34-positive fibroblastic tumor

SCFT is a distinctive, low-grade neoplasm of the skin and subcutaneous tissue, characterized by a consistent morphology and diffuse CD34 expression [321]. It predominantly arises in the lower extremities, particularly the thigh, and less frequently, in the arm, buttock, shoulder, and vulva [322-325]. SCFT typically affects middle-aged adults (median age, 38 years) and shows a slight male predominance [324-327]. Morphological, immuno-

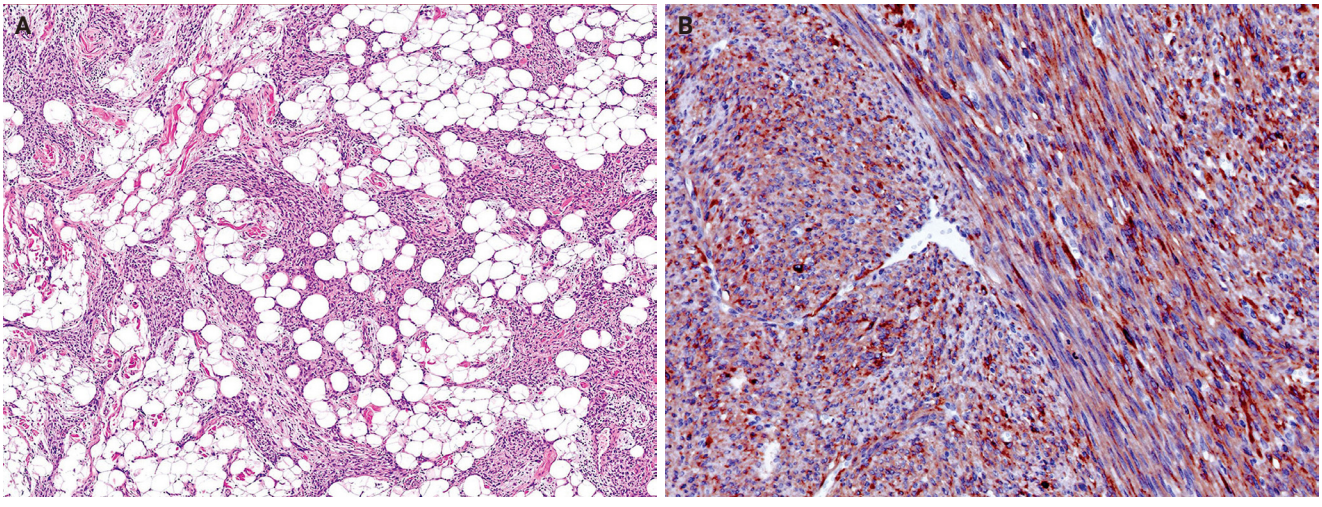

Fig. 15. NTRK-rearranged spindle cell neoplasm. (A) A tumor with a *TPR*::*NTRK1* fusion shows spindle cells infiltrating through subcutaneous fat in a lipofibromatosis-like pattern. (B) A tumor with a *TPM3*::*NTRK1* fusion shows diffuse immunoreactivity for pan-TRK. Reprinted from Suurmeijer and Davis. NTRK-rearranged spindle cell neoplasm. In: WHO Classification of Tumours Editorial Board, ed. WHO classification of tumours: skin tumours. 5th ed. [315], with permission from IARC Press.

https://doi.org/10.4132/jptm.2026.01.09

phenotypic, and molecular findings are identical to those of '*PRDM10*-rearranged soft tissue tumor', supporting their classification as a single entity [325,328]. However, the term 'SCFT' is retained because not all tumors demonstrate detectable *PRDM10* fusions. *PRDM10* rearrangements have been identified in approximately 60% of cases previously classified as SCFT or PRDM10-rearranged soft tissue tumors [325,328]. The prognosis is excellent [323,324].

Histologically, SCFTs are relatively well-circumscribed but partially infiltrative, composed of spindled to pleomorphic cells arranged in fascicles or sheets (Fig. 16A). Tumor cells have abundant eosinophilic cytoplasm, often granular or glassy, and lipidized cells are frequently observed. Nuclear pleomorphism ranges from moderate to marked, with bizarre, hyperchromatic nuclei, prominent nucleoli, and occasional intranuclear cytoplasmic pseudoinclusions. Mitotic activity is low, and necrosis is rare [322,323]. Mixed inflammatory infiltrates are common, and myxoid stroma or metaplastic bone may rarely be present [324]. Immunohistochemically, SCFTs exhibit diffuse CD34 expression and focal cytokeratin (AE1/AE3) positivity in approximately 70% of cases (Fig. 16B). The Ki-67 proliferation index is low (<5%) [324,325]. PRDM10 is consistently expressed [325], and CADM3 (SynCam3) expression has been reported in 95%–100% of cases [324,325].

CRTC1::*TRIM11* cutaneous tumors

CTCT is a dermal neoplasm composed of spindle and epithelioid cells with partial melanocytic differentiation, defined by the characteristic *CRTC1*::*TRIM11* fusion [329]. Recently recognized MITF pathway–activated tumors with melanocytic differentiation include three neoplasms defined by *ACT*::*MITF*, *MITF*::*CREM*, and *CRTC1*::*TRIM11* fusions. In the current WHO classification, *ACT*::*MITF*- and *MITF*::*CREM*-rearranged tumors are grouped as MITF pathway–activated melanocytic tumors within the melanocytic neoplasms family [330], whereas CTCTs are classified as soft tissue tumors of uncertain differentiation. CTCTs arise at various anatomical sites, most commonly in the extremities (upper, 40%; lower, 30%), followed by the trunk (15%) and, less frequently, the head or mucosal regions (oral and nasal) [331,332]. Approximately 50 cases of CTCT have been reported, with no sex predilection and an age range of 11–87 years (median age, 44 years) [331-338]. The molecular role of *CRTC1*::*TRIM11* fusion protein remains unclear; CRTC1 likely contributes to cell proliferation and differentiation by activating cAMP response element-binding protein 1 (CREB1), which subsequently upregulates MITF expression [339-341]. Clinically, CTCTs are usually indolent; however, local recurrence or metastasis occurs in approximately 10% of cases after excision. Confirmation of the *CRTC1*::*TRIM11* fusion is required for diagnosis.

Histologically, CTCTs are well-circumscribed, unencapsulated, dermal-based nodules that lack pigment and may resemble CCS. Tumors are composed of nests and intersecting fascicles of spindle to epithelioid cells with vesicular nuclei, prominent nucleoli, and abundant pale cytoplasm (Fig. 17A). Mitoses are present, but infrequent, and epidermal involvement is rare. Im-

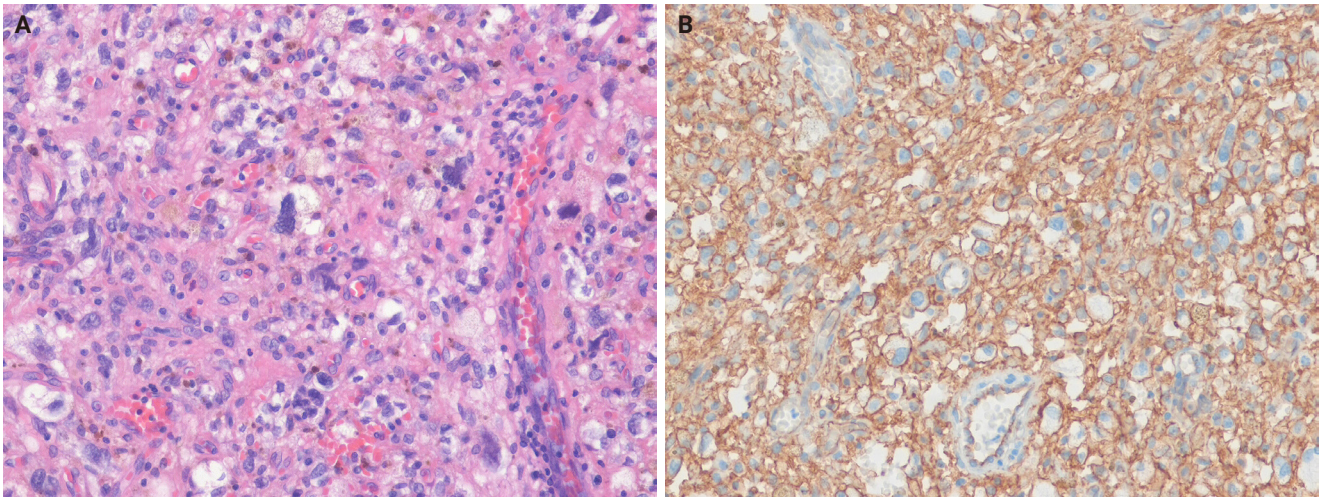

Fig. 16. Superficial CD34-positive fibroblastic tumor. (A) The tumor is composed of spindle to pleomorphic tumor cells with an associated inflammatory infiltrate. (B) The tumor cells show diffuse CD34 expression.

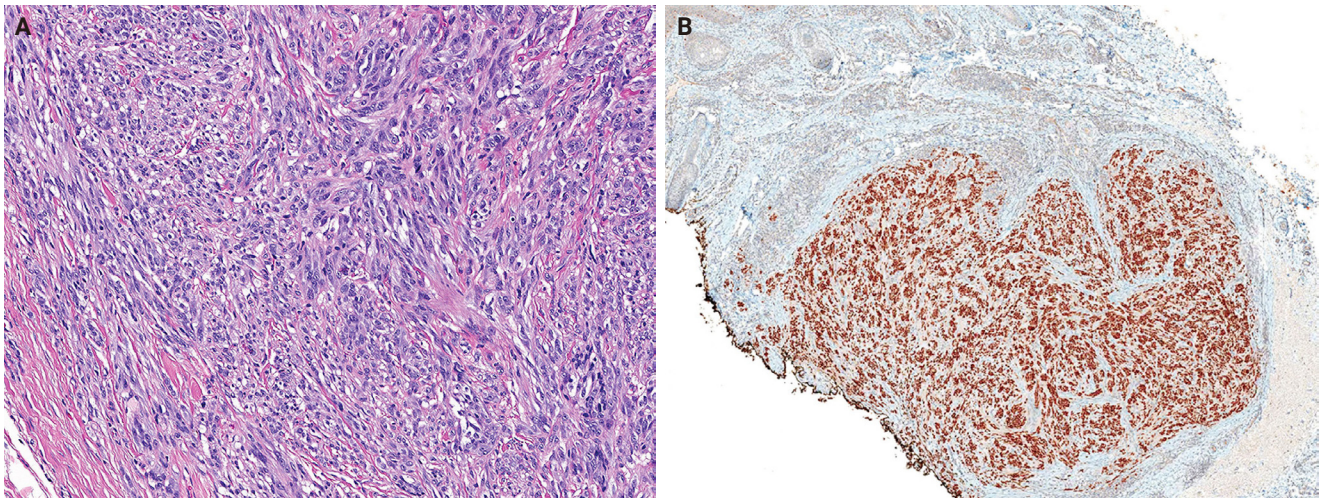

Fig. 17. *CRTC1*::*TRIM11* cutaneous tumor. (A) The tumor is composed of nests and long, intersecting fascicles of spindled and epithelioid cells with mild atypia in a fibrous stroma. (B) The tumor cells show diffuse nuclear positivity for SOX10. The dermal tumor is well-circumscribed and unencapsulated. Reprinted from de la Fouchardiere and Ko. *CRTC1*::*TRIM11* cutaneous tumour. In: WHO Classification of Tumours Editorial Board, ed. WHO classification of tumours: skin tumours. 5th ed. [329], with permission from IARC Press.

munohistochemically, CTCTs show diffuse SOX10 positivity (Fig. 17B). Approximately 50% of cases exhibit diffuse S100 protein staining, while melan-A (MART1) and HMB-45 display focal expression. Pan-TRK expression is present in approximately 60% of cases, and TRIM11 shows nuclear positivity at the tumor periphery [335-337]. The differential diagnoses include CCS and metastatic malignant melanoma, and definitive diagnosis requires confirmation of *CRTC1*::*TRIM11* fusion.

CONCLUSION

This review summarizes key updates and newly recognized entities of cutaneous soft tissue tumors included in the 5th edition of the WHO classification of skin tumors. This edition incorporates recent advances in the taxonomy of cutaneous soft tissue tumors and deepens understanding of their pathogenesis by integrating histological and molecular findings. Accurate diagnosis of cutaneous soft tissue tumors requires careful correlation of clinical, microscopic, immunohistochemical, and molecular findings, together with strict adherence to well-defined diagnostic criteria. Further studies are warranted to elucidate molecular pathogenesis and refine the classification of previously unrecognized cutaneous neoplasms.

Ethics Statement
Not applicable.

Availability of Data and Material
Data sharing not applicable to this article as no datasets were generated or analyzed during the study.

Code Availability
Not applicable.

ORCID
Joon Hyuk Choi https://orcid.org/0000-0002-8638-0360

Conflicts of Interest
J.H.C., a contributing editor of the *Journal of Pathology and Translational Medicine*, was not involved in the editorial evaluation or decision to publish this article.

Funding Statement
No funding to declare.

REFERENCES

1. WHO Classification of Tumours Editorial Board. WHO classification of tumours: skin tumours. 5th ed. Lyon: IARC Press, 2025.
2. Elder DE, Massi D, Scolyer RA, Willemze R. WHO classification of skin tumours. 4th ed. Lyon: IARC Press, 2018.
3. Papke DJ Jr, Hornick JL. Recent advances in the diagnosis, classification and molecular pathogenesis of cutaneous mesenchymal

https://doi.org/10.4132/jptm.2026.01.09

neoplasms. Histopathology 2022; 80: 216-32.
4. Fischer GM, Papke DJ. Gene fusions in superficial mesenchymal neoplasms: emerging entities and useful diagnostic adjuncts. Semin Diagn Pathol 2023; 40: 246-57.
5. Kalmykova AV, Baranovska-Andrigo V, Michal M. Update on cutaneous mesenchymal tumors in the 5th edition of WHO classification of skin tumors with an emphasis on new fusion-associated neoplasms. Virchows Arch 2024; 485: 777-92.
6. Ho J, Collie CJ. What's new in dermatopathology 2023: WHO 5th edition updates. J Pathol Transl Med 2023; 57: 337-40.
7. Requena L, Cheah AL, Patel RM. Naevus lipomatosus superficialis. In: WHO Classification of Tumours Editorial Board, ed. WHO classification of tumours: skin tumours. 5th ed. Lyon: IARC Press, 2025; 459-60.
8. Low I, Fritchie KJ, Ivan D. Lipoma. In: WHO Classification of Tumours Editorial Board, ed. WHO classification of tumours: skin tumours. 5th ed. Lyon: IARC Press, 2025; 461-2.
9. Low I, Calonje JE, Ivan D. Lipoma. In: Elder DE, Massi D, Scolyer RA, Willemze R. WHO classification of skin tumours. 4th ed. Lyon: IARC Press, 2018; 296-7.
10. Billings SD, Requena L. Angiolipoma. In: WHO Classification of Tumours Editorial Board, ed. WHO classification of tumours: skin tumours. 5th ed. Lyon: IARC Press, 2025; 463-4.
11. Sheng W, Lu L, Wang J. Cellular angiolipoma: a clinicopathological and immunohistochemical study of 12 cases. Am J Dermatopathol 2013; 35: 220-5.
12. Patel RM, Billings SD, Ud Din N, Wong D. Spindle cell/pleomorphic lipoma. In: WHO Classification of Tumours Editorial Board, ed. WHO classification of tumours: skin tumours. 5th ed. Lyon: IARC Press, 2025; 465-6.
13. Folpe AL, Gill AJ. Atypical lipomatous tumour. In: WHO Classification of Tumours Editorial Board, ed. WHO classification of tumours: skin tumours. 5th ed. Lyon: IARC Press, 2025; 467-8.
14. Mathew R, Morgan MB. Dermal atypical lipomatous tumor/well-differentiated liposarcoma obfuscated by epidermal inclusion cyst: a wolf in sheep's clothing? Am J Dermatopathol 2006; 28: 338-40.
15. Paredes BE, Mentzel T. Atypical lipomatous tumor/"well-differentiated liposarcoma" of the skin clinically presenting as a skin tag: clinicopathologic, immunohistochemical, and molecular analysis of 2 cases. Am J Dermatopathol 2011; 33: 603-7.
16. Yoshida A, Ushiku T, Motoi T, Shibata T, Fukayama M, Tsuda H. Well-differentiated liposarcoma with low-grade osteosarcomatous component: an underrecognized variant. Am J Surg Pathol 2010; 34: 1361-6.
17. Evans HL. Atypical lipomatous tumor, its variants, and its combined forms: a study of 61 cases, with a minimum follow-up of 10 years. Am J Surg Pathol 2007; 31: 1-14.
18. Patel RM, Folpe AL. Pleomorphic liposarcoma. In: WHO Classification of Tumours Editorial Board, ed. WHO classification of tumours: skin tumours. 5th ed. Lyon: IARC Press, 2025; 469-70.
19. Miettinen M, Enzinger FM. Epithelioid variant of pleomorphic liposarcoma: a study of 12 cases of a distinctive variant of high-grade liposarcoma. Mod Pathol 1999; 12: 722-8.
20. Pizem J, Matjasic A, Zupan A, Luzar B, Sekoranja D, Dimnik K. Fibroma of tendon sheath is defined by a *USP6* gene fusion-morphologic and molecular reappraisal of the entity. Mod Pathol 2021; 34: 1876-88.
21. Eisenberg JM, Buckwalter V JA, Snow AN, Davick J. Cellular fibroma of tendon sheath with novel *TNC-USP6* gene fusion clinically mimicking arthritis in a 7-year-old boy. Pediatr Dev Pathol 2022; 25: 192-6.
22. Mantilla JG, Gross JM, Liu YJ, Hoch BL, Ricciotti RW. Characterization of novel *USP6* gene rearrangements in a subset of so-called cellular fibroma of tendon sheath. Mod Pathol 2021; 34: 13-9.
23. Puls F, Hofvander J, Magnusson L, et al. *Fn1-EGF* gene fusions are recurrent in calcifying aponeurotic fibroma. J Pathol 2016; 238: 502-7.
24. Al-Ibraheemi A, Folpe AL, Perez-Atayde AR, et al. Aberrant receptor tyrosine kinase signaling in lipofibromatosis: a clinicopathological and molecular genetic study of 20 cases. Mod Pathol 2019; 32: 423-34.
25. Fetsch JF, Miettinen M. Calcifying aponeurotic fibroma: a clinicopathologic study of 22 cases arising in uncommon sites. Hum Pathol 1998; 29: 1504-10.
26. Wang WL, Al-Zaid T, Patel RM. Sclerotic fibroma. In: WHO Classification of Tumours Editorial Board, ed. WHO classification of tumours: skin tumours. 5th ed. Lyon: IARC Press, 2025; 475.
27. Cloutier JM, Shalin SC, Lindberg M, et al. Cutaneous pleomorphic fibromas arising in patients with germline *TP53* mutations. J Cutan Pathol 2020; 47: 734-41.
28. Linos K, Luzar B, O'Brien BH. Dermatofibroma (fibrous histiocytoma). In: WHO Classification of Tumours Editorial Board, ed. WHO classification of tumours: skin tumours. 5th ed. Lyon: IARC Press, 2025; 488-90.
29. Plaszczyca A, Nilsson J, Magnusson L, et al. Fusions involving protein kinase C and membrane-associated proteins in benign fibrous histiocytoma. Int J Biochem Cell Biol 2014; 53: 475-81.
30. Jedrych JJ, Duraisamy S, Karunamurthy A. Aneurysmal fibrous histiocytomas with recurrent rearrangement of the *PRKCD* gene

and *LAMTOR1-PRKCD* fusions. J Cutan Pathol 2018; 45: 966-8.
31. Panagopoulos I, Gorunova L, Bjerkehagen B, Lobmaier I, Heim S. *LAMTOR1-PRKCD* and *NUMA1-SFMBT1* fusion genes identified by RNA sequencing in aneurysmal benign fibrous histiocytoma with t(3;11)(p21;q13). Cancer Genet 2015; 208: 545-51.
32. Prieto VG, Andea AA, Nascimento AF. Superficial fibromatosis. In: WHO Classification of Tumours Editorial Board, ed. WHO classification of tumours: skin tumours. 5th ed. Lyon: IARC Press, 2025; 491-2.
33. Montgomery E, Lee JH, Abraham SC, Wu TT. Superficial fibromatoses are genetically distinct from deep fibromatoses. Mod Pathol 2001; 14: 695-701.
34. Redlich GC, Montgomery KD, Allgood GA, Joste NE. Plexiform fibrohistiocytic tumor with a clonal cytogenetic anomaly. Cancer Genet Cytogenet 1999; 108: 141-3.
35. Smith S, Fletcher CD, Smith MA, Gusterson BA. Cytogenetic analysis of a plexiform fibrohistiocytic tumor. Cancer Genet Cytogenet 1990; 48: 31-4.
36. Leclerc-Mercier S, Pedeutour F, Fabas T, Glorion C, Brousse N, Fraitag S. Plexiform fibrohistiocytic tumor with molecular and cytogenetic analysis. Pediatr Dermatol 2011; 28: 26-9.
37. Requena L. Cutaneous myxoma (superficial angiomyxoma). In: WHO Classification of Tumours Editorial Board, ed. WHO classification of tumours: skin tumours. 5th ed. Lyon: IARC Press, 2025; 499-500.
38. Veugelers M, Wilkes D, Burton K, et al. Comparative *PRKAR1A* genotype-phenotype analyses in humans with Carney complex and *prkar1a* haploinsufficient mice. Proc Natl Acad Sci U S A 2004; 101: 14222-7.
39. Wilkes D, McDermott DA, Basson CT. Clinical phenotypes and molecular genetic mechanisms of Carney complex. Lancet Oncol 2005; 6: 501-8.
40. Erickson-Johnson MR, Chou MM, Evers BR, et al. Nodular fasciitis: a novel model of transient neoplasia induced by *MYH9-USP6* gene fusion. Lab Invest 2011; 91: 1427-33.
41. Teramura Y, Yamazaki Y, Tanaka M, et al. Case of mesenchymal tumor with the *PPP6R3-USP6* fusion, possible nodular fasciitis with malignant transformation. Pathol Int 2019; 69: 706-9.
42. Papke DJ Jr, Oliveira AM, Chou MM, Fletcher CD. Morphologically malignant nodular fasciitis with *CALD1-USP6* fusion. Virchows Arch 2021; 479: 1007-12.
43. Lenz J, Michal M, Svajdler M, et al. Novel *EIF5A-USP6* gene fusion in nodular fasciitis associated with unusual pathologic features: a report of a case and review of the literature. Am J Dermatopathol 2020; 42: 539-43.
44. Dadone-Montaudie B, Alberti L, Duc A, et al. Alternative *PDGFD* rearrangements in dermatofibrosarcomas protuberans without *PDGFB* fusions. Mod Pathol 2018; 31: 1683-93.
45. Lee PH, Huang SC, Wu PS, et al. Molecular characterization of dermatofibrosarcoma protuberans: the clinicopathologic significance of uncommon fusion gene rearrangements and their diagnostic importance in the exclusively subcutaneous and circumscribed lesions. Am J Surg Pathol 2022; 46: 942-55.
46. Abbott JJ, Erickson-Johnson M, Wang X, Nascimento AG, Oliveira AM. Gains of *COL1A1-PDGFB* genomic copies occur in fibrosarcomatous transformation of dermatofibrosarcoma protuberans. Mod Pathol 2006; 19: 1512-8.
47. Hiraki-Hotokebuchi Y, Yamada Y, Kohashi K, et al. Alteration of PDGFRβ-Akt-mTOR pathway signaling in fibrosarcomatous transformation of dermatofibrosarcoma protuberans. Hum Pathol 2017; 67: 60-8.
48. Wang WL, Colebatch AJ, Gill AJ, Wang J. Dermatofibrosarcoma protuberans. In: WHO Classification of Tumours Editorial Board, ed. WHO classification of tumours: skin tumours. 5th ed. Lyon: IARC Press, 2025; 511-4.
49. Arbajian E, Hofvander J, Magnusson L, Mertens F. Deep sequencing of myxoinflammatory fibroblastic sarcoma. Genes Chromosomes Cancer 2020; 59: 309-17.
50. Suster D, Michal M, Huang H, et al. Myxoinflammatory fibroblastic sarcoma: an immunohistochemical and molecular genetic study of 73 cases. Mod Pathol 2020; 33: 2520-33.
51. Antonescu CR, Zhang L, Nielsen GP, Rosenberg AE, Dal Cin P, Fletcher CD. Consistent t(1;10) with rearrangements of *TGFBR3* and *MGEA5* in both myxoinflammatory fibroblastic sarcoma and hemosiderotic fibrolipomatous tumor. Genes Chromosomes Cancer 2011; 50: 757-64.
52. Zreik RT, Carter JM, Sukov WR, et al. *TGFBR3* and *MGEA5* rearrangements are much more common in "hybrid" hemosiderotic fibrolipomatous tumor-myxoinflammatory fibroblastic sarcomas than in classical myxoinflammatory fibroblastic sarcomas: a morphological and fluorescence in situ hybridization study. Hum Pathol 2016; 53: 14-24.
53. Carter JM, Sukov WR, Montgomery E, et al. *TGFBR3* and *MGEA5* rearrangements in pleomorphic hyalinizing angiectatic tumors and the spectrum of related neoplasms. Am J Surg Pathol 2014; 38: 1182-992.
54. Kao YC, Ranucci V, Zhang L, et al. Recurrent *BRAF* gene rearrangements in myxoinflammatory fibroblastic sarcomas, but not hemosiderotic fibrolipomatous tumors. Am J Surg Pathol 2017; 41: 1456-65.

https://doi.org/10.4132/jptm.2026.01.09

55. Huang HY, Billings SD, Creytens D, Shibata T. Myxofibrosarcoma. In: WHO Classification of Tumours Editorial Board, ed. WHO classification of tumours: skin tumours. 5th ed. Lyon: IARC Press, 2025; 517-8.
56. Willems SM, Debiec-Rychter M, Szuhai K, Hogendoorn PC, Sciot R. Local recurrence of myxofibrosarcoma is associated with increase in tumour grade and cytogenetic aberrations, suggesting a multistep tumour progression model. Mod Pathol 2006; 19: 407-16.
57. Cancer Genome Atlas Research Network. Comprehensive and integrated genomic characterization of adult soft tissue sarcomas. Cell 2017; 171: 950-65.
58. Ogura K, Hosoda F, Arai Y, et al. Integrated genetic and epigenetic analysis of myxofibrosarcoma. Nat Commun 2018; 9: 2765.
59. Li CF, Wang JM, Kang HY, et al. Characterization of gene amplification-driven *SKP2* overexpression in myxofibrosarcoma: potential implications in tumor progression and therapeutics. Clin Cancer Res 2012; 18: 1598-610.
60. Li CF, Fang FM, Lan J, et al. *AMACR* amplification in myxofibrosarcomas: a mechanism of overexpression that promotes cell proliferation with therapeutic relevance. Clin Cancer Res 2014; 20: 6141-52.
61. Okada T, Lee AY, Qin LX, et al. Integrin-α10 dependency identifies RAC and *RICTOR* as therapeutic targets in high-grade myxofibrosarcoma. Cancer Discov 2016; 6: 1148-65.
62. Calonje JE, Panse G. Fibrous papule. In: WHO Classification of Tumours Editorial Board, ed. WHO classification of tumours: skin tumours. 5th ed. Lyon: IARC Press, 2025; 483-4.
63. Damman J, Biswas A. Fibrous papule: a histopathologic review. Am J Dermatopathol 2018; 40: 551-60.
64. Schaffer JV, Gohara MA, McNiff JM, Aasi SZ, Dvoretzky I. Multiple facial angiofibromas: a cutaneous manifestation of Birt-Hogg-Dube syndrome. J Am Acad Dermatol 2005; 53(2 Suppl 1):S108-11.
65. Darling TN, Skarulis MC, Steinberg SM, Marx SJ, Spiegel AM, Turner M. Multiple facial angiofibromas and collagenomas in patients with multiple endocrine neoplasia type 1. Arch Dermatol 1997; 133: 853-7.
66. Chan JY, Wang KH, Fang CL, Chen WY. Fibrous papule of the face, similar to tuberous sclerosis complex-associated angiofibroma, shows activation of the mammalian target of rapamycin pathway: evidence for a novel therapeutic strategy? PLoS One 2014; 9: e89467.
67. Bansal C, Stewart D, Li A, Cockerell CJ. Histologic variants of fibrous papule. J Cutan Pathol 2005; 32: 424-8.
68. Krauland K, Patel AB. Junctional melanocytic hyperplasia overlying benign fibrous papule: an under-recognized variant of a common lesion. J Cutan Pathol 2020; 47: 1220-3.
69. Fraitag Spinner S, Billings SD. Fibroblastic connective tissue naevus. WHO Classification of Tumours Editorial Board. WHO classification of tumours: skin tumours. 5th ed. Lyon: IARC Press, 2025; 485-6.
70. de Feraudy S, Fletcher CD. Fibroblastic connective tissue nevus: a rare cutaneous lesion analyzed in a series of 25 cases. Am J Surg Pathol 2012; 36: 1509-15.
71. Pennacchia I, Kutzner H, Kazakov DV, Mentzel T. Fibroblastic connective tissue nevus: clinicopathological and immunohistochemical study of 14 cases. J Cutan Pathol 2017; 44: 827-34.
72. Velez MJ, Billings SD, Weaver JA. Fibroblastic connective tissue nevus. J Cutan Pathol 2016; 43: 75-9.
73. Tallegas M, Fraitag S, Binet A, et al. Novel *KHDRBS1-NTRK3* rearrangement in a congenital pediatric CD34-positive skin tumor: a case report. Virchows Arch 2019; 474: 111-5.
74. Lynch MC, Samson TD, Zaenglein AL, Chung CG. Evolution of fibroblastic connective tissue nevus in an infant. Am J Dermatopathol 2017; 39: 225-7.
75. Ohata M, Fujiwara S, Yoshioka A, et al. Agminated fibroblastic connective tissue nevus in a 1-year-old boy. Pediatr Dermatol 2019; 36: 997-8.
76. Downey C, Requena L, Bague S, Sanchez Martinez MA, Lloreta J, Baselga E. Agminated fibroblastic connective tissue nevus: a new clinical presentation. Pediatr Dermatol 2016; 33: e240-3.
77. Allemant Ortiz LJ, Calderon-Castrat X, Orellana Cortez A, Ingar Carbone B, Santos-Briz A. Congenital atrophic plaque: fibroblastic connective tissue nevus. Pediatr Dermatol 2017; 34: e216-8.
78. Oliveira AM, Rosenberg AE. Fibro-osseous tumour of digits. In: WHO Classification of Tumours Editorial Board, ed. WHO classification of tumours: skin tumours. 5th ed. Lyon: IARC Press, 2025; 487.
79. Dupree WB, Enzinger FM. Fibro-osseous pseudotumor of the digits. Cancer 1986; 58: 2103-9.
80. Flucke U, Shepard SJ, Bekers EM, et al. Fibro-osseous pseudotumor of digits: expanding the spectrum of clonal transient neoplasms harboring *USP6* rearrangement. Ann Diagn Pathol 2018; 35: 53-5.
81. Svajdler M, Michal M, Martinek P, et al. Fibro-osseous pseudotumor of digits and myositis ossificans show consistent *COL1A1-USP6* rearrangement: a clinicopathological and genetic study of 27 cases. Hum Pathol 2019; 88: 39-47.
82. de Silva MV, Reid R. Myositis ossificans and fibroosseous pseudo-

tumor of digits: a clinicopathological review of 64 cases with emphasis on diagnostic pitfalls. Int J Surg Pathol 2003; 11: 187-95.
83. Wang JC, Li WS, Kao YC, et al. Clinicopathological and molecular characterisation of *USP6*-rearranged soft tissue neoplasms: the evidence of genetic relatedness indicates an expanding family with variable bone-forming capacity. Histopathology 2021; 78: 676-89.
84. Rosenberg AE. Pseudosarcomas of soft tissue. Arch Pathol Lab Med 2008; 132: 579-86.
85. Laskin WB. Inclusion body fibromatosis. In: WHO Classification of Tumours Editorial Board, ed. WHO classification of tumours: skin tumours. 5th ed. Lyon: IARC Press, 2025; 493-4.
86. Coffin CM, Dehner LP. Fibroblastic-myofibroblastic tumors in children and adolescents: a clinicopathologic study of 108 examples in 103 patients. Pediatr Pathol 1991; 11: 569-88.
87. Chung EB. Pitfalls in diagnosing benign soft tissue tumors in infancy and childhood. Pathol Annu 1985; 20 Pt 2: 323-86.
88. Plusje LG, Bastiaens M, Chang A, Hogendoorn PC. Infantile-type digital fibromatosis tumour in an adult. Br J Dermatol 2000; 143: 1107-8.
89. Laskin WB, Miettinen M, Fetsch JF. Infantile digital fibroma/fibromatosis: a clinicopathologic and immunohistochemical study of 69 tumors from 57 patients with long-term follow-up. Am J Surg Pathol 2009; 33: 1-13.
90. Purdy LJ, Colby TV. Infantile digital fibromatosis occurring outside the digit. Am J Surg Pathol 1984; 8: 787-90.
91. Allen PW. Recurring digital fibrous tumours of childhood. Pathology 1972; 4: 215-23.
92. Mukai M, Torikata C, Iri H, Hata J, Naito M, Shimoda T. Immunohistochemical identification of aggregated actin filaments in formalin-fixed, paraffin-embedded sections. I. A study of infantile digital fibromatosis by a new pretreatment. Am J Surg Pathol 1992; 16: 110-5.
93. Henderson H, Peng YJ, Salter DM. Anti-calponin 1 antibodies highlight intracytoplasmic inclusions of infantile digital fibromatosis. Histopathology 2014; 64: 752-5.
94. McNiff J, Roy SF. Multinucleate cell angiohistiocytoma. In: WHO Classification of Tumours Editorial Board, ed. WHO classification of tumours: skin tumours. 5th ed. Lyon: IARC Press, 2025; 503-4.
95. Cribier B, Gambini C, Rainero M, Grosshans E. Multinucleate cell angiohistiocytoma: a review and report of four cases. Acta Derm Venereol 1995; 75: 337-9.
96. Frew JW. Multinucleate cell angiohistiocytoma: clinicopathological correlation of 142 cases with insights into etiology and pathogenesis. Am J Dermatopathol 2015; 37: 222-8.
97. Roy SF, Dong D, Myung P, McNiff JM. Multinucleate cell angiohistiocytoma: a clinicopathologic study of 62 cases and proposed diagnostic criteria. J Cutan Pathol 2019; 46: 563-9.
98. Jia QN, Qiao J, Qu T. Generalized multinucleate cell angiohistiocytoma with possible origin from fibroblasts: a clinicopathological study of 15 cases. J Dermatol 2021; 48: 114-9.
99. Cesinaro AM, Roncati L, Maiorana A. Estrogen receptor alpha overexpression in multinucleate cell angiohistiocytoma: new insights into the pathogenesis of a reactive process. Am J Dermatopathol 2010; 32: 655-9.
100. Jaconelli L, Kanitakis J, Ktiouet S, Faure M, Claudy A. Multinucleate cell angiohistiocytoma: report of three new cases and literature review. Dermatol Online J 2009; 15: 4.
101. Suurmeijer AJ, Habeeb O, Michael M, Thway K. *EWSR1*::*SMAD3*-rearranged fibroblastic tumour. In: WHO Classification of Tumours Editorial Board, ed. WHO classification of tumours: skin tumours. 5th ed. Lyon: IARC Press, 2025; 509-10.
102. Michal M, Berry RS, Rubin BP, et al. *EWSR1-SMAD3*-rearranged fibroblastic tumor: an emerging entity in an increasingly more complex group of fibroblastic/myofibroblastic neoplasms. Am J Surg Pathol 2018; 42: 1325-33.
103. Habeeb O, Korty KE, Azzato EM, et al. *EWSR1-SMAD3* rearranged fibroblastic tumor: case series and review. J Cutan Pathol 2021; 48: 255-62.
104. Calonje JE, Marusic Z, North PE, Sangueza OP. Tufted haemangioma. In: WHO Classification of Tumours Editorial Board, ed. WHO classification of tumours: skin tumours. 5th ed. Lyon: IARC Press, 2025; 530-1.
105. Ten Broek RW, Koelsche C, Eijkelenboom A, et al. Kaposiform hemangioendothelioma and tufted angioma: (epi)genetic analysis including genome-wide methylation profiling. Ann Diagn Pathol 2020; 44: 151434.
106. Requena L, Calonje JE, Fisher C. Postradiation atypical vascular lesion. In: WHO Classification of Tumours Editorial Board, ed. WHO classification of tumours: skin tumours. 5th ed. Lyon: IARC Press, 2025; 551-2.
107. Hornick JL, Billings SD, Calonje JE, Folpe AL, Requena L. Hobnail haemangioendotheliomas. In: WHO Classification of Tumours Editorial Board, ed. WHO classification of tumours: skin tumours. 5th ed. Lyon: IARC Press, 2025; 557-8.
108. Groesser L, Peterhof E, Evert M, Landthaler M, Berneburg M, Hafner C. *BRAF* and *RAS* mutations in sporadic and secondary pyogenic granuloma. J Invest Dermatol 2016; 136: 481-6.
109. Jansen P, Muller H, Lodde GC, et al. *GNA14*, *GNA11*, and *GNAQ* mutations are frequent in benign but not malignant cutaneous vascular tumors. Front Genet 2021; 12: 663272.

https://doi.org/10.4132/jptm.2026.01.09

110. Liau JY, Lee JC, Tsai JH, Chen CC, Chung YC, Wang YH. High frequency of *GNA14*, *GNAQ*, and *GNA11* mutations in cherry hemangioma: a histopathological and molecular study of 85 cases indicating *GNA14* as the most commonly mutated gene in vascular neoplasms. Mod Pathol 2019; 32: 1657-65.
111. Legendre P, Norkowski E, Le Pelletier F, et al. Glomeruloid haemangioma: a possible consequence of elevated VEGF in POEMS and Erdheim-Chester disease. Eur J Dermatol 2018; 28: 784-9.
112. Calonje JE, Marusic Z, North PE, Sangueza OP. Epithelioid haemangioma. In: WHO Classification of Tumours Editorial Board, ed. WHO classification of tumours: skin tumours. 5th ed. Lyon: IARC Press, 2025; 528-9.
113. Ortins-Pina A, Llamas-Velasco M, Turpin S, Soares-de-Almeida L, Filipe P, Kutzner H. *FOSB* immunoreactivity in endothelia of epithelioid hemangioma (angiolymphoid hyperplasia with eosinophilia). J Cutan Pathol 2018; 45: 395-402.
114. Calonje JE, Marusic Z, North PE, Sangueza OP. Arteriovenous malformation. In: WHO Classification of Tumours Editorial Board, ed. WHO classification of tumours: skin tumours. 5th ed. Lyon: IARC Press, 2025; 545-6.
115. Billings SD, Agaram NP, Calonje JE, Folpe AL, Hornick JL, Requena L. Pseudomyogenic haemangioendothelioma. In: WHO Classification of Tumours Editorial Board, ed. WHO classification of tumours: skin tumours. 5th ed. Lyon: IARC Press, 2025; 553-4.
116. Walther C, Tayebwa J, Lilljebjorn H, et al. A novel *SERPINE1-FOSB* fusion gene results in transcriptional up-regulation of FOSB in pseudomyogenic haemangioendothelioma. J Pathol 2014; 232: 534-40.
117. Zhu G, Benayed R, Ho C, et al. Diagnosis of known sarcoma fusions and novel fusion partners by targeted RNA sequencing with identification of a recurrent *ACTB-FOSB* fusion in pseudomyogenic hemangioendothelioma. Mod Pathol 2019; 32: 609-20.
118. Panagopoulos I, Lobmaier I, Gorunova L, Heim S. Fusion of the genes *WWTR1* and *FOSB* in pseudomyogenic hemangioendothelioma. Cancer Genomics Proteomics 2019; 16: 293-8.
119. Bridge JA, Sumegi J, Royce T, Baker M, Linos K. A novel *CLTC-FOSB* gene fusion in pseudomyogenic hemangioendothelioma of bone. Genes Chromosomes Cancer 2021; 60: 38-42.
120. Hakar MH, White K, Hansford BG, Swensen J, Davis JL. Novel *EGFL7-FOSB* fusion in pseudomyogenic haemangioendothelioma with widely metastatic disease. Histopathology 2021; 79: 888-91.
121. Hornick JL, Billings SD, Calonje JE, Folpe AL, Requena L. Epithelioid haemangioendothelioma. In: WHO Classification of Tumours Editorial Board, ed. WHO classification of tumours: skin tumours. 5th ed. Lyon: IARC Press, 2025; 555-6.
122. Errani C, Zhang L, Sung YS, et al. A novel *WWTR1-CAMTA1* gene fusion is a consistent abnormality in epithelioid hemangioendothelioma of different anatomic sites. Genes Chromosomes Cancer 2011; 50: 644-53.
123. Antonescu CR, Le Loarer F, Mosquera JM, et al. Novel *YAP1-TFE3* fusion defines a distinct subset of epithelioid hemangioendothelioma. Genes Chromosomes Cancer 2013; 52: 775-84.
124. Dermawan JK, Azzato EM, Billings SD, et al. *YAP1-TFE3*-fused hemangioendothelioma: a multi-institutional clinicopathologic study of 24 genetically-confirmed cases. Mod Pathol 2021; 34: 2211-21.
125. Anderson WJ, Fletcher CD, Hornick JL. Loss of expression of YAP1 C-terminus as an ancillary marker for epithelioid hemangioendothelioma variant with *YAP1-TFE3* fusion and other YAP1-related vascular neoplasms. Mod Pathol 2021; 34: 2036-42.
126. Hornick JL, Billings SD, Folpe AL, Requena L, Rubin BP. Composite haemangioendothelioma. In: WHO Classification of Tumours Editorial Board, ed. WHO classification of tumours: skin tumours. 5th ed. Lyon: IARC Press, 2025; 559-60.
127. Antonescu CR, Dickson BC, Sung YS, et al. Recurrent *YAP1* and *MAML2* gene rearrangements in retiform and composite hemangioendothelioma. Am J Surg Pathol 2020; 44: 1677-84.
128. Perry KD, Al-Lbraheemi A, Rubin BP, et al. Composite hemangioendothelioma with neuroendocrine marker expression: an aggressive variant. Mod Pathol 2017; 30: 1589-602.
129. Dermawan JK, Westra WH, Antonescu CR. Recurrent *PTBP1*::*MAML2* fusions in composite hemangioendothelioma with neuroendocrine differentiation: a report of two cases involving neck lymph nodes. Genes Chromosomes Cancer 2022; 61: 187-93.
130. Grayson W, Dezube BJ, Doyle LA, Pantanowitz L. Kaposi sarcoma. In: WHO Classification of Tumours Editorial Board, ed. WHO classification of tumours: skin tumours. 5th ed. Lyon: IARC Press, 2025; 561-5.
131. Kiuru-Kuhlefelt S, Sarlomo-Rikala M, Larramendy ML, et al. *FGF4* and *INT2* oncogenes are amplified and expressed in Kaposi's sarcoma. Mod Pathol 2000; 13: 433-7.
132. Pyakurel P, Montag U, Castanos-Velez E, et al. CGH of microdissected Kaposi's sarcoma lesions reveals recurrent loss of chromosome Y in early and additional chromosomal changes in late tumour stages. AIDS 2006; 20: 1805-12.
133. Billings SD, Brenn T, Hornick JL, Thway K. Cutaneous angiosarcoma. In: WHO Classification of Tumours Editorial Board,

ed. WHO classification of tumours: skin tumours. 5th ed. Lyon: IARC Press, 2025; 566-7.
134. Painter CA, Jain E, Tomson BN, et al. The angiosarcoma project: enabling genomic and clinical discoveries in a rare cancer through patient-partnered research. Nat Med 2020; 26: 181-7.
135. Manner J, Radlwimmer B, Hohenberger P, et al. *MYC* high level gene amplification is a distinctive feature of angiosarcomas after irradiation or chronic lymphedema. Am J Pathol 2010; 176: 34-9.
136. Ko JS, Billings SD, Lanigan CP, Buehler D, Fernandez AP, Tubbs RR. Fully automated dual-color dual-hapten silver in situ hybridization staining for *MYC* amplification: a diagnostic tool for discriminating secondary angiosarcoma. J Cutan Pathol 2014; 41: 286-92.
137. Fernandez AP, Sun Y, Tubbs RR, Goldblum JR, Billings SD. Fish for *MYC* amplification and anti-MYC immunohistochemistry: useful diagnostic tools in the assessment of secondary angiosarcoma and atypical vascular proliferations. J Cutan Pathol 2012; 39: 234-42.
138. Winderlich M, Keller L, Cagna G, et al. VE-PTP controls blood vessel development by balancing Tie-2 activity. J Cell Biol 2009; 185: 657-71.
139. Behjati S, Tarpey PS, Sheldon H, et al. Recurrent *PTPRB* and *PLCG1* mutations in angiosarcoma. Nat Genet 2014; 46: 376-9.
140. Antonescu CR, Yoshida A, Guo T, et al. *KDR* activating mutations in human angiosarcomas are sensitive to specific kinase inhibitors. Cancer Res 2009; 69: 7175-9.
141. Torrence D, Antonescu CR. The genetics of vascular tumours: an update. Histopathology 2022; 80: 19-32.
142. Huang SC, Zhang L, Sung YS, et al. Recurrent CIC gene abnormalities in angiosarcomas: a molecular study of 120 cases with concurrent investigation of *PLCG1*, *KDR*, *MYC*, and *FLT4* gene alterations. Am J Surg Pathol 2016; 40: 645-55.
143. Calonje JE, Marusic Z, North PE, Sangueza OP. Papillary haemangioma. In: WHO Classification of Tumours Editorial Board, ed. WHO classification of tumours: skin tumours. 5th ed. Lyon: IARC Press, 2025; 525.
144. Suurmeijer AJ, Fletcher CD. Papillary haemangioma: a distinctive cutaneous haemangioma of the head and neck area containing eosinophilic hyaline globules. Histopathology 2007; 51: 638-48.
145. Maloney N, Miller P, Linos K. Papillary hemangioma: an under-recognized entity not to be confused with glomeruloid hemangioma. Am J Dermatopathol 2020; 42: 211-4.
146. Marusic Z, Calonje JE, North PE, Sangueza OP. Poikilodermatous plaque-like haemangioma. In: WHO Classification of Tumours Editorial Board, ed. WHO classification of tumours: skin tumours. 5th ed. Lyon: IARC Press, 2025; 540-1.
147. Semkova K, Carr R, Grainger M, et al. Poikilodermatous plaque-like hemangioma: case series of a newly defined entity. J Am Acad Dermatol 2019; 81: 1257-70.
148. Sullivan M, Hartman R, Mahalingam M. Poikilodermatous plaque-like hemangioma: a benign vasoformative entity with reproducible histopathologic and clinical features. J Cutan Pathol 2020; 47: 950-3.
149. Calonje JE, Marusic Z, North PE, Sangueza OP. Acquired elastotic haemangioma. In: WHO Classification of Tumours Editorial Board, ed. WHO classification of tumours: skin tumours. 5th ed. Lyon: IARC Press, 2025; 542.
150. Requena L, Kutzner H, Mentzel T. Acquired elastotic hemangioma: a clinicopathologic variant of hemangioma. J Am Acad Dermatol 2002; 47: 371-6.
151. Jeunon T, Carvalho Wagnes Stofler ME, Teixeira Rezende P, Staccioli Castro M, Jeunon-Sousa MA. Acquired elastotic hemangioma: a case report and review of 49 previously reported cases. Am J Dermatopathol 2020; 42: 244-50.
152. Fanburg-Smith JC, Michal M, Partanen TA, Alitalo K, Miettinen M. Papillary intralymphatic angioendothelioma (PILA): a report of twelve cases of a distinctive vascular tumor with phenotypic features of lymphatic vessels. Am J Surg Pathol 1999; 23: 1004-10.
153. Li B, Li Y, Tian XY, Li Z. Unusual multifocal intraosseous papillary intralymphatic angioendothelioma (Dabska tumor) of facial bones: a case report and review of literature. Diagn Pathol 2013; 8: 160.
154. Gambarotti M, Righi A, Sbaraglia M, et al. Intraosseous papillary intralymphatic angioendothelioma (PILA): one new case and review of the literature. Clin Sarcoma Res 2018; 8: 1.
155. Calonje E, Fletcher CD, Wilson-Jones E, Rosai J. Retiform hemangioendothelioma: a distinctive form of low-grade angiosarcoma delineated in a series of 15 cases. Am J Surg Pathol 1994; 18: 115-25.
156. Tan D, Kraybill W, Cheney RT, Khoury T. Retiform hemangioendothelioma: a case report and review of the literature. J Cutan Pathol 2005; 32: 634-7.
157. Arriola AG, Taylor LA, Asemota E, et al. Atypical retiform hemangioendothelioma arising in a patient with Milroy disease: a case report and review of the literature. J Cutan Pathol 2017; 44: 98-103.
158. Emberger M, Laimer M, Steiner H, Zelger B. Retiform hemangioendothelioma: presentation of a case expressing D2-40. J Cutan Pathol 2009; 36: 987-90.
159. Miettinen M, Wang ZF. Prox1 transcription factor as a marker for

https://doi.org/10.4132/jptm.2026.01.09

vascular tumors-evaluation of 314 vascular endothelial and 1086 nonvascular tumors. Am J Surg Pathol 2012; 36: 351-9.
160. Jackett LA, Folpe AL. Glomus tumour. In: WHO Classification of Tumours Editorial Board, ed. WHO classification of tumours: skin tumours. 5th ed. Lyon: IARC Press, 2025; 568-70.
161. Mosquera JM, Sboner A, Zhang L, et al. Novel *MIR143-NOTCH* fusions in benign and malignant glomus tumors. Genes Chromosomes Cancer 2013; 52: 1075-87.
162. Agaram NP, Zhang L, Jungbluth AA, Dickson BC, Antonescu CR. A molecular reappraisal of glomus tumors and related pericytic neoplasms with emphasis on *NOTCH*-gene fusions. Am J Surg Pathol 2020; 44: 1556-62.
163. Chakrapani A, Warrick A, Nelson D, Beadling C, Corless CL. *BRAF* and *KRAS* mutations in sporadic glomus tumors. Am J Dermatopathol 2012; 34: 533-5.
164. Karamzadeh Dashti N, Bahrami A, Lee SJ, et al. *BRAF* V600E mutations occur in a subset of glomus tumors, and are associated with malignant histologic characteristics. Am J Surg Pathol 2017; 41: 1532-41.
165. Agaimy A, Agaram NP, Luzar B, Michal M. Myopericytoma. In: WHO Classification of Tumours Editorial Board, ed. WHO classification of tumours: skin tumours. 5th ed. Lyon: IARC Press, 2025; 571-2.
166. Dahlen A, Fletcher CD, Mertens F, et al. Activation of the GLI oncogene through fusion with the beta-actin gene (*ACTB*) in a group of distinctive pericytic neoplasms: pericytoma with t(7;12). Am J Pathol 2004; 164: 1645-53.
167. Antonescu CR, Sung YS, Zhang L, Agaram NP, Fletcher CD. Recurrent *SRF-RELA* fusions define a novel subset of cellular myofibroma/myopericytoma: a potential diagnostic pitfall with sarcomas with myogenic differentiation. Am J Surg Pathol 2017; 41: 677-84.
168. Patel RM, Agaram NP, Michal M, Requena L. Angioleiomyoma. In: WHO Classification of Tumours Editorial Board, ed. WHO classification of tumours: skin tumours. 5th ed. Lyon: IARC Press, 2025; 575-6.
169. Welborn J, Fenner S, Parks R. Angioleiomyoma: a benign tumor with karyotypic aberrations. Cancer Genet Cytogenet 2010; 199: 147-8.
170. Shen J, Shrestha S, Yen YH, et al. The pericyte antigen RGS5 in perivascular soft tissue tumors. Hum Pathol 2016; 47: 121-31.
171. Agaimy A, Agaram NP, Luzar B, Michal M. Myofibroma and myofibromatosis. In: WHO Classification of Tumours Editorial Board, ed. WHO classification of tumours: skin tumours. 5th ed. Lyon: IARC Press, 2025; 573-4.
172. Oudijk L, den Bakker MA, Hop WC, et al. Solitary, multifocal and generalized myofibromas: clinicopathological and immunohistochemical features of 114 cases. Histopathology 2012; 60: E1-11.
173. Martignetti JA, Tian L, Li D, et al. Mutations in *PDGFRB* cause autosomal-dominant infantile myofibromatosis. Am J Hum Genet 2013; 92: 1001-7.
174. Agaimy A, Bieg M, Michal M, et al. Recurrent somatic PDGFRB mutations in sporadic infantile/solitary adult myofibromas but not in angioleiomyomas and myopericytomas. Am J Surg Pathol 2017; 41: 195-203.
175. Nihous H, Macagno N, Baud-Massiere J, et al. Genetic variant of SRF-rearranged myofibroma with a misleading nuclear expression of STAT6 and STAT6 involvement as 3' fusion partner. Virchows Arch 2021; 478: 597-603.
176. Folpe AL, Elston D. Atypical intradermal smooth muscle neoplasm. In: WHO Classification of Tumours Editorial Board, ed. WHO classification of tumours: skin tumours. 5th ed. Lyon: IARC Press, 2025; 583-4.
177. Kraft S, Fletcher CD. Atypical intradermal smooth muscle neoplasms: clinicopathologic analysis of 84 cases and a reappraisal of cutaneous "leiomyosarcoma". Am J Surg Pathol 2011; 35: 599-607.
178. Spinner S, Davis JL. Smooth muscle hamartoma. In: WHO Classification of Tumours Editorial Board, ed. WHO classification of tumours: skin tumours. 5th ed. Lyon: IARC Press, 2025; 577-8.
179. Gonzalez IA, Dehner LP. Smooth muscle hamartoma and striated muscle hamartoma: clinicopathologic characterization of two rare entities and literature review. J Cutan Pathol 2021; 48: 237-46.
180. Garcia-Gavin J, Perez-Perez L, Allegue F, Perez-Pedrosa A, Ortiz-Rey JA, Zulaica A. Multiple congenital familial smooth muscle hamartoma in two siblings. Dermatol Online J 2012; 18: 7.
181. Schnur RE, Herzberg AJ, Spinner N, et al. Variability in the Michelin tire syndrome: a child with multiple anomalies, smooth muscle hamartoma, and familial paracentric inversion of chromosome 7q. J Am Acad Dermatol 1993; 28: 364-70.
182. Zarineh A, Kozovska ME, Brown WG, Elder DE, Rabkin MS. Smooth muscle hamartoma associated with a congenital pattern melanocytic nevus, a case report and review of the literature. J Cutan Pathol 2008; 35 Suppl 1: 83-6.
183. Atzmony L, Ugwu N, Zaki TD, Antaya RJ, Choate KA. Post-zygotic *ACTB* mutations underlie congenital smooth muscle hamartomas. J Cutan Pathol 2020; 47: 681-5.
184. Johnson MD, Jacobs AH. Congenital smooth muscle hamartoma:

a report of six cases and a review of the literature. Arch Dermatol 1989; 125: 820-2.
185. Pitjadi TM, Chetty R, Ramdial PK, Watanabe R. EBV-associated smooth muscle tumour. In: WHO Classification of Tumours Editorial Board, ed. WHO classification of tumours: skin tumours. 5th ed. Lyon: IARC Press, 2025; 581-2.
186. Deyrup AT, Lee VK, Hill CE, et al. Epstein-Barr virus-associated smooth muscle tumors are distinctive mesenchymal tumors reflecting multiple infection events: a clinicopathologic and molecular analysis of 29 tumors from 19 patients. Am J Surg Pathol 2006; 30: 75-82.
187. Dekate J, Chetty R. Epstein-Barr virus-associated smooth muscle tumor. Arch Pathol Lab Med 2016; 140: 718-22.
188. Pitjadi TM, Grayson W. Epstein-Barr virus-associated smooth muscle tumour: a case series with a significant proportion of tumours showing proclivity for cutaneous soft tissues. Dermatopathology (Basel) 2019; 6: 133-46.
189. Hussein K, Rath B, Ludewig B, Kreipe H, Jonigk D. Clinico-pathological characteristics of different types of immunodeficiency-associated smooth muscle tumours. Eur J Cancer 2014; 50: 2417-24.
190. Issarachaikul R, Shuangshoti S, Suankratay C. Epstein-Barr virus-associated smooth muscle tumors in AIDS patients: a largest case (series). Intern Med 2014; 53: 2391-6.
191. Lee ES, Locker J, Nalesnik M, et al. The association of Epstein-Barr virus with smooth-muscle tumors occurring after organ transplantation. N Engl J Med 1995; 332: 19-25.
192. McClain KL, Leach CT, Jenson HB, et al. Association of Epstein-Barr virus with leiomyosarcomas in young people with AIDS. N Engl J Med 1995; 332: 12-8.
193. Ong KW, Teo M, Lee V, et al. Expression of EBV latent antigens, mammalian target of rapamycin, and tumor suppression genes in EBV-positive smooth muscle tumors: clinical and therapeutic implications. Clin Cancer Res 2009; 15: 5350-8.
194. Jonigk D, Laenger F, Maegel L, et al. Molecular and clinicopathological analysis of Epstein-Barr virus-associated posttransplant smooth muscle tumors. Am J Transplant 2012; 12: 1908-17.
195. Galeano-Piedrahita E, Rico AM, Suarez AC, Walter AL. Cutaneous smooth muscle tumors associated with Epstein-Barr virus in an adult patient with HIV. An Bras Dermatol 2021; 96: 184-7.
196. Matin RN, Ieremia E. Cutaneous Epstein-Barr virus-associated smooth muscle tumor in immunosuppression. J Cutan Pathol 2021; 48: 325-9.
197. Ferguson PM, Hollann TJ. Solitary circumscribed neuroma. In: WHO Classification of Tumours Editorial Board, ed. WHO classification of tumours: skin tumours. 5th ed. Lyon: IARC Press, 2025; 587-8.
198. Dry SM. Dermal nerve sheath myxoma. In: WHO Classification of Tumours Editorial Board, ed. WHO classification of tumours: skin tumours. 5th ed. Lyon: IARC Press, 2025; 589-90.
199. Fetsch JF, Laskin WB, Hallman JR, Lupton GP, Miettinen M. Neurothekeoma: an analysis of 178 tumors with detailed immunohistochemical data and long-term patient follow-up information. Am J Surg Pathol 2007; 31: 1103-14.
200. Fetsch JF, Laskin WB, Miettinen M. Nerve sheath myxoma: a clinicopathologic and immunohistochemical analysis of 57 morphologically distinctive, S-100 protein- and GFAP-positive, myxoid peripheral nerve sheath tumors with a predilection for the extremities and a high local recurrence rate. Am J Surg Pathol 2005; 29: 1615-24.
201. Sheth S, Li X, Binder S, Dry SM. Differential gene expression profiles of neurothekeomas and nerve sheath myxomas by microarray analysis. Mod Pathol 2011; 24: 343-54.
202. Zelger B, Hornick JL. Perineurioma. In: WHO Classification of Tumours Editorial Board, ed. WHO classification of tumours: skin tumours. 5th ed. Lyon: IARC Press, 2025; 591-2.
203. Giannini C, Scheithauer BW, Jenkins RB, et al. Soft-tissue perineurioma: evidence for an abnormality of chromosome 22, criteria for diagnosis, and review of the literature. Am J Surg Pathol 1997; 21: 164-73.
204. Pitchford CW, Schwartz HS, Atkinson JB, Cates JM. Soft tissue perineurioma in a patient with neurofibromatosis type 2: a tumor not previously associated with the NF2 syndrome. Am J Surg Pathol 2006; 30: 1624-9.
205. Carter JM, Wu Y, Blessing MM, et al. Recurrent genomic alterations in soft tissue perineuriomas. Am J Surg Pathol 2018; 42: 1708-14.
206. Brock JE, Perez-Atayde AR, Kozakewich HP, Richkind KE, Fletcher JA, Vargas SO. Cytogenetic aberrations in perineurioma: variation with subtype. Am J Surg Pathol 2005; 29: 1164-9.
207. Sato K, Ueda Y, Miwa S, Yokogawa A, Ozaki M, Katsuda S. Low-grade malignant soft-tissue perineurioma: interphase fluorescence in situ hybridization. Pathol Int 2008; 58: 718-22.
208. Shea CR, Perry A, Tetzlaff M. Neurofibroma. In: WHO Classification of Tumours Editorial Board, ed. WHO classification of tumours: skin tumours. 5th ed. Lyon: IARC Press, 2025; 593-5.
209. Wilson BN, John AM, Handler MZ, Schwartz RA. Neurofibromatosis type 1: new developments in genetics and treatment. J Am Acad Dermatol 2021; 84: 1667-76.
210. Rhodes SD, He Y, Smith A, et al. Cdkn2a (Arf) loss drives

https://doi.org/10.4132/jptm.2026.01.09

NF1-associated atypical neurofibroma and malignant transformation. Hum Mol Genet 2019; 28: 2752-62.
211. Yeh I, Jo VY, Perry A. Schwannoma. In: WHO Classification of Tumours Editorial Board, ed. WHO classification of tumours: skin tumours. 5th ed. Lyon: IARC Press, 2025; 596-7.
212. Reis-Filho JS. Granular cell tumour. In: WHO Classification of Tumours Editorial Board, ed. WHO classification of tumours: skin tumours. 5th ed. Lyon: IARC Press, 2025; 598-600.
213. Pareja F, Brandes AH, Basili T, et al. Loss-of-function mutations in *ATP6AP1* and *ATP6AP2* in granular cell tumors. Nat Commun 2018; 9: 3533.
214. Fanburg-Smith JC, Meis-Kindblom JM, Fante R, Kindblom LG. Malignant granular cell tumor of soft tissue: diagnostic criteria and clinicopathologic correlation. Am J Surg Pathol 1998; 22: 779-94.
215. Nasser H, Ahmed Y, Szpunar SM, Kowalski PJ. Malignant granular cell tumor: a look into the diagnostic criteria. Pathol Res Pract 2011; 207: 164-8.
216. Kapur P, Rakheja D, Balani JP, Roy LC, Amirkhan RH, Hoang MP. Phosphorylated histone H3, Ki-67, p21, fatty acid synthase, and cleaved caspase-3 expression in benign and atypical granular cell tumors. Arch Pathol Lab Med 2007; 131: 57-64.
217. Nielsen GP, Chi P, Hornick JL. Malignant peripheral nerve sheath tumour. In: WHO Classification of Tumours Editorial Board, ed. WHO classification of tumours: skin tumours. 5th ed. Lyon: IARC Press, 2025; 603-5.
218. Lee W, Teckie S, Wiesner T, et al. PrC2 is recurrently inactivated through *EED* or *SUZ12* loss in malignant peripheral nerve sheath tumors. Nat Genet 2014; 46: 1227-32.
219. Zhang M, Wang Y, Jones S, et al. Somatic mutations of *SUZ12* in malignant peripheral nerve sheath tumors. Nat Genet 2014; 46: 1170-2.
220. Pemov A, Hansen NF, Sindiri S, et al. Low mutation burden and frequent loss of *CDKN2A/B* and *SMARCA2*, but not PRC2, define premalignant neurofibromatosis type 1-associated atypical neurofibromas. Neuro Oncol 2019; 21: 981-92.
221. Prieto-Granada CN, Wiesner T, Messina JL, Jungbluth AA, Chi P, Antonescu CR. Loss of H3K27me3 expression is a highly sensitive marker for sporadic and radiation-induced MPNST. Am J Surg Pathol 2016; 40: 479-89.
222. Schaefer IM, Fletcher CD, Hornick JL. Loss of H3K27 trimethylation distinguishes malignant peripheral nerve sheath tumors from histologic mimics. Mod Pathol 2016; 29: 4-13.
223. Schaefer IM, Dong F, Garcia EP, Fletcher CD, Jo VY. Recurrent *SMARCB1* inactivation in epithelioid malignant peripheral nerve sheath tumors. Am J Surg Pathol 2019; 43: 835-43.
224. Jo VY, Fletcher CD. Smarcb1/Ini1 loss in epithelioid schwannoma: a clinicopathologic and immunohistochemical study of 65 cases. Am J Surg Pathol 2017; 41: 1013-22.
225. Marusic Z, Calonje JE. Dermal hyperneury/epithelial sheath neuroma. In: WHO Classification of Tumours Editorial Board, ed. WHO classification of tumours: skin tumours. 5th ed. Lyon: IARC Press, 2025; 585-6.
226. Ieremia E, Marusic Z, Mudaliar V, et al. Expanding the clinical spectrum of dermal hyperneury: report of nine new cases and a review of the literature. Histopathology 2019; 75: 738-45.
227. Requena L, Grosshans E, Kutzner H, et al. Epithelial sheath neuroma: a new entity. Am J Surg Pathol 2000; 24: 190-6.
228. Schaffer JV, Kamino H, Witkiewicz A, McNiff JM, Orlow SJ. Mucocutaneous neuromas: an underrecognized manifestation of PTEN hamartoma-tumor syndrome. Arch Dermatol 2006; 142: 625-32.
229. Winkelmann RK, Carney JA. Cutaneous neuropathology in multiple endocrine neoplasia, type 2b. J Invest Dermatol 1982; 79: 307-12.
230. Alegria-Landa V, Jo-Velasco M, Robledo M, Requena L. Dermal hyperneury and multiple sclerotic fibromas in multiple endocrine neoplasia type 2A syndrome. JAMA Dermatol 2017; 153: 1298-301.
231. Rhee DY, Chung WK, Chang SE, Lee MW, Choi JH, Moon KC. A case of cutaneous nerve hypertrophy: association with multiple endocrine neoplasia type 2 or neurofibromatosis type 2? J Cutan Pathol 2008; 35: 1156-8.
232. Starink TM, van der Veen JP, Arwert F, et al. The Cowden syndrome: a clinical and genetic study in 21 patients. Clin Genet 1986; 29: 222-33.
233. Ohtake Y, Hayat U, Li S. Pten inhibition and axon regeneration and neural repair. Neural Regen Res 2015; 10: 1363-8.
234. Noparstak M, Zaycosky M, Saeed S. Epithelial sheath neuroma with extension to the subcutis. J Cutan Pathol 2018; 45: 705-7.
235. Stemmer-Rachamimov AO, Hornick JL. Hybrid nerve sheath tumours. In: WHO Classification of Tumours Editorial Board, ed. WHO classification of tumours: skin tumours. 5th ed. Lyon: IARC Press, 2025; 601-2.
236. Hornick JL, Bundock EA, Fletcher CD. Hybrid schwannoma/perineurioma: clinicopathologic analysis of 42 distinctive benign nerve sheath tumors. Am J Surg Pathol 2009; 33: 1554-61.
237. Feany MB, Anthony DC, Fletcher CD. Nerve sheath tumours with hybrid features of neurofibroma and schwannoma: a conceptual challenge. Histopathology 1998; 32: 405-10.

238. Michal M, Kazakov DV, Belousova I, Bisceglia M, Zamecnik M, Mukensnabl P. A benign neoplasm with histopathological features of both schwannoma and retiform perineurioma (benign schwannoma-perineurioma): a report of six cases of a distinctive soft tissue tumor with a predilection for the fingers. Virchows Arch 2004; 445: 347-53.
239. Harder A, Wesemann M, Hagel C, et al. Hybrid neurofibroma/schwannoma is overrepresented among schwannomatosis and neurofibromatosis patients. Am J Surg Pathol 2012; 36: 702-9.
240. MacCollin M, Chiocca EA, Evans DG, et al. Diagnostic criteria for schwannomatosis. Neurology 2005; 64: 1838-45.
241. Inatomi Y, Ito T, Nagae K, et al. Hybrid perineurioma-neurofibroma in a patient with neurofibromatosis type 1, clinically mimicking malignant peripheral nerve sheath tumor. Eur J Dermatol 2014; 24: 412-3.
242. Kacerovska D, Michal M, Kuroda N, et al. Hybrid peripheral nerve sheath tumors, including a malignant variant in type 1 neurofibromatosis. Am J Dermatopathol 2013; 35: 641-9.
243. Dickson BC, Antonescu CR, Demicco EG, et al. Hybrid schwannoma-perineurioma frequently harbors *VGLL3* rearrangement. Mod Pathol 2021; 34: 1116-24.
244. Agaimy A. Microscopic intraneural perineurial cell proliferations in patients with neurofibromatosis type 1. Ann Diagn Pathol 2014; 18: 95-8.
245. Requena L, Hornick JL. Cellular neurothekeoma. In: WHO Classification of Tumours Editorial Board, ed. WHO classification of tumours: skin tumours. 5th ed. Lyon: IARC Press, 2025; 606-7.
246. Barnhill RL. Nerve sheath myxoma (neurothekeoma). J Cutan Pathol 1994; 21: 91-3.
247. Abdaljaleel M, North JP. Positive MITF and NKI/C3 expression in cellular neurothekeoma and dermatofibroma. Appl Immunohistochem Mol Morphol 2021; 29: 440-5.
248. Argenyi ZB, LeBoit PE, Santa Cruz D, Swanson PE, Kutzner H. Nerve sheath myxoma (neurothekeoma) of the skin: light microscopic and immunohistochemical reappraisal of the cellular variant. J Cutan Pathol 1993; 20: 294-303.
249. Wang AR, May D, Bourne P, Scott G. PGP9.5: a marker for cellular neurothekeoma. Am J Surg Pathol 1999; 23: 1401-7.
250. Fullen DR, Lowe L, Su LD. Antibody to S100A6 protein is a sensitive immunohistochemical marker for neurothekeoma. J Cutan Pathol 2003; 30: 118-22.
251. Suarez A, High WA. Immunohistochemical analysis of KBA.62 in 18 neurothekeomas: a potential marker for differentiating neurothekeoma, but a marker that may lead to confusion with melanocytic tumors. J Cutan Pathol 2014; 41: 36-41.
252. Cesinaro AM, Piana S, Paganelli A, Pedroni G, Santandrea G, Maiorana A. Prame expression in cellular neurothekeoma: a study of 11 cases. J Cutan Pathol 2022; 49: 338-42.
253. Lazar AJ, Yeh I. Non-neural granular cell tumour. In: WHO Classification of Tumours Editorial Board, ed. WHO classification of tumours: skin tumours. 5th ed. Lyon: IARC Press, 2025; 610-1.
254. Cohen JN, Yeh I, Jordan RC, et al. Cutaneous non-neural granular cell tumors harbor recurrent *ALK* gene fusions. Am J Surg Pathol 2018; 42: 1133-42.
255. Beer TW, Calonje JE. Atypical fibroxanthoma. In: WHO Classification of Tumours Editorial Board, ed. WHO classification of tumours: skin tumours. 5th ed. Lyon: IARC Press, 2025; 618-20.
256. Griewank KG, Wiesner T, Murali R, et al. Atypical fibroxanthoma and pleomorphic dermal sarcoma harbor frequent *NOTCH1/2* and *FAT1* mutations and similar DNA copy number alteration profiles. Mod Pathol 2018; 31: 418-28.
257. Koelsche C, Stichel D, Griewank KG, et al. Genome-wide methylation profiling and copy number analysis in atypical fibroxanthomas and pleomorphic dermal sarcomas indicate a similar molecular phenotype. Clin Sarcoma Res 2019; 9: 2.
258. Ak M, Kahraman A, Arnold FM, et al. Clinicopathological and genomic profiles of atypical fibroxanthoma and pleomorphic dermal sarcoma identify overlapping signatures with a high mutational burden. Genes (Basel) 2021; 12: 974.
259. Harding-Jackson N, Sangueza M, Mackinnon A, Suster S, Plaza JA. Spindle cell atypical fibroxanthoma: myofibroblastic differentiation represents a diagnostic pitfall in this variant of AFX. Am J Dermatopathol 2015; 37: 509-14.
260. Tardio JC, Pinedo F, Aramburu JA, et al. Clear cell atypical fibroxanthoma: clinicopathological study of 6 cases and review of the literature with special emphasis on the differential diagnosis. Am J Dermatopathol 2016; 38: 586-92.
261. Diaz-Cascajo C, Borghi S, Bonczkowitz M. Pigmented atypical fibroxanthoma. Histopathology 1998; 33: 537-41.
262. Dummer R, Luzar B, Miller K. Pleomorphic dermal sarcoma. In: WHO Classification of Tumours Editorial Board, ed. WHO classification of tumours: skin tumours. 5th ed. Lyon: IARC Press, 2025; 623-4.
263. Patel RM, Le Loarer F, Nielsen TO, Oda Y. Epithelioid sarcoma. In: WHO Classification of Tumours Editorial Board, ed. WHO classification of tumours: skin tumours. 5th ed. Lyon: IARC Press, 2025; 625-6.
264. Kohashi K, Yamamoto H, Yamada Y, et al. Swi/Snf chromatin-remodeling complex status in *SMARCB1*/INI1-preserved epithelioid sarcoma. Am J Surg Pathol 2018; 42: 312-8.

https://doi.org/10.4132/jptm.2026.01.09

265. Jamshidi F, Bashashati A, Shumansky K, et al. The genomic landscape of epithelioid sarcoma cell lines and tumours. J Pathol 2016; 238: 63-73.
266. Busam KJ, Fritchie KJ, Luzar B. Dermal clear cells sarcoma. In: WHO Classification of Tumours Editorial Board, ed. WHO classification of tumours: skin tumours. 5th ed. Lyon: IARC Press, 2025; 629-30.
267. Raghavan SS, Wang JY, Toland A, et al. Diffuse PRAME expression is highly specific for malignant melanoma in the distinction from clear cell sarcoma. J Cutan Pathol 2020; 47: 1226-8.
268. Kline N, Menge TD, Hrycaj SM, et al. Prame expression in challenging dermal melanocytic neoplasms and soft tissue tumors with melanocytic differentiation. Am J Dermatopathol 2022; 44: 404-10.
269. Patel RM, de Alava E, Scolyer RA. Ewing sarcoma. In: WHO Classification of Tumours Editorial Board, ed. WHO classification of tumours: skin tumours. 5th ed. Lyon: IARC Press, 2025; 631-2.
270. Choi EY, Gardner JM, Lucas DR, McHugh JB, Patel RM. Ewing sarcoma. Semin Diagn Pathol 2014; 31: 39-47.
271. Hasegawa SL, Davison JM, Rutten A, Fletcher JA, Fletcher CD. Primary cutaneous Ewing's sarcoma: immunophenotypic and molecular cytogenetic evaluation of five cases. Am J Surg Pathol 1998; 22: 310-8.
272. Machado I, Llombart B, Calabuig-Farinas S, Llombart-Bosch A. Superficial Ewing's sarcoma family of tumors: a clinicopathological study with differential diagnoses. J Cutan Pathol 2011; 38: 636-43.
273. Requena L, Hornick JL. Epithelioid fibrous histiocytoma. In: WHO Classification of Tumours Editorial Board, ed. WHO classification of tumours: skin tumours. 5th ed. Lyon: IARC Press, 2025; 608-9.
274. Glusac EJ, Barr RJ, Everett MA, Pitha J, Santa Cruz DJ. Epithelioid cell histiocytoma: a report of 10 cases including a new cellular variant. Am J Surg Pathol 1994; 18: 583-90.
275. Singh Gomez C, Calonje E, Fletcher CD. Epithelioid benign fibrous histiocytoma of skin: clinico-pathological analysis of 20 cases of a poorly known variant. Histopathology 1994; 24: 123-9.
276. Doyle LA, Marino-Enriquez A, Fletcher CD, Hornick JL. *ALK* rearrangement and overexpression in epithelioid fibrous histiocytoma. Mod Pathol 2015; 28: 904-12.
277. Walther C, Hofvander J, Nilsson J, et al. Gene fusion detection in formalin-fixed paraffin-embedded benign fibrous histiocytomas using fluorescence in situ hybridization and RNA sequencing. Lab Invest 2015; 95: 1071-6.
278. Jedrych J, Nikiforova M, Kennedy TF, Ho J. Epithelioid cell histiocytoma of the skin with clonal *ALK* gene rearrangement resulting in *VCL-ALK* and *SQSTM1-ALK* gene fusions. Br J Dermatol 2015; 172: 1427-9.
279. Dickson BC, Swanson D, Charames GS, Fletcher CD, Hornick JL. Epithelioid fibrous histiocytoma: molecular characterization of *ALK* fusion partners in 23 cases. Mod Pathol 2018; 31: 753-62.
280. Kazakov DV, Kyrpychova L, Martinek P, et al. ALK gene fusions in epithelioid fibrous histiocytoma: a study of 14 cases, with new histopathological findings. Am J Dermatopathol 2018; 40: 805-14.
281. Georgantzoglou N, Green D, Winnick KN, et al. Molecular investigation of *ALK*-rearranged epithelioid fibrous histiocytomas identifies *CLTC* as a novel fusion partner and evidence of fusion-independent transcription activation. Genes Chromosomes Cancer 2022; 61: 471-80.
282. Wright GR, Archibald CW, Fontaine D, Dakin-Hache K, Walsh NM. Epithelioid fibrous histiocytoma with chondroblastoma-like features: a report of a rare entity and discussion of related diagnostic challenges. Am J Dermatopathol 2022; 44: e11-5.
283. Murigu T, Bhatt N, Miller K, Palmer A, Melegh Z. Spindle cell-predominant epithelioid fibrous histiocytoma. Histopathology 2018; 72: 1233-6.
284. Kazlouskaya V, Ho J, Jedrych J, Karunamurthy A. Spindle cell variant of epithelioid cell histiocytoma (spindle cell histiocytoma) with *ALK* gene fusions: cases series and review of the literature. J Cutan Pathol 2021; 48: 837-41.
285. Moayed-Alaei L, Vargas AC, Adybeik D, Maclean F, Moir D. Analyzing the morphological spectrum of epithelioid fibrous histiocytoma and the immunohistochemical performance of the ALK D5F3 and ALK1 clones. Hum Pathol 2022; 120: 46-56.
286. Doyle LA, Fletcher CD. EMA positivity in epithelioid fibrous histiocytoma: a potential diagnostic pitfall. J Cutan Pathol 2011; 38: 697-703.
287. Doyle LA, Argani P, Hornick JL. PEComa. In: WHO Classification of Tumours Editorial Board, ed. WHO classification of tumours: skin tumours. 5th ed. Lyon: IARC Press, 2025; 612-3.
288. Liegl B, Hornick JL, Fletcher CD. Primary cutaneous PEComa: distinctive clear cell lesions of skin. Am J Surg Pathol 2008; 32: 608-14.
289. Stuart LN, Tipton RG, DeWall MR, et al. Primary cutaneous perivascular epithelioid cell tumor (PEComa): five new cases and review of the literature. J Cutan Pathol 2017; 44: 713-21.
290. Greveling K, Winnepenninckx VJL, Nagtzaam IF, et al. Malignant perivascular epithelioid cell tumor: a case report of a cutaneous

tumor on the cheek of a male patient. J Am Acad Dermatol 2013; 69: e262-4.
291. Odono EI, Tan KB, Tay SY, Lee VK. Cutaneous "fibroma-like" perivascular epithelioid cell tumor: a case report and review of literature. J Cutan Pathol 2020; 47: 548-53.
292. Pan CC, Chung MY, Ng KF, et al. Constant allelic alteration on chromosome 16p (*TSC2* gene) in perivascular epithelioid cell tumour (PEComa): genetic evidence for the relationship of PEComa with angiomyolipoma. J Pathol 2008; 214: 387-93.
293. Agaram NP, Sung YS, Zhang L, et al. Dichotomy of genetic abnormalities in PEComas with therapeutic implications. Am J Surg Pathol 2015; 39: 813-25.
294. Folpe AL, Mentzel T, Lehr HA, Fisher C, Balzer BL, Weiss SW. Perivascular epithelioid cell neoplasms of soft tissue and gynecologic origin: a clinicopathologic study of 26 cases and review of the literature. Am J Surg Pathol 2005; 29: 1558-75.
295. Doyle LA, Hornick JL, Fletcher CD. Pecoma of the gastrointestinal tract: clinicopathologic study of 35 cases with evaluation of prognostic parameters. Am J Surg Pathol 2013; 37: 1769-82.
296. Bennett JA, Braga AC, Pinto A, et al. Uterine PEComas: a morphologic, immunohistochemical, and molecular analysis of 32 tumors. Am J Surg Pathol 2018; 42: 1370-83.
297. Cole DW, Menge TD, Renati S, et al. Primary cutaneous malignant perivascular epithelioid cell tumor: case of a rare tumor with review of the literature. J Cutan Pathol 2021; 48: 1088-93.
298. Folpe AL, Kwiatkowski DJ. Perivascular epithelioid cell neoplasms: pathology and pathogenesis. Hum Pathol 2010; 41: 1-15.
299. Hornick JL, Fletcher CD. Sclerosing PEComa: clinicopathologic analysis of a distinctive variant with a predilection for the retroperitoneum. Am J Surg Pathol 2008; 32: 493-501.
300. Rekhi B, Chen G. Angiomatoid fibrous histiocytoma. In: WHO Classification of Tumours Editorial Board, ed. WHO classification of tumours: skin tumours. 5th ed. Lyon: IARC Press, 2025; 614-5.
301. Fanburg-Smith JC, Miettinen M. Angiomatoid "malignant" fibrous histiocytoma: a clinicopathologic study of 158 cases and further exploration of the myoid phenotype. Hum Pathol 1999; 30: 1336-43.
302. Costa MJ, Weiss SW. Angiomatoid malignant fibrous histiocytoma: a follow-up study of 108 cases with evaluation of possible histologic predictors of outcome. Am J Surg Pathol 1990; 14: 1126-32.
303. Antonescu CR, Dal Cin P, Nafa K, et al. *EWSR1-CREB1* is the predominant gene fusion in angiomatoid fibrous histiocytoma. Genes Chromosomes Cancer 2007; 46: 1051-60.
304. Rekhi B, Adamane S, Ghodke K, Desai S, Jambhekar NA. Angiomatoid fibrous histiocytoma: clinicopathological spectrum of five cases, including *EWSR1-CREB1* positive result in a single case. Indian J Pathol Microbiol 2016; 59: 148-52.
305. Rossi S, Szuhai K, Ijszenga M, et al. *EWSR1-CREB1* and *EWSR1-ATF1* fusion genes in angiomatoid fibrous histiocytoma. Clin Cancer Res 2007; 13: 7322-8.
306. Hallor KH, Mertens F, Jin Y, et al. Fusion of the *EWSR1* and *ATF1* genes without expression of the MITF-M transcript in angiomatoid fibrous histiocytoma. Genes Chromosomes Cancer 2005; 44: 97-102.
307. Raddaoui E, Donner LR, Panagopoulos I. Fusion of the *FUS* and *ATF1* genes in a large, deep-seated angiomatoid fibrous histiocytoma. Diagn Mol Pathol 2002; 11: 157-62.
308. Waters BL, Panagopoulos I, Allen EF. Genetic characterization of angiomatoid fibrous histiocytoma identifies fusion of the *FUS* and *ATF-1* genes induced by a chromosomal translocation involving bands 12q13 and 16p11. Cancer Genet Cytogenet 2000; 121: 109-16.
309. Thway K, Fisher C. Angiomatoid fibrous histiocytoma: the current status of pathology and genetics. Arch Pathol Lab Med 2015; 139: 674-82.
310. Kao YC, Lan J, Tai HC, et al. Angiomatoid fibrous histiocytoma: clinicopathological and molecular characterisation with emphasis on variant histomorphology. J Clin Pathol 2014; 67: 210-5.
311. Hasegawa T, Seki K, Ono K, Hirohashi S. Angiomatoid (malignant) fibrous histiocytoma: a peculiar low-grade tumor showing immunophenotypic heterogeneity and ultrastructural variations. Pathol Int 2000; 50: 731-8.
312. Schaefer IM, Fletcher CD. Myxoid variant of so-called angiomatoid "malignant fibrous histiocytoma": clinicopathologic characterization in a series of 21 cases. Am J Surg Pathol 2014; 38: 816-23.
313. Chen G, Folpe AL, Colby TV, et al. Angiomatoid fibrous histiocytoma: unusual sites and unusual morphology. Mod Pathol 2011; 24: 1560-70.
314. Berklite L, John I, Ranganathan S, Parafioriti A, Alaggio R. Sox9 immunohistochemistry in the distinction of angiomatoid fibrous histiocytoma from histologic mimics: diagnostic utility and pitfalls. Appl Immunohistochem Mol Morphol 2020; 28: 635-40.
315. Suurmeijer AJ, Davis JL. NTRK-rearranged spindle cell neoplasm. In: WHO Classification of Tumours Editorial Board, ed. WHO classification of tumours: skin tumours. 5th ed. Lyon: IARC Press, 2025; 616-7.
316. Agaram NP, Zhang L, Sung YS, et al. Recurrent *NTRK1* gene

https://doi.org/10.4132/jptm.2026.01.09

fusions define a novel subset of locally aggressive lipofibromatosis-like neural tumors. Am J Surg Pathol 2016; 40: 1407-16.
317. Antonescu CR, Dickson BC, Swanson D, et al. Spindle cell tumors with *RET* gene fusions exhibit a morphologic spectrum akin to tumors with *NTRK* gene fusions. Am J Surg Pathol 2019; 43: 1384-91.
318. Kao YC, Suurmeijer AJ, Argani P, et al. Soft tissue tumors characterized by a wide spectrum of kinase fusions share a lipofibromatosis-like neural tumor pattern. Genes Chromosomes Cancer 2020; 59: 575-83.
319. Davis JL, Lockwood CM, Stohr B, et al. Expanding the spectrum of pediatric NTRK-rearranged mesenchymal tumors. Am J Surg Pathol 2019; 43: 435-45.
320. Hung YP, Fletcher CD, Hornick JL. Evaluation of pan-TRK immunohistochemistry in infantile fibrosarcoma, lipofibromatosis-like neural tumour and histological mimics. Histopathology 2018; 73: 634-44.
321. Rekhi B, Folpe AL, Yu L. Superficial CD34-positive fibroblastic tumour. In: WHO Classification of Tumours Editorial Board, ed. WHO classification of tumours: skin tumours. 5th ed. Lyon: IARC Press, 2025; 621-2.
322. Carter JM, Weiss SW, Linos K, DiCaudo DJ, Folpe AL. Superficial CD34-positive fibroblastic tumor: report of 18 cases of a distinctive low-grade mesenchymal neoplasm of intermediate (borderline) malignancy. Mod Pathol 2014; 27: 294-302.
323. Lao IW, Yu L, Wang J. Superficial CD34-positive fibroblastic tumour: a clinicopathological and immunohistochemical study of an additional series. Histopathology 2017; 70: 394-401.
324. Perret R, Michal M, Carr RA, et al. Superficial CD34-positive fibroblastic tumor and PRDM10-rearranged soft tissue tumor are overlapping entities: a comprehensive study of 20 cases. Histopathology 2021; 79: 810-25.
325. Puls F, Carter JM, Pillay N, et al. Overlapping morphological, immunohistochemical and genetic features of superficial CD34-positive fibroblastic tumor and PRDM10-rearranged soft tissue tumor. Mod Pathol 2022; 35: 767-76.
326. Ding L, Xu WJ, Tao XY, Zhang L, Cai ZG. Clinicopathological features of superficial CD34-positive fibroblastic tumor. World J Clin Cases 2021; 9: 2739-50.
327. Mao X, Sun YY, Deng ML, Ma T, Yu L. Superficial CD34-positive fibroblastic tumor: report of two cases and review of literature. Int J Clin Exp Pathol 2020; 13: 38-43.
328. Puls F, Pillay N, Fagman H, et al. *PRDM10*-rearranged soft tissue tumor: a clinicopathologic study of 9 cases. Am J Surg Pathol 2019; 43: 504-13.
329. de la Fouchardiere A, Ko JS. *CRTC1*::*TRIM11* cutaneous tumour. In: WHO Classification of Tumours Editorial Board, ed. WHO classification of tumours: skin tumours. 5th ed. Lyon: IARC Press, 2025; 627-8.
330. de la Fouchardiere A, Hanna J. MITF pathway–activated melanocytic tumours. In: WHO Classification of Tumours Editorial Board, ed. WHO classification of tumours: skin tumours. 5th ed. Lyon: IARC Press, 2025; 136-7.
331. Hanna J, Ko JS, Billings SD, et al. Cutaneous melanocytic tumor with *CRTC1*::*TRIM11* translocation: an emerging entity analyzed in a series of 41 cases. Am J Surg Pathol 2022; 46: 1457-66.
332. Cellier L, Perron E, Pissaloux D, et al. Cutaneous melanocytoma with *CRTC1-TRIM11* fusion: report of 5 cases resembling clear cell sarcoma. Am J Surg Pathol 2018; 42: 382-91.
333. Ko JS, Wang L, Billings SD, et al. *CRTC1-TRIM11* fusion defined melanocytic tumors: a series of four cases. J Cutan Pathol 2019; 46: 810-8.
334. Bontoux C, Baroudjian B, Le Maignan C, et al. *CRTC1-TRIM11* fusion in a case of metastatic clear cell sarcoma: are crtc1-trim11 fusion-bearing tumors melanocytomas or clear cell sarcomas? Am J Surg Pathol 2019; 43: 861-3.
335. Kashima J, Motoi T, Nishimaki M, et al. A case report of cutaneous melanocytoma with *CRTC1-TRIM11* fusion: is CMCT distinct from clear cell sarcoma of soft tissue? Pathol Int 2019; 69: 496-501.
336. Parra O, Bridge JA, Busam KJ, Shalin SC, Linos K. Dermal melanocytic tumor with *CRTC1-TRIM11* fusion: report of two additional cases with review of the literature of an emerging entity. J Cutan Pathol 2021; 48: 915-24.
337. Vest BE, Harview CL, Liu V, et al. Cutaneous melanocytic tumor with *CRTC1*::*TRIM11* fusion and prominent epidermal involvement: a case report. J Cutan Pathol 2022; 49: 1025-30.
338. Yang L, Yin Z, Wei J, et al. Cutaneous melanocytic tumour with *CRTC1*::*TRIM11* fusion in a case with recurrent local lymph node and distant pulmonary metastases at early stage: aggressive rather than indolent? Histopathology 2023; 82: 368-71.
339. Iourgenko V, Zhang W, Mickanin C, et al. Identification of a family of cAMP response element-binding protein coactivators by genome-scale functional analysis in mammalian cells. Proc Natl Acad Sci U S A 2003; 100: 12147-52.
340. Conkright MD, Canettieri G, Screaton R, et al. Torcs: transducers of regulated CREB activity. Mol Cell 2003; 12: 413-23.
341. Kawakami A, Fisher DE. The master role of microphthalmia-associated transcription factor in melanocyte and melanoma biology. Lab Invest 2017; 97: 649-56.

JPTM

ORIGINAL ARTICLE

pISSN 2383-7837 · eISSN 2383-7845

Journal of Pathology and Translational Medicine 2026; 60: 184-192
https://doi.org/10.4132/jptm.2025.10.22

Prevalence of HER2-ultralow breast cancer in South Korea: a multicenter study by reassessment of HER2-zero cases

Min Chong Kim[1*], Eun Yoon Cho[2*], Hee Jin Lee[3], Ji Shin Lee[4], Jee Yeon Kim[5], Wan Seop Kim[6], Chungyeul Kim[7], Sun-Young Jun[8], Hye Jeong Choi[9], So Mang Lee[9], Ahrong Kim[5,10], Ji-Young Kim[11], Jeong Yun Shim[11], Gyungyub Gong[3], Young Kyung Bae[12]

[1]Department of Pathology, Yeungnam University Medical Center, Daegu, Korea
[2]Department of Pathology and Translational Genomics, Samsung Medical Center, Sungkyunkwan University School of Medicine, Seoul, Korea
[3]Department of Pathology, Asan Medical Center, University of Ulsan College of Medicine, Seoul, Korea
[4]Department of Pathology, Chonnam National University Medical School, Gwangju, Korea
[5]Department of Pathology, Pusan National University Yangsan Hospital, Pusan National University School of Medicine, Yangsan, Korea
[6]Department of Pathology, Konkuk University School of Medicine, Seoul, Korea
[7]Department of Pathology, Korea University Guro Hospital, Korea University College of Medicine, Seoul, Korea
[8]Department of Pathology, Incheon St. Mary's Hospital, College of Medicine, The Catholic University of Korea, Seoul, Korea
[9]Department of Pathology, Ulsan University Hospital, University of Ulsan College of Medicine, Ulsan, Korea
[10]Department of Pathology, Pusan National University Hospital, Busan, Korea
[11]Department of Pathology, CHA Gangnam Medical Center, CHA University School of Medicine, Seoul, Korea
[12]Department of Pathology, Yeungnam University College of Medicine, Daegu, Korea

Graphical abstract

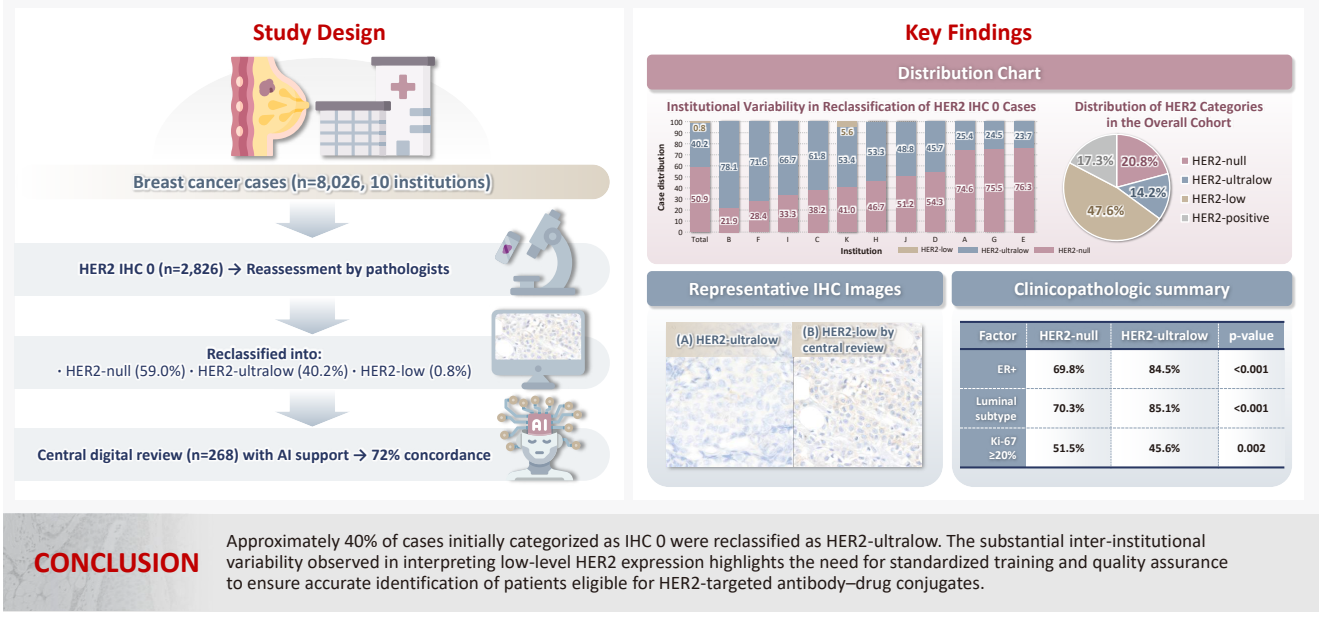

JPTM

ORIGINAL ARTICLE

pISSN 2383-7837 · eISSN 2383-7845

Journal of Pathology and Translational Medicine 2026; 60: 184-192
https://doi.org/10.4132/jptm.2025.10.22

Prevalence of HER2-ultralow breast cancer in South Korea: a multicenter study by reassessment of HER2-zero cases

Min Chong Kim[1*], Eun Yoon Cho[2*], Hee Jin Lee[3], Ji Shin Lee[4], Jee Yeon Kim[5], Wan Seop Kim[6], Chungyeul Kim[7], Sun-Young Jun[8], Hye Jeong Choi[9], So Mang Lee[9], Ahrong Kim[5,10], Ji-Young Kim[11], Jeong Yun Shim[11], Gyungyub Gong[3], Young Kyung Bae[12]

[1]Department of Pathology, Yeungnam University Medical Center, Daegu, Korea
[2]Department of Pathology and Translational Genomics, Samsung Medical Center, Sungkyunkwan University School of Medicine, Seoul, Korea
[3]Department of Pathology, Asan Medical Center, University of Ulsan College of Medicine, Seoul, Korea
[4]Department of Pathology, Chonnam National University Medical School, Gwangju, Korea
[5]Department of Pathology, Pusan National University Yangsan Hospital, Pusan National University School of Medicine, Yangsan, Korea
[6]Department of Pathology, Konkuk University School of Medicine, Seoul, Korea
[7]Department of Pathology, Korea University Guro Hospital, Korea University College of Medicine, Seoul, Korea
[8]Department of Pathology, Incheon St. Mary's Hospital, College of Medicine, The Catholic University of Korea, Seoul, Korea
[9]Department of Pathology, Ulsan University Hospital, University of Ulsan College of Medicine, Ulsan, Korea
[10]Department of Pathology, Pusan National University Hospital, Busan, Korea
[11]Department of Pathology, CHA Gangnam Medical Center, CHA University School of Medicine, Seoul, Korea
[12]Department of Pathology, Yeungnam University College of Medicine, Daegu, Korea

Background: This study aimed to determine the prevalence of human epidermal growth factor receptor 2 (HER2)–ultralow breast cancer among cases initially classified as HER2 immunohistochemistry (IHC) 0 and assess interobserver variability in interpreting low-level HER2 expression. **Methods:** In this multicenter retrospective study, all invasive breast cancer cases diagnosed between January and December 2022 across 10 Korean institutions were retrieved. Institutional pathologists reexamined HER2 IHC slides originally reported as IHC 0 according to the 2018 American Society of Clinical Oncology/College of American Pathologists guidelines and reclassified them as HER2-null (0), HER2-ultralow (0+), or HER2-low (1+). Slides from 10% of HER2-null and HER2-ultralow cases were digitized for central review and independently assessed by two pathologists, with discrepancies resolved by consensus. **Results:** Among 8,026 cases, 2,836 cases (35.5%) were initially reported as IHC 0. Upon re-review, 1,673 (59.0%), 1,139 (40.2%), and 24 (0.8%) cases were reclassified as HER2-null, HER2-ultralow, and HER2-low, respectively. The prevalence of HER2-ultralow breast cancer varied considerably across institutions (23.7%–78.1%). Central review of 268 digitized cases showed concordance in 193 cases (72.0%). Among the 75 discordant cases, 54 tumors (72.0%) were upgraded from HER2-null to HER2-ultralow, and 18 (24.0%) tumors were upgraded from HER2-ultralow to HER2-low. Furthermore, two tumors (2.7%) were downgraded from HER2-ultralow to HER2-null. **Conclusions:** Approximately 40% of cases initially categorized as IHC 0 were reclassified as HER2-ultralow. The substantial inter-institutional variability observed in interpreting low-level HER2 expression highlights the need for standardized training and quality assurance to ensure accurate identification of patients eligible for HER2-targeted antibody–drug conjugates.

Keywords: Breast neoplasms; HER2 protein, ultralow; Multicenter study; Prevalence

Received: September 17, 2025 **Revised:** October 17, 2025 **Accepted:** October 21, 2025

Corresponding Author: Young Kyung Bae, MD, PhD
Department of Pathology, Yeungnam University College of Medicine, 170 Hyeonchung-ro, Nam-gu, Daegu 42415, Korea
Tel: +82-53-640-6755, Fax: +82-53-622-8432, E-mail: ykbae@ynu.ac.kr

Gyungyub Gong, MD, PhD
Department of Pathology, Asan Medical Center, University of Ulsan College of Medicine, 88 Olympic-ro 43-gil, Songpa-gu, Seoul 05505, Korea
Tel: +82-2-2010-4554, Fax: +82-2-472-7898, E-mail: gygong@amc.seoul.kr

*Min Chong Kim and Eun Yoon Cho contributed equally to this work.

INTRODUCTION

Accurate assessment of human epidermal growth factor receptor 2 (HER2) status is essential for the management of breast cancer (BC), as it guides therapeutic decisions and provides important prognostic information. HER2 status is traditionally determined by immunohistochemistry (IHC) and in situ hybridization (ISH) assays, which classify tumors as HER2-positive (IHC 3+ or 2+ with ISH amplification) or HER2-negative (IHC 0, 1+, or 2+ without ISH amplification), directing the use of HER2-targeted therapy or conventional treatment. Therefore, diagnostic efforts have primarily focused on differentiating HER2-overexpressed/amplified tumors from non-overexpressed/non-amplified counterparts [1-4].

However, the advent of trastuzumab deruxtecan (T-DXd), a novel antibody–drug conjugate (ADC), has drawn attention to a subset of tumors termed HER2-low BCs. These tumors, previously categorized as HER2-negative, have demonstrated significant therapeutic responses to T-DXd therapy [5,6]. The HER2-low category includes tumors defined as IHC 1+ or IHC 2+ without gene amplification by ISH. The latest American Society of Clinical Oncology (ASCO)/College of American Pathologists (CAP) guidelines for HER2 testing recommend including a footnote in pathology reports highlighting the potential eligibility of patients with HER2-low expression for T-DXd therapy [7]. More recently, an additional subgroup known as HER2-ultralow has emerged. HER2-ultralow tumors are defined as IHC 0 with faint but detectable membranous staining (IHC >0 and <1+) and have also demonstrated responsiveness to T-DXd [8]. Recognition of the HER2-ultralow subgroup has prompted pathologists to further subclassify HER2 IHC 0 tumors into HER2-null (complete absence of membranous staining) and HER2-ultralow [9], even though IHC assays were not originally designed for such fine gradiations [10]. Consequently, several studies have reported low interobserver agreement in differentiating between HER2-null, HER2-ultralow, and HER2-low cases [11-14].

T-DXd initially received accelerated approval from the U.S. Food and Drug Administration (FDA) in December 2019 for treating adult patients with unresectable or metastatic HER2-positive BC after two or more prior anti-HER2 regimens. In January 2025, the indication was expanded to include patients with hormone receptor–positive, unresectable or metastatic HER2-low or HER2-ultralow BC following endocrine therapy [15,16]. In South Korea, the Ministry of Food and Drug Safety (MFDS) approved T-DXd in September 2022 for HER2-positive breast and gastric cancers and subsequently expanded its use in May 2024 to include patients with metastatic HER2-low BC [17,18]. Approval for HER2-ultralow disease is anticipated in the near future.

We previously conducted a nationwide, multicenter study involving 25 Korean institutions that evaluated the frequency of HER2-low BC, inter-institutional variability, and technical factors influencing HER2 IHC interpretation [19]. That study revealed substantial inter-institutional heterogeneity and highlighted the need for standardized diagnostic protocols. Building upon these findings, the present study aimed to specifically examine the incidence of HER2-ultralow tumors among cases initially categorized as IHC 0.

The primary objective of this study was to determine the proportion of HER2-ultralow tumors within the IHC 0 cohort, thereby establishing baseline epidemiologic data in the Korean BC patient population in the context of expanding HER2-targeted ADC therapies. In addition, we evaluated inter-pathologist concordance in interpreting minimal HER2 expression, a critical issue as indications for T-DXd are expected to include HER2-ultralow disease.

MATERIALS AND METHODS

Study population

Of the 25 institutions involved in our previous nationwide study [19], 10 institutions participated in the present study. All participating centers were accredited by the Korean Society of Pathology Quality Assessment Program and had successfully completed the periodic Korean Institute of Genetic Testing Evaluation Quality Assessment Program. Ethical approval for this study was obtained from the institutional review board of each participating institution. This retrospective study included all cases of invasive BC diagnosed between January 2022 and December 2022. Cases with microinvasive carcinoma or those resected after neoadjuvant systemic therapy were excluded. For patients with multiple ipsilateral tumors, the largest lesion was selected as the representative tumor for analysis. Baseline clinicopathologic variables collected included sex, age at diagnosis, type of specimen, estrogen receptor (ER) status, progesterone receptor (PR) status, and Ki-67 labeling index (LI). ER, PR, and HER2 results were interpreted according to the 2018 ASCO/CAP guidelines. Molecular subtypes were classified based on immunohistochemical surrogate markers, using a Ki-67 cutoff

of 20% to distinguish luminal A (ER+/PR+, low Ki-67) from luminal B (ER+/PR±, high Ki-67) subtypes. Among the 10 institutions, eight institutions used conventional light microscopy for HER2 assessment, and two institutions utilized digital pathology (DP) systems with visual assessment of digitalized images. A schematic overview of the study design is presented in Fig. 1.

Rescoring of HER2 IHC 0 slides

Pathologists at each institution re-evaluated HER2 IHC slides that had originally been reported as IHC 0 at the time of diagnosis. The slides were reclassified into three categories based on the latest 2025 CAP biomarker reporting template: HER2-null (complete absence of membranous staining), HER2-ultralow (faint or weak, incomplete membranous staining in <10% of tumor cells), or HER2-low (IHC score of 1+ or 2+, without HER2 gene amplification) [9]. For clarity, HER2-negative was defined as an IHC score of 0, 1+, or 2+ with a negative ISH result. Following reclassification, all data were submitted for centralized analysis.

Selective central review of IHC slides

Each participating institution submitted 10 % of its slides from the HER2 null and HER2 ultralow subgroups for central review. These slides were digitized using a whole slide scanner (SG300, Philips Healthcare, Amsterdam, Netherlands) and independently assessed by two pathologists (MCK and EYC) with support from PathoAiD-QantiIHC (Aivis, Seoul, Korea), an artificial intelligence (AI)–based analysis platform. The software was used exclusively to detect faint membranous staining patterns in large tumor sections. Nevertheless, the final HER2 classification was determined by consensus between the two pathologists and was not determined by the algorithm alone. The results of the central review were then compared with the local interpretations provided by each institution.

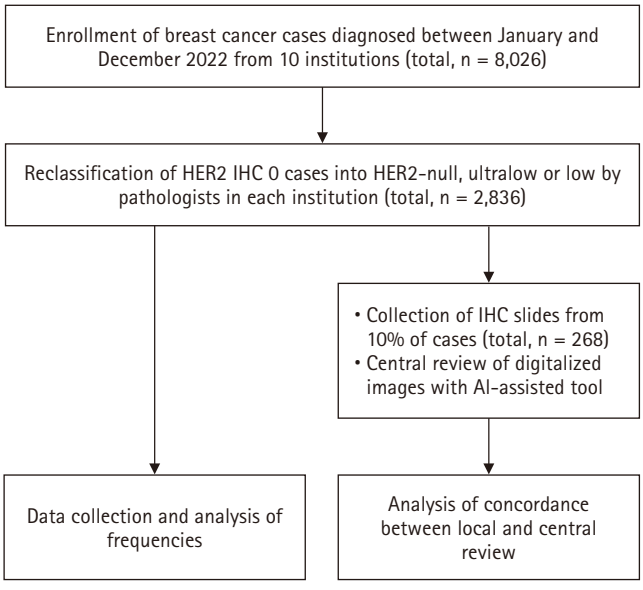

Fig. 1. Flow chart of study design. AI, artificial intelligence; HER2, human epidermal growth factor receptor 2; IHC, immunohistochemistry.

Statistical analysis

Statistical analyses were performed using SPSS ver. 27.0 (IBM Corp., Armonk, NY, USA). Categorical variables were compared using the chi-square test or Fisher's exact test, whereas continuous variables were analyzed using the unpaired t-test. Concordance between institutional and central reviews was evaluated using Cohen's κ coefficient. A κ-value ≥ 0.8 was interpreted as almost perfect agreement, while a value between 0.6 and 0.8 indicated substantial agreement [20]. A p-value < .05 was considered statistically significant.

RESULTS

Incidence of HER2-ultralow cases among tumors initially categorized as IHC 0

A total of 8,026 invasive BC cases were included from the 10 participating institutions. Of these cases, 2,836 cases had been initially classified as HER2 IHC 0. Upon re-evaluation by institutional pathologists, 1,673 (59.0%), 1,139 (40.2%), and 24 (0.8%) cases were reclassified as HER2-null, HER2-ultralow, and HER2-low, respectively. The institutional prevalence of HER2-ultralow BC among HER2 IHC 0 cases ranged from 23.7% to 78.1%. The distribution of reclassified HER2 IHC 0 cases across institutions is illustrated in Fig. 2.

In the overall cohort, the distribution of HER2 category was as follows: HER2-null: 1,673 (20.8%), HER2-ultralow: 1,139 (14.2%), HER2-low: 3,822 (47.6%), and HER2-positive: 1,392 (17.3%). The institutional distribution of cases according to HER2 category is summarized in Supplementary Table S1. Among the 6,634 HER2-negative cases, the proportions of HER2-null, HER2-ultralow, and HER2-low were 25.2%, 17.2%, and 57.6%, respectively.

https://doi.org/10.4132/jptm.2025.10.22

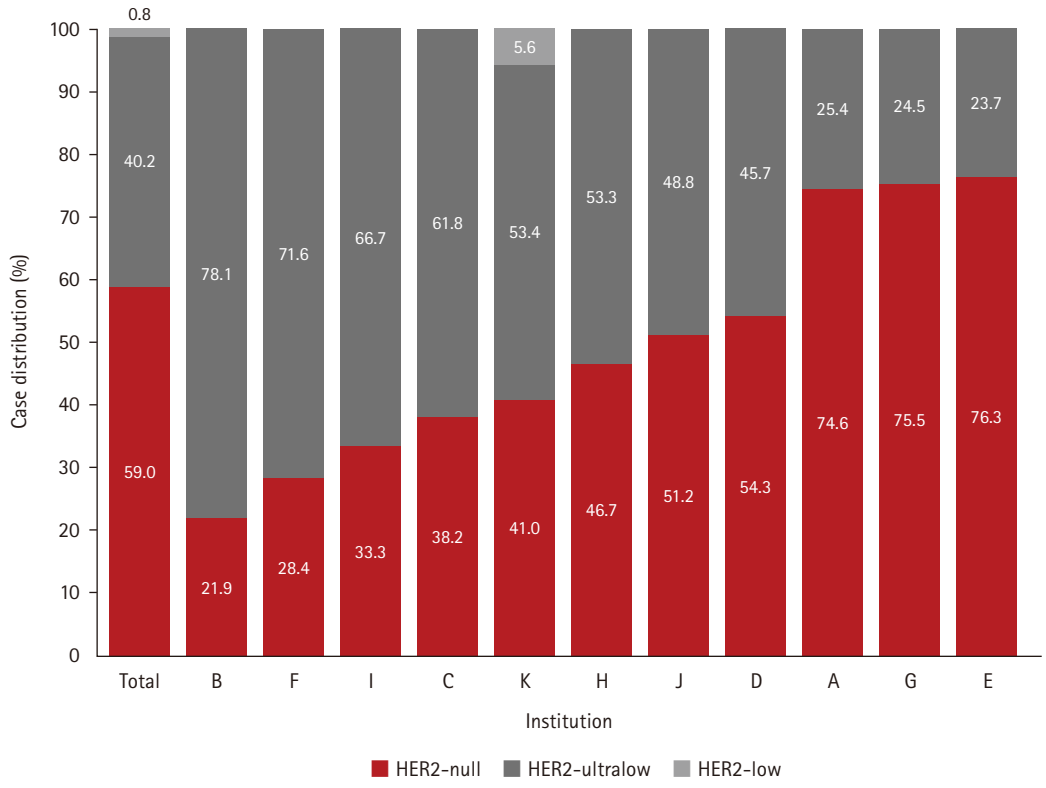

Fig. 2. Reclassification of human epidermal growth factor receptor 2 (HER2) immunohistochemistry 0 cases by institutional pathologists.

Table 1. Comparison of HER2 IHC interpretation results between institutional and central reviews

HER2 results by institutional review	HER2 results by central review			
	Null	Ultralow	Low	Total
Null	101 (64.7)	54 (34.6)	1 (0.6)	156 (100)
Ultralow	2 (1.8)	92 (82.1)	18 (16.1)	112 (100)
Total	103	146	19	268

Values are presented as number (%).
HER2, human epidermal growth factor receptor 2; IHC, immunohistochemistry.

Concordance between institutional and central reviews of HER2 IHC 0 slides

A total of 268 HER2 IHC slides, initially interpreted as HER2-null or HER2-ultralow by institutional pathologists, underwent central review by two pathologists. Representative images for discrepant cases between institutional and central reviews were provided in Supplementary Fig. S1. Overall agreement between institutional and central reviews was achieved in 193 (72.0%) cases (Table 1). When HER2 expression was dichotomized into HER2-null and HER2-ultralow/low, the Cohen's κ coefficient was 0.59 (95% confidence interval [CI], 0.51 to 0.68), indicating moderate agreement. When excluding the 19 cases classified as HER2-low by central review and comparing only HER2-null with HER2-ultralow, the κ value was 0.57 (95% CI, 0.48 to 0.66) with 77.5% agreement.

Among the 75 discordant cases, 54 tumors (72.0%) were reclassified from HER2-null to HER2-ultralow, and one tumor (1.3%) was reclassified from HER2-null to HER2-low. Another 18 tumors (24.0%) were upgraded from HER2-ultralow to HER2-low, whereas the remaining two tumors (2.7%) were downgraded from HER2-ultralow to HER2-null. Overall, the majority of discordant cases were upgraded in HER2 category following central review.

Comparison of clinicopathologic features between HER2-null and HER2-ultralow groups

The clinicopathologic characteristics of the HER2-null and HER2-ultralow subgroups are summarized in Table 2. In comparison with HER2-null tumors, HER2-ultralow tumors were more frequently diagnosed from surgical specimens (63.0% vs. 49.8%, p < .001) and found in slightly older patients (mean age, 54.6 vs. 53.6 years; p =.015). HER2-ultralow tumors also demonstrated a higher rate of ER positivity (84.5% vs. 69.8%, p < .001), and fewer HER2-ultralow tumors had a high Ki-67 LI when using a 20% cutoff (48.5% vs. 54.4%, p = .038). In terms of histologic grade, compared with HER2-ultralow cancers, HER2-null cancers were likely to be high-grade tumors (30.5% vs. 21.9%, p < .001). Overall, HER2-ultralow tumors were predominantly ER-positive/luminal-type tumors, whereas HER2-null tumors were more commonly associated with triple-negative BC profiles.

DISCUSSION

In this multicenter study, we focused on the prevalence of HER2-ultralow BC among cases initially reported as HER2 IHC 0 and interobserver variability in distinguishing low levels of HER2 expression. Upon re-evaluation, 40.2% (range, 23.7% to 78.1%) and 0.8% of HER2 IHC 0 cases were reclassified as HER2-ultralow and HER2-low, respectively. The incidence of HER2-ultralow cases was 14.2% in the total cohort and 17.2% among HER2-negative patients. These findings are somewhat consistent with previous studies, which have reported HER2-ultralow frequencies of 10.6%–17.5% among all BCs and 23.7%–29% among HER2-negative BCs [11-13,21].

Consistent with our previous findings on HER2-low BC incidence [19], there was considerable inter-institutional variability in the frequency of HER2-ultralow tumors within the HER2 IHC 0 group. This variation may be attributed to technical and

Table 2. Comparison of clinicopathologic characteristics between HER2-null and HER2-ultralow

Clinicopathologic factor	No. of cases (n=2,812)	HER2-null (n=1,673)	HER2-ultralow (n=1,139)	p-value
Age (yr)				
Mean ± SD		53.63 ± 11.91	54.62 ± 11.63	.015
Range		23–97	23–89	
Specimen type				
Biopsy	1,261	840 (50.2)	421 (37.0)	<.001
Resection	1,551	833 (49.8)	718 (63.0)	
Histologic type				
No special type	2,429	1,454 (86.9)	975 (85.6)	.321
Special type	383	219 (13.1)	164 (14.4)	
ER status				
Negative	682	505 (30.2)	177 (15.5)	<.001
Positive	2,130	1,168 (69.8)	962 (84.5)	
PR status				
Negative	936	648 (38.7)	288 (25.3)	<.001
Positive	1,876	1,025 (61.3)	851 (74.7)	
Histologic grade[a]				
Grade 1 and 2	1,965	1,101 (69.5)	864 (78.1)	<.001
Grade 3	725	483 (30.5)	242 (21.9)	
Ki-67 LI				
<20	1,431	811 (48.5)	620 (54.4)	.002
≥20	1,381	862 (51.5)	519 (45.6)	
Molecular subtype				
Luminal A and B	2,145	1,176 (70.3)	969 (85.1)	<.001
TNBC	667	497 (29.7)	170 (14.9)	

HER2, human epidermal growth factor receptor 2; SD, standard deviation; ER, estrogen receptor; PR, progesterone receptor; LI, labeling index; TNBC, triple-negative breast cancer.
[a]Cases with missing histologic grade (n = 122) were excluded from the analysis.

https://doi.org/10.4132/jptm.2025.10.22

interpretive factors. As previously described [19], institutional pathology laboratories use different IHC protocols, including staining platforms, antigen retrieval solutions, primary antibody sources, incubation conditions, and detection kits. Even minor adjustments to staining protocols, such as extended antigen retrieval or prolonged antibody incubation, can enhance HER2 staining and shift classification toward the HER2-low category [22-24]. This issue is particularly relevant when evaluating borderline HER2 expression, such as HER2-ultralow. To minimize variability, adoption of standardized protocols based on those used in the DESTINY-Breast04 and DESTINY-Breast06 trials could improve consistency across institutions [25]. In addition, laboratories should pay attention to the management of pre-analytic factors, ensuring that cold ischemic time does not exceed 1 hour and formalin fixation lasts between 6 and 72 hours [26].

Interpretive challenges also contribute to inter-institutional variability in the HER2-ultralow subgroup. Historically, cases now classified as HER2-ultralow (0+) were simply reported as IHC 0, and there was no clinical impetus to distinguish them from HER2-null (0) tumors. The introduction of T-DXd has altered this paradigm. Gao et al. [27] reported an inter-pathologist concordance rate of 69.7% (κ = 0.487) when classifying cases as HER2-low, HER2-ultralow, or HER2-null, with the lowest agreement for the HER2-ultralow subgroup (κ = 0.278). Similarly, Mehta et al. [28] reported an overall concordance rate of 57% and found that the κ value was only 0.17 for the HER2-ultralow subgroup, compared with 0.21 for 1+, 0.47 for null (0), and 0.57 for 2+. These findings suggest that despite guideline adherence, diagnostic reproducibility at lower levels of HER2 expression remains a critical issue. Encouragingly, targeted training of pathologists has been shown to improve interobserver agreement in the interpretation of the HER2-low category [29-31], and this approach may benefit the assessment of HER2-ultralow tumors.

In the present study, a 72% concordance rate was observed between institutional and central reviews of 268 IHC 0 slides. Notably, 97% of the discordant cases were upgraded in HER2 category following central review, most commonly from HER2-null to HER2-ultralow. Central review utilized digitalized images with assistance from an AI-based tool, PathoAiD-Quanti-IHC. The AI system facilitated the identification of borderline cases, improving efficiency and clarity. Kovacs et al. [32] reported higher HER2 scores when using digitalized slides instead of conventional microscopy due to enhanced visualization of membranous staining. Furthermore, compared with conventional assessment, an AI model identified more HER2-low and HER2-ultralow cases, thereby improving detection accuracy. Krishnamurthy et al. [33] demonstrated that the use of an AI-assisted tool increased interobserver agreement from 75.0% (digital manual review) to 83.7% and scoring accuracy from 85.3% to 88.0%. Notably, for distinguishing HER2 0 from 1+ cases, AI improved interobserver agreement (69.8% to 87.4%) and accuracy (81.9% to 88.8%). Similarly, Wu et al. [34] found that an AI algorithm significantly improved both the overall consistency and accuracy of HER2 IHC 0 and 1+ evaluation, especially in heterogeneous cases and among less-experienced pathologists. Overall, these studies suggest that AI-assisted image analysis may be useful for reducing interobserver variability and may serve as a valuable adjunct to standard pathology in the assessment of borderline HER2 expression. However, further research is required to determine whether treatment decisions based on AI-assisted classification will lead to improved clinical outcomes.

In terms of clinicopathologic characteristics, we observed that older patient age, lower histologic grade, higher ER positivity, and lower Ki-67 expression were associated with HER2-ultralow tumors compared with HER2-null tumors. These findings are consistent with those reported by Hu et al. [12], suggesting that HER2-ultralow tumors are more closely related to HER2-low than to HER2-null tumors. In contrast, Chen et al. [11] did not observe significant differences between HER2-ultralow and HER2-null tumors but reported differences between HER2-ultralow and HER2-low tumors in lymph node stage, hormone receptor status, and Ki-67 LI. Importantly, neither study found meaningful differences in disease-free survival among the HER2-null, HER2-ultralow, and HER2-low subgroups [11,12]. Taken together, these findings support the view that HER2-negative BC encompasses biologically diverse tumors [26]. However, at present, subclassification into HER2-null, HER2-ultralow, and HER2-low appears to be primarily relevant for guiding therapeutic decisions, particularly for selecting candidates for T-DXd, rather than for defining distinct biological subtypes.

This study showed that HER2-ultralow expression was more common in surgical specimens than in core biopsies. However, this finding should be interpreted with caution because the two specimen types were not matched on a case-by-case basis, and differences in tissue volume were not strictly controlled. Even so, HER2-ultralow tumors often exhibit pronounced intratumoral heterogeneity; therefore, it is reasonable to assume that

larger tumor volumes may increase the likelihood of detecting HER2 ultralow expression when examined thoroughly. Several studies on HER2-low cases have supported this concept [35-37]. Accordingly, retesting HER2 on the surgical specimen, rather than relying solely on the initial biopsy result, may provide patients with an additional opportunity to receive T-DXd.

This study has several limitations. First, we did not evaluate the diagnostic experience of pathologists or the pre-analytic and analytic factors of HER2 IHC, which may have contributed to inter-institutional variability. Second, the central review was limited to a subset (10%) of the total cases. Third, inter-pathologist concordance was not assessed under standardized conditions. The central review used AI, while institutional reviews did not—so the discrepancy may partly reflect tool availability, not just interobserver variability. Despite these limitations, this work represents the first multicenter investigation in South Korea to examine the prevalence of HER2-ultralow BC and provides valuable baseline epidemiologic data for future research on HER2-targeted ADCs.

In conclusion, approximately 40% of BC cases initially categorized as IHC 0 were reclassified as HER2-ultralow with considerable inter-institutional variability (range, 23.7% to 78.1%). To enhance diagnostic accuracy and consistency, future efforts should focus on standardization of HER2 staining protocols, training of pathologists in low-level HER2 interpretation, and incorporating DP with AI-assisted image analysis. These strategies may support more reliable identification of patients who could benefit from novel HER2-targeted therapies such as T-DXd.

Supplementary Information

The Data Supplement is available with this article at https://doi.org/10.4132/jptm.2025.10.22.

Ethics Statement

This study was approved by the Institutional Review Board of each participating hospital (YUMC 2023-03-004, SMC 2023-02-077-002, PNUYH 05-2023-066, AMC 2023-0386, CNUHH-2025-028, KUH 2023-08-084, OC23RCDI0037, UUH 2023-05-037, PNUH 2303-008-124, and 2023GR0151), and the requirement for informed consent was waived.

Availability of Data and Material

The datasets generated or analyzed during the study are available from the corresponding author on reasonable request.

Code Availability

Not applicable.

ORCID

Min Chong Kim	https://orcid.org/0000-0003-2798-863X
Eun Yoon Cho	https://orcid.org/0000-0003-4675-4492
Hee Jin Lee	https://orcid.org/0000-0002-4963-6603
Ji Shin Lee	https://orcid.org/0000-0003-4634-2228
Jee Yeon Kim	https://orcid.org/0000-0002-0503-984X
Wan Seop Kim	https://orcid.org/0000-0001-7704-5942
Chungyeul Kim	https://orcid.org/0000-0002-9636-5228
Sun-Young Jun	https://orcid.org/0000-0002-3007-2094
Hye Jeong Choi	https://orcid.org/0000-0002-5124-8589
So Mang Lee	https://orcid.org/0009-0009-0208-0116
Ahrong Kim	https://orcid.org/0000-0003-2317-8920
Ji-Young Kim	https://orcid.org/0000-0003-3741-6838
Jeong Yun Shim	https://orcid.org/0000-0002-4628-6660
Gyungyub Gong	https://orcid.org/0000-0001-5743-0712
Young Kyung Bae	https://orcid.org/0000-0002-6689-9413

Author Contributions

Conceptualization: GYG, YKB. Data curation: MCK, EYC, HJL, JSL, JYK, WSK, CYK, SYJ, HJC, SML, ARK, JYK, JYS, GYG, YKB. Formal analysis: MCK, EYC, YKB. Investigation: EYC, MCK. Methodology: MCK, EYC, GYG, YKB. Supervision: GYG, YKB. Writing—original draft: MCK, EYC. Writing—review & editing: GYG, YKB. Approval of final manuscript: all authors.

Conflicts of Interest

Y.K.B., a contributing editor of the *Journal of Pathology and Translational Medicine*, was not involved in the editorial evaluation or decision to publish this article. All remaining authors have declared no conflicts of interest.

Funding Statement

No funding to declare.

Acknowledgments

This study was supported by Korean Society of Pathologists Grant (KSPG2023-03).

REFERENCES

1. Wolff AC, Hammond ME, Schwartz JN, et al. American Society

of Clinical Oncology/College of American Pathologists guideline recommendations for human epidermal growth factor receptor 2 testing in breast cancer. Arch Pathol Lab Med 2007; 131: 18-43.
2. Wolff AC, Hammond ME, Hicks DG, et al. Recommendations for human epidermal growth factor receptor 2 testing in breast cancer: American Society of Clinical Oncology/College of American Pathologists clinical practice guideline update. J Clin Oncol 2013; 31: 3997-4013.
3. Wolff AC, Hammond ME, Allison KH, et al. Human epidermal growth factor receptor 2 testing in breast cancer: American Society of Clinical Oncology/College of American Pathologists clinical practice guideline focused update. J Clin Oncol 2018; 36: 2105-22.
4. Ruschoff J, Lebeau A, Kreipe H, et al. Assessing HER2 testing quality in breast cancer: variables that influence HER2 positivity rate from a large, multicenter, observational study in Germany. Mod Pathol 2017; 30: 217-26.
5. Modi S, Jacot W, Yamashita T, et al. Trastuzumab deruxtecan in previously treated HER2-low advanced breast cancer. N Engl J Med 2022; 387: 9-20.
6. Modi S, Park H, Murthy RK, et al. Antitumor activity and safety of trastuzumab deruxtecan in patients with HER2-low-expressing advanced breast cancer: results from a phase Ib study. J Clin Oncol 2020; 38: 1887-96.
7. Wolff AC, Somerfield MR, Dowsett M, et al. Human epidermal growth factor receptor 2 testing in breast cancer. Arch Pathol Lab Med 2023; 147: 993-1000.
8. Bardia A, Hu X, Dent R, et al. Trastuzumab deruxtecan after endocrine therapy in metastatic breast cancer. N Engl J Med 2024; 391: 2110-22.
9. College of American Pathologists. Reporting template for reporting results of biomarker testing of specimens from patients with carcinoma of the breast, version 1.6.0.0 [Internet]. Northfield: College of American Pathologists, 2025 [cited 2025 Aug 13]. Available from: https://documents.cap.org/documents/New-Cancer-Protocols-March-2025/Breast.Bmk_1.6.0.0.REL.CAPCP.pdf.
10. Wolff AC, McShane LM, Allison KH. Trastuzumab deruxtecan in low or ultralow HER2 metastatic breast cancer. N Engl J Med 2025; 392: 829.
11. Chen Z, Jia H, Zhang H, et al. Is HER2 ultra-low breast cancer different from HER2 null or HER2 low breast cancer?: a study of 1363 patients. Breast Cancer Res Treat 2023; 202: 313-23.
12. Hu Y, Jones D, Zhao W, Tozbikian G, Parwani AV, Li Z. Incidence, clinicopathologic features, and follow-up results of human epidermal growth factor receptor-2-ultralow breast carcinoma. Mod Pathol 2025; 38: 100783.
13. Lv H, Yue J, Zhang Q, et al. Prevalence and concordance of HER2-low and HER2-ultralow status between historical and rescored results in a multicentre study of breast cancer patients in China. Breast Cancer Res 2025; 27: 45.
14. Wu S, Shang J, Li Z, et al. Interobserver consistency and diagnostic challenges in HER2-ultralow breast cancer: a multicenter study. ESMO Open 2025; 10: 104127.
15. Dilawari A, Zhang H, Shah M, et al. US Food and Drug Administration approval summary: trastuzumab deruxtecan for the treatment of adult patients with hormone receptor-positive, unresectable or metastatic human epidermal growth factor receptor 2-low or human epidermal growth factor receptor 2-ultralow breast cancer. J Clin Oncol 2025; 43: 2942-51.
16. Narayan P, Osgood CL, Singh H, et al. FDA approval summary: fam-trastuzumab deruxtecan-nxki for the treatment of unresectable or metastatic HER2-positive breast cancer. Clin Cancer Res 2021; 27: 4478-85.
17. Domestic approval of Enhertu opens new ways to treat breast and stomach cancer [Internet]. Seoul: Korea Biomedical Review, c2017-2025 [cited 2025 Aug 27]. Available from: https://www.koreabiomed.com/news/articleView.html?idxno=14632.
18. Enhertu receives expanded indication for breast and lung cancer [Internet]. Seoul: Korea Biomedical Review, c2017-2025 [cited 2025 Aug 27]. Available from: https://www.koreabiomed.com/news/articleView.html?idxno=24091.
19. Kim MC, Cho EY, Park SY, et al. A nationwide study on HER2-low breast cancer in South Korea: its incidence of 2022 real world data and the importance of immunohistochemical staining protocols. Cancer Res Treat 2024; 56: 1096-104.
20. Landis JR, Koch GG. The measurement of observer agreement for categorical data. Biometrics 1977; 33: 159-74.
21. Akay S, Emiroglu M, Kelten Talu C, Unal OU. Comparison of clinicopathological characteristics for HER2-null, HER2-ultralow and HER2-low breast cancer: a single-center study. Medicina (Kaunas) 2025; 61: 719.
22. Kim MC, Kwon SY, Jung HR, Bae YK. Impact of immunohistochemistry staining conditions on the incidence of human epidermal growth factor receptor 2 (HER2)-low breast cancer. Virchows Arch 2024; 485: 1117-25.
23. Chen YY, Yang CF, Hsu CY. The impact of modified staining method on HER2 immunohistochemical staining for HER2-low breast cancer. Pathology 2024; 56: 122-4.
24. Garrido C, Manoogian M, Ghambire D, et al. Analytical and clinical validation of PATHWAY Anti-HER-2/neu (4B5) antibody to

assess HER2-low status for trastuzumab deruxtecan treatment in breast cancer. Virchows Arch 2024; 484: 1005-14.
25. Shami R, Salgado R, Bardia A, et al. Analytical and clinical validation of PATHWAY HER2 (4B5) assay for assessment of HER2-low/HER2-ultralow status and eligibility for trastuzumab deruxtecan in DESTINY-Breast06. ESMO Open 2025; 10: 105310.
26. Ivanova M, Porta FM, D'Ercole M, et al. Standardized pathology report for HER2 testing in compliance with 2023 ASCO/CAP updates and 2023 ESMO consensus statements on HER2-low breast cancer. Virchows Arch 2024; 484: 3-14.
27. Gao Y, Hong R, Wang J, Pang J, Wu S, Liang Z. Molecular and clinicopathological characteristics of invasive breast cancers with HER2-ultralow expression. Hum Pathol 2025; 158: 105796.
28. Mehta S, Iyengar A, Barman H, et al. Prevalence of "HER2 ultra-low" among patients with advanced breast cancer with historical IHC0 status. J Clin Oncol 2024; 42: e13156.
29. Denkert C, Sperling F, Pehl A, et al. Report of a national external quality assessment program for HER2-low expression in breast cancer-options for increased accuracy with standardized methodology. Virchows Arch 2025 Aug 5 [Epub]. https://doi.org/10.1007/s00428-025-04139-w.
30. Ruschoff J, Penner A, Ellis IO, et al. Global study on the accuracy of human epidermal growth factor receptor 2-low diagnosis in breast cancer. Arch Pathol Lab Med 2025; 149: 431-8.
31. Farshid G, Armes J, Dessauvagie B, et al. Independent validation of a HER2-low focused immunohistochemistry scoring system for enhanced pathologist precision and consistency. Mod Pathol 2025; 38: 100693.
32. Kovacs A, Klint L, Linderholm B, Parris TZ. Changes in HER-2low and HER2-ultralow status in 47 advanced breast carcinoma core biopsies, matching surgical specimens, and their distant metastases assessed by conventional light microscopy, digital pathology, and artificial intelligence. Breast Cancer Res Treat 2025; 213: 397-408.
33. Krishnamurthy S, Schnitt SJ, Vincent-Salomon A, et al. Fully automated artificial intelligence solution for human epidermal growth factor receptor 2 immunohistochemistry scoring in breast cancer: a multireader study. JCO Precis Oncol 2024; 8: e2400353.
34. Wu S, Yue M, Zhang J, et al. The role of artificial intelligence in accurate interpretation of HER2 immunohistochemical scores 0 and 1+ in breast cancer. Mod Pathol 2023; 36: 100054.
35. Baez-Navarro X, van Bockstal MR, Andrinopoulou ER, van Deurzen CHM. HER2-low breast cancer: incidence, clinicopathologic features, and survival outcomes from real-world data of a large nationwide cohort. Mod Pathol 2023; 36: 100087.
36. Lu Y, Zhu S, Tong Y, et al. HER2-low status is not accurate in breast cancer core needle biopsy samples: an analysis of 5610 consecutive patients. Cancers (Basel) 2022; 14: 6200.
37. Na S, Kim M, Park Y, et al. Concordance of HER2 status between core needle biopsy and surgical resection specimens of breast cancer: an analysis focusing on the HER2-low status. Breast Cancer 2024; 31: 705-16.

https://doi.org/10.4132/jptm.2025.10.22

JPTM

ORIGINAL ARTICLE

pISSN 2383-7837 · eISSN 2383-7845

Journal of Pathology and Translational Medicine 2026; 60: 193-201
https://doi.org/10.4132/jptm.2025.11.07

Correlation between *HER2* gene copy number and immunohistochemistry categories in HER2-negative breast cancer: diagnostic utility for differentiating HER2-null, ultralow, and low tumors

Min Chong Kim[1], Young Kyung Bae[2]

[1]Department of Pathology, Yeungnam University Medical Center, Daegu, Korea
[2]Department of Pathology, Yeungnam University College of Medicine, Daegu, Korea

Graphical abstract

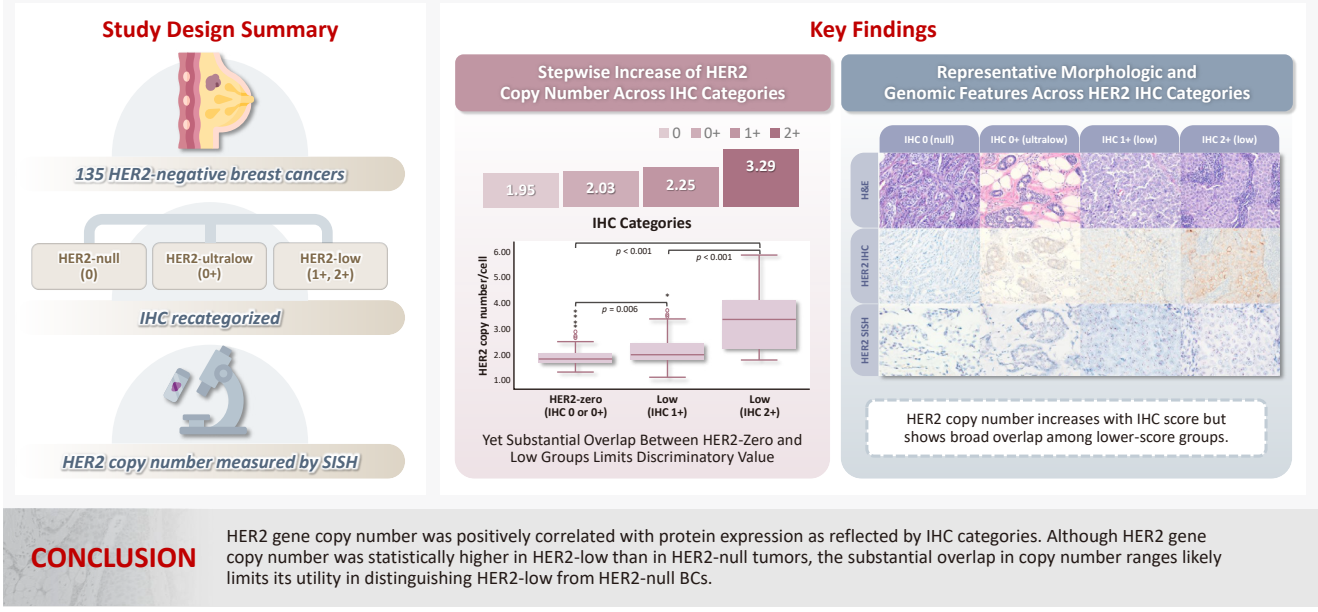

CONCLUSION HER2 gene copy number was positively correlated with protein expression as reflected by IHC categories. Although HER2 gene copy number was statistically higher in HER2-low than in HER2-null tumors, the substantial overlap in copy number ranges likely limits its utility in distinguishing HER2-low from HER2-null BCs.

Kim MC et al. Journal of pathology and translational medicine

JPTM

ORIGINAL ARTICLE

pISSN 2383-7837 · eISSN 2383-7845

Journal of Pathology and Translational Medicine 2026; 60: 193-201
https://doi.org/10.4132/jptm.2025.11.07

Correlation between *HER2* gene copy number and immunohistochemistry categories in HER2-negative breast cancer: diagnostic utility for differentiating HER2-null, ultralow, and low tumors

Min Chong Kim[1], Young Kyung Bae[2]

[1]Department of Pathology, Yeungnam University Medical Center, Daegu, Korea
[2]Department of Pathology, Yeungnam University College of Medicine, Daegu, Korea

Background: The recent recognition of human epidermal growth factor receptor 2 (HER2)–low and HER2-ultralow breast cancers (BCs) has expanded the therapeutic relevance of HER2 testing in the antibody-drug conjugate era. However, the biological continuum of HER2 expression measured by immunohistochemistry (IHC) and its relationship with the *HER2* gene copy number remain unclear. **Methods:** We retrospectively analyzed 135 HER2-negative invasive BCs and reclassified them as HER2-null (IHC 0), HER2-ultralow (0+), or HER2-low (1+ or 2+ without amplification). *HER2* gene copy number was determined using silver-enhanced in situ hybridization. Statistical analyses were performed to compare *HER2* copy number among IHC categories and evaluate the discriminatory value of *HER2* copy number for distinguishing IHC subgroups. **Results:** The mean *HER2* copy number increased stepwise across IHC categories: 1.95 ± 0.54 (null), 2.03 ± 0.43 (ultralow), 2.25 ± 0.65 (low, 1+), and 3.29 ± 1.05 (low, 2+). Significant differences were observed between the ultralow and low groups ($p = .003$) and between the null and low groups ($p < .001$), but not between the null and ultralow groups or between the ultralow and 1+ groups. **Conclusions:** *HER2* gene copy number was positively correlated with protein expression as reflected by IHC categories. Although *HER2* gene copy number was statistically higher in HER2-low than in HER2-null tumors, the substantial overlap in copy number ranges likely limits its utility in distinguishing HER2-low from HER2-null BCs.

Keywords: Breast neoplasms; Genes, erbB-2; In situ hybridization; DNA copy number variations; trastuzumab deruxtecan

INTRODUCTION

Human epidermal growth factor receptor 2 (HER2) status is a critical biomarker in breast cancer (BC), guiding both treatment decisions and prognostic evaluations [1,2]. Traditionally, based on immunohistochemistry (IHC) and in situ hybridization (ISH) assays, HER2 status has been classified as negative (IHC score 0, 1+, or 2+ with ISH-negative for gene amplification) or positive (score 3+ or 2+ with ISH-positive) [3-5]. HER2-targeted therapies have primarily benefited patients with HER2-positive tumors [6,7], while cases of HER2-negative BC have been managed with conventional chemotherapy and, in hormone receptor (HR)–positive cases, endocrine therapy.

Recently, a new subset of HER2-expressing tumors (HER2-low tumors) has been recognized [8]. This category includes tumors with IHC scores of 1+ or 2+ with ISH negativity. The clinical relevance of HER2-low tumors has grown with the development of novel antibody-drug conjugates (ADCs), such as trastuzumab deruxtecan (T-DXd), which have demonstrated efficacy in treating HER2-low BC [9,10]. Consequently, the distinction between HER2 0 and 1+ has become increasingly important in pathology practice, as it affects the eligibility of

Received: September 1, 2025 **Revised:** October 21, 2025 **Accepted:** November 7, 2025
Corresponding Author: Young Kyung Bae, MD, PhD
Department of Pathology, Yeungnam University College of Medicine, 170 Hyeonchung-ro, Nam-gu, Daegu 42415, Korea
Tel: +82-53-640-6755, Fax: +82-53-640-6769, E-mail: ykbae@ynu.ac.kr

patients for HER2-targeted therapies [11,12]. Similarly, differentiating between HER2 1+ and 2+ is now more clinically relevant, as it affects both treatment decisions and the necessity for reflex ISH testing in HER2 2+ cases.

As the therapeutic landscape expands, recent evidence has shown that T-DXd may also be effective in HER2-ultralow tumors with minimal but detectable HER2 expression, extending the potential benefit of ADCs beyond the traditional HER2-low category [13]. This finding has brought renewed attention to the HER2 IHC 0 group, suggesting that it is not a uniform population. The finding underscores the importance of further subclassifying IHC score 0 into HER2-null (0/absent membrane staining) and HER2-ultralow (0+/with membrane staining) [14]. This evolving classification represents a significant shift and a major diagnostic challenge in pathology, requiring more refined interpretation of HER2 IHC staining. Given that patients with HER2-null tumors and those with HER2-ultralow tumors may not derive the same therapeutic benefits, precise and reproducible classification is essential for optimizing treatment strategies and expanding access to emerging HER2-targeted therapies. However, a comparably high variability for HER2-low or HER2-ultralow between pathologists has been reported in retrospective studies [15-17], and the quality assurance results are still lower compared with classical HER2 proficiency tests focusing on HER2 3+ tumors [18].

Despite the increasing clinical relevance of HER2-low and HER2-ultralow classifications, the biological continuum of HER2 expression, from truly negative (HER2-null) to minimally positive (HER2-ultralow and low), remains insufficiently understood. In addition, although only a few recent studies have explored this topic [15,16,19], the correlation between HER2 protein expression and *HER2* gene copy number assessed by ISH has not been clearly established. Elucidating this relationship will be essential for refining diagnostic thresholds and enhancing the accuracy and reproducibility of HER2 classification in clinical practice.

In this study, we analyzed the distribution of *HER2* gene copy numbers across IHC categories to determine whether quantitative assessments of *HER2* gene status could support more precise classification of HER2-null, HER2-ultralow, and HER2-low tumors, with potential implications for ADC therapy.

MATERIALS AND METHODS

Case selection

This study included patients diagnosed with invasive BC who underwent surgery between April and August 2023 at Yeungnam University Hospital (YUH) in Daegu, South Korea. Patients who had received neoadjuvant systemic therapy or presented with tumors measuring less than 0.5 cm were excluded. HER2 IHC was performed using the 4B5 clone antibody (Ventana Medical Systems, Tucson, AZ, USA) on a Ventana autostainer, following standard protocols. HER2 protein expression was interpreted as 0, 1+, 2+, or 3+ according to the 2018 American Society of Clinical Oncology/College of American Pathologists (ASCO/CAP) guidelines [5]. At the time of diagnosis, cases with a score of 2+ underwent reflex silver-enhanced in situ hybridization (SISH) using the INFORM HER2 DNA probe (Ventana Medical Systems) to determine *HER2* gene amplification status. For cases with IHC results available from both core needle biopsy and surgical specimens, the score from the surgical specimen was considered the representative value. Cases classified as HER2-negative (IHC 0, 1+, or 2+ with SISH-negative) were included in the study, whereas those with IHC 3+ or 2+ with SISH positivity (indicating gene amplification) were excluded.

In this study, IHC slides were reviewed by an experienced pathologist (Y.K.B.), and cases originally reported as score 0 (HER2-zero) were reclassified as HER2-null (IHC 0/absent membrane staining) or HER2-ultralow (IHC 0+/incomplete and faint/barely perceptible membrane staining in ≤10% of tumor cells) [14].

HER2 SISH

The average *HER2* gene copy numbers for IHC 2+ cases were obtained from pathology reports. In this study, SISH was performed on surgical specimens of cases with IHC scores of 0, 0+, or 1+. *HER2* and CEP17 signals were counted in at least 20 non-overlapping nuclei of invasive tumor cells, with IHC categories blinded during the assessment. The average *HER2* copy number per cell and the *HER2*/CEP17 ratio were calculated in accordance with the 2018 ASCO/CAP guidelines [5].

Statistical analysis

All statistical analyses were conducted using SPSS ver. 29.0 for Windows (IBM Corp., Armonk, NY, USA). After exploratory data analysis, differences in the average *HER2* gene copy num-

https://doi.org/10.4132/jptm.2025.11.07

ber among the IHC category groups were assessed using the Kruskal-Wallis test. A p-value <.05 was considered statistically significant. Post hoc pairwise comparisons were conducted using the Mann-Whitney U test with the Bonferroni method. The adjusted significance level was determined by dividing 0.05 by the number of pairwise comparisons. Receiver operating characteristic (ROC) curve analyses were performed to determine potential cutoff values for distinguishing HER2-low (1+ or 2+) from HER2-zero BCs. The area under the curve (AUC) was interpreted as follows: 0.6–0.7 indicated poor discrimination, 0.7–0.8 acceptable, 0.8–0.9 good, and ≥0.9 excellent overall performance.

RESULTS

Study population and clinicopathologic characteristics

During the study period, 176 patients were diagnosed with BC and underwent surgery. Of these, 15 patients were excluded due to HER2 positivity, 16 due to the unavailability of HER2 IHC slides, and 10 because their tumors measured less than 0.5 cm, resulting in a final study population of 135 patients. The distribution of HER2 IHC scores in the study cohort was as follows: HER2 0 in 34 patients (25.2%), 0+ in 21 (15.6%), 1+ in 50 (37.0%), and 2+ in 30 (22.2%). Clinicopathologic characteristics of the patients are summarized in Table 1. All variables, including age, histologic type, histologic grade, tumor size, lymph node status, HR expression, and Ki-67 labeling index, did not differ significantly among the HER2-null (0), HER2-ultralow (0+), and HER2-low (1+ and 2+) groups (Table 2).

Table 1. Baseline characteristics of the study population

Characteristic	No. (%)
Age (yr)	
<50	44 (32.6)
≥50	91 (67.4)
Histological type	
IC, NST	111 (82.2)
ILC	11 (8.1)
Others	13 (9.6)
Grade	
I	37 (27.4)
II	44 (32.6)
III	54 (40.0)
Tumor size	
pT1	96 (71.1)
pT2	35 (25.9)
pT3	3 (2.2)
pT4	1 (0.7)
LN status	
pN0	101 (74.8)
pN1	29 (21.5)
pN2	2 (1.5)
pN3	3 (2.2)
ER	
Negative	22 (16.3)
Positive	113 (83.7)
PR	
Negative	32 (23.7)
Positive	103 (76.3)
HER2 IHC score	
0	34 (25.2)
0+	21 (15.6)
1+	50 (37.0)
2+	30 (22.2)
Ki-67 LI (%)	
<20	51 (37.8)
≥20	84 (62.2)
Total	135 (100)

IC, NST, invasive carcinoma of no special type; ILC, invasive lobular carcinoma; LN, lymph node; ER, estrogen receptor; PR, progesterone receptor; HER2, human epidermal growth factor receptor 2; IHC, immunohistochemistry; LI, labeling index.

Comparison of *HER2* gene copy number according to HER2 IHC categories

The mean *HER2* gene copy number was 1.95 ± 0.54 (range, 1.05 to 3.65) in the HER2-null (IHC 0) group, 2.03 ± 0.43 (range, 1.50 to 3.45) in the HER2-ultralow (0+) group, and 2.64 ± 0.96 (range, 1.15 to 5.75) in the HER2-low (1+ or 2+) group. Within the HER2-low group, the mean values were 2.25 ± 0.65 (range, 1.15 to 4.55) for the IHC 1+ subgroup and 3.29 ± 1.05 (range, 1.80 to 5.75) in the IHC 2+ subgroup. Notably, the ranges of *HER2* gene copy numbers were broad and exhibited considerable overlap. Representative hematoxylin and eosin, HER2 IHC, and SISH images from cases corresponding to each HER2 IHC category are shown in Fig. 1.

In the statistical analyses, *HER2* gene copy numbers differed significantly among the HER2-null, HER2-ultralow, and HER2-low groups ($p < .001$). Pairwise comparisons were performed using the Mann-Whitney U test. A total of three post hoc comparisons were conducted (null vs. ultralow, ultralow vs. low, and null vs. low), and the significance threshold was adjusted to $p < .017$ (0.05/3) using Bonferroni's method. Statistically significant

Table 2. Comparison of clinicopathologic characteristics according to HER2 protein expression status in HER2-negative breast cancers

	No. (%)			p-value			
	HER2-null (0) (n = 34)	HER2-ultralow (0+) (n = 21)	HER2-low (1+ & 2+) (n = 80)	All	HER2-null vs. HER2-ultralow	HER2-null vs. HER2-low	HER2-ultralow vs. HER2-low
Age (yr)				.180	.064	.338	.198
<50	8 (23.5)	10 (47.6)	26 (32.5)				
≥50	26 (76.5)	11 (52.4)	54 (67.5)				
Histological type				.930	.680	.927	.734
IC, NST	27 (79.4)	18 (85.7)	66 (82.5)				
ILC	3 (8.8)	2 (9.5)	6 (7.5)				
Others	4 (11.8)	1 (4.8)	8 (10.0)				
Grade				.575	.546	.809	.244
I	10 (29.4)	8 (38.1)	19 (23.8)				
II	11 (32.4)	4 (19.0)	29 (36.3)				
III	13 (38.2)	9 (42.9)	32 (40.0)				
Tumor size				.199	.186	.551	.183
pT1	27 (79.4)	15 (71.4)	54 (67.5)				
pT2	7 (20.6)	4 (19.0)	24 (30.0)				
pT3	0	2 (9.5)	1 (1.3)				
pT4	0	0	1 (1.3)				
LN status				.429	.413	.326	.521
pN0	24 (70.6)	15 (71.4)	62 (77.5)				
pN1	10 (29.4)	5 (23.8)	14 (17.5)				
pN2	0	1 (4.8)	1 (1.3)				
pN3	0	0	3 (3.8)				
ER				.337	.779	.267	.297
Negative	7 (20.6)	5 (23.8)	10 (12.5)				
Positive	27 (79.4)	16 (76.2)	70 (87.5)				
PR				.710	.865	.543	.560
Negative	9 (26.5)	6 (28.6)	17 (21.3)				
Positive	25 (73.5)	15 (71.4)	63 (78.8)				
Ki-67 LI (%)				.655	.660	.358	.792
<20	15 (44.1)	8 (38.1)	28 (35.0)				
≥20	19 (55.9)	13 (61.9)	52 (65.0)				

HER2, human epidermal growth factor receptor 2; IC, NST, invasive carcinoma of no special type; ILC, invasive lobular carcinoma; LN, lymph node; ER, estrogen receptor; PR, progesterone receptor; LI, labeling index.

differences were observed between the ultralow and low groups ($p = .003$) and between the null and low groups ($p < .001$). However, no significant difference was found between the null and ultralow groups ($p = .110$) (Fig. 2A).

When the HER2-low category was further subdivided into IHC 1+ and IHC 2+ subgroups, the *HER2* copy number differed significantly among the four groups ($p < .001$). Pairwise comparisons, with an adjusted significance threshold of $p < .008$ (0.05/6) revealed statistically significant differences between the following pairs: HER2-null vs. IHC 1+ ($p = .003$), HER2-null vs. IHC 2+ ($p < .001$), HER2-ultralow vs. IHC 2+ ($p < .001$), and IHC 1+ vs. IHC 2+ ($p < .001$). No significant difference was observed between the HER2-ultralow and IHC 1+ ($p = .173$) (Fig. 2B).

When HER2 0 and 0+ scores were combined as HER2-zero, *HER2* gene copy numbers differed significantly among the three groups ($p < .001$). In the post hoc analysis (adjusted $p < .017$ [0.05/3]), significant differences in *HER2* copy number were found between HER2-zero vs. IHC 1+ ($p = .006$) and between HER2-zero vs. IHC 2+ ($p < .001$) (Fig. 2C).

https://doi.org/10.4132/jptm.2025.11.07

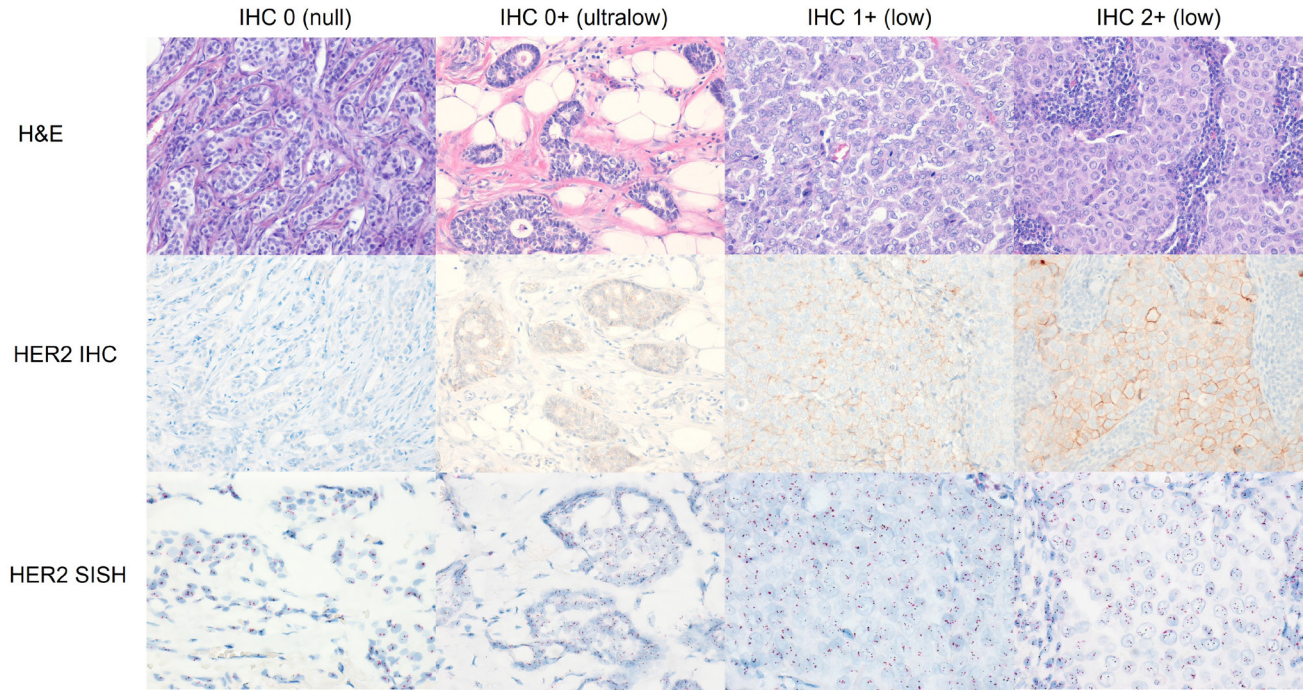

Fig. 1. Representative hematoxylin and eosin (H&E), human epidermal growth factor receptor 2 (HER2) immunohistochemistry (IHC), and *HER2* silver-enhanced in situ hybridization (SISH) images from cases corresponding to each HER2 IHC category. The mean *HER2* gene copy numbers for IHC 0, 0+, 1+, and 2+ cases were 1.95, 2.03, 2.25, and 3.29, respectively.

ROC curve analysis

Because no significant difference was observed in *HER2* copy number between the HER2-null and HER2-ultralow groups, ROC curve analyses were conducted to evaluate the predictive performance of *HER2* copy number in distinguishing HER2-zero (IHC 0 or 0+) from HER2-low (IHC 1+ or 2+) groups. The optimal cutoff value, determined using the Youden Index, was 2.125, yielding 60% sensitivity and 80% specificity. These results indicate that patients with a *HER2* copy number ≥ 2.125 are more likely to exhibit HER2-low status. The AUC for this classification was 0.747, indicating acceptable predictive performance (95% confidence interval [CI], 0.664 to 0.830; $p < .001$) (Fig. 3A).

Subgroup analyses were also conducted. The ROC curve analysis comparing HER2-zero and IHC 2+ groups identified an optimal cutoff value of 2.125, with an AUC of 0.898 (95% CI, 0.832 to 0.965; $p < .001$), reflecting good predictive capability (Fig. 3B). In contrast, the AUC for distinguishing HER2-zero from IHC 1+ was 0.656 (95% CI, 0.552 to 0.760; $p = .003$), indicating poor discrimination (Fig. 3C). To distinguish between IHC 1+ and IHC 2+, the optimal threshold was 2.625, yielding 70% sensitivity and 78% specificity, with an AUC of 0.809 (95% CI, 0.712 to 0.906; $p < .001$) (Fig. 3D).

DISCUSSION

This study demonstrated that the majority of HER2-negative BCs exhibited either HER2-low (59%) or HER2-ultralow (16%) expression patterns. Only a quarter of HER2-negative BCs were classified as HER2-null. In the comparative analysis of clinicopathologic features with varying HER2 expressions, no significant differences were observed in clinicopathological variables, including age, histologic type, tumor size, lymph node status, HR expression, and the Ki-67 labeling index. This result aligns with previous observations that HER2-low and HER2-ultralow BCs may not represent independent biological subtypes [16,20]. Unlike previous studies [16,20], the lack of a significant correlation between HER2 expression levels and HR status in our cohort may be explained by our study design, which excluded patients with HER2-positive BC and those who underwent surgery after neoadjuvant systemic therapy. This exclusion likely resulted in the underrepresentation of HR-negative patients in our cohort, thereby limiting our ability to replicate the associations reported in earlier studies.

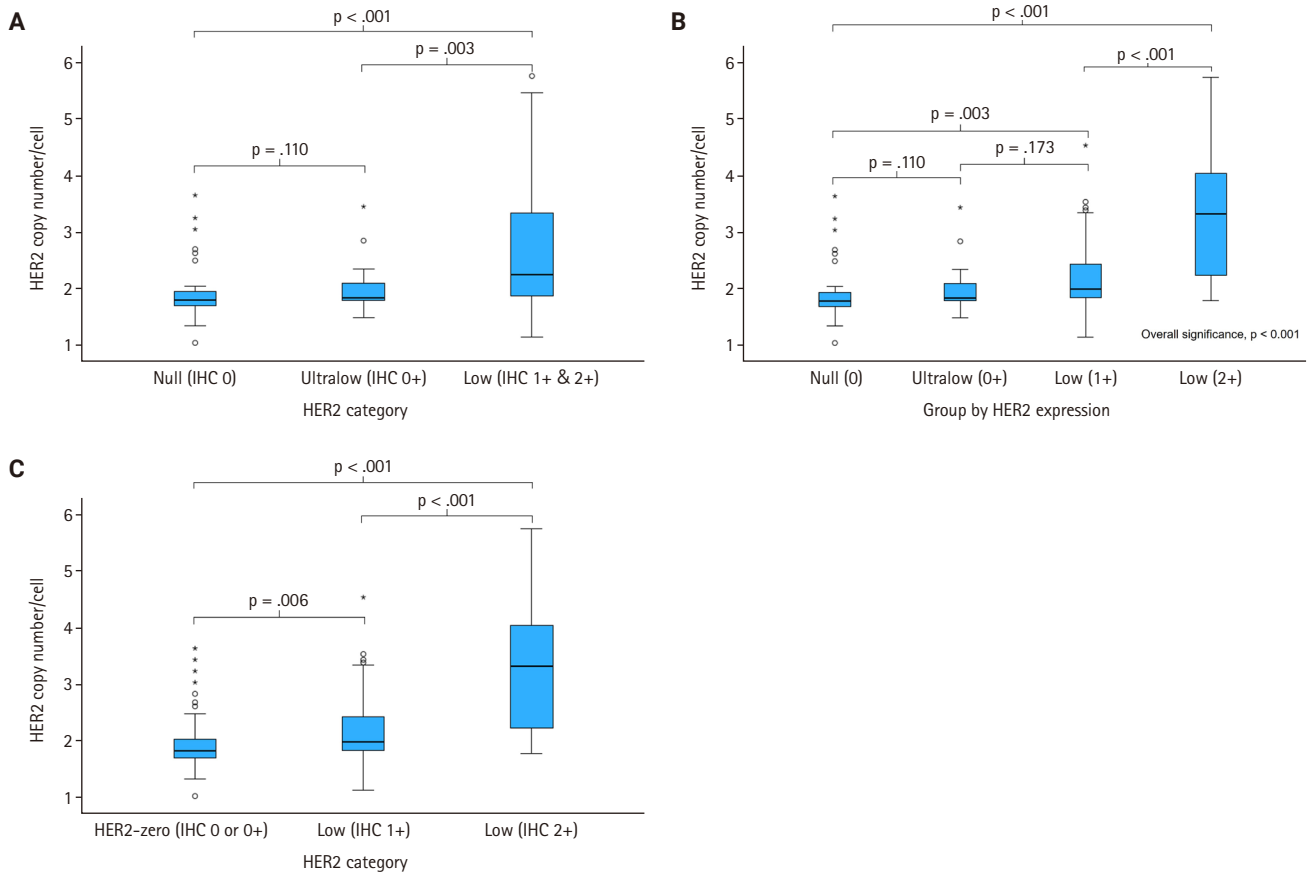

Fig. 2. Comparison of human epidermal growth factor receptor 2 (*HER2*) gene copy number among different HER2 immunohistochemistry (IHC) categories. (A) Comparison among HER2-null (IHC 0), HER2-ultralow (0+), and HER2-low (1+ or 2+) groups. (B) Comparison among HER2-null (IHC 0), HER2-ultralow (0+), HER2 IHC 1+ and HER2 IHC 2+ groups. (C) Comparison among HER2-zero (IHC 0 and 0+), HER2 IHC 1+ and HER2 IHC 2+ groups.

With the recent demonstration that T-DXd is effective not only in HER2-low but also in HER2-ultralow BCs [13], the distinction between HER2-null and HER2-ultralow, rather than between HER2-zero and 1+, has emerged as a major diagnostic challenge for pathologists. In the study by Baez-Navarro et al. [15], pathologists achieved much higher diagnostic agreement when they grouped ultralow, 1+, and 2+ and separated them from the null group, compared with analyzing all IHC categories separately (74.3% vs. 9.5%). When null and ultralow were combined into one group and 1+ and 2+ into another, the agreement rate was 52.4%. Gao et al. [16] also reported that simplified categorization of HER2 IHC (HER2-detected vs. undetected) improved concordance to 84.8%, compared with 69.7% when all subcategories (HER2-undetected, HER2-ultralow, and HER2-low) were considered separately. These findings suggest that interobserver agreement in HER2 IHC interpretation peaks when an "all-or-nothing" principle is applied.

This study aimed to determine whether *HER2* copy numbers determined by SISH could improve discrimination among different HER2 IHC groups (HER2-null vs. ultralow, ultralow vs. 1+, and 1+ vs. 2+). However, the mean *HER2* copy number did not differ significantly between the HER2-null and ultralow groups or between the ultralow and 1+ groups, whereas significant differences were found between the 1+ and 2+ groups and between the HER2-null and HER2-low (1+ or 2+) groups. This finding suggests that HER2-ultralow cancers may not constitute a distinct molecular entity but rather exist along a biological continuum of HER2 expression, marked by subtle variations at the protein level without corresponding changes in gene copy number.

Our results are partly consistent with, but also differ from previous reports [15,16,19]. For example, Baez-Navarro et al. [15,19]

https://doi.org/10.4132/jptm.2025.11.07

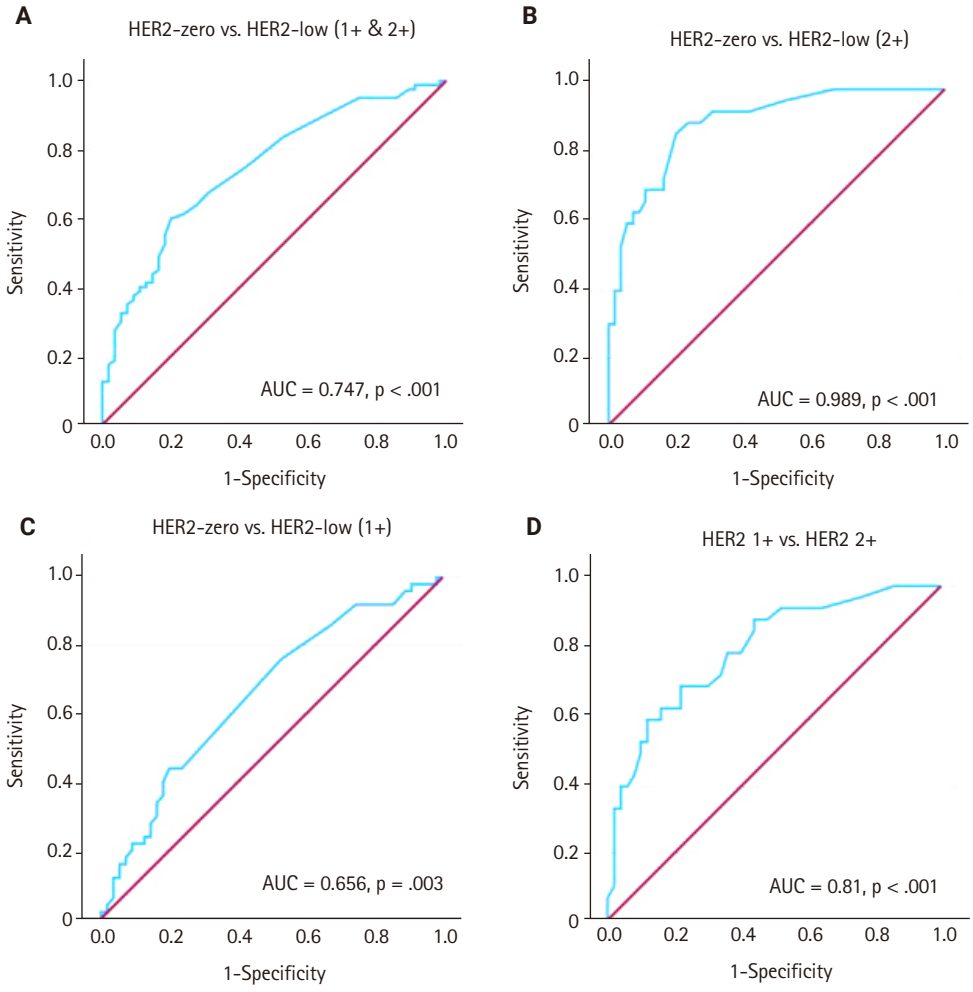

Fig. 3. Receiver operating characteristic curve analysis evaluating the predictive performance of the human epidermal growth factor receptor 2 (*HER2*) copy number in distinguishing (A) between the HER2-zero and HER2-low (immunohistochemistry 1+ or 2+) groups, (B) the HER2-zero and 2+ groups, (C) the HER2-zero and 1+ groups, and (D) the 1+ and 2+ groups. AUC, area under the curve.

found no statistically significant differences in the mean *HER2* copy number between IHC 0 and 1+, regardless of whether the ultralow group was included (null/ultralow vs. 1+ or null vs. 1+), which contrasts with our finding of significantly higher *HER2* copy numbers in 1+ compared with HER2-null tumors. In contrast, they reported results consistent with ours in that HER2-ultralow tumors displayed intermediate values without statistical significance when compared with either HER2-null or 1+. Gao et al. [16] reported results consistent with our findings and partly consistent with those of Baez-Navarro et al. [19], showing that HER2-low BCs had significantly higher *HER2* copy numbers than their HER2-null counterparts, whereas HER2-ultralow tumors showed intermediate values without statistically significant differences when compared with either HER2-null or HER2-low tumors. However, they observed *HER2* copy number variations across varying HER2 expression subgroups in HR-negative tumors, but not in HR-positive tumors. In our study, we did not perform subgroup analyses by HR status because the majority of our cases (84%) were HR-positive, and the number of HR-negative cases (n = 22) was too small to yield meaningful results.

Unlike other studies that employed fluorescence in situ hybridization (FISH), we used SISH. Notably, the mean *HER2* copy numbers observed in each IHC group were slightly higher than those reported in previous FISH-based studies [15,16,19] (HER2-null: 1.95 ± 0.54 vs. 1.88 ± 0.23; ultralow: 2.03 ± 0.43 vs. 1.97 ± 0.28; low: 2.64 ± 0.96 vs. 2.04 ± 0.33). This discrepancy may be attributable to the advantages of bright-field ISH, which facilitates clear visualization of tumor cell morphology and

more accurate signal enumeration within invasive tumor areas.

In a previous study analyzing the HER2 IHC score and mRNA expression [19], a significant difference in mRNA expression was observed between the HER2-null and 1+ groups, whereas no significant differences were found between HER2-null and ultralow or between ultralow and 1+. These findings are closely aligned with our *HER2* copy number results. Similar findings were reported by Yue et al. [21], except that they detected a significant difference in mRNA expression levels between the ultralow and 1+ groups. Shu et al. [22] reported that HER2 1+ tumors were more similar to HER2 0 tumors than to HER2 2+ tumors, due to diverse clinicopathologic factors and overlapping HER2 mRNA levels, suggesting that the current definition of HER2-low expression, with the lower boundary set at IHC 1+, may be inaccurate. However, HER2-low BC has not been regarded as an independent biological subtype, as no substantial molecular differences between HER2-low and HER2-0 tumors have been demonstrated after adjusting for HR expression [11]. Consequently, HER2-low should be considered a heterogeneous group that requires distinction from HER2-null because of its potential implications for ADC therapy.

Although neither our study nor previous studies [15,16,19,21] have demonstrated statistically significant differences in the *HER2* gene copy number or mRNA expression between HER2-null and ultralow tumors or between ultralow and 1+ tumors, both measures exhibited a stepwise increase, being higher in the ultralow group than in the HER2-null group, and higher still in the 1+ group compared with the ultralow group. These findings support the notion that HER2 protein expression is correlated with both mRNA expression and gene copy number. However, HER2 expression is regulated by a complex interplay of genomic, transcriptional, and post-translational mechanisms, including mRNA transcription efficiency, receptor recycling, and degradation processes. Therefore, assessing *HER2* copy number alone as an indicator of HER2 IHC categorization constitutes a limitation of this study.

In conclusion, our study demonstrated that the *HER2* gene copy number is positively correlated with HER2 protein expression as reflected by IHC categories. Although the *HER2* gene copy number was statistically higher in HER2-low than in HER2-null BCs, the broad overlap in signal ranges limits its ability to reliably distinguish between these two categories. Future studies with larger cohorts and the integration of artificial intelligence–assisted image analysis are warranted to validate these findings and further clarify the clinical applicability of the *HER2* gene copy number in predicting responsiveness to ADC therapy.

Ethics Statement

This study was approved by the Institutional Review Board of YUH (IRB No. 2025-03-057), which waived the requirement for informed consent.

Availability of Data and Material

The datasets generated or analyzed during the study are available from the corresponding author on reasonable request.

Code Availability

Not applicable.

ORCID

Min Chong Kim https://orcid.org/0000-0003-2798-863X
Young Kyung Bae https://orcid.org/0000-0002-6689-9413

Author Contributions

Conceptualization: YKB. Data curation: MCK, YKB. Formal analysis: MCK, YKB. Investigation: YKB. Methodology: MCK, YKB. Writing—original draft: MCK, YKB. Writing—review & editing: YKB. Approval of final manuscript: all authors.

Conflicts of Interest

Y.K.B., a contributing editor of the *Journal of Pathology and Translational Medicine*, was not involved in the editorial evaluation or decision to publish this article. The remaining author has declared no conflicts of interest.

Funding Statement

No funding to declare.

REFERENCES

1. Ross JS, Fletcher JA, Linette GP, et al. The HER-2/neu gene and protein in breast cancer 2003: biomarker and target of therapy. Oncologist 2003; 8: 307-25.
2. Harris L, Fritsche H, Mennel R, et al. American Society of Clinical Oncology 2007 update of recommendations for the use of tumor markers in breast cancer. J Clin Oncol 2007; 25: 5287-312.
3. Wolff AC, Hammond ME, Hicks DG, et al. Recommendations for human epidermal growth factor receptor 2 testing in breast

https://doi.org/10.4132/jptm.2025.11.07

cancer: American Society of Clinical Oncology/College of American Pathologists clinical practice guideline update. J Clin Oncol 2013; 31: 3997-4013.
4. Wolff AC, Hammond ME, Schwartz JN, et al. American Society of Clinical Oncology/College of American Pathologists guideline recommendations for human epidermal growth factor receptor 2 testing in breast cancer. J Clin Oncol 2007; 25: 118-45.
5. Wolff AC, Hammond ME, Allison KH, et al. Human epidermal growth factor receptor 2 testing in breast cancer: American Society of Clinical Oncology/College of American Pathologists clinical practice guideline focused update. J Clin Oncol 2018; 36: 2105-22.
6. Early Breast Cancer Trialists' Collaborative Group (EBCTCG). Trastuzumab for early-stage, HER2-positive breast cancer: a meta-analysis of 13 864 women in seven randomised trials. Lancet Oncol 2021; 22: 1139-50.
7. Slamon D, Eiermann W, Robert N, et al. Adjuvant trastuzumab in HER2-positive breast cancer. N Engl J Med 2011; 365: 1273-83.
8. Tarantino P, Hamilton E, Tolaney SM, et al. HER2-low breast cancer: pathological and clinical landscape. J Clin Oncol 2020; 38: 1951-62.
9. Modi S, Park H, Murthy RK, et al. Antitumor activity and safety of trastuzumab deruxtecan in patients with HER2-low-expressing advanced breast cancer: results from a phase Ib study. J Clin Oncol 2020; 38: 1887-96.
10. Modi S, Jacot W, Yamashita T, et al. Trastuzumab deruxtecan in previously treated HER2-low advanced breast cancer. N Engl J Med 2022; 387: 9-20.
11. Tarantino P, Viale G, Press MF, et al. Esmo expert consensus statements (ECS) on the definition, diagnosis, and management of HER2-low breast cancer. Ann Oncol 2023; 34: 645-59.
12. Wolff AC, Somerfield MR, Dowsett M, et al. Human epidermal growth factor receptor 2 testing in breast cancer: ASCO-College of American Pathologists guideline update. J Clin Oncol 2023; 41: 3867-72.
13. Bardia A, Hu X, Dent R, et al. Trastuzumab deruxtecan after endocrine therapy in metastatic breast cancer. N Engl J Med 2024; 391: 2110-22.
14. College of American Pathologists. Reporting template for reporting results of biomarker testing of specimens from patients with carcinoma of the breast, version: 1.6.0.0 [Internet]. Northfield: College of American Pathologists, 2025 [cited 2025 Jul 1]. Available from: https://documents.cap.org/documents/New-Cancer-Protocols-March-2025/Breast.Bmk_1.6.0.0.REL.CAPCP.pdf.
15. Baez-Navarro X, van Bockstal MR, Nawawi D, et al. Interobserver variation in the assessment of immunohistochemistry expression levels in HER2-negative breast cancer: can we improve the identification of low levels of HER2 expression by adjusting the criteria? An international interobserver study. Mod Pathol 2023; 36: 100009.
16. Gao Y, Hong R, Wang J, Pang J, Wu S, Liang Z. Molecular and clinicopathological characteristics of invasive breast cancers with HER2-ultralow expression. Hum Pathol 2025; 158: 105796.
17. Kim MC, Cho EY, Park SY, et al. A nationwide study on HER2-low breast cancer in South Korea: its incidence of 2022 real world data and the importance of immunohistochemical staining protocols. Cancer Res Treat 2024; 56: 1096-104.
18. Denkert C, Sperling F, Pehl A, et al. Report of a national external quality assessment program for HER2-low expression in breast cancer-options for increased accuracy with standardized methodology. Virchows Arch 2025 Aug 5 [Epub]. https://doi.org/10.1007/s00428-025-04139-w.
19. Baez-Navarro X, van Bockstal MR, van der Made A, van Deurzen CH. A comparison between immunohistochemistry and mRNA expression to identify human epidermal growth factor receptor 2-low breast cancer. Arch Pathol Lab Med 2025; 149: 635-42.
20. Baez-Navarro X, van Bockstal MR, Andrinopoulou ER, van Deurzen CH. HER2-low breast cancer: incidence, clinicopathologic features, and survival outcomes from real-world data of a large nationwide cohort. Mod Pathol 2023; 36: 100087.
21. Yue M, Wu S, Wang X, et al. RT-qPCR is helpful to distinguish the clinicopathological features of HER2 immunohistochemistry 0 and 1. Pathol Res Pract 2023; 247: 154532.
22. Shu L, Tong Y, Li Z, Chen X, Shen K. Can HER2 1+ breast cancer be considered as HER2-low tumor? A comparison of clinicopathological features, quantitative HER2 mRNA levels, and prognosis among HER2-negative breast cancer. Cancers (Basel) 2022; 14: 4250.

JPTM

ORIGINAL ARTICLE

pISSN 2383-7837 · eISSN 2383-7845

Journal of Pathology and Translational Medicine 2026; 60: 202-213
https://doi.org/10.4132/jptm.2025.11.05

Multicenter evaluation of the PASS score as a negative predictive tool and the impact of inter-observer variability in pheochromocytoma and paraganglioma risk stratification

Sungyeon Jung[1], Hye-Ri Shin[1], Su-Jin Shin[2], Hee Young Na[3], Soon-Won Hong[4], So Yeon Park[3], Chan Kwon Jung[5], Kyeong Cheon Jung[1], Young Lyun Oh[6], Jae-Kyung Won[1]

[1]Department of Pathology, Seoul National University Hospital, Seoul National University College of Medicine, Seoul, Korea
[2]Department of Pathology, Gangnam Severance Hospital, Yonsei University College of Medicine, Seoul, Korea
[3]Department of Pathology, Seoul National University Bundang Hospital, Seoul National University College of Medicine, Seongnam, Korea
[4]Department of Pathology, Yongin Severance Hospital, Yonsei University College of Medicine, Yongin, Korea
[5]Department of Pathology, Seoul St. Mary's Hospital, College of Medicine, The Catholic University of Korea, Seoul, Korea
[6]Department of Pathology, Samsung Medical Center, Sungkyunkwan University School of Medicine, Seoul, Korea

Graphical abstract

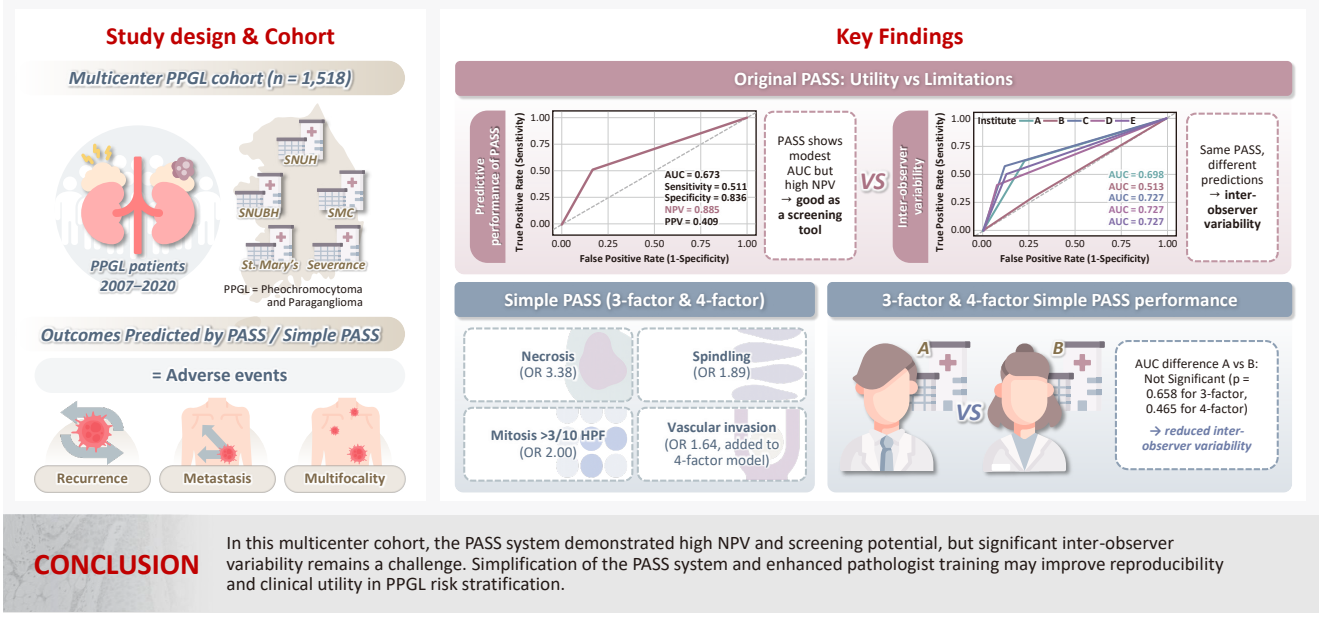

CONCLUSION In this multicenter cohort, the PASS system demonstrated high NPV and screening potential, but significant inter-observer variability remains a challenge. Simplification of the PASS system and enhanced pathologist training may improve reproducibility and clinical utility in PPGL risk stratification.

Jung SY et al. Journal of pathology and translational medicine

JPTM

ORIGINAL ARTICLE

pISSN 2383-7837 · eISSN 2383-7845

Journal of Pathology and Translational Medicine 2026; 60: 202-213
https://doi.org/10.4132/jptm.2025.11.05

Multicenter evaluation of the PASS score as a negative predictive tool and the impact of inter-observer variability in pheochromocytoma and paraganglioma risk stratification

Sungyeon Jung[1], Hye-Ri Shin[1], Su-Jin Shin[2], Hee Young Na[3], Soon-Won Hong[4], So Yeon Park[3], Chan Kwon Jung[5], Kyeong Cheon Jung[1], Young Lyun Oh[6], Jae-Kyung Won[1]

[1]Department of Pathology, Seoul National University Hospital, Seoul National University College of Medicine, Seoul, Korea
[2]Department of Pathology, Gangnam Severance Hospital, Yonsei University College of Medicine, Seoul, Korea
[3]Department of Pathology, Seoul National University Bundang Hospital, Seoul National University College of Medicine, Seongnam, Korea
[4]Department of Pathology, Yongin Severance Hospital, Yonsei University College of Medicine, Yongin, Korea
[5]Department of Pathology, Seoul St. Mary's Hospital, College of Medicine, The Catholic University of Korea, Seoul, Korea
[6]Department of Pathology, Samsung Medical Center, Sungkyunkwan University School of Medicine, Seoul, Korea

Background: The Pheochromocytoma of the Adrenal Gland Scaled Score (PASS) is widely used for risk stratification in pheochromocytoma and paraganglioma (PPGL), but its clinical utility is limited by inter-observer variability of its parameters and inconsistent predictive performance. **Methods:** We conducted a multicenter retrospective study of 1,518 patients with PPGL from five tertiary referral centers in Korea. Prognostic utility of PASS system was assessed using logistic regression, Kaplan-Meier analysis, and receiver operating characteristic (ROC) curve analysis. Inter-observer variability was inferred by comparing area under the ROC curve (AUCs) across institutions. Simplified PASS systems were developed based on multivariable analysis of key histopathological parameters. **Results:** The PASS system was a significant predictor of adverse events and recurrence-free survival. Although the PASS system demonstrated only modest discriminative ability (AUC, 0.673), it showed a high negative predictive value (NPV, 0.885), supporting its usefulness as a screening tool for benign behavior. However, there was significant inter-institutional variability in PASS performance (AUC; range, 0.513 to 0.727; $p < .05$). The 3-factor Simple PASS, which incorporates necrosis, spindling, and mitotic figures, exhibited less inter-observer variation. The 4-factor Simple PASS, which adds vascular invasion to the 3-factor model, also showed reduced inter-observer variability and improved AUC and NPV compared to the original PASS system. **Conclusions:** In this multicenter cohort, the PASS system demonstrated high NPV and screening potential, but significant inter-observer variability remains a challenge. Simplification of the PASS system and enhanced pathologist training may improve reproducibility and clinical utility in PPGL risk stratification.

Keywords: Paraganglioma; Pheochromocytoma; Neoplasm grading; Observer variation

INTRODUCTION

Pheochromocytomas, which are now categorized as adrenal paragangliomas (PPGL) and PPGL are rare neuroendocrine tumors arising from the adrenal medulla and the paraganglia of the autonomic nervous system, respectively, with diverse clinical behaviors ranging from benign to highly aggressive forms [1-3]. Accurate prognostication remains a challenge due to the heterogeneous nature of these tumors and the lack of universally accepted histopathological grading systems [1-3]. The Pheochromocytoma of the Adrenal Gland Scaled Score (PASS) has been proposed to stratify the risk of malignancy and adverse clinical

Received: August 21, 2025 **Revised:** October 13, 2025 **Accepted:** November 5, 2025
Corresponding Author: Jae-Kyung Won, MD, PhD
Department of Pathology, Seoul National University Hospital, Seoul National University College of Medicine, 101 Daehak-ro, Jongno-gu, Seoul 03080, Korea
Tel: +82-2-2072-4895, Fax: +82-2-743-5530, E-mail: jkwon@snuh.org

outcomes [4,5]. However, limitations such as inter-observer variability and inconsistent predictive performance have been reported, raising concerns about its clinical utility [6-9].

The PASS, originally developed by Thompson, incorporates multiple histopathological parameters but lacks quantitative standards for each, leading to variability in interpretation and application across institutions [4,6-11]. Previous research has demonstrated that the PASS, despite its modest overall performance, maintains a high negative predictive value (NPV), suggesting a potential role as a screening tool [5,12-14].

Given these challenges, there is a need to refine prognostic models for PPGL to improve reproducibility and predictive accuracy. Recent efforts to develop a simplified scoring system, focusing on key histopathological features with the strongest associations to adverse events, have shown promise in reducing inter-observer variability and enhancing prognostic performance [5,11,15-18]. This multicenter study aims to evaluate the prognostic significance of the PASS across five tertiary referral centers in Korea, assess inter-institutional variability, and validate the utility of simplified PASS scoring systems for risk stratification in PPGL patients.

MATERIALS AND METHODS

Study cohort and data collection

Five tertiary referral centers in Korea participated in this multicenter study investigating the prognostic factors for paragangliomas. The participating institutions were Seoul National University Hospital (SNUH), Seoul National University Bundang Hospital (SNUBH), Samsung Medical Center (SMC), Seoul St. Mary's Hospital, and Severance Hospital. All data were fully anonymized and merged prior to analysis, so that investigators were blinded to the identity of the contributing institutions.

A total of 1,523 patients diagnosed with PPGL from 2007 to 2020 in 5 hospitals were initially identified. Among these, three cases of gangliocytic paraganglioma and two cases of cauda equina paraganglioma were excluded from the cohort, as these entities are currently classified as composite gangliocytoma/neuroma and neuroendocrine tumor, and cauda equina neuroendocrine tumor, respectively, according to the latest World Health Organization (WHO) classification of endocrine and neuroendocrine tumors [1]. Therefore, the final study cohort comprised 1,518 patients.

Of the total cohort, PASS information was available in 1,079 cases.

Definition of clinical outcomes

Adverse events were defined as the presence of recurrence, metastasis, or multifocality. Recurrence was defined as tumor relapsing in the vicinity of the operative bed. Metastasis was defined as pathologically or radiologically confirmed tumor spread to sites outside the operative bed, specifically bone and lymph nodes [17,19-21]. Multifocality was defined as the presence of additional tumors, excluding bone or lymph node, detected at the time of pathological diagnosis. Recurrence-free survival (RFS) was defined as the interval from the date of surgery to the most recent follow-up or the time when an adverse event occurred.

Statistical analysis

All statistical analyses were performed using R Software (R Foundation for Statistical Computing, Vienna, Austria). Continuous variables were compared using analysis of variance (ANOVA), and categorical variables were analyzed with Fisher's exact test. Survival outcomes were evaluated with Kaplan-Meier plots and the log-rank test in the subset of 363 cases with available RFS data. Univariable and multivariable Cox proportional hazards models were used to assess prognostic factors for RFS in these 363 cases. For adverse event outcomes, univariable and multivariable logistic regression analyses were conducted separately for patients with available PASS data (n = 1,079). Pairwise Delong test was performed for comparison of area under the receiver operating characteristic curve (AUC) among five institutes. A two-sided p-value < .05 was considered statistically significant.

RESULTS

Baseline characteristics

The baseline characteristics of the study cohort are summarized in Table 1. Mean age, sex distribution, tumor size, tumor localization, PASS, and disease status are presented for each hospital. Significant differences in mean age were observed among the institutes (ANOVA, $p < .05$); specifically, hospital D had a higher mean age compared to hospitals A and E. PASS also differed significantly among groups, with hospital A exhibiting higher scores than the other hospitals. For categorical variables such as sex, tumor localization, and disease status, the proportions are reported in Table 1. For tumor localization, cases of paraganglioma in which the localization could not be identified in the electronic medical records were classified as unknown. Statisti-

Table 1. Baseline characteristics of this cohort

Characteristic	Hospital A (n = 366)	Hospital B (n = 188)	Hospital C (n = 532)	Hospital D (n = 117)	Hospital E (n = 315)	p-value
Sex						.849[a]
Female	184 (50.3)	97 (51.6)	277 (52.1)	66 (56.4)	162 (51.4)	
Male	182 (49.7)	91 (48.4)	255 (47.9)	51 (43.6)	153 (48.6)	
Age (yr)	49.59 ± 15.90	51.71 ± 14.38	51.36 ± 15.27	54.80 ± 14.26	49.49 ± 15.27	.005[b]
Tumor size (cm)	4.67 ± 2.90	4.55 ± 2.59	4.44 ± 2.79	4.42 ± 2.49	4.09 ± 2.91	.255[b]
Localization						<.001[c]
Adrenal gland	218 (59.6)	110 (58.5)	326 (61.3)	71 (60.7)	178 (56.5)	
Head and neck	32 (8.7)	19 (10.1)	47 (8.8)	9 (7.8)	55 (17.5)	
Thorax	8 (2.2)	0	4 (0.8)	0	2 (0.6)	
Abdomen/pelvis	99 (27.0)	50 (26.6)	117 (22.0)	33 (28.2)	71 (22.5)	
Spinal cord	9 (2.5)	5 (2.7)	7 (1.3)	2 (1.7)	6 (1.9)	
Unknown	0	4 (2.1)	31 (5.8)	2 (1.7)	3 (1.0)	
PASS score	3.79 ± 3.27	3.03 ± 3.04	2.52 ± 2.73	2.26 ± 2.37	2.44 ± 2.70	<.001[b]
Status of disease						<.001[c]
NED	286 (78.1)	164 (87.2)	502 (94.4)	106 (90.6)	301 (95.6)	
Recurrence	21 (5.7)	1 (0.5)	4 (0.8)	6 (5.1)	3 (1.0)	
Metastasis	38 (10.4)	9 (4.8)	18 (3.4)	2 (1.7)	5 (1.6)	
Multiplicity	21 (5.7)	14 (7.4)	8 (1.5)	3 (2.6)	6 (1.9)	

Values are presented as number (%) or mean±SD.
PASS, Pheochromocytoma of the Adrenal Gland Scaled Score; NED, no evidence of disease; SD, standard deviation.
[a]Pearson's chi-squared test; [b]One-way analysis of means, [c]Fisher's exact test.

Table 2. Logistic regression analysis for adverse events

Variable	Univariable analysis		Multivariable analysis	
	OR (95% CI)	p-value	OR (95% CI)	p-value
Sex	-	.731		.562
Female	-		-	
Male	0.95 (0.70–1.29)		0.90 (0.62–1.29)	
Age (per 10 years)	0.75 (0.68–0.83)	<.001	0.68 (0.60–0.76)	<.001
Tumor size (per 1 cm)	1.13 (1.07–1.18)	<.001	1.05 (0.98–1.11)	.167
Localization		<.001		.055
Adrenal	-		-	
Extra-adrenal	0.37 (0.26–0.54)		0.67 (0.44–1.01)	
PASS score		<.001		<.001
Low risk (0–3)	-		-	
Intermediate risk (4–5)	2.52 (1.59–3.93)		2.05 (1.22–3.35)	
High risk (≥6)	5.41 (3.69–7.94)		4.83 (3.12–7.50)	

OR, odds ratio; CI, confidence interval; PASS, Pheochromocytoma of the Adrenal Gland Scaled Score.

cally significant differences among hospitals were identified for localization and disease state (Fisher's exact test; p-values are shown in Table 1).

PASS as prognostic indicator of adverse events

Univariable and multivariable logistic regression analyses were performed to evaluate the odds ratios of each variable in the total cohort of 1,518 cases (Table 2). In univariable analysis, all variables except sex were statistically significant. However, in multivariable analysis, only age (per 10 years) (odds ratio [OR], 0.68; 95% confidence interval [CI], 0.60 to 0.76; p < .001) and PASS category (intermediate risk [4–5]: OR, 2.05; 95% CI, 1.22 to 3.35; high risk (≥6): OR, 4.83; 95% CI, 3.12 to 7.50; p < .001) remained significant.

https://doi.org/10.4132/jptm.2025.11.05

Kaplan-Meier survival analyses were conducted for the 363 cases with available survival data. Survival curves were stratified by age (≤45 years vs. >45 years), sex, tumor localization (adrenal vs. extra-adrenal), tumor size (≤5.0 cm vs. >5.0 cm), and PASS category (low risk [≤3], intermediate risk [4–5], high risk [≥6]), as shown in Fig. 1. According to the log-rank test, significant differences in survival were observed for age and PASS score categories (all p < .001). In contrast, sex, tumor localization, and tumor size did not show statistically significant differences in survival.

Cox proportional hazards regression analysis for disease-free survival indicated that all variables except sex were statistically significant in univariable analysis (Table 3). In multivariable analysis, age (per 10 years) (hazard ratio [HR], 0.71; 95% CI,

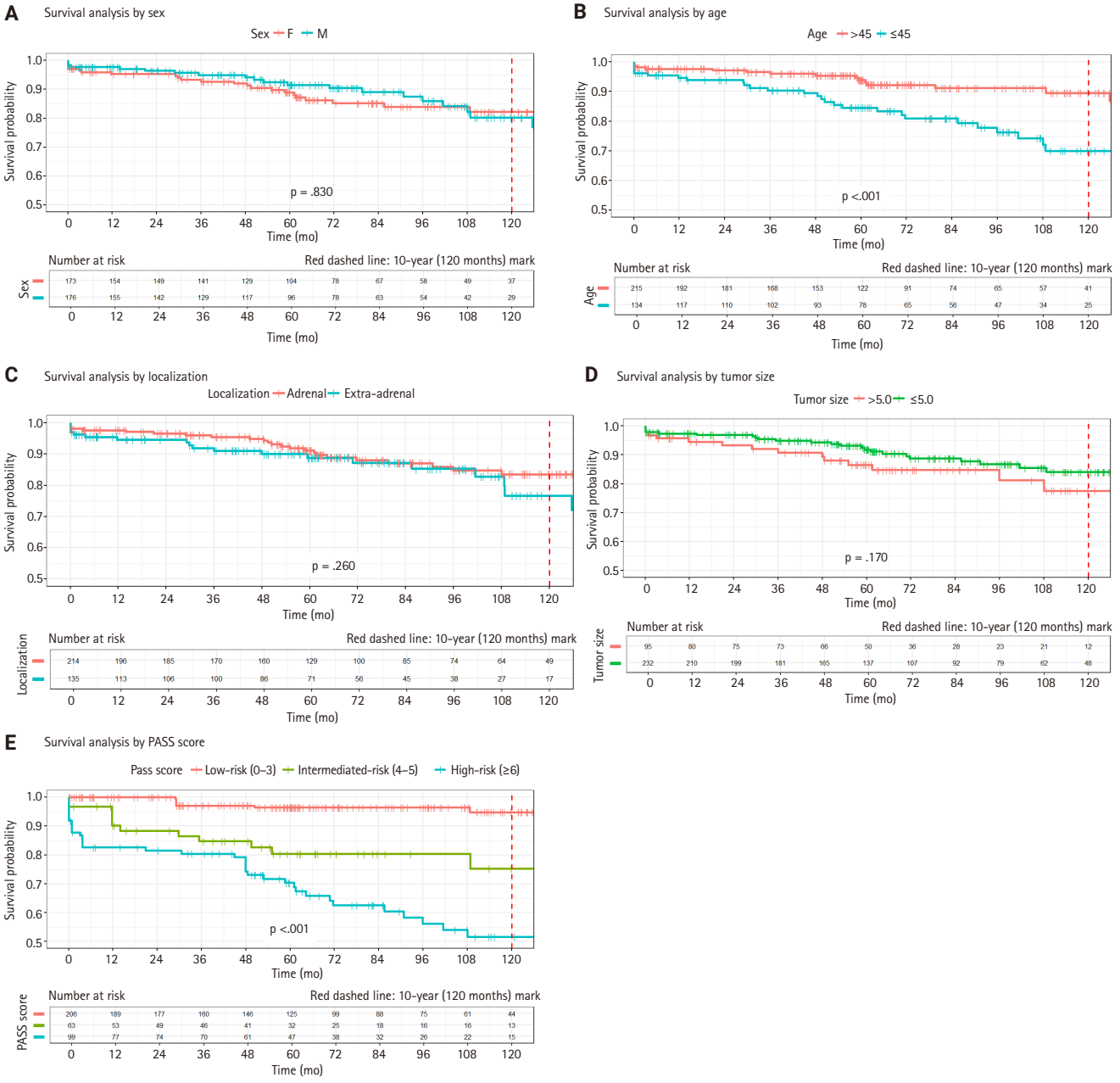

Fig. 1. Kaplan-Meier survival curves for 363 cases with available survival data. Significant differences in survival were observed for age (B) and Pheochromocytoma of the Adrenal Gland Scaled Score (PASS) score (E) categories (p < .001, log-rank test). No statistically significant differences are found for sex (A), tumor localization (C), or tumor size (D).

Table 3. Cox proportional HR analysis for DFS

Variable	Univariable analysis			Multivariable analysis	
	10-Year DFS (%)	HR (95% CI)	p-value	HR (95% CI)	p-value
Sex			.400		
Female	79	-			
Male	78	0.81 (0.50–1.33)			
Age (per 10 years)		0.76 (0.65–0.89)	<.001	0.71 (0.60–0.83)	<.001
Tumor size (per 1 cm)		1.13 (1.05–1.22)	.003	1.05 (0.95–1.15)	.300
Localization			.002		<.001
Adrenal	84	-		-	
Extra-adrenal	72	2.14 (1.31–3.50)		2.96 (1.71–5.14)	
PASS score			<.001		<.001
Low risk (0–3)		-		-	
Intermediate risk (4–5)		4.38 (1.99–9.67)		6.12 (2.30–16.3)	
High risk (≥6)		7.75 (3.94–15.2)		12.5 (5.49–28.5)	

HR, hazard ratio; DFS, disease-free survival; CI, confidence interval; PASS, Pheochromocytoma of the Adrenal Gland Scaled Score.

0.60 to 0.83; p < .001), localization (extra-adrenal: HR, 2.96; 95% CI, 1.71 to 5.14; p < .001), and PASS category (intermediate risk [4–5]: HR, 6.12; 95% CI, 2.3 to 16.3; high risk [≥6]: HR, 12.5; 95% CI, 5.49 to 28.5; p < .001) remained significant. Both multivariable logistic regression and Cox proportional hazards analyses demonstrated the prognostic significance of histopathological grading systems.

The screening role of PASS: high NPV offsets modest predictive performance

The predictive performance of the PASS score for adverse events was further evaluated using logistic regression-based receiver operating characteristic (ROC) curve analysis, as summarized in Fig. 2A. The PASS demonstrated an AUC of 0.673, sensitivity of 0.511, specificity of 0.836, NPV of 0.885, and positive predictive value (PPV) of 0.409. The grid plot demonstrated a low incidence of adverse events in the low-risk group (53 of 720 patients [7.4%]) and a comparatively higher incidence in both the intermediate-risk group (32 of 169 patients [18.9%]) and the high-risk group (59 of 190 patients [31.1%]) (Fig. 2B). Previous studies, including a recent meta-analysis, have also suggested that the high NPV of the PASS supports its utility as a screening tool for risk stratification in pheochromocytoma and PPGL [14]. Our findings are consistent with these prior reports, indicating that while the predictive accuracy of the PASS system alone may be suboptimal, its high NPV renders it a valuable prognostic grading system.

Inter-observer variability of the PASS

The PASS is composed of multiple histopathological parameters, many of which lack quantitative or objective criteria. As a result, concerns have been raised regarding inter-observer variability in its application [8,9]. To further assess this issue, the predictive performance of the PASS for adverse events was evaluated across five different hospitals. The AUC for each institution was as follows: hospital A, 0.698; hospital B, 0.513; hospital C, 0.727; hospital D, 0.665; and hospital E, 0.687 (Fig. 2C). Pairwise DeLong tests revealed statistically significant differences in AUC between hospital A and hospital B, as well as between hospital B and hospital C (p < .05) (Table 4). These findings indirectly demonstrate inter-observer variability in the application of the PASS score, or at the very least, highlight discrepancies in its predictive performance among different institutions.

The distribution of positive cases for each PASS parameter in the adverse event group revealed that nuclear pleomorphism, capsular invasion, and nuclear hyperchromasia were the most frequently observed features (Fig. 3A). Notably, when the proportion of each PASS parameter was further analyzed across the four participating institutes, substantial variation was observed in several parameters—including capsular invasion and nuclear hyperchromasia (Fig. 3B). These findings not only identify which parameters are most commonly seen in the adverse event group but also suggest inter-observer variability in PASS parameter assessment among institutions, underscoring the limitation of applying PASS.

https://doi.org/10.4132/jptm.2025.11.05

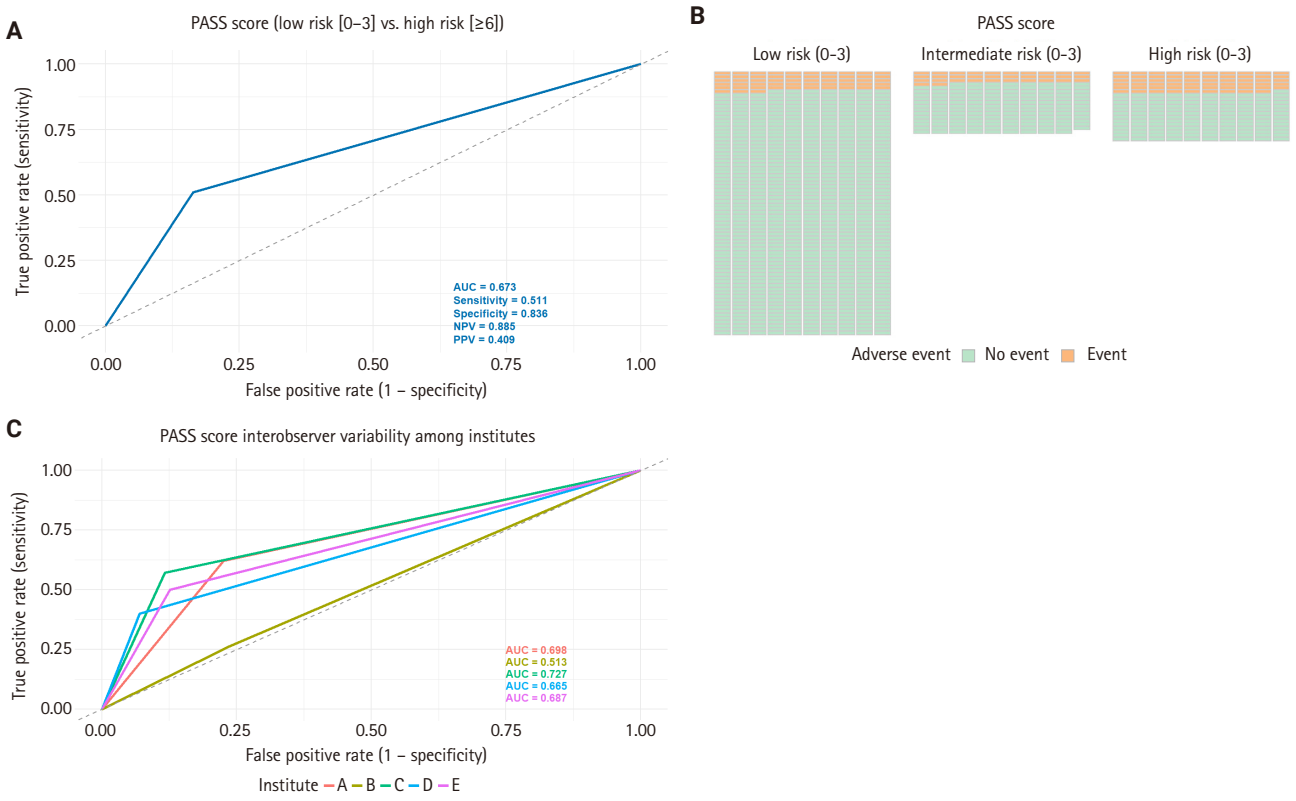

Fig. 2. Predictive performance of Pheochromocytoma of the Adrenal Gland Scaled Score (PASS) for adverse events and its inter-observer variability. (A) Receiver operating characteristic (ROC) curve for the PASS score and (B) grid plot showing the distribution of adverse events by PASS risk group. (C) Comparison of the area under the ROC curve (AUC) for the PASS score across five institutions. Notable variability in AUC values illustrates inter-observer differences in predictive performance among centers. NPV, negative predictive value; PPV, positive predictive value.

Table 4. AUC of PASS score by institutes

Institute	AUC	p-value; pair-wise Delong test				
		vs. A	vs. B	vs. C	vs. D	vs. E
A	0.698	-	.005	.654	.719	.943
B	0.513			.008	.128	.265
C	0.727				.535	.796
D	0.665					.896
E	0.687					

AUC, area under the receiver operating characteristic curve; PASS, Pheochromocytoma of the Adrenal Gland Scaled Score.

Multivariable analysis of PASS parameters and development of the Simple PASS

Multivariable logistic regression analysis was conducted on 560 samples with available PASS parameter scoring to evaluate the association between individual PASS parameters and adverse events (Table 5). Among the PASS parameters, only confluent necrosis, tumor cell spindling, and mitotic figures (>3 per 10 high-power fields [HPF]) were statistically significant. Specifically, confluent necrosis was associated with an OR of 3.38 (95% CI, 1.76 to 6.52; p < .001), tumor cell spindling with an OR of 1.89 (95% CI, 1.13 to 3.12; p =.016), and mitotic figures (>3/10 HPF) with an OR of 2.00 (95% CI, 1.10 to 3.58; p = .023). These three parameters were included in the 3-factor Simple PASS, while vascular invasion—despite its marginal significance (OR,

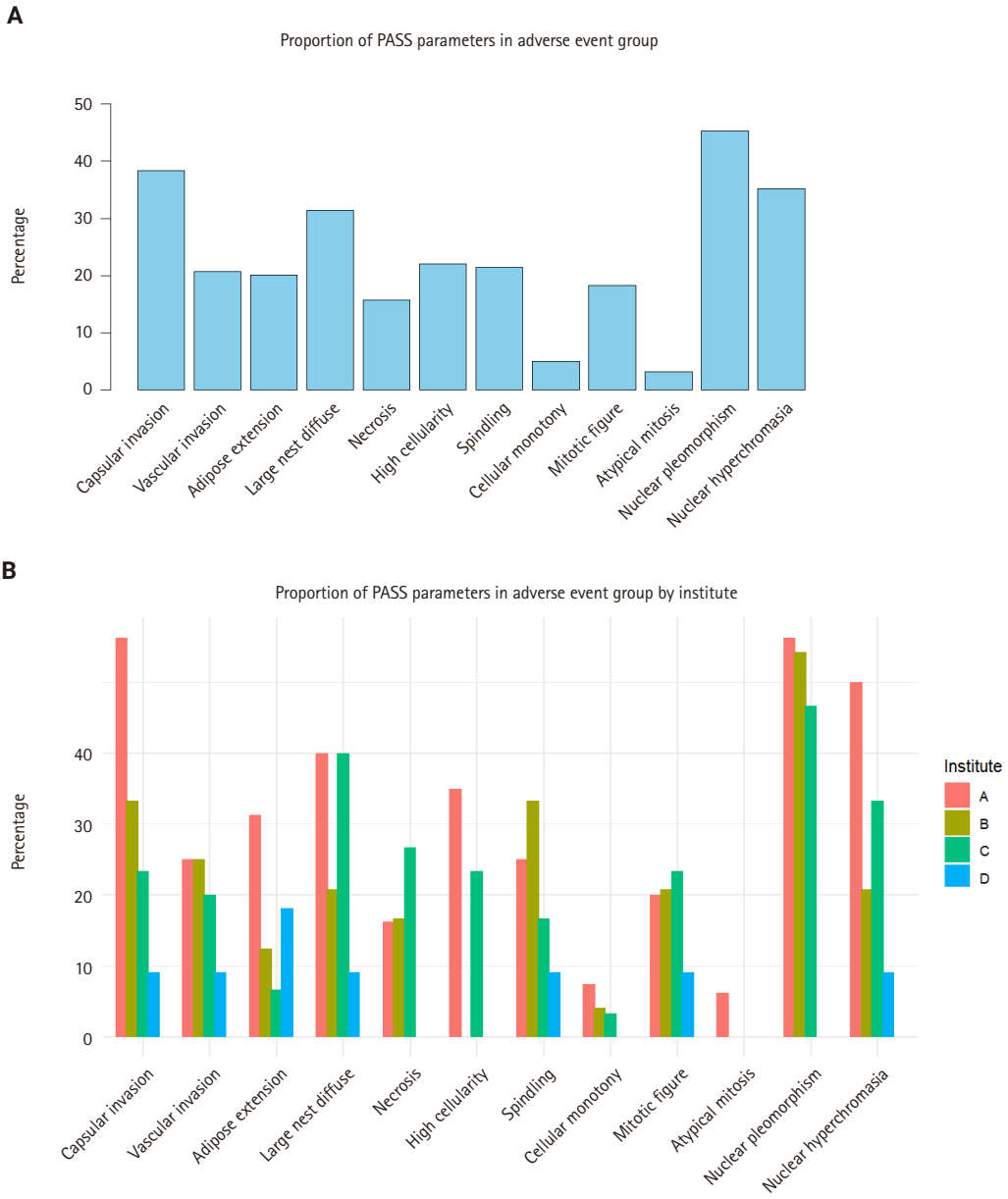

Fig. 3. Proportion of Pheochromocytoma of the Adrenal Gland Scaled Score (PASS) parameters in adverse event group. (A) Proportion of positive cases for each PASS parameter in the adverse event group. Parameters are displayed in order of frequency across the entire cohort. (B) Proportion of positive cases for each PASS parameter in the adverse event group, stratified by institute. The variable distribution across centers highlights inter-observer variability.

1.64; 95% CI, 0.94 to 2.83; p = .080)—was added to the 4-factor Simple PASS. This decision took into account that other scoring systems, such as GAPP (grading of adrenal pheochromocytoma and paraganglioma) and COPPS (COmposite Pheochromocytoma/paraganglioma Prognostic Score), also incorporate vascular invasion as a parameter [5,18].

Based on these odds ratios, the 3-factor Simple PASS was developed by assigning 3 points to confluent necrosis, 2 points to spindling, and 2 points to increased mitotic figures. ROC curve analysis identified an optimal cut-off of 1 point according to the Youden index, indicating that the presence of any single parameter was sufficient to classify a case as high-risk. When high risk was defined as the presence of one or more parameters, subsequent ROC analysis yielded an AUC of 0.646, sensitivity

https://doi.org/10.4132/jptm.2025.11.05

Table 5. ORs of PASS parameter for adverse event

Variable	Univariable analysis		Multivariable analysis	
	OR (95% CI)	p-value	OR (95% CI)	p-value
Capsular invasion	1.58 (1.06–2.35)	.024	1.14 (0.67–1.90)	.622
Vascular invasion	2.26 (1.38–3.64)	.001	1.64 (0.94–2.83)	.080
Extension into adipose tissue	1.70 (1.05–3.64)	.031	1.00 (0.54–1.86)	.994
Large cell nest or diffuse growth >10%	1.97 (1.29–2.98)	<.001	1.35 (0.83–2.19)	.222
Confluent necrosis	4.26 (2.33–7.86)	<.001	3.38 (1.76–6.52)	<.001
High cellularity	1.61 (1.01–2.53)	.045	1.01 (0.59–1.70)	.971
Tumor cell spindling	2.05 (1.27–3.28)	.004	1.89 (1.13–3.12)	.016
Cellular monotony	1.97 (0.77–4.71)	.150	1.11 (0.39–2.94)	.832
Mitotic figure (>3/10 HPF)	2.69 (1.58–4.51)	<.001	2.00 (1.10–3.58)	.023
Atypical mitosis	1.41 (0.44–3.88)	.537	0.49 (0.14–1.55)	.232
Pleomorphic nuclei	1.85 (1.24–2.76)	.002	1.26 (0.78–2.03)	.345
Hyperchromatic nuclei	1.70 (1.13–2.54)	.010	1.23 (0.75–2.00)	.412

OR, odds ratio; PASS, Pheochromocytoma of the Adrenal Gland Scaled Score; CI, confidence interval; HPF, high-power field.

of 0.519, specificity of 0.740, NPV of 0.837, and PPV of 0.374 (Fig. 4A). Furthermore, the 4-factor Simple PASS was created by adding vascular invasion, assigned one point, to the original 3-factor model. Using the same optimal cut-off of 1 point, as determined by the Youden index, ROC analysis demonstrated an AUC of 0.701, sensitivity of 0.497, specificity of 0.891, NPV of 0.938, and PPV of 0.374 (Fig. 4B). Notably, the 4-factor Simple PASS showed improved AUC, specificity, and NPV compared to the original PASS.

When comparing the performance of the simplified PASS systems between hospitals A and B, the difference in AUC was less pronounced than that observed with the original PASS in both simplified models (Fig. 4C, D). Importantly, the difference in AUC between the two hospitals for the simplified PASS was not statistically significant (DeLong test p = .658 for the 3-factor model and .465 for the 4-factor model), in contrast to the significant difference observed with the original PASS score (p = .005). These findings suggest that applying the simplified PASS reduces inter-observer variability.

DISCUSSION

The clinical utility of the PASS system for risk stratification in PPGL has been demonstrated in numerous previous studies, supporting their roles as prognostic indicators for adverse clinical outcomes [10-14,16,22]. In the present multicenter study, we validated the prognostic impact of PASS using what is, to the best of our knowledge, the largest cohort to date. Our results align with prior research, confirming that PASS is associated with adverse events and RFS. Specifically, multivariable logistic regression analysis in our cohort of 1,518 cases revealed that age and PASS were independent predictors of adverse events, with age per 10 years having an OR of 0.68 (95% CI, 0.60 to 0.76; p < .001) and high-risk PASS scores (≥6) conferring an OR of 4.83 (95% CI, 3.12 to 7.50; p < .001). ROC curve analysis showed that the PASS score had an AUC of 0.673, sensitivity of 0.511, specificity of 0.836, and a notably high NPV of 0.885. These findings are consistent with previous meta-analyses and large-scale studies, which have emphasized the high NPV of the PASS as a screening tool, despite its modest overall discriminative performance [5,12-14]. The association between younger age and adverse events may be explained by the fact that adverse events often involve multiplicity, and younger patients are more likely to carry germline mutations and exhibit multiplicity [23-25]. Further studies are warranted to precisely define adverse events using genetic profiles, to distinguish true adverse events from mere multiplicity.

A major advantage of the PASS system is its simplicity and cost-effectiveness, as it can be assessed solely on histopathological grounds without the need for additional molecular or clinical data [5,12]. However, the PASS system incorporates numerous parameters, many of which lack quantitative definitions, leading to substantial inter-observer variability [6-9]. This issue has been widely recognized in the literature, and our multicenter analysis provides further robust evidence that both the diagnostic validity and interpretative application of the PASS score are subject to considerable variability across institutions. Specifically, diagnostic performance as measured by AUC

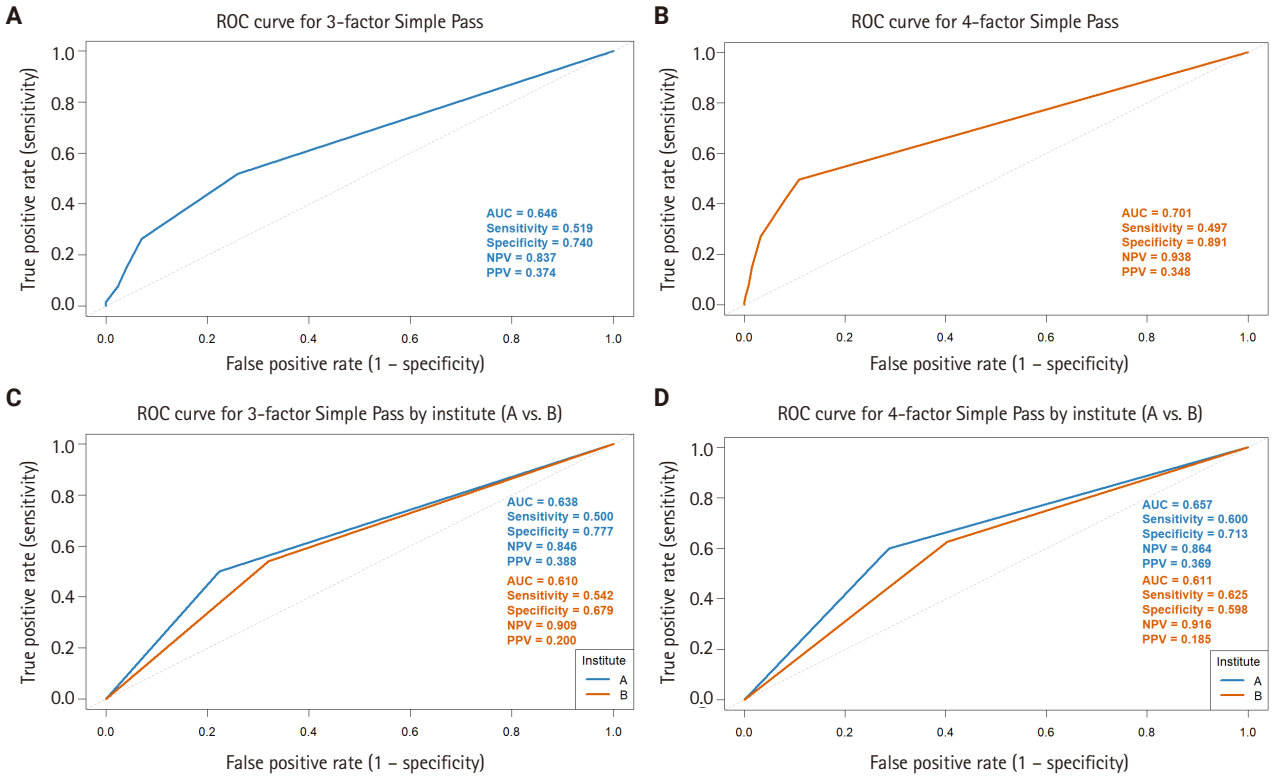

Fig. 4. Simplified Pheochromocytoma of the Adrenal Gland Scaled Score (PASS) models. (A) Receiver operating characteristic (ROC) curve analysis of the 3-factor Simple PASS, constructed by only confluent necrosis, spindling, and high mitotic count (3>10 high-power fields). (B) ROC curve analysis of the 4-factor Simple PASS, adding vascular invasion to the 3-factor model. The 4-factor Simple PASS demonstrates improved area under the ROC curve (AUC), specificity, and negative predictive value compared to the original PASS system. (C, D) Comparison of the AUC for both Simple PASS systems between hospitals A and B. Unlike the original PASS system, the differences of AUC between the two institutions in both simplified models are not statistically significant, suggesting reduced inter-observer variability with the simplified scoring system. NPV, negative predictive value; PPV, positive predictive value.

ranged from 0.513 to 0.727 among the five participating centers, with statistically significant pairwise differences observed in certain comparisons. Furthermore, our detailed exploration of individual PASS parameters demonstrated substantial heterogeneity in their assessment: for instance, capsular invasion and nuclear hyperchromasia showed pronounced discrepancies in the proportion of positive cases among centers. Such inter-institutional differences are likely attributable to variability in pathologists' interpretation and implementation of the PASS criteria. These results underscore the persistent challenge of inter-observer variability.

In response to the limitations of the PASS, several alternative grading systems have been introduced, including the GAPP and other composite models [15-18]. However, each of these systems has its own constraints, such as limited validation, reliance on additional clinical or biochemical data, or continued subjectivity in parameter assessment. Despite these limitations, the PASS remains a valuable screening tool due to its high NPV, and ease of use based solely on histopathology [14].

To address inter-observer variability and improve the prognostic performance of PASS, we conducted multivariable analysis to identify the parameters most strongly associated with adverse events. Based on these results and previous studies, confluent necrosis, tumor cell spindling, and increased mitotic figures (>3/10 HPF) were incorporated into a 3-factor simplified PASS scoring system, while vascular invasion was additionally included to develop a 4-factor simplified PASS. Notably, the 4-factor model—where single presence of vascular invasion, necrosis, spindling and increased mitosis can be assigned as high-risk group—demonstrated improved AUC (0.701), specificity (0.891), and NPV (0.938) compared to the original PASS score, despite the reduced number of parameters. Furthermore,

https://doi.org/10.4132/jptm.2025.11.05

when comparing the performance of both simplified PASS systems between hospitals A and B, the difference in AUC was not statistically significant, suggesting reduced inter-observer variability relative to the original PASS system.

This study has several limitations. First, we did not review pathological slides or revise the initially diagnosed PASS to avoid retrospective bias, as the main goal of this study was to evaluate how well the PASS system performs in real-world practice with respect to diagnostic accuracy and inter-observer variability. During data collection, we realized that the absence of a refined consensus on the definitions of each parameter might have contributed to inter-observer variability, underscoring the high demand for precise and standardized definitions of each factor. As a multicenter retrospective analysis, the completeness and consistency of data collection may be suboptimal. While the relationship between PASS score and adverse events was the primary focus, survival data and detailed PASS parameter information was limited, resulting in smaller sample sizes (n = 560) for some analyses. Furthermore, we did not directly assess inter-observer agreement by having multiple pathologists independently review the same slides; rather, we inferred variability indirectly by comparing AUCs for adverse event prediction across institutions. Future studies should incorporate direct inter-observer concordance assessments to more precisely quantify variability. Another limitation concerns the definition of adverse events. Given that PPGL can arise anywhere along the paraganglionic system, distinguishing between multifocality, metastasis, and recurrence can be challenging, and these categories may overlap biologically [26,27]. We included multifocal tumors as adverse events but recognize that their biological behavior may differ from truly metastatic or recurrent tumors, potentially diminishing the predictive power of the PASS [28,29]. Additionally, previous studies suggest patients with germline mutations are more prone to multifocal PPGL, and immunohistochemistry (IHC) for S-100 and SOX-10 can be used to distinguish metastasis from multifocal tumors [18,23-25]. Taken together, future research should incorporate genetic data and additional IHC study to distinguish multifocal cases from metastasis and refine the definition of adverse events accordingly.

In conclusion, this study validates the prognostic impact of the PASS in the largest cohort of PPGL patients to date, confirming the high NPV and screening potential of the PASS. However, significant inter-observer variability remains a major challenge. Efforts to reduce this variability—such as enhanced training for pathologists and simplification of the PASS system—are warranted. Our findings highlight the importance of focusing on key histopathological parameters and support ongoing initiatives to streamline and standardize risk stratification in paraganglioma.

Ethics Statement

The study protocol was approved by the Institutional Review Board of Seoul National University Hospital (IRB no. H-2108-062-1243) and conducted in accordance with the principles of the Declaration of Helsinki. Formal written informed consent was not required with a waiver by the appropriate IRB and/or national research ethics committee.

Availability of Data and Material

Data supporting the findings of this study are available from the corresponding author on reasonable request.

Code Availability

Not applicable.

ORCID

Sungyeon Jung	https://orcid.org/0009-0007-2650-3350
Hye-Ri Shin	https://orcid.org/0000-0001-5797-4197
Su-Jin Shin	https://orcid.org/0000-0001-9114-8438
Hee Young Na	https://orcid.org/0000-0002-2464-0665
Soon-Won Hong	https://orcid.org/0000-0002-0324-2414
So Yeon Park	https://orcid.org/0000-0002-0299-7268
Chan Kwon Jung	https://orcid.org/0000-0001-6843-3708
Kyeong Cheon Jung	https://orcid.org/0000-0002-7741-7184
Young Lyun Oh	https://orcid.org/0000-0002-9127-4642
Jae-Kyung Won	https://orcid.org/0000-0003-1459-8093

Author Contributions

Conceptualization: SJ, JKW. Formal analysis: SJ. Investigation: all authors. Methodology: SJ, JKW. Project Administration: CKJ. Supervision: JKW, KCJ. Visualization: SJ. Writing—original draft: SJ. Writing—review and editing: JKW, KCJ. Approval of final manuscript: all authors.

Conflicts of Interest

C.K.J. and S.Y.P., the editors-in-chief and S.W.H., contributing editor of the *Journal of Pathology and Translational Medicine,* were not involved in the editorial evaluation or decision to publish this article. All remaining authors have declared no conflicts of interest.

Funding Statement
This research was supported by The Korean Society of Pathologists Grant No. KSPG2021-01.

REFERENCES

1. WHO Classification of Tumours Editorial Board. Endocrine and neuroendocrine tumours. 5th ed. Lyon: IARC, 2022.
2. Fishbein L. Pheochromocytoma and paraganglioma: genetics, diagnosis, and treatment. Hematol Oncol Clin North Am 2016; 30: 135-50.
3. Lenders JW, Duh QY, Eisenhofer G, et al. Pheochromocytoma and paraganglioma: an endocrine society clinical practice guideline. J Clin Endocrinol Metab 2014; 99: 1915-42.
4. Thompson LD. Pheochromocytoma of the adrenal gland scaled score (PASS) to separate benign from malignant neoplasms: a clinicopathologic and immunophenotypic study of 100 cases. Am J Surg Pathol 2002; 26: 551-66.
5. Kimura N, Takayanagi R, Takizawa N, et al. Pathological grading for predicting metastasis in phaeochromocytoma and paraganglioma. Endocr Relat Cancer 2014; 21: 405-14.
6. Bima C, Bioletto F, Lopez C, et al. Clinical and pathological tools for predicting recurrence and/or metastasis in patients with pheochromocytoma and paraganglioma. Biomedicines 2022; 10: 1813.
7. Stenman A, Zedenius J, Juhlin CC. Over-diagnosis of potential malignant behavior in MEN 2A-associated pheochromocytomas using the PASS and GAPP algorithms. Langenbecks Arch Surg 2018; 403: 785-90.
8. Wachtel H, Hutchens T, Baraban E, et al. Predicting metastatic potential in pheochromocytoma and paraganglioma: a comparison of PASS and GAPP scoring systems. J Clin Endocrinol Metab 2020; 105: e4661-70.
9. Wu D, Tischler AS, Lloyd RV, et al. Observer variation in the application of the Pheochromocytoma of the adrenal gland scaled score. Am J Surg Pathol 2009; 33: 599-608.
10. Mondal A, Sengupta M, Dey S, et al. Clinicopathological study of adrenal pheochromocytoma and extra-adrenal paragangliomas with reference to GAPP and PASS scoring systems. Indian J Pathol Microbiol 2024; 67: 852-8.
11. Yamazaki Y, Gao X, Pecori A, et al. Recent advances in histopathological and molecular diagnosis in pheochromocytoma and paraganglioma: challenges for predicting metastasis in individual patients. Front Endocrinol (Lausanne) 2020; 11: 587769.
12. Koh JM, Ahn SH, Kim H, et al. Validation of pathological grading systems for predicting metastatic potential in pheochromocytoma and paraganglioma. PLoS One 2017; 12: e0187398.
13. Kimura N, Takekoshi K, Naruse M. Risk stratification on pheochromocytoma and paraganglioma from laboratory and clinical medicine. J Clin Med 2018; 7: 242.
14. Stenman A, Zedenius J, Juhlin CC. The value of histological algorithms to predict the malignancy potential of pheochromocytomas and abdominal paragangliomas-a meta-analysis and systematic review of the literature. Cancers (Basel) 2019; 11: 225.
15. Cho YY, Kwak MK, Lee SE, et al. A clinical prediction model to estimate the metastatic potential of pheochromocytoma/paraganglioma: ASES score. Surgery 2018; 164: 511-7.
16. Li Q, Lan Z, Jiang Y, Wang R, Li Z, Jiang X. Validation and evaluation of 5 scoring systems for predicting metastatic risk in pheochromocytoma and paraganglioma. Am J Surg Pathol 2024; 48: 855-65.
17. Park SS, Ahn CH, Lee S, et al. Preoperative prediction of metastatic pheochromocytoma and paraganglioma using clinical, genetic, and biochemical markers: a cohort study. J Intern Med 2024; 296: 68-79.
18. Pierre C, Agopiantz M, Brunaud L, et al. COPPS, a composite score integrating pathological features, PS100 and SDHB losses, predicts the risk of metastasis and progression-free survival in pheochromocytomas/paragangliomas. Virchows Arch 2019; 474: 721-34.
19. Ku EJ, Kim KJ, Kim JH, et al. Diagnosis for pheochromocytoma and paraganglioma: a joint position statement of the Korean pheochromocytoma and paraganglioma task force. Endocrinol Metab (Seoul) 2021; 36: 322-38.
20. Yokomoto-Umakoshi M, Umakoshi H, Tsuiki M, et al. Paraganglioma as a risk factor for bone metastasis. Endocr J 2018; 65: 253-60.
21. Zhu X, Huang Z, Dong L, Zhao H, Lu H. A case report of primary colonic paraganglioma with lymph node metastasis. Front Surg 2022; 9: 961514.
22. Agarwal A, Mehrotra PK, Jain M, et al. Size of the tumor and pheochromocytoma of the adrenal gland scaled score (PASS): can they predict malignancy? World J Surg 2010; 34: 3022-8.
23. Barontini M, Levin G, Sanso G. Characteristics of pheochromocytoma in a 4- to 20-year-old population. Ann N Y Acad Sci 2006; 1073: 30-7.
24. Else T, Greenberg S, Fishbein L. Hereditary paraganglioma-pheochromocytoma syndromes. In: Adam MP, Bick S, Mirzaa GM, Pagon RA, Wallace SE, Amemiya A, eds. GeneReviews. Seattle: University of Washington, Seattle, 2018.

https://doi.org/10.4132/jptm.2025.11.05

25. Pamporaki C, Hamplova B, Peitzsch M, et al. Characteristics of pediatric vs adult pheochromocytomas and paragangliomas. J Clin Endocrinol Metab 2017; 102: 1122-32.
26. Asa SL, Ezzat S, Mete O. The diagnosis and clinical significance of paragangliomas in unusual locations. J Clin Med 2018; 7: 280.
27. Juhlin CC, Mete O. Advances in adrenal and extra-adrenal paraganglioma: practical synopsis for pathologists. Adv Anat Pathol 2023; 30: 47-57.
28. Brewczynski A, Kolasinska-Cwikla A, Jablonska B, Wyrwicz L. Pheochromocytomas and paragangliomas-current management. Cancers (Basel) 2025; 17: 1029.
29. Mete O, Juhlin CC. Recent progress in the pathologic classification of pheochromocytomas and paragangliomas. Best Pract Res Clin Endocrinol Metab 2024; 38: 101958.

JPTM

ORIGINAL ARTICLE

pISSN 2383-7837 · eISSN 2383-7845

Journal of Pathology and Translational Medicine 2026; 60: 214-219
https://doi.org/10.4132/jptm.2025.12.06

Mutational status of non-invasive follicular thyroid neoplasm with papillary-like nuclear features (NIFTP): molecular analysis should be performed for NIFTPs with nuclear score 3

Ayaka Sako[1,2], Mitsuyoshi Hirokawa[3], Michiko Matsuse[1,4], Miyoko Higuchi[3], Akira Miyauchi[5], Takashi Akamizu[6], Atsushi Kawakami[2,7], Norisato Mitsutake[1,4]

[1]Department of Molecular Oncology, Atomic Bomb Disease Institute, Nagasaki University, Nagasaki, Japan
[2]Department of Endocrinology and Metabolism, Nagasaki University Hospital, Nagasaki, Japan
[3]Department of Diagnostic Pathology and Cytology, Kuma Hospital, Kobe, Japan
[4]Thyroid Cancer Collaborative Research Center, Nagasaki University, Nagasaki, Japan
[5]Department of Surgery, Kuma Hospital, Kobe, Japan
[6]Department of Internal Medicine, Kuma Hospital, Kobe, Japan
[7]Division of Advanced Preventive Medical Sciences, Department of Immunology and Rheumatology, Nagasaki University Graduate School of Biomedical Sciences, Nagasaki, Japan

Graphical abstract

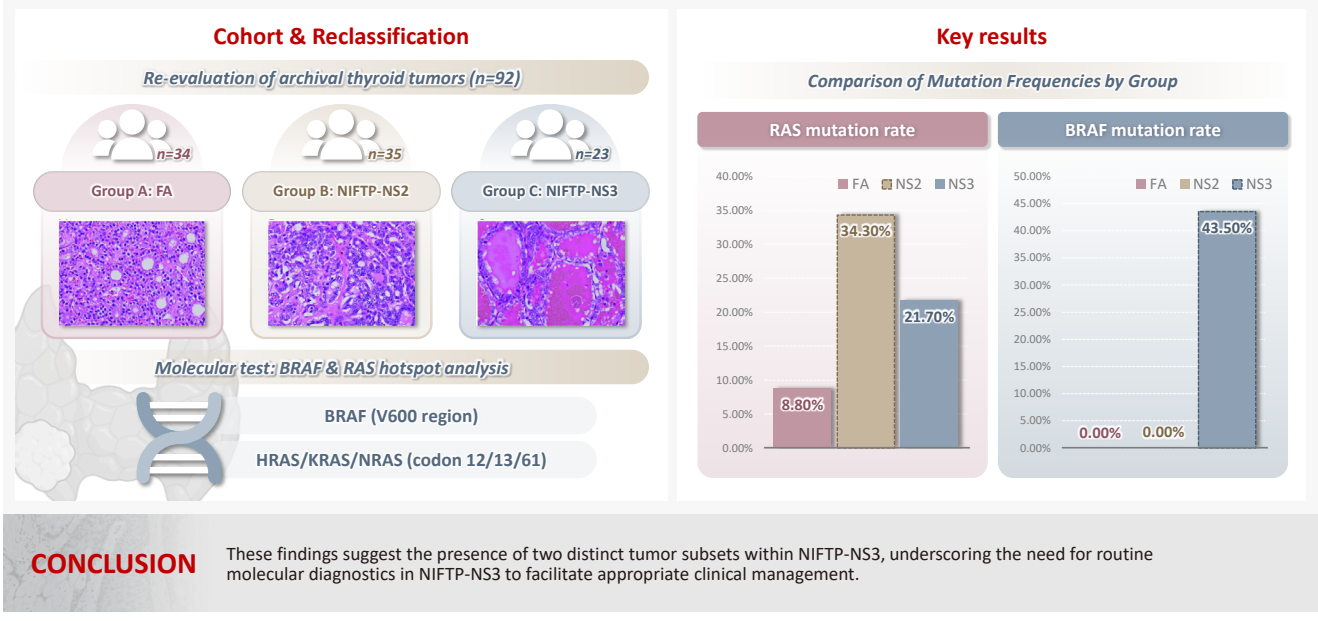

JPTM

ORIGINAL ARTICLE

pISSN 2383-7837 · eISSN 2383-7845

Journal of Pathology and Translational Medicine 2026; 60: 214-219
https://doi.org/10.4132/jptm.2025.12.06

Mutational status of non-invasive follicular thyroid neoplasm with papillary-like nuclear features (NIFTP): molecular analysis should be performed for NIFTPs with nuclear score 3

Ayaka Sako[1,2], Mitsuyoshi Hirokawa[3], Michiko Matsuse[1,4], Miyoko Higuchi[3], Akira Miyauchi[5], Takashi Akamizu[6], Atsushi Kawakami[2,7], Norisato Mitsutake[1,4]

[1]Department of Molecular Oncology, Atomic Bomb Disease Institute, Nagasaki University, Nagasaki, Japan
[2]Department of Endocrinology and Metabolism, Nagasaki University Hospital, Nagasaki, Japan
[3]Department of Diagnostic Pathology and Cytology, Kuma Hospital, Kobe, Japan
[4]Thyroid Cancer Collaborative Research Center, Nagasaki University, Nagasaki, Japan
[5]Department of Surgery, Kuma Hospital, Kobe, Japan
[6]Department of Internal Medicine, Kuma Hospital, Kobe, Japan
[7]Division of Advanced Preventive Medical Sciences, Department of Immunology and Rheumatology, Nagasaki University Graduate School of Biomedical Sciences, Nagasaki, Japan

Background: The classification of non-invasive follicular thyroid neoplasm with papillary-like nuclear features (NIFTP) was introduced to prevent the overtreatment of indolent tumors that were formerly diagnosed as non-invasive encapsulated follicular variant papillary thyroid carcinomas (NIEFV-PTCs). Although NIFTP was initially estimated to account for 10%–20% of papillary thyroid carcinomas in Western populations, its incidence is substantially lower in Asian cohorts. However, a multi-institutional Japanese study revealed that 31.0% of tumors previously diagnosed as follicular adenomas (FAs) were reclassified as NIFTPs. NIFTP diagnosis requires a nuclear score (NS) of 2–3, and according to the recent World Health Organization criteria, molecular analysis is recommended, but not mandatory, to exclude high-risk subtypes, namely cases with the *BRAF*^{V600E} mutation, particularly for NS3 tumors. **Methods:** We performed genetic analysis on 92 archival thyroid tumor samples, including 69 previously diagnosed as FA, of which 34 remained as FA upon re-evaluation (group A) and 35 were reclassified as NIFTP with NS2 (group B). Additional 23 tumors previously diagnosed as NIEFV-PTC were reclassified as NIFTP with NS3 (group C). **Results:** *RAS* mutations were detected in 8.8%, 34.3%, and 21.7% of the tumor samples in groups A, B, and C, respectively, whereas *BRAF* mutations were present in 43.5% of the tumor samples in group C only. **Conclusions:** These findings suggest the presence of two distinct tumor subsets within NIFTP-NS3, underscoring the need for routine molecular diagnostics in NIFTP-NS3 to facilitate appropriate clinical management.

Keywords: Thyroid neoplasms; NIFTP; Nuclear score; Oncogenes

INTRODUCTION

Non-invasive follicular thyroid neoplasm with papillary-like nuclear features (NIFTP) was introduced as a new classification in 2016 [1] and categorized as a borderline tumor in the 4th edition of the World Health Organization (WHO) classification [2]. These tumors were formerly classified as non-invasive encapsulated follicular variant of papillary thyroid carcinomas (NIEFV-PTCs); however, preventing overtreatment due to their indolent biological behavior was considered necessary. Therefore, the term "neoplasm" was adopted for NIFTP. Recently, NIFTP has been categorized as a low-risk neoplasm in the 5th

Received: October 14, 2025 **Revised:** December 1, 2025 **Accepted:** December 6, 2025
Corresponding Author: Norisato Mitsutake, MD, PhD
Department of Molecular Oncology, Atomic Bomb Disease Institute, Nagasaki University, 1-12-4 Sakamoto, Nagasaki 852-8523, Japan
Tel: +81-95-819-7116, Fax: +81-95-819-7117, E-mail: mitsu@nagasaki-u.ac.jp

edition of the WHO classification [3].

The diagnostic criteria for NIFTP have undergone slight changes. The original diagnostic criteria allowed for less than 1% papillae [1]. However, broader use of the "less than 1% papillae" criterion resulted in metastasis being observed in 4%–6% of tumors diagnosed as NIFTP [4]. According to the 5th edition of the WHO classification [3], the term "<1% true papillae" is used and defined as a fibrovascular core lined by cells with score 2–3 nuclei. In addition, the new criteria introduced not only changes to the morphological criteria but also recommendation for molecular analysis, although such testing is not mandatory [3]. The detection of the *BRAF*^{V600E} mutation by immunostaining or genotyping excludes the diagnosis.

The proportion of NIFTP among PTC cases has been reported to be approximately 10%–20% [5]; however, that in Asian countries has been reported to be considerably lower (0.8%) [6]. According to a multi-institutional study in Japan that assessed more than 4,000 nodules [7], 0.9% of tumors initially diagnosed as PTCs before the introduction of NIFTPs were reclassified as NIFTP. Notably, 31.0% of follicular adenomas (FAs) were recategorized as NIFTPs. This finding suggests that the introduction of NIFTP, which was originally intended to downgrade certain tumors from cancer to neoplasm, resulted in an upgrade in Japan.

The nuclear score (NS) is used to evaluate the nuclear features of PTC, ranging from 0 to 3, based on so-called papillary nuclear features such as grooves, pseudoinclusions, and clearing, and NS2–3 is required for the diagnosis of NIFTP. In the aforementioned Japanese multi-institutional study, most patients initially diagnosed with FA exhibited NS2 [7]. In other words, NIFTPs with NS2 had been diagnosed as PTC in Western countries, whereas they had been diagnosed as FA in Japan.

In the new criteria, molecular analysis or immunohistochemistry (IHC) is recommended to check for the *BRAF*^{V600E} mutation or other driver mutations (*RET* fusions, *TERT* promoter, or *TP53*) to exclude high-risk tumors, especially for NIFTPs with NS3 [4]. Therefore, tumors with these mutations should not be diagnosed as NIFTP. This is because a small proportion of NIFTPs were found to have metastases, and many harbored the *BRAF*^{V600E} mutation [4]. These findings highlight the importance of the differences between NS2 and NS3. This difference may reflect biologically distinct tumor characteristics. Comprehensive genomic and transcriptomic analyses conducted in the Cancer Genome Atlas study have revealed that PTCs can be classified into *BRAF*- and *RAS*-like tumors [8]. This distinction may also apply to tumors that fulfill the histological criteria for NIFTP. Therefore, in the present study, we conducted mutational analyses of *BRAF* and *RAS* to clarify the differences between these tumors.

MATERIALS AND METHODS

A total of 92 tumor samples that were resected at Kuma Hospital and matched the following three criteria (A–C) were used in this study. These patients were diagnosed with FA or NIEFV-PTC between 2017 and 2021 before the disease entity NIFTP was introduced into Japanese practice. (A) Thirty-four tumors with an original diagnosis of FA were still diagnosed as FA after re-evaluation. (B) Thirty-five tumors with an original diagnosis of FA were diagnosed as NIFTP after re-evaluation. (C) Twenty-three tumors with an original diagnosis of NIEFV-PTC were diagnosed as NIFTP after re-evaluation. The tumors in groups B and C had NS2 and NS3, respectively. Representative histological images are shown in Fig. 1. The re-diagnosis was made in accordance with the 5th edition of the WHO classification by a pathologist (MHiro) who specializes in thyroid pathology. Only tumors with unambiguous classifications were included. Uncertain malignant potential cases with questionable capsular invasion and/or tumors with NS between 1 and 2 were exclud-

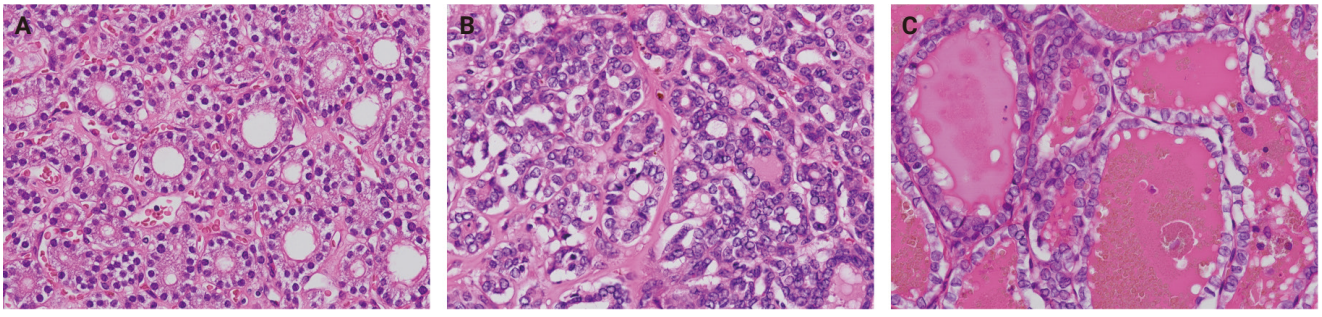

Fig. 1. Representative histopathological images are shown. (A) Group A. (B) Group B. (C) Group C.

ed. Note that we re-reviewed only slides that were preserved in the pathology department, and therefore all portions of each tumor were not examined. Patient demographics and tumor sizes are summarized in Table 1. It should be noted that these cases were intentionally selected and may therefore contain substantial selection bias.

DNA was extracted from formalin-fixed, paraffin-embedded (FFPE) sections using an AllPrep DNA/RNA FFPE kit (QIAGEN, Hilden, Germany). The mutational status of *BRAF* (around V600) and *HRAS*, *KRAS*, and *NRAS* (codons 12, 13, and 61) was analyzed by direct Sanger sequencing. First, polymerase chain reaction (PCR) was performed using KOD SYBR qPCR Mix (TOYOBO, Osaka, Japan), and the PCR product was treated with ExoSAP-IT Express (Thermo Fisher Scientific, Waltham, MA, USA). Sequencing analysis was performed using a BigDye Terminator sequencing kit v3.1 (Thermo Fisher Scientific) and an ABI3100 sequencer (Thermo Fisher Scientific). The primers used in this study are listed in Table 2.

For samples whose PCR amplification was not successful, droplet digital PCR (ddPCR) was performed. PrimePCR for ddPCR *NRAS* Q61 (#12001006), *KRAS* G12/G13 (#1863506), and *KRAS* Q61 (#12001626) Screening Kits (Bio-Rad, Hercules, CA, USA), ddPCR Mutation Assay *KRAS* p.Q61R (dHsaMDV2010135) and *HRAS* p.Q61R (dHsaMDV2510576) (Bio-Rad), a QX100 droplet generator (Bio-Rad), and a QX200 droplet reader (Bio-Rad) were used for the ddPCR analysis.

RESULTS

The frequencies of *RAS* mutations in groups A, B, and C were 8.8%, 34.3%, and 21.7%, respectively. In group A, two *NRAS* Q61R and one *HRAS* Q61R were detected. In group B (NIFTP-NS2), eight *NRAS* Q61R, two *HRAS* Q61R, one *KRAS* G12/13, and one *KRAS* Q61R were detected. In group C (NIFTP-NS3), two *NRAS* Q61R, two *HRAS* Q61R, and one *KRAS* Q61R were detected. The $BRAF^{V600E}$ mutation was found in eight cases in group C but not in group A or B. Additionally, a relatively rare *BRAF* mutation, c.1799_1801delTGA, resulting in p.V600_K601delinsE, was detected in two cases in group C. *BRAF* mutations were detected in 43.5% of the cases in group C. The summarized data are listed in Table 3. We assessed whether any morphological differences existed between *BRAF*- and *RAS*-mutated tumors in group 3, but none were identified.

Table 1. Summary of age, sex, and tumor size of groups A–C

	Group A (FA) (n = 34)	Group B (NIFTP-NS2) (n = 35)	Group C (NIFTP-NS3) (n = 23)
Age (yr), median (IQR)	51 (45–66)	50 (40–64)	64 (39–71)
Sex (male:female)	7:27	5:18	7:28
Tumor size (mm), median (IQR)	45.5 (36.3–54.3)	36.0 (26.0–47.0)	19.0 (16.0–27.0)

FA, follicular adenoma; NIFTP, non-invasive follicular thyroid neoplasm with papillary-like nuclear features; NS, nuclear score; IQR, interquartile range.

Table 2. Primer sequences

Primer ID	Primer sequence	Product size (bp)	Annealing temp (°C)
HRAS cod12 F2	5′-CCTGAGGAGCGATGACGGAA-3′	135	65
HRAS cod12 R2	5′-GCGCCAGGCTCACCTCTAT-3′		
pHRAS cod60 F	5′-GGAGACGTGCCTGTTGGACAT-3′	134	56
pHRAS cod60 R	5′-TGTCCTCAAAAGACTTGGTGTTGT-3′		
pKRAS cod12 F	5′-TGATAGTGTATTAACCTTATGTGTGACATGTT-3′	151	56
pKRAS cod12 R	5′-AATTAGCTGTATCGTCAAGGCACTC-3′		
pKRAS cod60 F	5′-GGTGCACTGTAATAATCCAGACTGTGT-3′	161	2-step
pKRAS cod60 R	5′-GCCCTCCCCAGTCCTCATG-3′		
NRAS ex2 F	5′-CTTGCTGGTGTGAAATGACTGAG-3′	187	65
NRAS cod12 R	5′-GGTAAAGATGATCCGACAAGTGAG-3′		
BRAF 146int14ex15F	5′-ACTACACCTCAGATATATTTCTTCATGA-3′	146	62
BRAF 146ex15int15R	5′-AGCCTCAATTCTTACCATCCACA-3′		

https://doi.org/10.4132/jptm.2025.12.06

Table 3. The frequencies of *RAS/BRAF* mutations in FA, NIFTP-NS2, and NIFTP-NS3

Mutation	Group A (FA) (n = 34)	Group B (NIFTP-NS2) (n = 35)	Group C (NIFTP-NS3) (n = 23)
RAS mutation			
NRAS Q61	2	8	2
HRAS Q61R	1	2	2
KRAS G12/13	0	1	0
KRAS Q61R	0	1	1
RAS total	3 (8.8)	12 (34.3)	5 (21.7)
BRAF mutation			
BRAF V600E	0	0	8
BRAF V600_K601delinsE	0	0	2
BRAF total	0	0	10 (43.5)

Values are presented as number (%).
FA, follicular adenoma; NIFTP, non-invasive follicular thyroid neoplasm with papillary-like nuclear features; NS, nuclear score.

DISCUSSION

The present study clearly showed that there are two pathogenetically distinct types of tumors in NIFTP-NS3. One was characterized by *RAS* mutations (i.e., *RAS*-like tumors), and the other by the $BRAF^{V600E}$ mutation (i.e., *BRAF*-like tumors). The characteristics of these tumors are entirely different. Given that the NIFTP category was originally established to downgrade the classification from cancer to neoplasm, the inability to make this distinction based solely on hematoxylin and eosin–stained slides seems to be a significant issue. The WHO recommends genetic testing, but it is not mandatory.

The frequency of *RAS* mutations in group A (FA) was 8.8%, which was lower than that in group B (NIFTP-NS2) (34.3%). According to previous reports, the frequencies of *RAS* mutations in FAs were 18% [9], 19.6% [10], and 30% [11], while those in NIFTPs were 29.6% [1], 54% [12], and 67% [13]. These findings suggest that NIFTPs exhibit a higher frequency of *RAS* mutations than FAs. One possible explanation is that NIFTP-NS2 is predominantly driven by *RAS* mutations, whereas FA may involve other driver events. Nevertheless, the presence of shared mutations also indicates a degree of molecular overlap between the two. Additionally, we selected cases with typical histological subtypes for each group, which may have contributed to the results.

No tumors in group B (NIFTP-NS2) harbored *BRAF* mutations, whereas 43.5% of the tumors in group C (NIFTP-NS3) did ($BRAF^{V600E}$: 34.8%); such tumors should not be classified as NIFTP. Therefore, an accurate diagnosis of NIFTP-NS3 requires confirmation of the *BRAF* mutational status. When molecular testing is not available, at minimum, IHC for RAS^{Q61R} and/or $BRAF^{V600E}$ should be considered. In this context, tumors that are histologically NIFTP-NS3 but harbor the *BRAF* mutation may be more appropriately referred to as "encapsulated classic PTC with predominant follicular architecture."

In this study, we detected a relatively rare *BRAF* mutation, p.V600_K601delinsE. Torregrossa et al. [14] reported that this mutation is the second most frequent rare mutation (except for V600E) occurring near V600, following K601E. One study reported its presence in aggressive histological subtypes [15], while the aforementioned study suggested that it is not highly aggressive. However, owing to the limited number of cases, its exact characteristics, including whether it should be classified as NIFTP, remain unclear.

Japanese pathologists have long maintained a diagnostic practice that differentiates between NIFTP-NS0–2 and NIFTP-NS3 rather than between NS0–1 and NS2–3. This perspective may have worked well in clinical practice, given that only HE-stained sections are available, and is also supported by molecular genetics. Therefore, the necessity of the NIFTP concept in Japan has been questioned in clinical practice. However, unification is essential in science for accurate communication and data comparison. If NIFTP is to be defined as a *RAS*-like tumor, genetic testing (or at least IHC) should be mandated for at least the NS3 cases. This also raises concerns regarding the current diagnostic categorization, which combines NIFTP-NS2 and NIFTP-NS3 under the same diagnosis of NIFTP. Attempts have been made to distinguish *BRAF*-like tumors from *RAS*-like tumors based on morphology [16,17], and such differentiation, if feasible, would greatly contribute to the clinical management of thyroid tumors. However, in our study, no morphological differences could be identified between *BRAF*-like and *RAS*-like tumors within group 3. In the future, studies should perhaps be conducted to investigate whether analyses of morphological features using, for example, artificial intelligence, can distinguish between *BRAF*-like and non-*BRAF*-like tumors.

$BRAF^{V600E}$ can also be detected by IHC using mutation-specific antibodies. Two meta-analyses evaluating the diagnostic accuracy of this approach reported sensitivities of 96.8% (95% confidence interval [CI], 94.1 to 98.3) and 100% (95% CI, 97 to 100), with specificities of 86.3% (95% CI, 80.7 to 90.4) and 84% (95% CI, 72 to 91), respectively [18,19]. Although the sensitiv-

ity was consistently high, the specificity was somewhat lower, and substantial inter-institutional heterogeneity was noted, suggesting that some caution is advisable in clinical applications. However, one study has reported very high sensitivity (99.3%) and 100% specificity, suggesting that optimization of the methodology may be crucial [20].

This study had several limitations. First, all the tissue samples were collected from a single institution, which introduced the possibility of sampling bias. Second, since the present study included only cases with typical histopathological features, some degree of selection bias cannot be ruled out. Third, genetic alterations other than those in *RAS* and *BRAF* hotspots were not evaluated. Fourth, not all *RAS* mutation variants may have been detected, particularly in samples with lower DNA quality.

In conclusion, NIFTP-NS3 contains tumors with at least two distinct characteristics, and we believe that molecular diagnostics are necessary. Otherwise, NS3 may require a different classification.

Ethics Statement

The study protocol was approved by the Institutional Review Boards of Kuma Hospital (#20231012-4, Oct 12, 2023) and Nagasaki University Graduate School of Biomedical Sciences (#20170502-14, Mar 17, 2025). The study was conducted in accordance with the ethical standards of the 1964 Declaration of Helsinki and its later amendments. Informed consent was obtained from all participants.

Availability of Data and Material

The datasets generated or analyzed during the study are available from the corresponding author on reasonable request.

Code Availability

Not applicable.

ORCID

Ayaka Sako https://orcid.org/0009-0005-2372-2449
Mitsuyoshi Hirokawa https://orcid.org/0000-0001-5558-7142
Michiko Matsuse https://orcid.org/0000-0001-6178-3342
Miyoko Higuchi https://orcid.org/0000-0001-8262-2652
Akira Miyauchi https://orcid.org/0000-0003-0041-197X
Takashi Akamizu https://orcid.org/0000-0003-4960-8271
Atsushi Kawakami https://orcid.org/0000-0002-1512-8782
Norisato Mitsutake https://orcid.org/0000-0002-2744-8046

Author Contributions

Conceptualization: MH (Mitsuyoshi Hirokawa), NM. Data curation: AS, MM. Formal analysis: AS, MM. Funding acquisition: MM, NM. Investigation: AS, MM. Methodology: AS, MM, NM. Project administration: MH (Mitsuyoshi Hirokawa), NM. Resources: MH (Mitsuyoshi Hirokawa), MH (Miyoko Higuchi), AM, TA. Supervision: AK, NM. Visualization: AS. Writing—original draft: AS, NM. Writing—review & editing: MH (Mitsuyoshi Hirokawa), NM. Approval of final manuscript: all authors.

Conflicts of Interest

The authors declare that they have no potential conflicts of interest.

Funding Statement

This study was supported in part by Grants-in-Aid for Scientific Research (JSPS KAKENHI) Grant Numbers 23H02860, 20KK0217, and 22K07668, the Program of the Network-Type Joint Usage/Research Center for Radiation Disaster Medical Science, and intramurally by the Atomic Bomb Disease Institute, Nagasaki University.

REFERENCES

1. Nikiforov YE, Seethala RR, Tallini G, et al. Nomenclature revision for encapsulated follicular variant of papillary thyroid carcinoma: a paradigm shift to reduce overtreatment of indolent tumors. JAMA Oncol 2016; 2: 1023-9.
2. Lloyd RV, Osamura RY, Kloppel G, Rosai J. WHO classification of tumours of endocrine organs. 4th ed. Vol. 10. Lyon: International Agency for Research on Cancer, 2017.
3. WHO Classification of Tumours Editorial Board. WHO classification of tumours, 5th edition. Endocrine and neuroendocrine tumours. Vol. 10. Lyon: International Agency for Research on Cancer, 2025.
4. Nikiforov YE, Baloch ZW, Hodak SP, et al. Change in diagnostic criteria for noninvasive follicular thyroid neoplasm with papillarylike nuclear features. JAMA Oncol 2018; 4: 1125-6.
5. Rana C, Vuong HG, Nguyen TQ, et al. The incidence of noninvasive follicular thyroid neoplasm with papillary-like nuclear features: a meta-analysis assessing worldwide impact of the reclassification. Thyroid 2021; 31: 1502-13.
6. Bychkov A, Hirokawa M, Jung CK, et al. Low rate of noninvasive follicular thyroid neoplasm with papillary-like nuclear features in Asian practice. Thyroid 2017; 27: 983-4.

https://doi.org/10.4132/jptm.2025.12.06

7. Hirokawa M, Ito M, Motoi N, et al. Prevalence and diagnostic significance of non-invasive follicular thyroid neoplasm with papillary-like nuclear features in Japan: a multi-institutional study. Pathol Int 2024; 74: 26-32.
8. Cancer Genome Atlas Research Network. Integrated genomic characterization of papillary thyroid carcinoma. Cell 2014; 159: 676-90.
9. Esapa CT, Johnson SJ, Kendall-Taylor P, Lennard TW, Harris PE. Prevalence of Ras mutations in thyroid neoplasia. Clin Endocrinol (Oxf) 1999; 50: 529-35.
10. Vasko V, Ferrand M, Di Cristofaro J, Carayon P, Henry JF, de Micco C. Specific pattern of RAS oncogene mutations in follicular thyroid tumors. J Clin Endocrinol Metab 2003; 88: 2745-52.
11. Fukahori M, Yoshida A, Hayashi H, et al. The associations between RAS mutations and clinical characteristics in follicular thyroid tumors: new insights from a single center and a large patient cohort. Thyroid 2012; 22: 683-9.
12. Zhao L, Dias-Santagata D, Sadow PM, Faquin WC. Cytological, molecular, and clinical features of noninvasive follicular thyroid neoplasm with papillary-like nuclear features versus invasive forms of follicular variant of papillary thyroid carcinoma. Cancer Cytopathol 2017; 125: 323-31.
13. Brandler TC, Liu CZ, Cho M, et al. Does noninvasive follicular thyroid neoplasm with papillary-like nuclear features (NIFTP) have a unique molecular profile? Am J Clin Pathol 2018; 150: 451-60.
14. Torregrossa L, Viola D, Sensi E, et al. Papillary thyroid carcinoma with rare exon 15 BRAF mutation has indolent behavior: a single-institution experience. J Clin Endocrinol Metab 2016; 101: 4413-20.
15. Barollo S, Pezzani R, Cristiani A, et al. Prevalence, tumorigenic role, and biochemical implications of rare BRAF alterations. Thyroid 2014; 24: 809-19.
16. Jung CK, Bychkov A, Song DE, et al. Molecular correlates and nuclear features of encapsulated follicular-patterned thyroid neoplasms. Endocrinol Metab (Seoul) 2021; 36: 123-33.
17. Kim C, Agarwal S, Bychkov A, et al. Differentiating BRAF V600E- and RAS-like alterations in encapsulated follicular patterned tumors through histologic features: a validation study. Virchows Arch 2024; 484: 645-56.
18. Singarayer R, Mete O, Perrier L, et al. A systematic review and meta-analysis of the diagnostic performance of BRAF V600E immunohistochemistry in thyroid histopathology. Endocr Pathol 2019; 30: 201-18.
19. Parker KG, White MG, Cipriani NA. Comparison of molecular methods and BRAF immunohistochemistry (VE1 clone) for the detection of BRAF V600E mutation in papillary thyroid carcinoma: a meta-analysis. Head Neck Pathol 2020; 14: 1067-79.
20. Choden S, Keelawat S, Jung CK, Bychkov A. VE1 immunohistochemistry improves the limit of genotyping for detecting BRAFV600E mutation in papillary thyroid cancer. Cancers (Basel) 2020; 12: 596.

JPTM

ORIGINAL ARTICLE

pISSN 2383-7837 · eISSN 2383-7845

Journal of Pathology and Translational Medicine 2026; 60: 220-230
https://doi.org/10.4132/jptm.2025.12.15

Deep learning–driven immunohistochemical analysis of renal lymphatics for chronic kidney disease: bioinformatic and histopathological study

Xin Xu[1], YanPing Lin[1], Guangchang Pei[1], Rui Zeng[1,2,3,4], Gang Xu[1,2,3,4]

[1]Division of Nephrology, Tongji Hospital, Tongji Medical College, Huazhong University of Science and Technology, Wuhan, China
[2]Key Laboratory of Organ Transplantation, Ministry of Education, Chinese Academy of Medical Sciences, Wuhan, China
[3]NHC Key Laboratory of Organ Transplantation, Chinese Academy of Medical Sciences, Wuhan, China
[4]Key Laboratory of Organ Transplantation, Chinese Academy of Medical Sciences, Wuhan, China

Graphical abstract

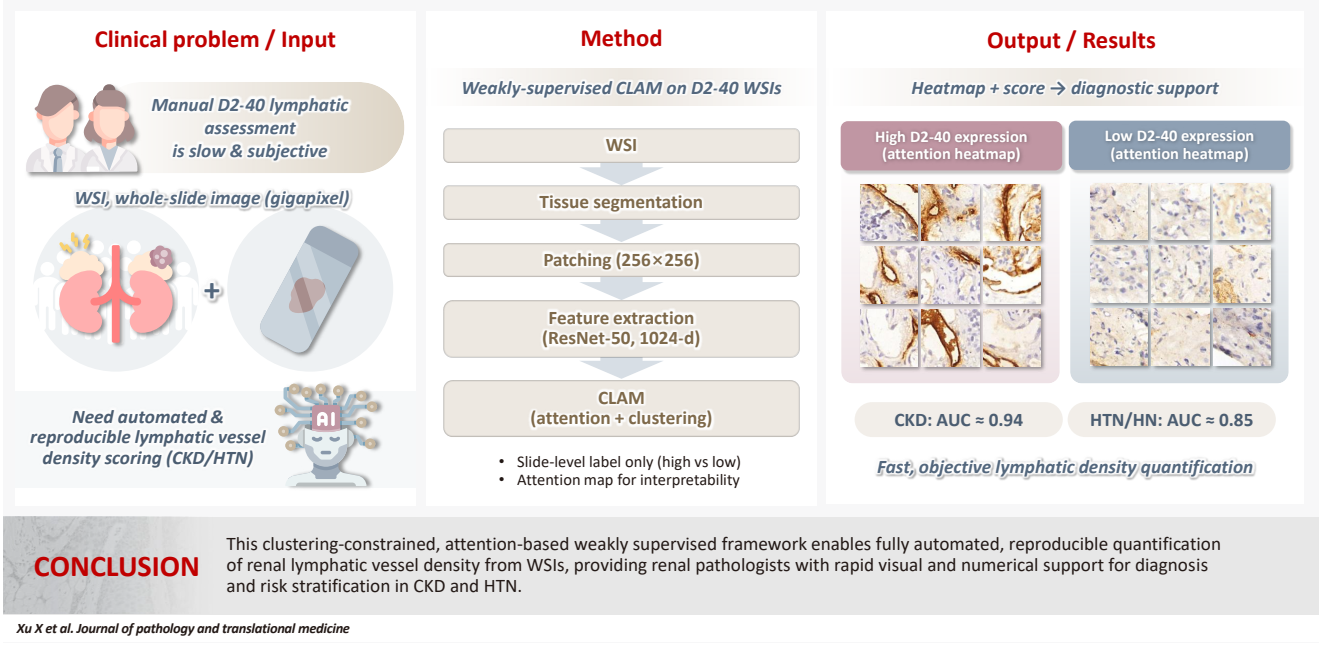

JPTM

ORIGINAL ARTICLE

pISSN 2383-7837 · eISSN 2383-7845

Journal of Pathology and Translational Medicine 2026; 60: 220-230
https://doi.org/10.4132/jptm.2025.12.15

Deep learning–driven immunohistochemical analysis of renal lymphatics for chronic kidney disease: bioinformatic and histopathological study

Xin Xu[1], YanPing Lin[1], Guangchang Pei[1], Rui Zeng[1,2,3,4], Gang Xu[1,2,3,4]

[1]Division of Nephrology, Tongji Hospital, Tongji Medical College, Huazhong University of Science and Technology, Wuhan, China
[2]Key Laboratory of Organ Transplantation, Ministry of Education, Chinese Academy of Medical Sciences, Wuhan, China
[3]NHC Key Laboratory of Organ Transplantation, Chinese Academy of Medical Sciences, Wuhan, China
[4]Key Laboratory of Organ Transplantation, Chinese Academy of Medical Sciences, Wuhan, China

Background: Renal lymphatic vessel density is clinically relevant in kidney disease but is still assessed by slow, subjective visual estimation. We evaluated a weakly supervised, attention-based multiple-instance learning framework for automated detection and quantification of renal lymphatic vessel density on D2-40-stained whole-slide images (WSIs). **Methods:** Two independent internal datasets from Tongji Hospital were collected, including 198 cases of chronic kidney disease (CKD) and 50 cases of hypertensive nephropathy (HTN). All biopsies were immunohistochemically stained for D2-40 and digitized as WSIs. Pathologists provided only slide-level labels (D2-40 high vs. D2-40 low). Tissue regions were automatically segmented, tiled into patches, and encoded using a pretrained convolutional neural network. Patch embeddings were then analyzed with a clustering-constrained attention multiple-instance learning (CLAM) model. Unlike conventional multiple-instance learning (MIL) methods that only weight instances, CLAM jointly performs attention-based instance selection and instance-level clustering to distinguish positive from negative evidence within each slide, yielding more discriminative slide-level features and interpretable attention maps. Performance was compared with a classic MIL model trained on the same features. **Results:** CLAM achieved area under the receiver operating characteristic curves of 0.942 and 0.858 on the CKD and HTN datasets, respectively, outperforming classic MIL (0.866 and 0.801). Attention maps highlighted lymphatic-rich regions consistent with renal pathologists' assessments. **Conclusions:** This clustering-constrained, attention-based weakly supervised framework enables fully automated, reproducible quantification of renal lymphatic vessel density from WSIs, providing renal pathologists with rapid visual and numerical support for diagnosis and risk stratification in CKD and HTN.

Keywords: Deep-learning; Pathology; Kidney; Lymphatic vessels

INTRODUCTION

Artificial intelligence is increasingly used in medical image classification [1], bringing clear benefits to clinical care [2,3]. In this context, digital pathology is transforming traditional pathology workflows [4,5]. Histopathological images—long considered the diagnostic gold standard, especially in oncology [6]—are typically examined manually by pathologists on

Received: October 30, 2025 **Revised:** December 4, 2025 **Accepted:** December 15, 2025
Corresponding Author: Gang Xu, MD, PhD
Division of Nephrology, Department of Internal Medicine, Tongji Hospital, Tongji Medical College, Huazhong University of Science and Technology, 1095# Jiefang Ave., Wuhan 430030, China
Tel: +86-27-8366-8406, Fax: +86-27-8366-8406, E-mail: xugang@tjh.tjmu.edu.cn

Rui Zeng, MD, PhD
Division of Nephrology, Department of Internal Medicine, Tongji Hospital, Tongji Medical College, Huazhong University of Science and Technology, 1095# Jiefang Ave., Wuhan 430030, China
Tel: +86-27-8366-8406, Fax: +86-27-8366-8406, E-mail: zengrui@tjh.tjmu.edu.cn

hematoxylin and eosin (H&E), periodic acid–Schiff, and Masson-stained slides, a process that is highly time-consuming, labor-intensive, and dependent on extensive expert training [6].

Whole-slide scanning converts tissue on glass slides into high-resolution digital whole-slide images (WSIs), which are now widely used for diagnosis in clinical practice. Because disease-positive regions often occupy only a small fraction of the tissue, WSIs contain a large number of disease-negative patches, and their typical gigapixel resolution (e.g., 30,000 × 30,000) makes direct analysis challenging. To address this issue, recent work has focused on multi-level attention-based frameworks that aim to solve clinical problems using substantially fewer annotations. Notably, seminal multiple-instance learning (MIL)–based approaches—including iterative MIL, task-specific multi-level MIL, and deep hierarchical MIL—as well as techniques such as digital pathology image deblurring, have substantially advanced WSI preprocessing and downstream model performance [7-12].

Through a series of advanced processes, including image auto-detection, annotation, segmentation, training, and evaluation, it progressively extracts features from the input images. This technology transforms imaging information into structured data, ultimately yielding valuable diagnostic insights [13]. Such innovations markedly reduce the workload for pathologists and enhance the efficiency of clinical practice, enabling more timely and accurate diagnoses [14].

Lymphatic vessels serve as a crucial conduit between adaptive immunity and renal pathology [15,16]. An expanding body of research has confirmed close associations between lymphatic vessels and multiple organ systems, including the central nervous system and the cardiovascular system [17–19]. Similarly, renal lymphatic vessel density is linked to a variety of kidney diseases [15]. For example, increased renal lymphatic density in IgA nephropathy is closely associated with poor prognosis [20]. Our group has also shown correlations between renal lymphatics and IgA nephropathy, membranous nephropathy, and lupus nephritis, and found that lymphatic expansion increases the risk of adverse outcomes such as crescentic glomerulonephritis [15,16].

This study integrates computer vision with weakly supervised learning to analyze renal immunohistochemical WSIs: two independent internal cohorts were collected, all slides were stained for the lymphatic marker D2-40 and digitized, and pathologists provided slide-level annotations classifying WSIs as D2-40 high or D2-40 low; an open-source WSI pipeline automatically segmented tissue and extracted patches, which were passed through a pre-trained convolutional neural network (CNN) to obtain feature vectors that were then fed into an attention-based model, and finally the clustering-constrained attention multiple-instance learning (CLAM) algorithm aggregated local patch information into a global slide representation to distinguish slides with high versus low D2-40 expression.

MATERIALS AND METHODS

Renal biopsy specimens

This study complied with the Declaration of Helsinki and was approved by the Clinical Research Ethics Committee of Huazhong University of Science and Technology (TJ-IRB202303121); all human kidney biopsy specimens were obtained from hospitalized patients in the nephrology department of Tongji Hospital with written informed consent. The cohort comprised 320 chronic kidney disease (CKD) patients and 122 hypertensive nephropathy patients. The inclusion and screening flow of the cohort is shown in Fig. 1.

Immunohistochemistry

Paraffin sections were baked at 60°C for 1 hour, dewaxed through graded xylene/ethanol immersions, and subjected to microwave-mediated antigen retrieval. Endogenous peroxidase was blocked with H_2O_2, followed by serum blocking. Slides were incubated with D2-40 antibodies, then treated with secondaries. Imaging employed an Olympus DP73 microscope (Tokyo, Japan); digitization utilized a 3DHistech Pannoramic SCAN platform (3DHISTECH Ltd., Budapest, Hungary).

Manual annotation

Three pathology experts independently reviewed and annotated all stained slides. A diagnosis was accepted as ground truth when at least two pathologists agreed. WSIs were labeled as high or low renal lymphatic expression based on D2-40 staining.

WSIs preprocess

Segmentation

WSIs were downsampled by 32× and converted from RGB to HSV. Tissue masks were generated using saturation thresholds, refined with median blur and morphological closing. Slides with failed segmentation were excluded, removing 122 slides from dataset 1 and 72 from dataset 2.

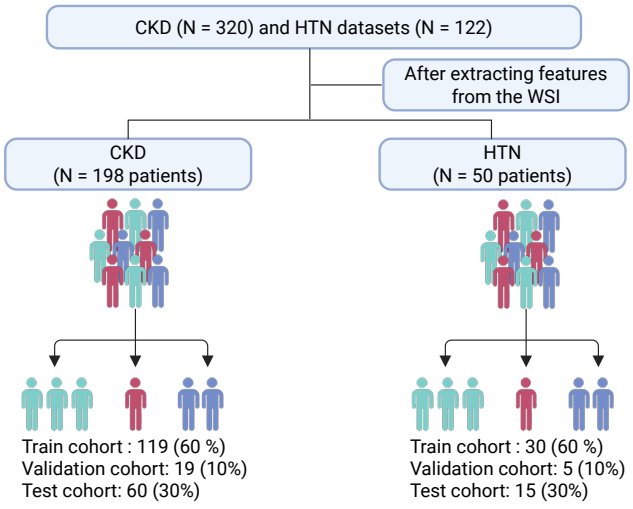

Fig. 1. The inclusion and screening flow of the cohort. CKD, chronic kidney disease; HTN, hypertensive nephropathy; WSI, whole slide image.

Patching and feature extracting

From each tissue mask, 256 × 256 pixel patches were extracted and stored with coordinates and metadata in .h5 files. We used a ResNet-50 pretrained on ImageNet to extract image features during training. Patch size and stride were 256 × 256 and 256, respectively. Each patch was converted into a 1,024-dimensional feature vector. Training was performed on a single consumer-grade GPU with a batch size of 8 (Fig. 2).

Deep-learning algorithm

We trained a CLAM framework on slide-level labels and, for comparison, a classical MIL model on the same data. During training, patches were randomly sampled with a batch size of 512. For validation and testing, per-patch predictions within each slide were computed and averaged to obtain slide-level scores. Performance was evaluated every 100,000 patches; early stopping was triggered after 20 epochs without improvement in validation loss. The checkpoint with the lowest validation loss was used for test evaluation for both CLAM and MIL. We utilized the cross-entropy loss function and optimized model parameters using stochastic gradient descent with the Adam optimizer, setting the learning rate at 2×10^{-4} and a weight decay of 1×10^{-5}. The hyperparameters were configured as follows: $\beta 1 = 0.9$, $\beta 2 = 0.999$, and $\varepsilon = 1 \times 10^{-8}$. All models were trained for a minimum of 50 epochs, with the potential to extend training up to 200 epochs if the early stopping criterion was not met. The validation loss was continuously monitored, and early stopping was triggered if no decrease was observed from a previous low for more than 20 consecutive epochs.

Computational hardware and software

Segmentation and stitching ran on an Intel i9-13900K CPU; feature extraction and model training used a single NVIDIA RTX 4090 GPU with batch parallelization and SSD-backed streaming. The pipeline was implemented in Python 3.10 using OpenSlide 3.4.1, OpenCV 4.9.0.8, and Pillow 10.3.0. Deep learning models were implemented in PyTorch (CUDA 12.1). Visualizations used matplotlib 3.8.4 and seaborn 0.13.2. The complete processing pipeline for WSIs, alongside the training and evaluation of deep learning models, is accessible at https://github.com/mahmoodlab/CLAM.

Interpretability and visualization

Model performance was assessed by area under the receiver operating characteristic (ROC) curve (AUC) and average classification error. Principal component analysis (PCA) was applied to patch-level features to visualize separation between D2-40 high and low WSIs. Data efficiency was examined using 25%, 50%, 75%, and 100% subsets. To illustrate discriminative regions, attention-derived heatmaps were generated to map lymphatic-rich areas across high and low D2-40 expression slides.

Statistical analysis

The AUC of the receiver-operating-characteristic curve was estimated using the Mann-Whitney U statistic, for which the algorithmic implementation is provided in the scikit-learn scientific computing library. For comparisons of multiple AUCs, we used the nonparametric Friedman test.

RESULTS

Model performance

To evaluate the CLAM algorithm with different attention branches, we trained models using a single attention branch (CLAM_SB) and multiple attention branches (CLAM_MB). On a WSI dataset of CKD, CLAM_MB achieved an AUC of 0.942 (0.913–0.971) (Fig. 3D), while CLAM_SB reached an AUC of 0.927 (0.887–0.968); the classic MIL method obtained an AUC of 0.866 (0.819–0.914). Although CLAM_MB yielded the highest AUC, CLAM_SB produced better sensitivity and specificity across datasets (Fig. 3A–C, F) and a lower balanced

https://doi.org/10.4132/jptm.2025.12.15

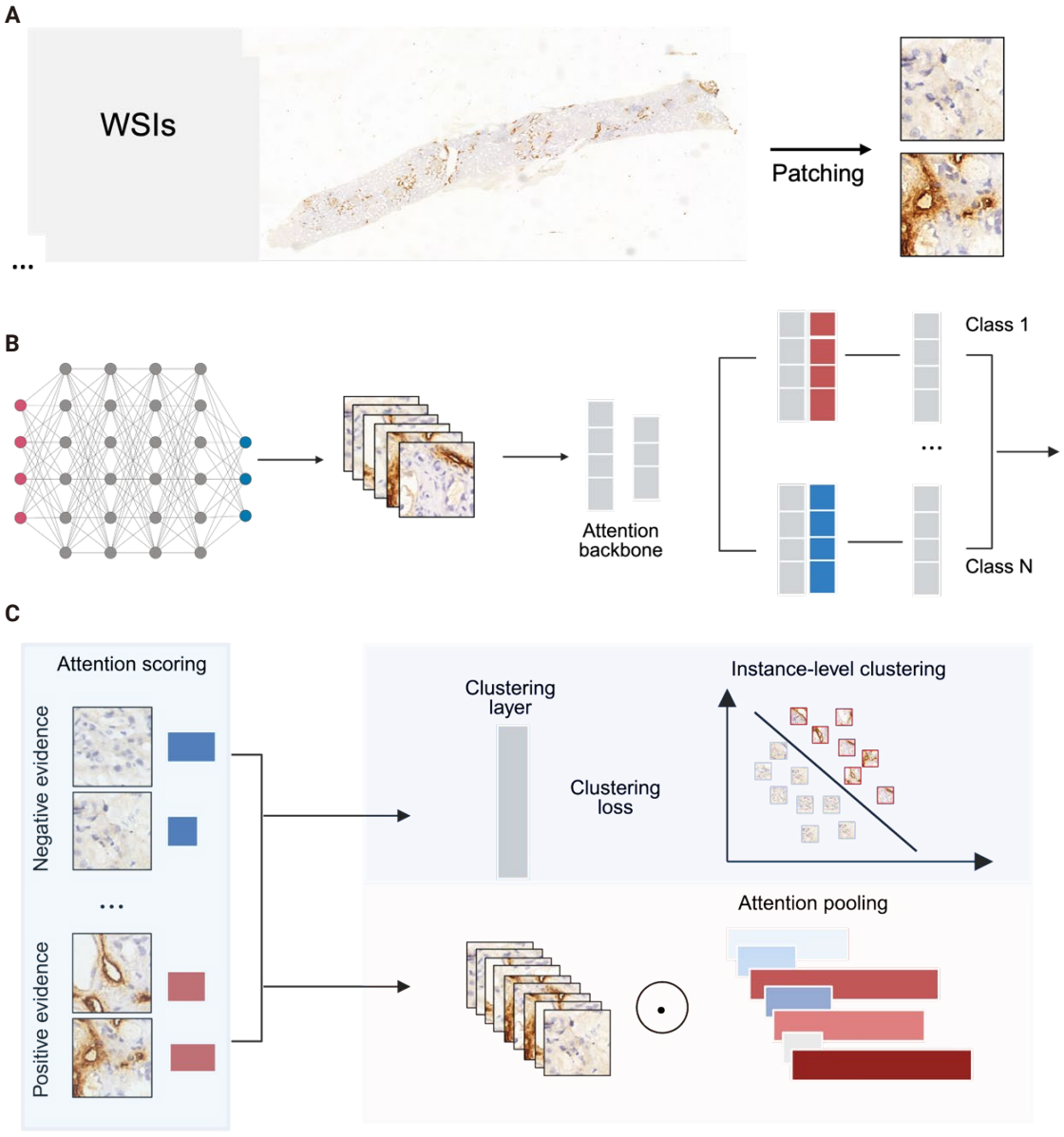

Fig. 2. Workflows for recognizing renal lymphatic vessel immunohistochemical whole slide images (WSIs) using deep learning methods. (A) Immunohistochemical WSIs marked with D2-40 undergo WSI image preprocessing through automatic patching. (B) The extracted patches are processed using a pre-trained convolutional neural network (CNN) to extract feature information. Each feature vector from the patches is then fed into an attention-based model for training and inference, ultimately separating positive and negative instances based on the attention scores. (C) The CLAM algorithm aggregates local information from the slide-level labels into an overall representation, distinguishing between kidney sections with high D2-40 expression (dark, top right) and low D2-40 expression (light, bottom left). Finally, the attention scores can be visualized as a heat map (right). CLAM, clustering-constrained attention multiple-instance learning.

error (Fig. 3E) compared with both CLAM_MB and MIL (Fig. 3F). We also compared the performance of two additional attention-mechanism variants—dual-stream MIL (DSMIL) and Transformer MIL (TransMIL)—on the CKD dataset. Their AUCs were 0.769 (0.620–0.918) and 0.843 (0.667–1.000), respectively, and both showed higher balanced error than CLAM (Fig. 3G, H).

To assess the effect of data volume on performance, we compared the CLAM model trained with 50 (25%), 99 (50%), 148 (75%), and 198 (100%) cases. The model exceeded an AUC of

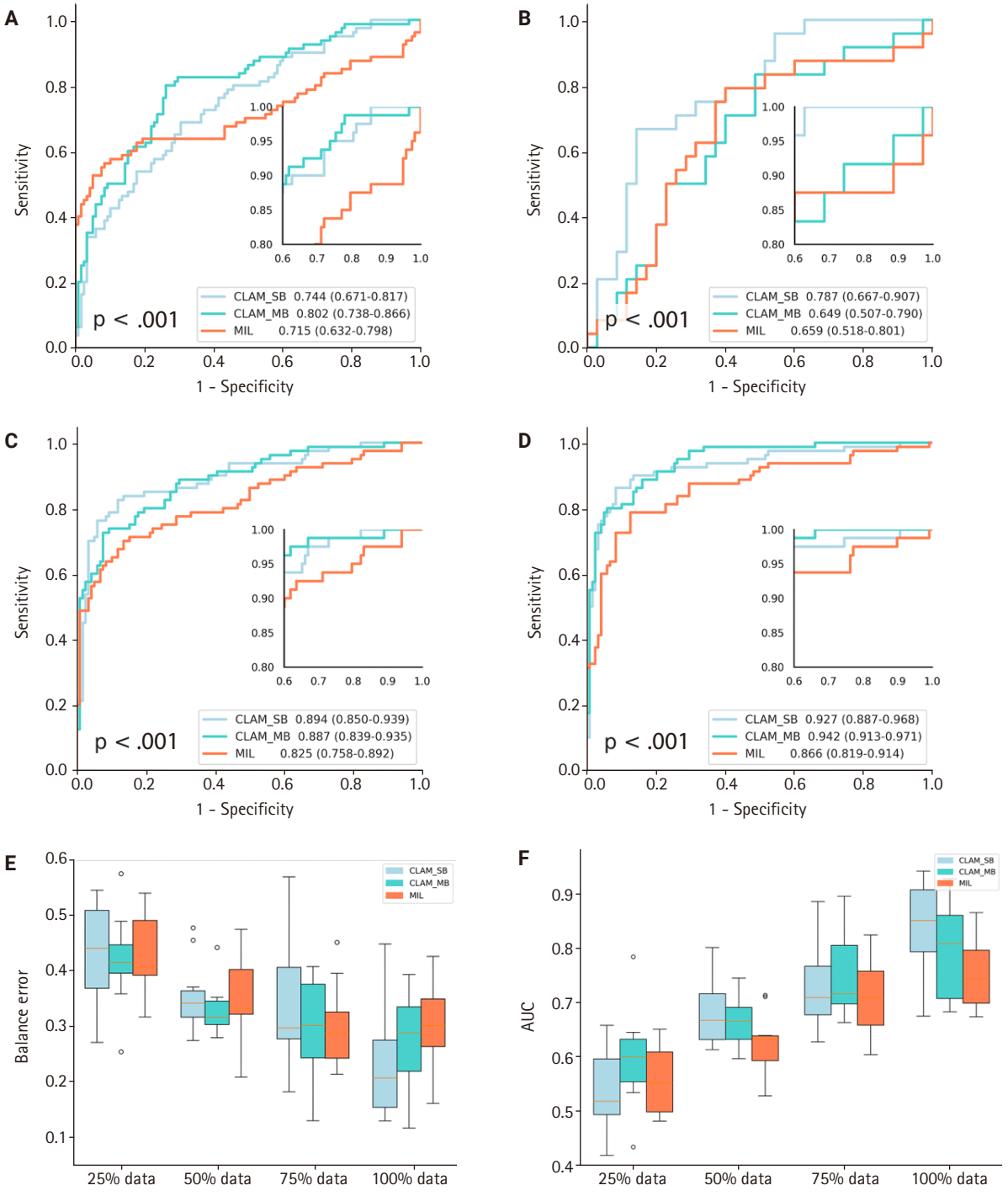

Fig. 3. Model performance analysis on dataset of chronic kidney disease (CKD). (A–D) The chronic kidney disease dataset is stratified into 25%, 50%, 75%, and 100% proportions, then the performances of the CLAM_SB, CLAM_MB, and MIL algorithms are compared sequentially. (E, F) The boxplot shows area under the receiver operating characteristic curve differences among the three algorithms across varying data amounts, and their performance is additionally compared in terms of balanced error. (G, H) Comparison of the performance of five models—CLAM_SB, CLAM_MB, MIL, DSMIL, and TransMIL—on the CKD dataset. CLAM_SB, clustering-constrained-attention multiple-instance single branch; CLAM_MB, clustering-constrained-attention multiple-instance multiple attention branches; MIL, multiple-instance learning; DSMIL, dual-stream MIL; TransMIL, transformer MIL. (Continued to next page)

https://doi.org/10.4132/jptm.2025.12.15

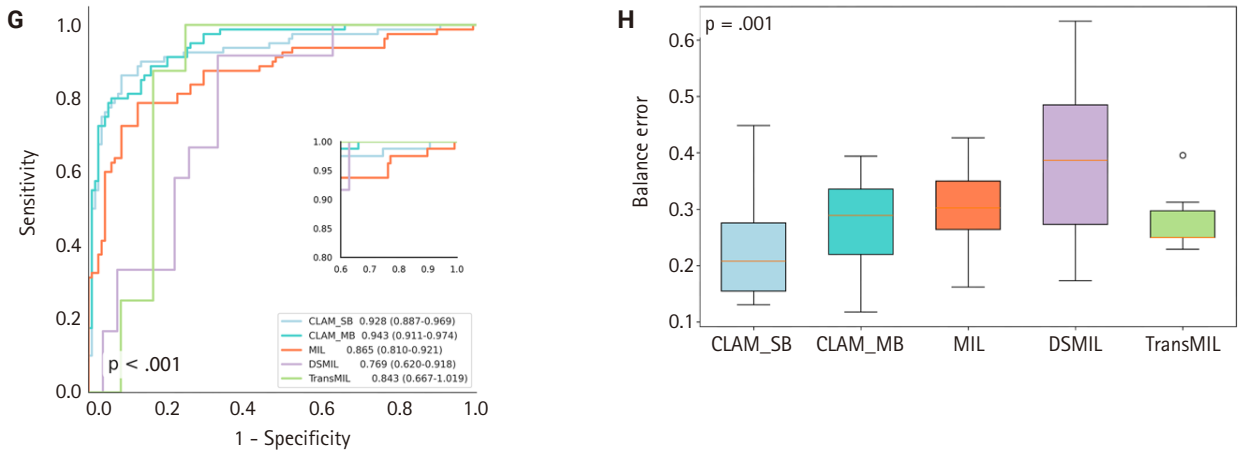

Fig. 3. (Continued from previous page)

90% on the CKD dataset only when trained with the full dataset (198 cases) (Supplementary Fig. S1). PCA visualization showed that after using more than 75% of the data (148 cases), classification of high-expression and low-expression D2-40 WSIs reached saturation, with no appreciable difference in category separation between the 75% and 100% training sets.

Model generalization

To evaluate generalization across datasets, we collected an independent set of hypertensive nephropathy WSIs stained with the lymphatic marker D2-40 and scanned at pixel resolution. The CLAM algorithm showed comparable discriminative performance on this hypertensive nephropathy cohort, achieving an AUC of 0.854 (0.742–0.965) (Fig. 4C) and a low balanced error of ~0.22 (Fig. 4D), regardless of whether CLAM_SB or CLAM_MB was used. When comparing models trained with 75% versus 100% of the data, CLAM_SB had an AUC of 0.690 (0.547–0.837), lower than CLAM_MB which reached 0.734 (0.593–0.875) at 75% (Fig. 4A, B); however, CLAM_SB outperformed CLAM_MB when trained on the full dataset, a difference that may reflect the small sample size. Overall, the weakly supervised CLAM algorithm demonstrated strong generalization across model variants. In contrast, the MIL model yielded an AUC of 0.801 (0.680–0.922) with a balanced error near 0.3. Because of sample-size constraints, PCA visualization was generated only for the 75% and 100% scenarios (Supplementary Fig. S2); notably, CLAM maintained robust discrimination even with as few as 50 cases.

Interpretation and visualization

Clinical pathologists base their diagnoses on staining patterns and cellular morphology observed under high magnification. To clarify how our deep learning model differentiates pathological slides, we incorporated an attention mechanism. Patches with high attention scores from CLAM were converted into percentages to create a normalized focus map that was mapped back to the original WSI coordinates, corresponding to high D2-40 expression regions, while low-attention areas corresponded to low D2-40 expression. This spatial attention map closely matched assessments made by simulated renal pathologists. From the automatically segmented D2-40 high and D2-40 low WSI labels, we selected nine high-magnification views for comparison: the nine high-attention patches showed markedly more prominent and darker lymphatic structures and staining than the low-attention patches (Fig. 5). To further demonstrate discriminative performance for the binary task, we overlaid heat maps to highlight color-coded regions; these heat maps offer supplementary diagnostic information that can aid pathologists' interpretation.

DISCUSSION

This study employed a weakly supervised learning algorithm to identify renal lymphatic vessel density in a CKD dataset and found that this deep learning approach outperformed traditional MIL algorithms as well as MIL variants DSMIL and TransMIL in terms of model performance. It offers a potential alternative to the current inefficient and subjective manual an-

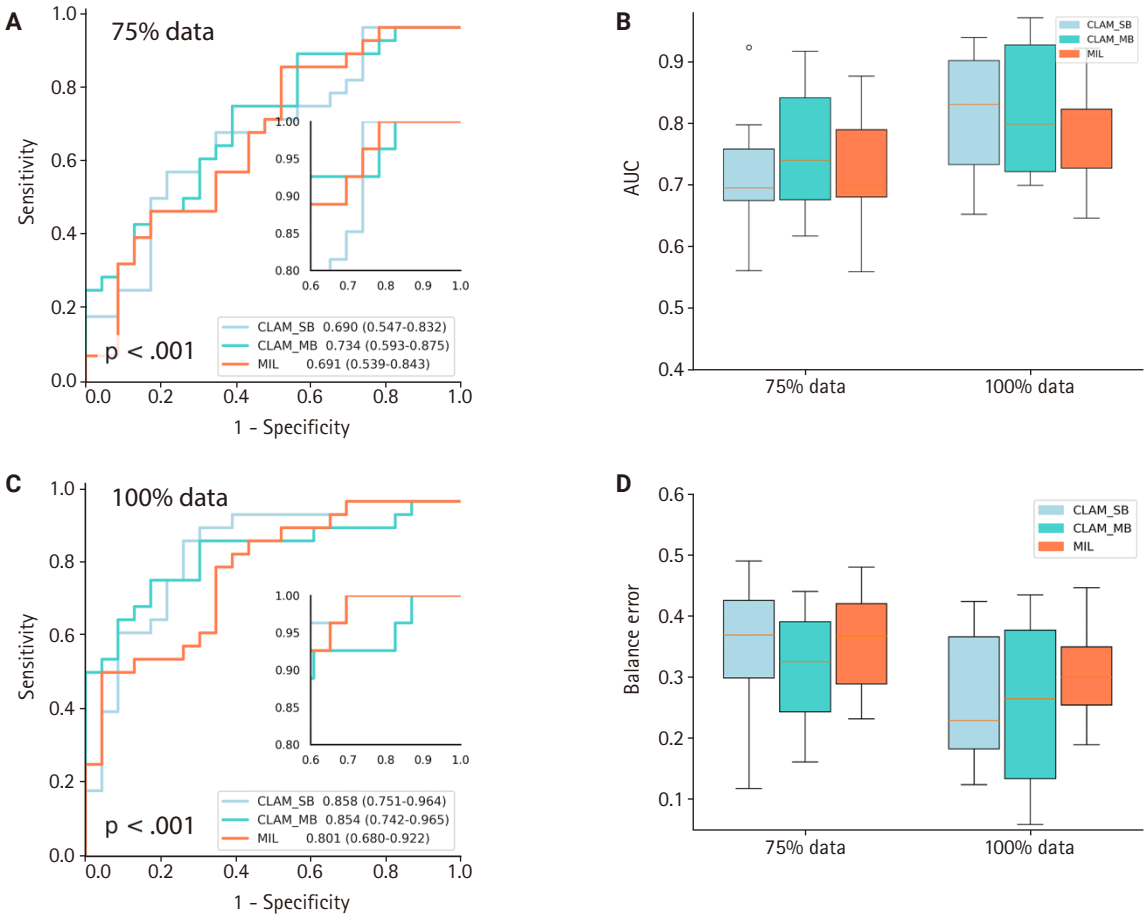

Fig. 4. Model generalization analysis on dataset of hypertensive nephropathy (HTN). (A, C) Three algorithms were compared for their generalization ability on HTN datasets at 75% and 100%. (B) The boxplot displays the differences in area under the receiver operating characteristic curve (AUC) among the three algorithms with 75% and 100 % data of HTN. (D) The performance of the three algorithms is compared from the perspective of balanced error. CLAM_SB, clustering-constrained-attention multiple-instance single branch; CLAM_MB, clustering-constrained-attention multiple-instance multiple attention branches; MIL, multiple-instance learning.

notation of pathology slides.

Since the introduction of large language models like ChatGPT in 2022 [17], a new era of artificial intelligence in computational pathology has begun. Open-source WSI-based pathology models such as cPath, TriPath, and Prov-GigaPath have sped up progress and reduced the need for manual annotations [18-21]. However, these models are mainly trained on H&E-stained tumor slide databases (e.g., TCGA, CAMELYON16/17) [22-24]. In renal pathology, most cases are non-tumor CKDs—such as IgA nephropathy, membranous nephropathy, and hypertensive nephropathy—and their diagnosis still depends on detailed pathological evaluation.

Lymphatic vessels serve as key immune conduits in kidney disease. Our 2019 study showed that renal injury triggers lymphatic endothelial cells to secrete CCL21 (C–C motif chemokine ligand 21), recruiting CCR7+ (C–C chemokine receptor type 7–positive) dendritic cells from renal lymph nodes. These dendritic cells activate lymph node–resident immune cells that return to the kidney via lymphatics, exacerbating inflammation and fibrosis [15]. Lopez Gelston et al. [25] further demonstrated that renal lymphatic expansion in hypertension promotes sodium and water excretion, reducing blood pressure. These findings highlight the dual roles of lymphatic vessels in immune signaling and fluid homeostasis in renal pathophysiology. Between 2020 and 2021, several studies elucidated key functions of renal lymphatic vessels in disease pathogenesis [26,27]. Increased renal lymphatic vessel density serves as an immune sentinel and is closely associated with fibrosis and inflamma-

https://doi.org/10.4132/jptm.2025.12.15

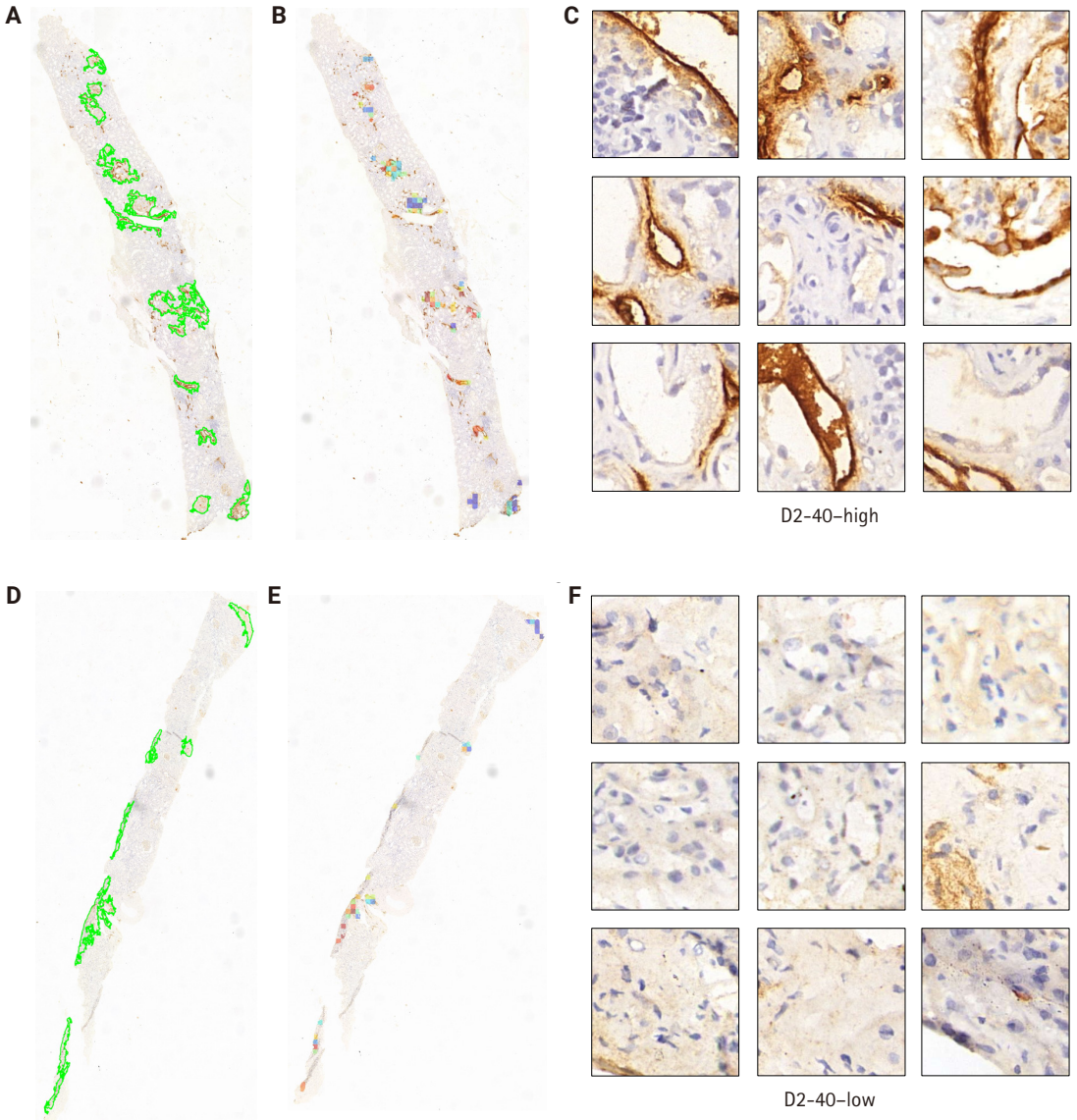

Fig. 5. Model of interpretability and visualization. (A, D) Automated segmentation of regions was performed for each slice. (B, E) Region of interest heatmaps were generated within the automatically segmented areas based on predicted attention scores. (C, F) Morphology of cells with high expression of D2-40 and low expression of D2-40 were predicted.

tion. Recent investigations show that lymphangiogenesis regulates blood pressure in salt-sensitive hypertension by promoting renal sodium excretion [28]. Enhanced lymphatic vessel formation accelerates sodium ion excretion, thereby lowering blood pressure [29]. Therefore, renal lymphatic vessel expression is clinically important for diagnosing and treating CKD.

In routine practice, pathologists select several fields for immunostaining rather than reviewing every high-magnification field, introducing subjectivity. To reduce bias and workload, we integrated machine learning with pathology using a CNN with attention scoring to predict pixel-level signals on WSIs. We applied the Mahmood lab's CLAM algorithm to an internal CKD dataset for the first time [30]. This high-throughput, interpretable method classifies WSIs with slide-level labels, avoiding region of interest extraction and patch annotations [31,32]. CLAM achieved an ROC of 0.99 on H&E renal tumor slides and supports binary and multiclass tasks with ROCs above 0.95 [33]. On CKD datasets, CLAM performed with ROC values near 0.95 and consistently outperformed classical MIL methods across different data sizes [33-36]. Similar advantages were ob-

served in an internal hypertensive nephropathy dataset. Overall, CLAM generalizes well across datasets with different distributions and sample sizes, demonstrating successful integration of deep learning with CKD research.

Although our CKD slides are limited, studying renal lymphatic vessels is important. Our dataset can serve as an internal resource to boost future large-scale models for lymphatic analysis in kidney disease. Clinically, lymphatic vessel expression is still scored manually; integrating our model into workflows could aid pathologists and save resources. This workflow can be broadly divided into the following components: First, we can label and scan patients' renal lymphatic-stained slides. Next, import the WSI pixel data into an image-analysis pipeline built on a pretrained model to perform patching, feature extraction, semantic segmentation, attention scoring, and visualization with heatmaps on renal biopsy specimens. Finally, the system provides lymphatic vessel count grading and risk stratification. This approach not only reduces patients' waiting time for results but also assists experienced pathologists in analyzing more challenging images.

However, this work still has certain limitations. For example, the WSI data come from a single center and there is staining variability between slides; finally, the determination of lymphatic vessel counts involves a degree of subjectivity.

In summary, this study applied a weakly supervised learning algorithm to a CKD dataset to quantify renal lymphatic vessel density, yielding a tool that can support clinical diagnosis and risk stratification in kidney disease.

Supplementary Information
The Data Supplement is available with this article at https://doi.org/10.4132/jptm.2025.12.15.

Ethics Statement
This research was conducted in accordance with the principles outlined in the Declaration of Helsinki. The use of all human tissue samples received approval from the Clinical Research Ethics Committee of Huazhong University of Science and Technology (TJ-IRB202303121). Human kidney biopsy specimens were obtained from hospitalized patients in the nephrology department of Tongji Hospital, with the informed consent of the patients secured through signed consent forms.

Availability of Data and Material
All the information required to assess the conclusions of this paper can be found within the paper itself and the Supplementary Materials. Any further data related to this study can be obtained by contacting the authors.

Code Availability
Not applicable.

ORCID
Xin Xu https://orcid.org/0000-0002-8900-5240
YanPing Lin https://orcid.org/0009-0003-4506-0488
Guangchang Pei https://orcid.org/0000-0002-1394-8058
Rui Zeng https://orcid.org/0000-0003-1808-9755
Gang Xu https://orcid.org/0000-0001-6862-0546

Author Contributions
Conceptualization: XX, GX. Data curation: YL. Formal analysis: GP. Investigation: XX. Funding acquisition: GX. Methodology: XX. Project administration: RZ. Resources: GX. Software: XX. Supervision: RZ, GX. Validation: GP. Visualization: XX. Writing—original draft: XX. Writing—review & editing: GP. Approval of final manuscript: all authors.

Conflicts of Interest
The authors declare that they have no potential conflicts of interest.

Funding Statement
This work was supported in part by projects from National Nature Science Foundation of China (No. 82070739) and the Major Research Plan of the National Natural Science Foundation of China (No. 82230021).

REFERENCES
1. Nagendran M, Chen Y, Lovejoy CA, et al. Artificial intelligence versus clinicians: systematic review of design, reporting standards, and claims of deep learning studies. BMJ 2020; 368: m689.
2. Litjens G, Kooi T, Bejnordi BE, et al. A survey on deep learning in medical image analysis. Med Image Anal 2017; 42: 60-88.
3. Chen RJ, Wang JJ, Williamson DF, et al. Algorithmic fairness in artificial intelligence for medicine and healthcare. Nat Biomed Eng 2023; 7: 719-42.
4. Madabhushi A, Lee G. Image analysis and machine learning in digital pathology: challenges and opportunities. Med Image Anal 2016; 33: 170-5.

5. Niazi MK, Parwani AV, Gurcan MN. Digital pathology and artificial intelligence. Lancet Oncol 2019; 20: e253-61.
6. Swanson K, Wu E, Zhang A, Alizadeh AA, Zou J. From patterns to patients: Advances in clinical machine learning for cancer diagnosis, prognosis, and treatment. Cell 2023; 186: 1772-91.
7. Zhou Y, Lu Y. Deep hierarchical multiple instance learning for whole slide image classification. In: 2022 IEEE 19th International Symposium on Biomedical Imaging (ISBI); 2022 Mar 28-31; Kolkata, India.
8. Zhou Y, Lu Y. Multiple instance learning with critical instance for whole slide image classification. In: 2023 IEEE 20th International Symposium on Biomedical Imaging (ISBI); 2023 Apr 18-21; Cartagena, Colombia.
9. Li B, Li Y, Eliceiri KW. Dual-stream multiple instance learning network for whole slide image classification with self-supervised contrastive learning. Conf Comput Vis Pattern Recognit Workshops 2021; 2021: 14318-28.
10. Zhou Y, Lu Y. Multiple instance learning with task-specific multi-level features for weakly annotated histopathological image classification. In: ICASSP 2022 - 2022 IEEE International Conference on Acoustics, Speech and Signal Processing (ICASSP); 2022 May 23-27; Singapore.
11. Zhou Y, Che S, Lu F, et al. Iterative multiple instance learning for weakly annotated whole slide image classification. Phys Med Biol 2023; 68: 155007.
12. Shao Z, Bian H, Chen Y, et al. TransMIL: transformer based correlated multiple instance learning for whole slide image classification. Adv Neural Inf Process Syst 2021; 34: 2136-47.
13. van der Laak J, Litjens G, Ciompi F. Deep learning in histopathology: the path to the clinic. Nat Med 2021; 27: 775-84.
14. Huang Z, Yang E, Shen J, et al. A pathologist-AI collaboration framework for enhancing diagnostic accuracies and efficiencies. Nat Biomed Eng 2025; 9: 455-70.
15. Pei G, Yao Y, Yang Q, et al. Lymphangiogenesis in kidney and lymph node mediates renal inflammation and fibrosis. Sci Adv 2019; 5: eaaw5075.
16. Hu D, Wang Z, Wang S, et al. Lymphatic vessels in patients with crescentic glomerulonephritis: association with renal pathology and prognosis. J Nephrol 2024; 37: 1285-98.
17. Vaswani A, Shazeer N, Parmar N, et al. Attention is all you need. arXiv 1706.03762 [Preprint]. 2017 [cited 2025 Oct 30]. Available from: https://doi.org/10.48550/arXiv.1706.03762.
18. Vaidya A, Chen RJ, Williamson DF, et al. Demographic bias in misdiagnosis by computational pathology models. Nat Med 2024; 30: 1174-90.
19. Song AH, Williams M, Williamson DF, et al. Analysis of 3D pathology samples using weakly supervised AI. Cell 2024; 187: 2502-20.
20. Xu H, Usuyama N, Bagga J, et al. A whole-slide foundation model for digital pathology from real-world data. Nature 2024; 630: 181-8.
21. Wang CW, Huang SC, Lee YC, Shen YJ, Meng SI, Gaol JL. Deep learning for bone marrow cell detection and classification on whole-slide images. Med Image Anal 2022; 75: 102270.
22. Kather JN, Heij LR, Grabsch HI, et al. Pan-cancer image-based detection of clinically actionable genetic alterations. Nat Cancer 2020; 1: 789-99.
23. Fu Y, Jung AW, Torne RV, et al. Pan-cancer computational histopathology reveals mutations, tumor composition and prognosis. Nat Cancer 2020; 1: 800-10.
24. Litjens G, Bandi P, Ehteshami Bejnordi B, et al. 1399 H&E-stained sentinel lymph node sections of breast cancer patients: the CAMELYON dataset. Gigascience 2018; 7: giy065.
25. Lopez Gelston CA, Balasubbramanian D, Abouelkheir GR, et al. Enhancing renal lymphatic expansion prevents hypertension in mice. Circ Res 2018; 122: 1094-101.
26. Barisoni L, Lafata KJ, Hewitt SM, Madabhushi A, Balis UG. Digital pathology and computational image analysis in nephropathology. Nat Rev Nephrol 2020; 16: 669-85.
27. Donnan MD, Kenig-Kozlovsky Y, Quaggin SE. The lymphatics in kidney health and disease. Nat Rev Nephrol 2021; 17: 655-75.
28. Zhuang T, Lei Y, Chang JJ, et al. A2AR-mediated lymphangiogenesis via VEGFR2 signaling prevents salt-sensitive hypertension. Eur Heart J 2023; 44: 2730-42.
29. Goodlett BL, Balasubbramanian D, Navaneethabalakrishnan S, et al. Genetically inducing renal lymphangiogenesis attenuates hypertension in mice. Clin Sci (Lond) 2022; 136: 1759-72.
30. Lu MY, Williamson DF, Chen TY, Chen RJ, Barbieri M, Mahmood F. Data-efficient and weakly supervised computational pathology on whole-slide images. Nat Biomed Eng 2021; 5: 555-70.
31. Nagpal K, Foote D, Liu Y, et al. Development and validation of a deep learning algorithm for improving Gleason scoring of prostate cancer. NPJ Digit Med 2019; 2: 48.
32. Ehteshami Bejnordi B, Veta M, Johannes van Diest P, et al. Diagnostic assessment of deep learning algorithms for detection of lymph node metastases in women with breast cancer. JAMA 2017; 318: 2199-210.
33. Nan T, Zheng S, Qiao S, et al. Deep learning quantifies pathologists' visual patterns for whole slide image diagnosis. Nat Commun 2025; 16: 5493.
34. Hu D, Dong Z, Liang K, Yu H, Wang S, Liu X. High-order topology for deep single-cell multiview fuzzy clustering. IEEE Trans Fuzzy Syst 2024; 32: 4448-59.

35. Hu D, Alshalali TA, Xu X, Yee PL, Shaikh ZA, Yang J. PAGM: partially-aligned global and marginal multi-view contrastive clustering for facial recognition in consumer electronics. IEEE Trans Consum Electron 2025 Oct 28 [Epub]. https://doi.org/10.1109/TCE.2025.3626525.
36. Quan H, Li X, Hu D, Nan T, Cui X. Dual-channel prototype network for few-shot pathology image classification. IEEE J Biomed Health Inform 2024; 28: 4132-44.

https://doi.org/10.4132/jptm.2025.12.15

JPTM

ORIGINAL ARTICLE

pISSN 2383-7837 · eISSN 2383-7845

Journal of Pathology and Translational Medicine 2026; 60: 231-245
https://doi.org/10.4132/jptm.2025.12.16

Can micro-CT distinguish between solid lung tumors? A comparative evaluation including solid adenocarcinoma, non-keratinizing squamous cell carcinoma, and carcinoid tumor

Selim Sevim[1], Serpil Dizbay Sak[1], Kaan Orhan[2], Arda Buyuksungur[3], Duru Karasoy[4], Hilal Ozakinci[1], Ayten Kayi Cangir[5]

[1]Department of Pathology, Ankara University Faculty of Medicine, Ankara, Türkiye
[2]Department of Oral and Maxillofacial Radiology, Ankara University Faculty of Dentistry, Ankara, Türkiye
[3]Department of Basic Medical Sciences, Ankara University Faculty of Dentistry, Ankara, Türkiye
[4]Department of Statistics, Hacettepe University Faculty of Science, Ankara, Türkiye
[5]Department of Thoracic Surgery, Ankara University Faculty of Medicine, Ankara, Türkiye

Graphical abstract

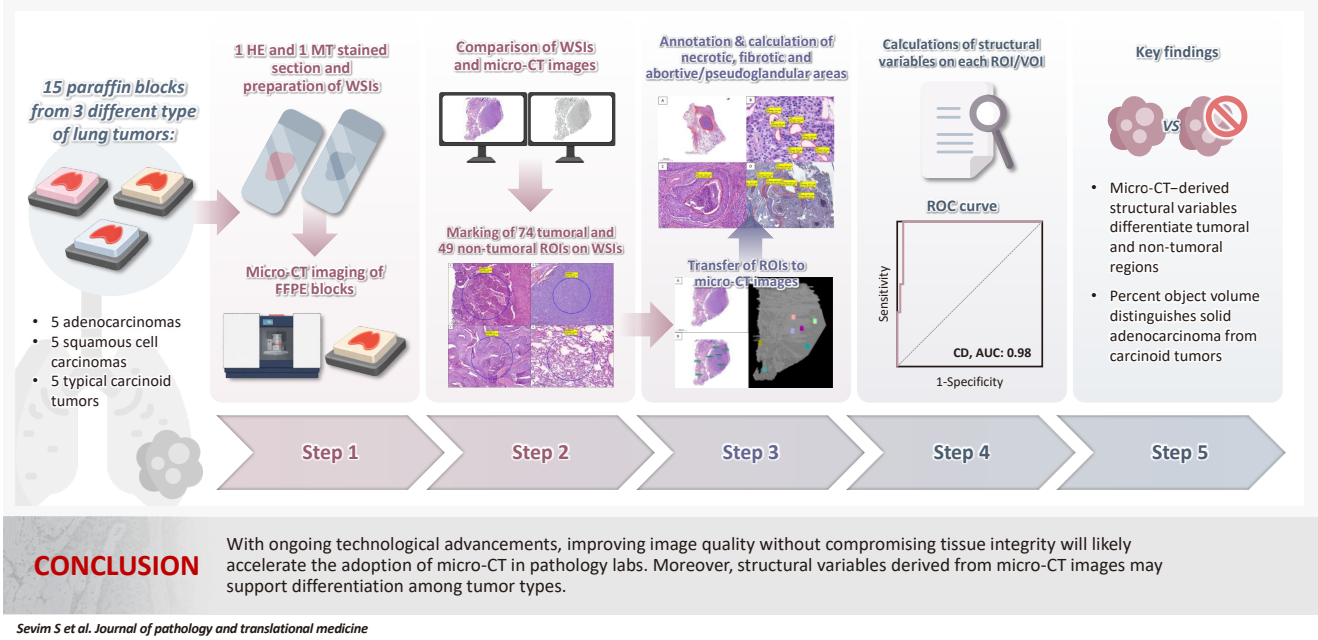

JPTM

ORIGINAL ARTICLE

pISSN 2383-7837 · eISSN 2383-7845

Journal of Pathology and Translational Medicine 2026; 60: 231-245
https://doi.org/10.4132/jptm.2025.12.16

Can micro-CT distinguish between solid lung tumors? A comparative evaluation including solid adenocarcinoma, non-keratinizing squamous cell carcinoma, and carcinoid tumor

Selim Sevim[1], Serpil Dizbay Sak[1], Kaan Orhan[2], Arda Buyuksungur[3], Duru Karasoy[4], Hilal Ozakinci[1], Ayten Kayi Cangir[5]

[1]Department of Pathology, Ankara University Faculty of Medicine, Ankara, Türkiye
[2]Department of Oral and Maxillofacial Radiology, Ankara University Faculty of Dentistry, Ankara, Türkiye
[3]Department of Basic Medical Sciences, Ankara University Faculty of Dentistry, Ankara, Türkiye
[4]Department of Statistics, Hacettepe University Faculty of Science, Ankara, Türkiye
[5]Department of Thoracic Surgery, Ankara University Faculty of Medicine, Ankara, Türkiye

Background: Some pulmonary carcinomas display a solid pattern, and immunohistochemistry is commonly used for tumor differentiation. Micro–computed tomography (micro-CT), with its ability to produce detailed three-dimensional images using small voxel sizes, may offer additional insights. This study investigates whether three solid tumor types, solid adenocarcinoma (sAC), non-keratinizing squamous cell carcinoma, and carcinoid tumor (CaT), can be differentiated using micro-CT. **Methods:** Fifteen paraffin blocks, five for each type, were scanned with micro-CT (Skyscan 1275, Bruker). These images were compared to whole slide images (WSIs) of the same tumors. Consequently, tumoral (n = 74) and non-tumoral (n = 49) regions of interest (tumor ROIs [tROIs] and non-tumor ROIs [ntROIs]) were selected on the micro-CT images and evaluated in terms of certain structural variables (percent object volume, structure model index, structure thickness, structure linear density, connectivity, connectivity density, open porosity, closed porosity) to investigate whether tumors can be differentiated from normal parenchyma and from each other. **Results:** Although detailed images comparable to WSIs could not be obtained, it was considered an important advantage to be able to examine the entire depth of the paraffin blocks. tROIs and ntROIs could be distinguished based on all variables ($p < .001$). Additionally, sAC showed a notable difference from CaT in "percent object volume" ($p = .011$). **Conclusions:** With ongoing technological advancements, improving image quality without compromising tissue integrity will likely accelerate the adoption of micro-CT in pathology labs. Moreover, structural variables derived from micro-CT images may support differentiation among tumor types.

Keywords: Computed tomography, X-Ray microtomography; Lung; Adenocarcinoma; Carcinoid tumor; Squamous cell carcinoma

INTRODUCTION

Histopathological classification plays a foundational role in both the diagnosis and clinical management of human tumors. Lung cancer is the leading cause of cancer-related death in both men and women worldwide [1]. The majority of lung malignancies are carcinomas, and these are categorized and graded based on criteria outlined in the World Health Organization (WHO) classification of thoracic tumors [2]. These tumors are traditionally classified into two categories: small cell and non–small cell carcinomas (NSCLCs) [3,4]. As is widely known, invasive adenocarcinomas (AC) and squamous cell carcinomas (SCCs) are part of the NSCLC group. In addition, carcinoid tumors (CaTs) are non–small cell neuroendocrine tumors of the

Received: November 12, 2025 **Revised:** December 10, 2025 **Accepted:** December 15, 2025
Corresponding Author: Serpil Dizbay Sak, MD
Department of Pathology, Ankara University Medical School, Ahmet Adnan Saygun Street No. 35, Sihhiye, 06230 Ankara, Türkiye
Tel: +90-532-620-0323, Fax: +90-3125958173, E-mail: serpildizbaysak@gmail.com

lung. In addition to morphological assessment, immunohistochemical analysis serves as an important adjunctive tool, particularly in the evaluation of solid subtypes of the mentioned tumors which can be challenging in that context [5].

Histopathological examination has long been a reliable method for the diagnosis of human tumors and for guiding therapeutic decision-making. However, its inherently two-dimensional (2D) nature represents a significant limitation. Although small biopsies and surgical specimens, such as lymph nodes assessed for metastasis, are entirely submitted for histopathological examination, large tumor specimens are routinely sampled according to pre-defined protocols [6]. In cases where the tumor is not small, it is generally not feasible to examine the entire lesion in conjunction with all its relationships to surrounding tissues. Additionally, standard histology typically evaluates only a 4-μm-thick section taken from the superficial portion of the paraffin block, manually cut on a microtome [7]. As a result, diagnostically relevant information may be lost in the discarded tissue or remain buried deeper within the paraffin block. Furthermore, multiple processing steps introduce the risk of artifacts [8,9], which may compromise accurate interpretation. Lastly, small biopsies of solid lung tumors may pose a diagnostic challenge due to limited tissue for further investigations [2] which mostly require disruption of the relevant tissue by cutting.

Computed tomography (CT) is an imaging method used to visualize the internal structure of specimens by acquiring 2D projections (radiographs) from multiple angles [10]. These projections are used to reconstruct the specimen and allow for analysis and visualization of its internal three-dimensional (3D) architecture [10,11]. The key distinction between standard CT and micro–computed tomography (micro-CT) lies in their resolution capabilities [12]. Micro-CT offers significantly higher resolution compared to conventional CT [12].

Micro-CT is commonly used in various fields such as materials science, biology, geology, and engineering for studying the internal structure and properties of materials [13,14]. Micro-CT, which allows in-vivo and ex-vivo examinations [15,16], has been implemented in the field of medicine with many animal studies [17-23] and the applicability of micro-CT in the examination of various tissues has been investigated [24-29]. Certain micro-CT devices allow comprehensive evaluation of tumors, including their spatial relationships with surrounding tissues, prior to disruption of the integrity of the surgical specimen [30]. In this direction, the applicability of micro-CT in the examination of the bone and dental lesions [31,32], spleen [33], breast [34,35], lung [18,36,37], heart [38,39], kidney [40], liver [41], thyroid [42], soft tissues [43,44], and vascular tissues [45,46] has been examined. Studies regarding pulmonary tissues mostly examine non-tumoral pathologies [47] in a wide spectrum of animal models. This spectrum comprises the effect of coronavirus disease 2019 [48], the effect of drugs that cause lung fibrosis [49], interstitial lung diseases [50], radiation effect [51], infective pathologies [52,53], and vascular structures [54]. Thus, studies concentrating on pulmonary tumors with micro-CT are exceptionally rare [36]. Beyond the morphologic information and 3D evaluation obtained from micro-CT images, structural variables can serve as complementary analytical measures [30]. Those variables are revealed by mathematical calculations and define the content of the structure examined in 2D or 3D [55].

The first aim of this study was to compare the histopathological images of three different types of solid-patterned lung tumors (solid adenocarcinoma [sAC], SCC, and CaT) with the images obtained by scanning the paraffin-embedded tumor tissues with micro-CT. The second goal was to investigate whether the structural variables calculated from micro-CT images can be used to differentiate these tumor types. These tumor types were intentionally selected because they cannot be reliably discriminated from one another on routine hematoxylin and eosin (H&E) sections and therefore require ancillary immunohistochemical studies for definitive classification. The objective was to determine whether these entities, which cannot be confidently distinguished by conventional light microscopic assessment, could be differentiated through quantitative analysis of micro-CT–derived structural variables. Additionally, the relationships between these variables and histopathological features such as necrosis, glandular/pseudo-glandular areas, and fibrosis within the tumors were investigated.

MATERIALS AND METHODS

Case selection

Pulmonary tumor tissues from 15 patients, who were operated and routinely diagnosed between 2016 and 2021 in Ankara University Faculty of Medicine (AUFM), were used in this study. All cases were formalin fixed, and paraffin embedded (FFPE). Among these 15 cases, five were diagnosed as sAC, five as non-keratinizing SCC and, five as typical CaTs after histopathological and immunohistochemical evaluation. These tumor types were selected for inclusion in this study based on

https://doi.org/10.4132/jptm.2025.12.16

their shared morphological appearance, characterized predominantly by a solid organizational pattern, which renders their distinction by routine light microscopic examination challenging, despite their substantially different biological and clinical profiles. Non-solid AC patterns such as lepidic, micropapillary, papillary, and acinar were intentionally avoided, as their inherently heterogeneous architectural morphology could introduce confounding effects.

One representative FFPE block including both the tumor tissue and normal pulmonary parenchyma was retrieved for each case. This approach ensured that both tumoral and adjacent non-tumoral areas were represented within a single FFPE block. In this part of the study, we excluded any blocks whose corresponding H&E slides demonstrated tumor spread through alveolar spaces (STAS) as it can lead to secondary solidification within the non-tumorous lung parenchyma through single cells, micropapillary clusters, or solid nests [56], thereby potentially introducing confounding effects in the assessment of structural variables. Each selected block was randomly labeled from 1 to 15 at this point, to provide a blind approach in subsequent steps. After anonymization, two new unstained sections of 4 μm were obtained from each FFPE block. One of these sections was stained with H&E and the other one was stained with Masson trichrome (MT) to facilitate evaluation of fibrotic areas.

Digitization and annotation of cases

H&E and MT sections were scanned using a whole slide image (WSI) scanning and imaging system (3D HISTECH, Budapest, Hungary; Pannoramic P250 Flash III and Panoramic Scanner ver. 3.0.2; Slide Viewer ver. 2.5, RTM) in AUFM, Department of Pathology. To ensure created section quality, all sections were scanned at ×40 magnification. A total of 30 WSIs of 15 cases were created. On 15 H&E-stained digital images, a total of 74 tumoral and 49 non-tumoral regions of interest (tumor ROIs [tROIs] and non-tumor ROIs [ntROIs]) each with an area of 1 mm^2 were annotated. Twenty-five tROIs (54.3%) and 21 ntROIs (45.7%) were marked from the sAC group. In CaTs, 24 tROIs (58.5%) and 17 ntROIs (41.5%) were selected. In the SCC group, 25 tROIs (69.4%) and 11 ntROIs (30.6%) were marked (Fig. 1).

In addition, for each case, the border of tumor was marked, and total area occupied by the tumor was calculated. Moreover, to compare with structural variables, areas occupied by necro-

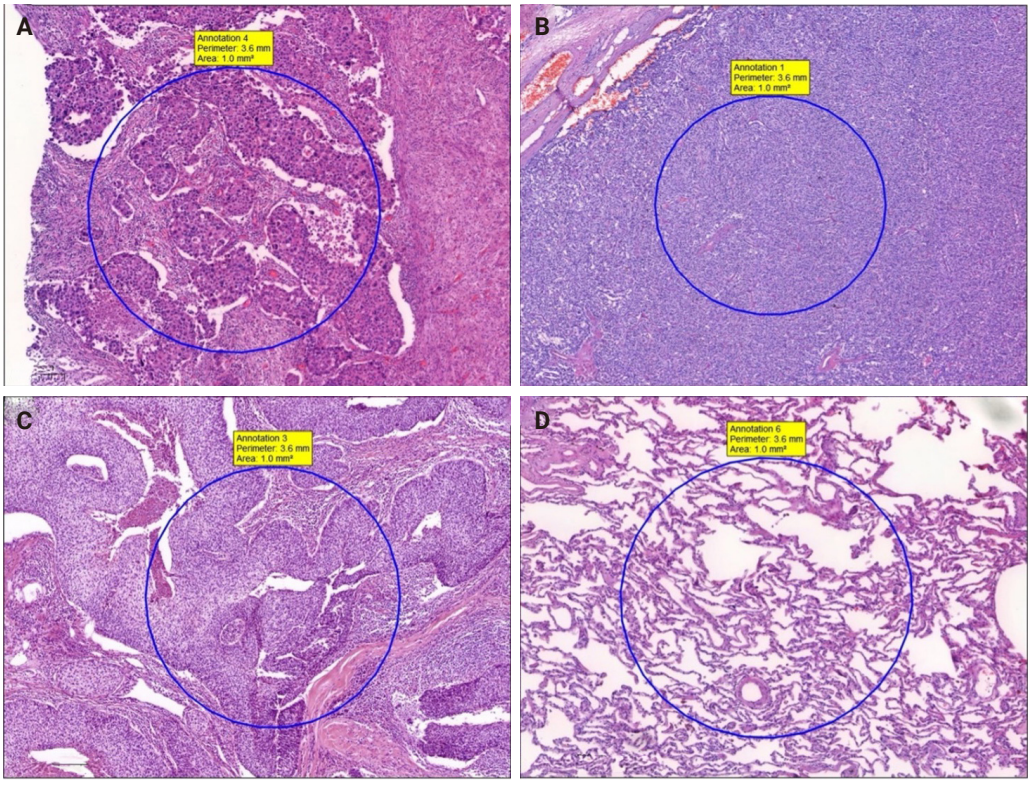

Fig. 1. Manual tumoral and non-tumoral annotations (A–D). Four regions of interest from a solid adenocarcinoma (sAC) (case 1), a carcinoid tumor (case 7), a squamous cell carcinoma (case 11), and non-tumoral lung parenchyma around sAC (case 1), respectively.

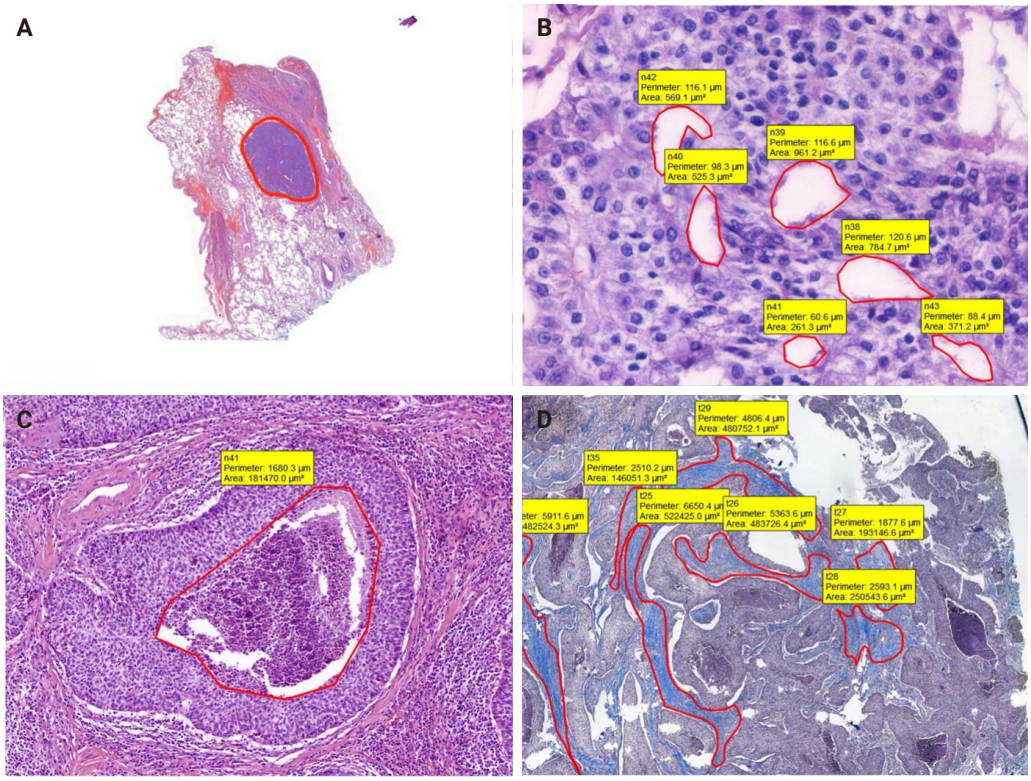

Fig. 2. Annotation examples of whole tumor, pseudo-glandular spaces, necrosis, and fibrosis. (A) Annotated whole tumor (case 2). (B) Pseudo-glandular spaces (case 8). (C) Necrosis in the middle of the tumor island (case 11). (D) Fibrotic areas (case 11, Masson trichrome).

sis, pseudo/abortive glandular areas, and fibrotic areas within the tumor were annotated on MT and H&E-stained WSIs. The ratio of the area occupied by the areas showing these three features to the entire tumor area was calculated (Fig. 2).

On H&E-stained sections, fibrosis, necrotic areas, and pseudo/abortive glandular structures, which are thought to have a possible impact on the X-ray absorption and the values of structural variables, were marked. For the whole dataset, a total of 1,789 areas in the sAC group, 1,885 areas in the CaT group, and 421 regions in SCC group were annotated.

On MT stained WSIs, 102 fibrotic areas in the sAC group, 109 fibrotic areas in the CaT group and 140 fibrotic areas in the SCC group were marked.

Micro-CT scanning

After obtaining H&E and MT sections, cassettes were gently removed from paraffin-embedded tissues using a knife. To ensure compatibility of micro-CT images and virtual histopathological slides, FFPE tissues were placed at the right angles with a specimen holder. High-resolution, desktop micro-CT system (Skyscan 1275, Bruker, Kontich, Belgium) was used to scan the tissues within paraffin. The scanning conditions were as follows: 32 kVp, 220-µA, without any filter, 10.1 µm pixel size, 50 millisecond exposure time, and 3 frame average. Scanning was carried out 360° with rotation at 0.2 steps. To minimize ring artifacts, flat field correction was carried out prior to each scanning. The mean time of scanning was around 30 minutes for each paraffin block. Other settings included beam hardening correction, as described in the manufacturer's manual and input of optimal contrast limits according to manufacturer's instructions, based on prior scanning and reconstruction of each sample. After the tissues were scanned, the paraffin blocks were remounted on corresponding cassettes and returned to the Archives of AUFM, Department of Pathology without compromising tissue integrity.

Micro-CT image analysis

The NRecon software (ver. 1.6.10.5, SkyScan, Bruker) was used with the modified algorithm described by Feldkamp et al. [57] to obtain axial, 2D, 1,000 × 1,000-pixel images via reconstruction of the raw data. For the reconstruction variables, ring artifact correction and smoothing were fixed at zero and

https://doi.org/10.4132/jptm.2025.12.16

the beam artifact correction was 38%. By using the NRecon software (SkyScan, Bruker), the images obtained by the scanner were reconstructed to show 2D slices of the specimen. The cross-sectional images were reconstructed to obtain the whole of the samples. The reconstructed images which were further processed in Skyscan CTVox for visualization (v. 3.3.1, SkyScan, Bruker) (Fig. 3).

CTAn (ver. 1.19.11.1, SkyScan, Bruker) was used for the quantitative measurements of the samples and the selection of the regions of interest (ROIs) and volume of interests (VOIs). Micro-CT images and corresponding annotated H&E images were examined side-by-side on two separate screens. Micro-CT images were viewed at different angles and depths and compared with WSIs. Afterwards, by choosing the micro-CT plane corresponding to the H&E section; all ROIs were transferred manually on the micro-CT images with the help of reference points (cartilage, vascular structures, bronchi, cystic areas, etc.). For further analysis, ROIs on micro-CT images and cubic VOIs with a total volume of 1 mm^3 under these ROIs were used. The ROI number generated on the H&E slides were also assigned to the corresponding VOIs. One micro-CT expert and one pathologist carried out the ROI detection of the micro-CT images.

To differentiate the malignant tissue from the normal tissue, a suitable threshold is required. For this instance, the original grayscale images were processed with a Gaussian low-pass filter for noise reduction, and a semi-automatic global threshold method was used. In that process, the middle value of the gray scale was calculated using semi-automatic global threshold. After the thresholding (binarization) process, an imposed image of black/white pixels was achieved. The binarization process was applied to all samples with the same parameters. All specifications of the CTAn software were used to analyze the 3D mi-

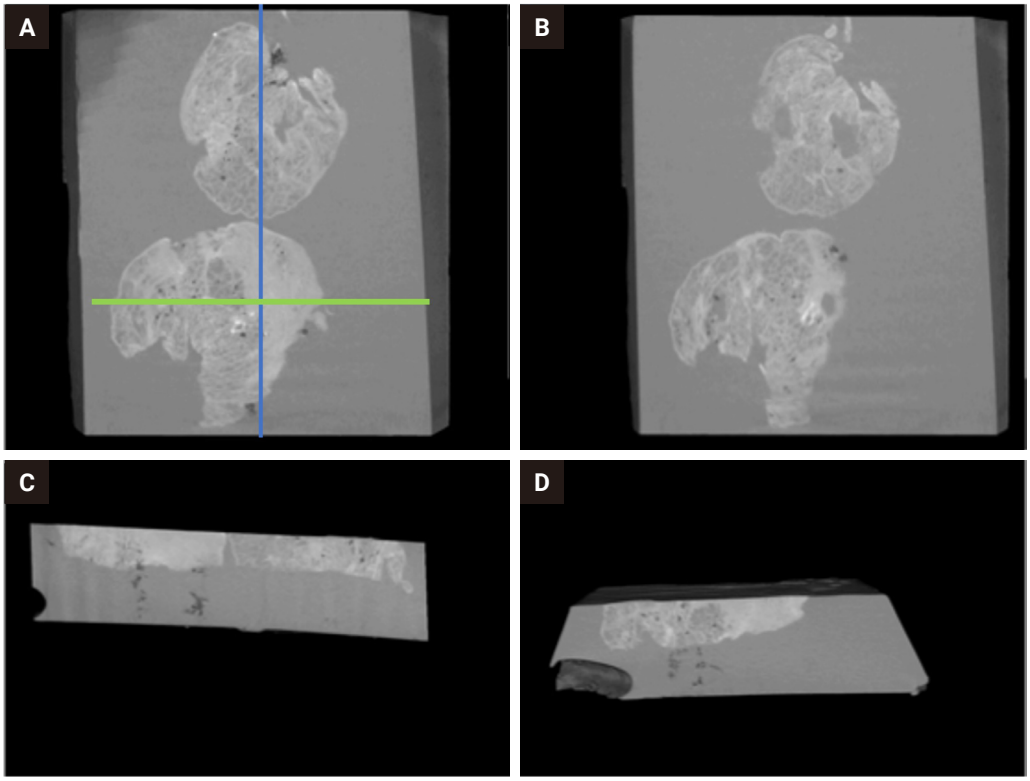

Fig. 3. Digital sections obtained from the paraffin block of an adenocarcinoma (A–D). A and B show relatively superficial (A) and deeper (B) levels of the block, respectively, parallel to the routine hematoxylin and eosin plane, demonstrating a reduction in the tumor size at the deeper level (B). (C) A section perpendicular to the block surface, oriented parallel to the long axis of the block, allowing visualization of both tissue samples within the block. (D) A section oriented parallel to the short axis showing only one of the tissue samples. The approximate orientations corresponding to sections C and D are indicated by the blue and green lines on Fig. 3A, respectively. Micro–computed tomography video of this block is also provided as a Supplementary Video S1. This video was obtained from a preliminary experiment and does not represent one of the cases in the present study.

croarchitecture of each sample. The following structural variables were calculated: percent object volume (POV), structure model index (SMI), structure thickness (ST), structure linear density (SLD), connectivity, connectivity density (CD), open porosity (OP), and closed porosity (CP).

Calculation of structural variables within ROIs/VOIs

The calculated structural variables are explained below: While connectivity and CD values were calculated in 3D (at VOI level), other variables were calculated in 2D (at ROI level).

POV is the percentage of the solid tissue occupancy in the analyzed VOI. This variable has been widely used in studies aiming to calculate bone-related trabecular bone loss and gain [58]. When formulated, it can be expressed as "POV = volume of solid tissue/volume of all relevant VOI" [59].

SMI describes the shape of the structures in the tissue. It shows the relative prevalence of rods and plates within the tissue. It allows to calculate the surface convex curvature in a 3D structure such as trabecular bone. For example, in osteoporosis, the difference between the deterioration of trabecular bone and the conversion from plate-like internal structures to rod-like architecture can be calculated with this variable [55,59].

ST determines the thickness of solid structures in the examined VOI. In other words, the ST provides a value indicating the 3D thickness. This value, which is calculated as "trabecular thickness" in bone studies, is called ST in general scientific terminology [55,59].

SLD corresponds to the number of trabeculae, a term widely used in bone studies. It refers to the number of solid area transitions per unit length on a random line along the VOI/ROI [55,59]. This value provides insight into the homogeneous or heterogeneous distribution of internal structures within the material.

Connectivity (C) is an indicator of the relationship between solid structures in a VOI. It is a measure of how many connections can be broken within a tissue before it splits into two separate parts. These variables reflect the relative positions of the components forming the internal structure of the material and their relationships with the porous architecture. CD refers to the value of C per unit volume [59]. C and CD analyses were calculated in 3D and integrated into the CTAn software. Both analyses use the Euler analysis [60].

Porosity (P) is a term used to express void/porous areas in a substance. Other terms used for P are pore number, pore volume, pore surface, and percentage of pores. The volume of all porous spaces in the material can be expressed as total porosity and is obtained by adding OP and CP. p-values are expressed as percentages [55]. An open pore is defined as a pore that is intersecting with the boundary of the ROI/VOI. Namely, an open pore is connected to the outside in 2D or 3D, while a closed pore is not [55]. A closed pore, on the other hand, refers to the pores that are completely surrounded by solid tissue as a result of the 3D evaluation of the material [55]. In this study, a closed pore is viewed as black pixels that were surrounded by a border of white pixels.

Statistical analysis

The relationships between the values obtained as a result of the calculations on the VOIs and the tumor type were investigated statistically. IBM SPSS Statistics ver. 23.0 (for Windows, IBM Corp., Armonk, NY, USA) software was used in all statistical analyses. Since the distribution of data was not normal, the non-parametric Kruskal-Wallis test was used to compare more than two groups, and the Mann-Whitney U test was used to compare two groups for all structural variables.

K-means clustering analysis was performed to classify the observations as tumor and non-tumor using all structural variables. The agreement of the cluster analysis results with tumor and tumor-free areas was examined by Cohen's Kappa coefficient. The receiver operating characteristic (ROC) analysis was used to find the optimal cut-off values in the variables to distinguish between those with and without tumors. The suitability of the classifications was evaluated with the area under the curve (AUC), and with the criteria of sensitivity and specificity.

The workflow of this study is summarized in Fig. 4.

RESULTS

Clinical, histopathological, immunophenotypic, and molecular characteristics of the tumors

Of the 15 tumors analyzed in this study, five were sAC, five were non-keratinizing SCC, and five were typical CaTs. Seven patients (46.7%) were female and eight (53.3%) were male. The mean age of the patients was found to be 61.4 years (range, 49 to 72 years). There was no statistically significant difference among tumor types in terms of tumor size, patient age, sex, localization, type of operation, pleural invasion, lymphovascular invasion, perineural invasion, STAS, multifocality, or lymph node metastasis. The characteristics of the cases are summarized in Supplementary Table S1 and S2.

https://doi.org/10.4132/jptm.2025.12.16

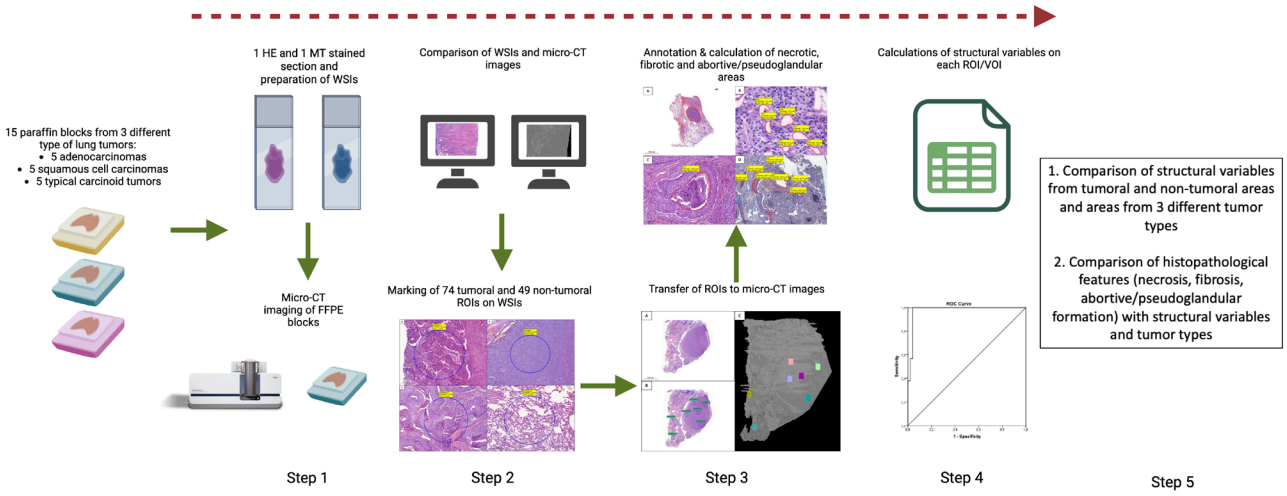

Fig. 4. Workflow of the current study. Created with BioRender.com. FFPE, formalin-fixed-paraffin-embedded; H&E, hematoxylin and eosin; MT, Masson trichrome; micro-CT, micro–computed tomography; ROI, region of interest; VOI, volume of interest; WSI, whole slide image.

Table 1. Descriptive statistics of structural variables for tumoral and non-tumoral areas

Variable	Tumoral	Non-tumoral	p-value
POV	84.41 ± 1.47	23.13 ± 2.14	<.001
SMI	0.32 ± 0.20	1.32 ± 0.17	<.001
ST	0.63 ± 0.22	0.30 ± 0.16	<.001
SLD	2.48 ± 0.36	1.40 ± 0.34	<.001
C	4,614.97 ± 936.87	870.12 ± 31.87	<.001
CD	69.86 ± 4.35	24.45 ± 10.02	<.001
OP	27.62 ± 7.22	72.63 ± 7.89	<.001
CP	2.60 ± 0.37	1.62 ± 0.42	<.001

Values are presented as mean ± SD.
POV, percent object volume; SMI, structure model index; ST, structure thickness; SLD, structure linear density; C, connectivity; CD, connectivity density; OP, open porosity; CP, closed porosity; SD, standard deviation.

Table 2. Kappa coefficients for the results obtained from cluster analysis, and ROC analysis results of tumoral and non-tumoral ROI/VOI

Variable	Kappa coefficient	Sensitivity	Specificity	AUC	Cut-off value
POV	1	1	1	1	55.21[a]
SMI	0.98	0.99	1	0.99	1.06[b]
ST	0.30	0.80	0.84	0.85	0.34[a]
SLD	0.87	0.99	0.96	0.95	1.84[a]
C	0.98	1	1	1	1,991[a]
CD	0.97	1	0.96	0.98	42.38[a]
OP	0.95	0.94	1	0.99	65.06[b]
CP	0.90	0.96	0.94	0.92	2.05[a]

ROC, receiver operating characteristic; ROI, region of interest; VOI, volume of interest; AUC, area under the curve; POV, percent object volume; SMI, structure model index; ST, structure thickness; SLD, structure linear density; C, connectivity; CD, connectivity density; OP, open porosity; CP, closed porosity.
[a]Tumor if ≥this value; [b]Non-tumor if <this value.

Comparison of tumoral and non-tumoral VOIs in terms of structural variables

Seventy-four tumoral and 49 non-tumoral VOIs and ROIs were compared in terms of structural variables. Variables that represent solid structures (POV, ST, SLD, C, CD, and CP) showed higher values in tumoral regions, whereas SMI and OP, which characterize highly porous structures such as lung parenchyma, were found to be higher in non-tumoral areas. According to this, POV, SMI, ST, SLD, C, CD, OP, and CP variables were found to be statistically significant in terms of separating tumoral and non-tumoral areas (all $p < .001$) (Table 1).

Based on the cluster analyses performed, Kappa, sensitivity, specificity, AUC, and cut-off values specific to each structural variable were determined. Except for ST, the lowest observed values among all variables were a kappa of 0.87, a sensitivity of 0.94, a specificity of 0.94, and an AUC of 0.92. These findings highlight that, when appropriate cut-off thresholds are applied, the numerical outputs of these variables can sharply discriminate between tumoral and non-tumoral regions. Additionally, when clustering was done by considering all nine variables described together, all the non-tumoral and tumoral ROIs were

Table 3. Descriptive statistics of structural variables for three tumor types and p-values

Variable	sAC	Non-keratinizing SCC	CaT	p-value
POV	84.80 ± 1.51 (82.65–87.36)	84.63 ± 1.66 (82.63–87.65)	83.85 ± 1.06 (82.45–86.36)	.035
SMI	0.34 ± 0.27 (0.12–1.32)	0.30 ± 0.15 (0.18–1.00)	0.31 ± 0.16 (0.19–1.00)	.497
ST	0.58 ± 0.24 (0.17–0.99)	0.61 ± 0.21 (0.23–0.88)	0.70 ± 0.23 (0.23–0.96)	.077
SLD	2.42 ± 0.43 (1.11–3.01)	2.55 ± 0.33 (2.16–3.10)	2.47 ± 0.33 (1.99–3.00)	.732
C	4,427.68 ± 1,030.33 (2,991–5,314)	4,552.16 ± 957.93 (3,199–5,277)	4,906.75 ± 764.36 (3,158–5,302)	.146
CD	69.20 ± 4.89 (59.86–73.76)	69.26 ± 4.48 (62.00–73.99)	71.19 ± 3.42 (61.98–73.99)	.365
OP	28.71 ± 8.55 (21.22–64.95)	26.06 ± 3.09 (21.05–31.58)	28.10 ± 8.68 (21.33–64.96)	.546
CP	2.64 ± 0.33 (1.54–3.05)	2.55 ± 0.31 (2.13–3.19)	2.60 ± 0.47 (1.26–3.08)	.287

Values are presented as mean ± SD (min–max).
sAC, solid adenocarcinoma; SCC, squamous cell carcinoma; CaT, carcinoid tumor; POV, percent object volume; SMI, structure model index; ST, structure thickness; SLD, structure linear density; C, connectivity; CD, connectivity density; OP, open porosity; CP, closed porosity; SD, standard deviation; min, minimum; max, maximum.

clustered correctly (kappa = 1). Table 2 summarizes the results of statistical analyses. ROCs are also shown in Supplementary Fig. S1.

Comparison of three tumor types in terms of structural variables

There was no statistically significant difference found among these three tumor types for SMI, ST, SLD, C, CD, OP, and CP (Table 3). However, a statistically significant difference was found among these three tumor types in terms of the POV (p = .035). When the origin of this difference was investigated with the Mann-Whitney U test: there was no statistically significant difference detected between sAC/SCC (p = .560) groups and CaT/SCC (p = .072) groups in terms of this variable. On the other hand, a statistically significant difference in POV was observed between the sAC and CaT ROIs (p = .011).

The relationship between histopathological features and structural variables

In the current study, fibrotic areas were expected to appear radiodense (white), while necrotic and pseudo/abortive glands were assumed to be radiolucent (black) on micro-CT images. To identify any possible differences within different tumors, 4,095 annotated ROIs across all tumors in H&Es were used. No statistically significant difference was found between tumor types (p = .141).

In terms of tumor types, it was concluded that the percentage of fibrotic areas to the overall tumoral area did not show a statistically significant difference (p = .102), on digitized MT sections (Supplementary Tables S3–S5).

DISCUSSION

In this study, we demonstrated the feasibility and applicability of micro-CT for non-destructive 3D structural analysis of FFPE blocks of solid pulmonary tumors. Using micro-CT scans, we successfully segmented tumoral versus non-tumoral compartments via quantitative structural variables. Taken together, we believe that our findings support the utility of micro-CT as a complementary tool for enhancing tissue characterization and morphology-driven assessments in human tumors, particularly when integrated with routine histopathological workflows.

Histopathological examination under light microscopy is the gold standard for diagnosing human tumors. This long-established technique is a very powerful tool and offers high-resolution imaging at relatively low cost. In pulmonary tumors, standardized guidelines are followed in the routine diagnostic process to highlight relevant and important prognostic findings

https://doi.org/10.4132/jptm.2025.12.16

[61]. When combined with immunohistochemistry and molecular approaches, light microscopy plays a critical role in both diagnosis and treatment planning. Despite its long-standing and indispensable role in routine practice, conventional histopathological approach is inherently limited as it depends on 2D sections obtained from the most superficial layers of paraffin blocks, which themselves represent only preselected portions of the specimens.

Technical developments in recent years have changed the daily practices of both histopathology laboratories and specialists. Currently, in some laboratories, routine histopathological evaluations are conducted using WSIs rather than conventional light microscopy [62]. It is possible to obtain 3D images using consecutive WSIs. For example, Hashimoto and colleagues investigated the 3D structure of human brain tissue through WSIs [63]. In this study, WSIs were created by digitizing H&E sections, and the material was reconstructed in 3D through consecutive layered 2D WSIs. However, this method has some caveats: to reliably scan the tissue in 3D, a minimum of 50 sections is necessary; and to obtain an optimal 3D model, at least 100–200 consecutive sections should be digitized and converted into 3D, using a dedicated software [64]. In routine pathology practice, the deeper portions of paraffin blocks are examined by preparing additional sections. However, tissue lost between sections due to trimming cannot be recovered unless all levels are stained and examined. Cutting and examining all levels is impractical due to internal regulations, cost, and workload. Consequently, deeper tissue features within the block, such as invasive components with potential diagnostic or prognostic significance, may remain undetected. Even with additional deep sectioning and extra gross sampling, important findings may still be missed in the final pathology report. On the other hand, using radiological methods, 3D images can be obtained. Thanks to the recent advancements, the images obtained via 3D techniques offer similar performances regarding high resolution of H&E [28,65-70]. Additionally, unlike routine sectioning, micro-CT enables digital slicing at any desired level without physically disrupting tissue integrity. For instance, in thyroid tumors, capsular invasion is a key diagnostic criterion. It has been shown that micro-CT increases the number of detected foci of capsular invasion compared to conventional 2D histology [42]. In such cases, it may be more accurate and easier to detect the invasion using micro-CT, rather than serial sectioning of the whole FFPE block. In this manner, the invasive properties of tumors and their proximity to surgical margins can be assessed prior to tissue disruption. It may potentially allow for a more efficient histopathological analysis with reduced sampling and cutting. In this study, we assessed the degree to which morphological characteristics of three different lung tumors could be discerned in micro-CT images of paraffin blocks. We were able to differentiate tumoral areas from surrounding lung parenchyma within the FFPE blocks, and in several cases, we noted that both the size and the configuration of the tumor changed in the deeper portions of the block relative to the superficial sections (Fig. 5). Furthermore, we could identify specific features such as bronchi, vascular structures, calcifications in the micro-CT images (Supplementary Video S1). Based on these observations, we believe that micro-CT enables an assessment of tumoral and non-tumoral parenchymal features in FFPE blocks.

Certain micro-CT systems possess sufficient capacity to enable the comprehensive evaluation of an entire surgical specimen without compromising its integrity [34,71]. The capability of micro-CT for 3D tissue visualization can be uti-

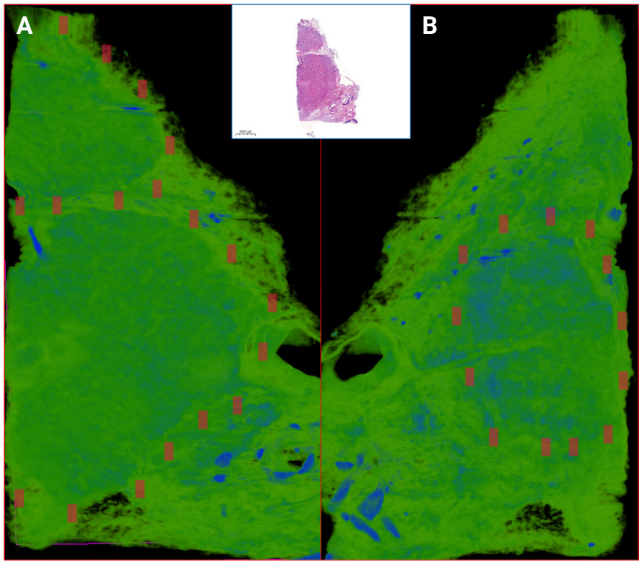

Fig. 5. Micro–computed tomography–generated automatic color-enhanced visualization of the most superficial (A) and a deeper portion (B) of the formalin-fixed-paraffin-embedded block (case 1). The corresponding hematoxylin and eosin whole slide image for the case is shown in the inset. Red markers delineate the tumor-containing area. This image demonstrates that the tumor area that appears larger in the superficial image is reduced in size in the image representing the deeper portion of the block. This finding highlights the potential advantage of a three-dimensional modality in enabling pathologists to more effectively select context-appropriate sections for further histologic evaluation.

lized during the macroscopic evaluation and sampling stage in histopathological examination of surgical materials, or during intraoperative consultations [72,73]. In fact, previous studies have identified that micro-CT may be valuable in assessing surgical margins, especially in breast carcinoma specimens [73]. Additionally, micro-CT has demonstrated superior capability in estimating tumor burden [42] and offered improved predictive performance in comparison to routine histopathological evaluation [28]. In the context of lung cancer, micro-CT has the potential to facilitate detection of vascular and pleural invasion sites, and identification of STAS which may remain inconspicuous on conventional 2D histological sections. In the setting of the increasing number of sublobar resections performed today, micro-CT may find a role in the intraoperative assessment of surgical margins. As another complementary tool to micro-CT and routine H&E staining, virtual staining is also offering another powerful method to obtain pseudo-H&E images [74]. For histopathologists, pseudo-H&E images (Supplementary Fig. S2) can be created in shades of pink and purple instead of grayscale images [75].

Micro-CT images, like H&E images, can serve as the basis for morphometric measurements and comparisons. Morphometric evaluations and comparisons that can be performed on micro-CT images can be mostly found in bone and dental lesions [76]. Nakamura et al. [77] investigated the recognizability of the lepidic pattern in 10 lung tumor resection specimens using micro-CT images. In this study, micro-CT images were able to distinguish between thin and thick alveolar walls suggesting that micro-CT could separate normal lung areas from lepidic AC. In the present study, various structural variables of the tumoral and non-tumoral areas were calculated based on micro-CT images. Similar to previous studies conducted by our team, structural variables were found to exhibit statistical differences between tumoral and non-tumoral regions, and it was also demonstrated that tROIs and ntROIs could be clustered separately using these structural variables [30,78].

The structural variables used in our study seem more relevant to material science and certain engineering fields rather than medicine. Elucidating the meaning of these structural variables and their relationship to the architectural features of diseased and normal tissues may facilitate the interpretation of tumor type divergence. Understanding the structural differences between non-tumoral tissue and tumoral tissue is relatively easy. For example, as revealed by our results, a higher density of interconnecting tumor cells in tROIs is reflected in higher POV, ST, SLD, C, and CD values than in normal lung parenchyma. The blind glandular or pseudo glandular areas within a tumor will result in a higher CP value, while high OP values are anticipated in lung tissue containing interconnecting air spaces. Hypothetically, different tumor types may also have identifiable differences in structural variables, although they may not be apparent visually. In this study, the POV variable showed a statistically significant difference between sAC and CaT groups. One possible explanation could be the higher cellular density of sAC compared to CaT. Non-tumoral features such as fibrosis, necrosis, and inflammatory foci may also have played a role in this result. Upon retrospective review of cases, although not statistically significant, it was observed that desmoplastic stroma/fibrosis was more prominent in sACs and SCCs compared to CaTs, which may be related with higher POV. It is estimated that X-ray absorption is higher in fibrotic areas, and therefore, this value is expected to be high. To confirm this, further investigations should be conducted with a larger number of cases. Different tissue components such as cartilage, lymph nodes, inflammatory cells, and vascular structures may also have an impact on structural variables.

In contrast, no significant differences were observed in other structural variables among the three tumor types. The lack of statistical difference in terms of other structural variables may be attributed to the shared architectural features across all tumor types examined in this study. However, a larger sample size might unveil more pronounced distinctions. On the other hand, tumors with different architectural features (e.g., papillary, micropapillary structures and glands), are more likely to diverge from each other in terms of one or more structural variables. In parallel to this, there may be differences among the tumor types in terms of other structural features that are not addressed in this study. For example, fractal dimension (FD), which is a quantitative descriptor of the geometric complexity, was not addressed in the present study. In medical materials, FD has been shown to capture diagnostically relevant alterations [79,80]. Higher FD values reflect more intricate and dense structures, while lower values indicate simpler and more sparse organization. As this structural feature was not examined in our study, we are unable to comment on potential differences across the solid tumor types included in our study. In addition, we believe that such numerical parameters could form the basis for artificial intelligence (AI) based classification models. Combining FD and other structural variables may significantly enhance the discriminatory power of deep learning algorithms. Thus, these

https://doi.org/10.4132/jptm.2025.12.16

parameters represent promising candidates for the development of novel digital biomarkers and translational diagnostic tools in future studies.

Micro-CT rapidly digitizes the internal and external 3D structures of a sample with high, often sub-micron, resolution [81]. As discussed, its key advantage lies in visualizing internal features without destroying the specimen. Micro-CT enables quantitative 3D analysis of structural variables such as density, porosity, and ST, making it ideal for rare or valuable samples [82]. However, higher resolution demands longer scan times and increased radiation exposure, which may damage genetic material [81]. Therefore, as molecular testing becomes increasingly central to tumor classification and targeted therapy, the potential effects of micro-CT on subsequent molecular analyses need careful evaluation.

There are some restrictions of the current study. First one is the limited number of cases per each tumor type. Although the number of patients included in the study was relatively small, the large number of analyzed areas (n = 123) partially compensates for this limitation. Consequently, we believe, this work stands as an important study in the field, evaluating a significant number of regions within the context of frequently encountered lung tumors with solid organization. A second limitation is that ROI-to-VOI transfer was performed manually instead of using an automated workflow. While this limits perfect one-to-one 100% correspondence, the objective was to ensure that selected areas reliably represented either tumoral or non-tumoral regions. Thus, it was assumed that this manual step had minimal impact on overall statistical outcomes. Additionally, WSIs were generated solely from the surface section of paraffin blocks and structural variable analyses were not performed in a fully 3D context, which may limit the depth of morphological assessments. Additionally, the average voxel size of the micro-CT used in our study is approximately 10 μm. However, contemporary micro-CT/nano-CT devices can achieve pixel sizes as small as 50–500 nm and highly precise resolutions [83].

In the context of rapidly advancing technology, it is anticipated that improvements in micro-CT technology, characterized by shorter scanning times and enhanced image quality, will enable 3D imaging approaches to approximate, and potentially match, the resolution achieved by conventional H&E sections. Therefore, diagnostic images can be created without compromising tissue integrity. In the era of AI algorithms, these approaches are expected to play an important role in diagnostic and prognostic assessment and, in time, may become more embedded in routine pathology practice. Therefore, the integration of micro-CT and other 3D imaging techniques with AI holds considerable promise for supporting pathologists in clinical decision-making.

Supplementary Information

The Data Supplement is available with this article at https://doi.org/10.4132/jptm.2025.12.16.

Ethics Statement

The study was conducted in accordance with the Declaration of Helsinki and approved by the Ankara University Faculty of Medicine Human Research Ethics Committee (I01-17-22). Written informed consent was obtained from all subjects involved in the study.

Availability of Data and Material

Generated and analyzed data during the current study are included in this article as tables, figures, and supplementary materials. Further inquiries can be directed to the corresponding author.

Code Availability

Not applicable.

ORCID

Selim Sevim https://orcid.org/0000-0002-3436-0464
Serpil Dizbay Sak https://orcid.org/0000-0003-3666-3095
Kaan Orhan https://orcid.org/0000-0001-6768-0176
Arda Buyuksungur https://orcid.org/0000-0002-1978-2888
Duru Karasoy https://orcid.org/0000-0002-2258-4479
Hilal Ozakinci https://orcid.org/0000-0001-7921-1000
Ayten Kayi Cangir https://orcid.org/0000-0002-2052-1642

Author Contributions

Conceptualization: SDS, SS. Data curation: SS, KO, AB. Formal analysis: DK. Investigation: SS, KO, AB. Funding acquisition: SDS, SS. Methodology: SS, SDS, AB, DK, HO, AKC. Project administration: SDS. Resources: KO. Supervision: SDS. Validation: SS, DK. Writing—original draft: SS, SDS. Writing—review & editing: SDS, KO, AKC. Approval of final manuscript: all authors.

Conflicts of Interest

The authors declare that they have no potential conflicts of interest.

Funding Statement
This study was supported by Ankara University Scientific Research Fund (BAP-2351).

Acknowledgments
The microscopic evaluation and quantification in this study is done by the digital pathology system obtained by Ankara University Scientific Research Fund (BAP) project (14A0230003).

REFERENCES

1. Luo G, Zhang Y, Rumgay H, et al. Estimated worldwide variation and trends in incidence of lung cancer by histological subtype in 2022 and over time: a population-based study. Lancet Respir Med 2025; 13: 348-63.
2. WHO Classification of Tumours Editorial Board. WHO classification of tumours: thoracic tumors. Lyon: International Agency for Research on Cancer, 2021.
3. Travis WD. Pathology and diagnosis of neuroendocrine tumors: lung neuroendocrine. Thorac Surg Clin 2014; 24: 257-66.
4. Osmani L, Askin F, Gabrielson E, Li QK. Current WHO guidelines and the critical role of immunohistochemical markers in the subclassification of non-small cell lung carcinoma (NSCLC): moving from targeted therapy to immunotherapy. Semin Cancer Biol 2018; 52: 103-9.
5. Inamura K. Update on immunohistochemistry for the diagnosis of lung cancer. Cancers (Basel) 2018; 10: 72.
6. Lott R, Tunnicliffe J, Sheppard E, et al. Practical guide to specimen handling in surgical pathology. Northfield: College of American Pathologists, 2015; 53.
7. Dempster WT. The mechanics of paraffin sectioning by the microtome. Anat Rec 1942; 84: 241-67.
8. Chatterjee S. Artefacts in histopathology. J Oral Maxillofac Pathol 2014; 18(Suppl 1):S111-6.
9. Taqi SA, Sami SA, Sami LB, Zaki SA. A review of artifacts in histopathology. J Oral Maxillofac Pathol 2018; 22: 279.
10. du Plessis A, Broeckhoven C, Guelpa A, le Roux SG. Laboratory x-ray micro-computed tomography: a user guideline for biological samples. Gigascience 2017; 6: 1-11.
11. Kotwaliwale N, Singh K, Kalne A, Jha SN, Seth N, Kar A. X-ray imaging methods for internal quality evaluation of agricultural produce. J Food Sci Technol 2014; 51: 1-15.
12. Saxena RC, Friedman S, Bly RA, et al. Comparison of micro-computed tomography and clinical computed tomography protocols for visualization of nasal cartilage before surgical planning for rhinoplasty. JAMA Facial Plast Surg 2019; 21: 237-43.
13. Salvo L, Suery M, Marmottant A, Limodin N, Bernard D. 3D imaging in material science: application of X-ray tomography. Comptes Rendus Phys 2010; 11: 641-9.
14. Kim BS, Park IK, Hoshiba T, et al. Design of artificial extracellular matrices for tissue engineering. Prog Polym Sci 2011; 36: 238-68.
15. Badea CT, Drangova M, Holdsworth DW, Johnson GA. In vivo small-animal imaging using micro-CT and digital subtraction angiography. Phys Med Biol 2008; 53: R319-50.
16. Eberspacher-Schweda MC, Schmitt K, Handschuh S, Fuchs-Baumgartinger A, Reiter AM. Diagnostic yield of micro-computed tomography (micro-CT) versus histopathology of a canine oral fibrosarcoma. J Vet Dent 2020; 37: 14-21.
17. Senter-Zapata M, Patel K, Bautista PA, Griffin M, Michaelson J, Yagi Y. The role of micro-CT in 3D histology imaging. Pathobiology 2016; 83: 140-7.
18. Schmitt VH, Schmitt C, Hollemann D, et al. Comparison of histological and computed tomographic measurements of pig lung bronchi. ERJ Open Res 2020; 6: 00500-2020.
19. Rodt T, von Falck C, Halter R, et al. In vivo microCT quantification of lung tumor growth in SPC-raf transgenic mice. Front Biosci (Landmark Ed) 2009; 14: 1939-44.
20. Geffre CP, Pond E, Pond GD, et al. Combined micro CT and histopathology for evaluation of skeletal metastasis in live animals. Am J Transl Res 2015; 7: 348-55.
21. Gallastegui A, Cheung J, Southard T, Hume KR. Volumetric and linear measurements of lung tumor burden from non-gated micro-CT imaging correlate with histological analysis in a genetically engineered mouse model of non-small cell lung cancer. Lab Anim 2018; 52: 457-69.
22. Deng L, Xiao SM, Qiang JW, Li YA, Zhang Y. Early lung adenocarcinoma in mice: micro-computed tomography manifestations and correlation with pathology. Transl Oncol 2017; 10: 311-7.
23. Taghavi-Farahabadi M, Mahmoudi M, Soudi S, Hashemi SM. Hypothesis for the management and treatment of the COVID-19-induced acute respiratory distress syndrome and lung injury using mesenchymal stem cell-derived exosomes. Med Hypotheses 2020; 144: 109865.
24. Jensen TH, Bech M, Binderup T, et al. Imaging of metastatic lymph nodes by X-ray phase-contrast micro-tomography. PLoS One 2013; 8: e54047.
25. Virta J, Hannula M, Tamminen I, et al. X-ray microtomography is a novel method for accurate evaluation of small-bowel mucosal morphology and surface area. Sci Rep 2020; 10: 13164.
26. Hutchinson JC, Shelmerdine SC, Simcock IC, Sebire NJ, Arthurs

https://doi.org/10.4132/jptm.2025.12.16

OJ. Early clinical applications for imaging at microscopic detail: microfocus computed tomography (micro-CT). Br J Radiol 2017; 90: 20170113.
27. Laguna-Castro S, Salminen A, Arponen O, et al. Micro-computed tomography in the evaluation of eosin-stained axillary lymph node biopsies of females diagnosed with breast cancer. Sci Rep 2024; 14: 28237.
28. Song AH, Williams M, Williamson DF, et al. Analysis of 3D pathology samples using weakly supervised AI. Cell 2024; 187: 2502-20.
29. Papazoglou AS, Karagiannidis E, Liatsos A, et al. Volumetric tissue imaging of surgical tissue specimens using micro-computed tomography: an emerging digital pathology modality for non-destructive, slide-free microscopy-clinical applications of digital pathology in 3 dimensions. Am J Clin Pathol 2023; 159: 242-54.
30. Kayi Cangir A, Dizbay Sak S, Gunes G, Orhan K. Differentiation of benign and malignant regions in paraffin embedded tissue blocks of pulmonary adenocarcinoma using micro CT scanning of paraffin tissue blocks: a pilot study for method validation. Surg Today 2021; 51: 1594-601.
31. Guerrero ME, Jacobs R, Loubele M, Schutyser F, Suetens P, van Steenberghe D. State-of-the-art on cone beam CT imaging for preoperative planning of implant placement. Clin Oral Investig 2006; 10: 1-7.
32. Mulder L, Koolstra JH, de Jonge HW, van Eijden TM. Architecture and mineralization of developing cortical and trabecular bone of the mandible. Anat Embryol (Berl) 2006; 211: 71-8.
33. Jiang L, Xu D, Sheng K. Anatomy-constrained synthesis for spleen segmentation improvement in unpaired mouse micro-CT scans with 3D CycleGAN. Biomed Phys Eng Express 2024; 10: 055019.
34. DiCorpo D, Tiwari A, Tang R, et al. The role of Micro-CT in imaging breast cancer specimens. Breast Cancer Res Treat 2020; 180: 343-57.
35. Brahimetaj R, Cornelis J, Jansen B. Micro-CT microcalcification analysis: a scoping review of current applications and future potential in breast cancer research. Tomography 2024; 10: 1716-29.
36. Dizbay Sak S, Sevim S, Buyuksungur A, Kayi Cangir A, Orhan K. The value of micro-CT in the diagnosis of lung carcinoma: a radio-histopathological perspective. Diagnostics (Basel) 2023; 13: 3262.
37. Bompoti A, Papazoglou AS, Moysidis DV, et al. Volumetric imaging of lung tissue at micrometer resolution: clinical applications of micro-CT for the diagnosis of pulmonary diseases. Diagnostics (Basel) 2021; 11: 2075.
38. Befera NT, Badea CT, Johnson GA. Comparison of 4D-microSPECT and microCT for murine cardiac function. Mol Imaging Biol 2014; 16: 235-45.
39. Papazoglou AS, Karagiannidis E, Moysidis DV, et al. Current clinical applications and potential perspective of micro-computed tomography in cardiovascular imaging: a systematic scoping review. Hellenic J Cardiol 2021; 62: 399-407.
40. Schambach SJ, Bag S, Schilling L, Groden C, Brockmann MA. Application of micro-CT in small animal imaging. Methods 2010; 50: 2-13.
41. Stroope A, Radtke B, Huang B, et al. Hepato-renal pathology in pkd2ws25/- mice, an animal model of autosomal dominant polycystic kidney disease. Am J Pathol 2010; 176: 1282-91.
42. Xu B, Teplov A, Ibrahim K, et al. Detection and assessment of capsular invasion, vascular invasion and lymph node metastasis volume in thyroid carcinoma using microCT scanning of paraffin tissue blocks (3D whole block imaging): a proof of concept. Mod Pathol 2020; 33: 2449-57.
43. Aoyagi H, Iwasaki S, Yoshizawa H, Tsuchikawa K. Three-dimensional observation of the mouse embryo by micro-computed tomography: Meckel's cartilage, otocyst, and/or muscle of tongue. Odontology 2012; 100: 137-43.
44. Jeffery NS, Stephenson RS, Gallagher JA, Jarvis JC, Cox PG. Micro-computed tomography with iodine staining resolves the arrangement of muscle fibres. J Biomech 2011; 44: 189-92.
45. Aoki T, Rodriguez-Porcel M, Matsuo Y, et al. Evaluation of coronary adventitial vasa vasorum using 3D optical coherence tomography: animal and human studies. Atherosclerosis 2015; 239: 203-8.
46. Grover SP, Saha P, Jenkins J, et al. Quantification of experimental venous thrombus resolution by longitudinal nanogold-enhanced micro-computed tomography. Thromb Res 2015; 136: 1285-90.
47. Scott AE, Vasilescu DM, Seal KA, et al. Three dimensional imaging of paraffin embedded human lung tissue samples by micro-computed tomography. PLoS One 2015; 10: e0126230.
48. Seldeslachts L, Cawthorne C, Kaptein SF, et al. Use of micro-computed tomography to visualize and quantify COVID-19 vaccine efficiency in free-breathing hamsters. Methods Mol Biol 2022; 2410: 177-92.
49. Yang X, Huang XJ, Chen Z, et al. A novel quantification method of lung fibrosis based on micro-CT images developed with the optimized pulmonary fibrosis mice model induced by bleomycin. Heliyon 2023; 9: e13598.
50. Wu EK, Eliseeva S, Rahimi H, Schwarz EM, Georas SN. Restrictive lung disease in TNF-transgenic mice: correlation of pulmonary function testing and micro-CT imaging. Exp Lung Res 2019; 45: 175-87.

51. McIlrath DR, Roach E, Porro G, Perez-Torres CJ. Feasibility of quantification of murine radiation-induced pulmonary fibrosis with microCT imaging. J Radiat Res 2021; 62: 976-81.
52. Ivanciuc T, Patrikeev I, Qu Y, et al. Micro-CT features of lung consolidation, collagen deposition and inflammation in experimental RSV infection are aggravated in the absence of Nrf2. Viruses 2023; 15: 1191.
53. Vanhoffelen E, Resendiz-Sharpe A, Velde GV. Microcomputed tomography to visualize and quantify fungal infection burden and inflammation in the mouse lung over time. Methods Mol Biol 2023; 2667: 211-24.
54. Grothausmann R, Labode J, Hernandez-Cerdan P, et al. Combination of microCT and light microscopy for generation-specific stereological analysis of pulmonary arterial branches: a proof-of-concept study. Histochem Cell Biol 2021; 155: 227-39.
55. Bruker-microCT. Morphometric parameters measured by Skyscan CT-analyser software. Reference manual. Billerica: Bruker, 2012.
56. Warth A. Spread through air spaces (STAS): a comprehensive update. Transl Lung Cancer Res 2017; 6: 501-7.
57. Feldkamp LA, Goldstein SA, Parfitt AM, Jesion G, Kleerekoper M. The direct examination of three-dimensional bone architecture in vitro by computed tomography. J Bone Miner Res 1989; 4: 3-11.
58. Lee DW, Koo KT, Seol YJ, et al. Bone regeneration effects of human allogenous bone substitutes: a preliminary study. J Periodontal Implant Sci 2010; 40: 132-8.
59. Orhan K. Micro-computed tomography (micro-CT) in medicine and engineering. Cham: Springer International Publishing, 2020.
60. Katsamenis OL, Olding M, Warner JA, et al. X-ray Micro-computed tomography for nondestructive three-dimensional (3D) X-ray histology. Am J Pathol 2019; 189: 1608-20.
61. Cooper WA, Webster F, Butnor KJ, et al. Data set for the reporting of lung cancer: recommendations from the International Collaboration on Cancer Reporting (ICCR). Histopathology 2025; 86: 665-80.
62. Farahani N, Parwani AV, Pantanowitz L. Whole slide imaging in pathology: advantages, limitations, and emerging perspectives. Pathol Lab Med Int 2015; 7: 23-33.
63. Hashimoto N, Bautista PA, Haneishi H, Snuderl M, Yagi Y. Development of a 2D image reconstruction and viewing system for histological images from multiple tissue blocks: towards high-resolution whole-organ 3D histological images. Pathobiology 2016; 83: 127-39.
64. Farahani N, Braun A, Jutt D, et al. Three-dimensional imaging and scanning: current and future applications for pathology. J Pathol Inform 2017; 8: 36.
65. Bishop KW, Barner LA, Han Q, et al. An end-to-end workflow for non-destructive 3D pathology. Nat Protoc 2024; 19: 1122-48.
66. Yang B, Lange M, Millett-Sikking A, et al. DaXi-high-resolution, large imaging volume and multi-view single-objective light-sheet microscopy. Nat Methods 2022; 19: 461-9.
67. Park J, Shin SJ, Kim G, et al. Revealing 3D microanatomical structures of unlabeled thick cancer tissues using holotomography and virtual H&E staining. Nat Commun 2025; 16: 4781.
68. Fujimoto JG, Pitris C, Boppart SA, Brezinski ME. Optical coherence tomography: an emerging technology for biomedical imaging and optical biopsy. Neoplasia 2000; 2: 9-25.
69. Lam S, Standish B, Baldwin C, et al. In vivo optical coherence tomography imaging of preinvasive bronchial lesions. Clin Cancer Res 2008; 14: 2006-11.
70. Forjaz A, Vaz E, Romero VM, et al. Three-dimensional assessments are necessary to determine the true, spatially resolved composition of tissues. Cell Rep Methods 2025; 5: 101075.
71. McClatchy DM 3rd, Zuurbier RA, Wells WA, Paulsen KD, Pogue BW. Micro-computed tomography enables rapid surgical margin assessment during breast conserving surgery (BCS): correlation of whole BCS micro-CT readings to final histopathology. Breast Cancer Res Treat 2018; 172: 587-95.
72. Troschel FM, Gottumukkala RV, DiCorpo D, et al. Feasibility of perioperative micro-computed tomography of human lung cancer specimens: a pilot study. Arch Pathol Lab Med 2019; 143: 319-25.
73. Qiu SQ, Dorrius MD, de Jongh SJ, et al. Micro-computed tomography (micro-CT) for intraoperative surgical margin assessment of breast cancer: a feasibility study in breast conserving surgery. Eur J Surg Oncol 2018; 44: 1708-13.
74. Bai B, Yang X, Li Y, Zhang Y, Pillar N, Ozcan A. Deep learning-enabled virtual histological staining of biological samples. Light Sci Appl 2023; 12: 57.
75. Kurz A, Muller H, Kather JN, Schneider L, Bucher TC, Brinker TJ. 3-Dimensional reconstruction from histopathological sections: a systematic review. Lab Invest 2024; 104: 102049.
76. Langheinrich AC, Stolle C, Kampschulte M, Lommel D, Rau WS, Bassaly B. Diagnostic value of ex-vivo three-dimensional micro-computed tomography imaging of primary nonhematopoietic human bone tumors: osteosarcoma versus chondrosarcoma. Acta Radiol 2008; 49: 940-8.
77. Nakamura S, Mori K, Iwano S, et al. Micro-computed tomography images of lung adenocarcinoma: detection of lepidic growth patterns. Nagoya J Med Sci 2020; 82: 25-31.
78. Cangir AK, Gunes SG, Orhan K, et al. Microcomputed tomog-

https://doi.org/10.4132/jptm.2025.12.16

raphy as a diagnostic tool for detection of lymph node metastasis in non-small cell lung cancer: a decision-support approach for pathological examination "A pilot study for method validation". J Pathol Inform 2024; 15: 100373.
79. Baish JW, Jain RK. Fractals and cancer. Cancer Res 2000; 60: 3683-8.
80. Cross SS. Fractals in pathology. J Pathol 1997; 182: 1-8.
81. Keklikoglou K, Arvanitidis C, Chatzigeorgiou G, et al. Micro-CT for biological and biomedical studies: a comparison of imaging techniques. J Imaging 2021; 7: 172.
82. Keklikoglou K, Faulwetter S, Chatzinikolaou E, et al. Micro-computed tomography for natural history specimens: a handbook of best practice protocols. Eur J Taxon 2019; 522: 1-55.
83. Manickam SS, Gelb J, McCutcheon JR. Pore structure characterization of asymmetric membranes: non-destructive characterization of porosity and tortuosity. J Membr Sci 2014; 454: 549-54.

JPTM

ORIGINAL ARTICLE

pISSN 2383-7837 · eISSN 2383-7845

Journal of Pathology and Translational Medicine 2026; 60: 246-262
https://doi.org/10.4132/jptm.2025.12.19

3-Dimensional reconstruction reveals frequent intraluminal growth of submucosal veins in surgically resected pT1 colorectal cancers

Jihyun Park[1], Mi-Ju Kim[2], Yeon Wook Kim[2], Byong-Wook Lee[3], Junyoung Shin[4], Jinho Shin[5], Chan-Gi Pack[6], Dong-Hoon Yang[7], Jihun Kim[5], In Ja Park[8], Ralph H. Hruban[9], Seung-Mo Hong[10]

[1]Department of Medical Science, Brain Korea 21 Project, Asan Medical Institute of Convergence Science and Technology, Asan Medical Center, University of Ulsan College of Medicine, Seoul, Korea
[2]Biomedical Research Center, Asan Institute for Life Sciences, Asan Medical Center, Seoul, Korea
[3]Cellular Imaging Core, Convergence Medicine Research Center, Asan Medical Center, University of Ulsan College of Medicine, Seoul, Korea
[4]Department of Pathology, National Cancer Center, Goyang, Korea
[5]Department of Pathology, Asan Medical Center, University of Ulsan College of Medicine, Seoul, Korea
[6]Department of Convergence Medicine, Asan Medical Center, University of Ulsan College of Medicine, Seoul, Korea
[7]Department of Gastroenterology, Asan Medical Center, University of Ulsan College of Medicine, Seoul, Korea
[8]Department of Colon and Rectal Surgery, Asan Medical Center, University of Ulsan College of Medicine, Seoul, Korea
[9]Department of Pathology, The Sol Goldman Pancreatic Cancer Research Center, Johns Hopkins School of Medicine, Baltimore, MD, USA
[10]Department of Pathology, Brain Korea 21 Project, Asan Medical Center, University of Ulsan College of Medicine, Seoul, Korea

Graphical abstract

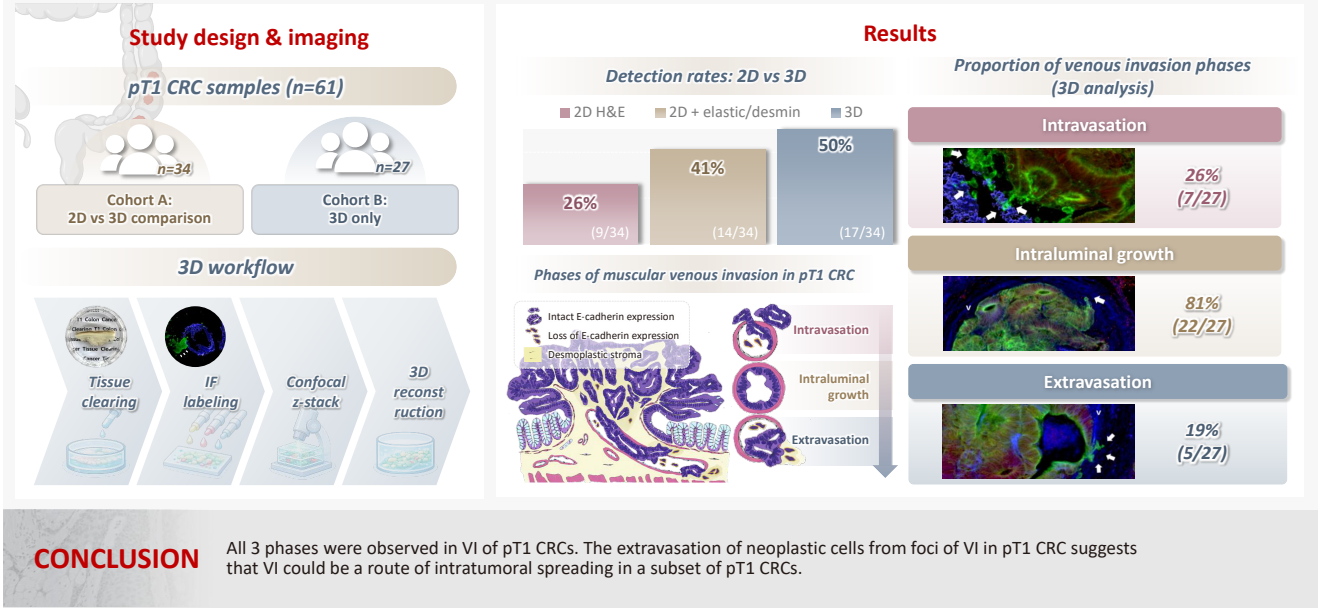

JPTM

ORIGINAL ARTICLE

pISSN 2383-7837 · eISSN 2383-7845

Journal of Pathology and Translational Medicine 2026; 60: 246-262
https://doi.org/10.4132/jptm.2025.12.19

3-Dimensional reconstruction reveals frequent intraluminal growth of submucosal veins in surgically resected pT1 colorectal cancers

Jihyun Park[1], Mi-Ju Kim[2], Yeon Wook Kim[2], Byong-Wook Lee[3], Junyoung Shin[4], Jinho Shin[5], Chan-Gi Pack[6], Dong-Hoon Yang[7], Jihun Kim[5], In Ja Park[8], Ralph H. Hruban[9], Seung-Mo Hong[10]

[1]Department of Medical Science, Brain Korea 21 Project, Asan Medical Institute of Convergence Science and Technology, Asan Medical Center, University of Ulsan College of Medicine, Seoul, Korea
[2]Biomedical Research Center, Asan Institute for Life Sciences, Asan Medical Center, Seoul, Korea
[3]Cellular Imaging Core, Convergence Medicine Research Center, Asan Medical Center, University of Ulsan College of Medicine, Seoul, Korea
[4]Department of Pathology, National Cancer Center, Goyang, Korea
[5]Department of Pathology, Asan Medical Center, University of Ulsan College of Medicine, Seoul, Korea
[6]Department of Convergence Medicine, Asan Medical Center, University of Ulsan College of Medicine, Seoul, Korea
[7]Department of Gastroenterology, Asan Medical Center, University of Ulsan College of Medicine, Seoul, Korea
[8]Department of Colon and Rectal Surgery, Asan Medical Center, University of Ulsan College of Medicine, Seoul, Korea
[9]Department of Pathology, The Sol Goldman Pancreatic Cancer Research Center, Johns Hopkins School of Medicine, Baltimore, MD, USA
[10]Department of Pathology, Brain Korea 21 Project, Asan Medical Center, University of Ulsan College of Medicine, Seoul, Korea

Background: Although venous invasion (VI) is associated with distant metastasis and observed in >50% of pT2–4 colorectal cancers (CRCs), the role of VI in pT1 CRCs is not well-defined. **Methods:** Thirty-four surgically resected pT1 CRCs were reevaluated for 2-dimensional (2D) VI using hematoxylin and eosin (H&E)–stained slides with additional elastic and desmin immunohistochemical staining (cohort A). Additionally, 27 pT1 CRCs without knowing VI status were selected for 3-dimensional (3D) VI evaluation only (cohort B). All 61 cases (cohorts A and B) were studied in 3D using tissue clearing. **Results:** VI was detected more commonly in 3D (17/34, 50.0%) than in 2D H&E slide evaluation (9/34, 26.5%, p = .047). When VI was identified in 3D (27/61, 44.3%), the most common phase was that of intraluminal growth (22/27, 81.5%), followed by intravasation (7/27, 25.9%) and extravasation (5/27, 18.5%). E-cadherin expression was characterized in 3D in foci of VI and varied in each phase of invasion. **Conclusions:** All three phases were observed in VI of pT1 CRCs. The extravasation of neoplastic cells from foci of VI in pT1 CRC suggests that VI could be a route of intratumoral spreading in a subset of pT1 CRCs.

Keywords: Colonic neoplasms; Submucosa; Veins; Neoplasm invasiveness; Cadherins; Imaging, Three-dimensional; Tissue clearing

INTRODUCTION

Colorectal cancer (CRC) is the second-most prevalent cancer with the third-highest mortality rate (11%) in Korea, whereas it is the third-most common cancer with the same mortality ranking in the United States [1,2]. The 5-year survival outcomes for individuals diagnosed with localized and regional CRC are 94% and 83%, respectively. However, the 5-year survival rate declines markedly to 20% among patients exhibiting distant metastases [1]. Distant metastases are detected in up to 16% of patients diagnosed with CRC, with the liver being the most common site [3,4]. Venous invasion (VI) is a critical step in the development of liver metastases as cancer cells can metastasize through the inferior mesenteric or portal veins [5-8]. VI can be detected in more than half of the surgically resected pathological pT2–T4 category (pT2–T4) CRCs with the help of stains,

Received: September 24, 2025 **Revised:** December 2, 2025 **Accepted:** December 19, 2025
Corresponding Author: Seung-Mo Hong, MD, PhD
Department of Pathology, Asan Medical Center, University of Ulsan College of Medicine, 88 Olympic-ro 43-gil, Songpa-gu, Seoul 05505, Korea
Tel: +82-2-3010-4558, Fax: +82-2-472-7898, E-mail: smhong28@gmail.com

such as elastic, that highlight vessels [9-12]. Recently performed 3-dimensional (3D) evaluation of VI of pT2–T4 CRCs revealed phases of intravasation, intraluminal growth, and extravasation associated with VI [12].

CRCs with invasion limited to the submucosal layer are classified as pT1, and, in the absence of metastases, these cancers can be cured by complete surgical resection [13]. Lymph node metastasis occurs in approximately 8% to 13% of pT1 CRCs and lymphovascular invasion is highly associated with increased risk of lymph node metastasis [14-21]. With conventional 2-dimensional (2D) hematoxylin and eosin (H&E)–stained slides only, distinguishing among the different types of vessels, including small lymphatic vessels, capillaries, and postcapillary venules (vessels lacking a distinct smooth muscle layer), is extremely difficult, which is why all invasion into all of these vessels are collectively called lymphovascular invasion [22]. Since it is difficult to distinguish lymphatic invasion only with the commonly used H&E-stained slides, elastic staining, and desmin immunohistochemical staining can be performed to confirm the presence of VI and differentiate it from lymphatic invasion [23,24]. VI can be observed in any layer of the colorectum. However, its role in pT1 CRCs has not been systematically well-defined.

Therefore, the purpose of the present study is to investigate the patterns of VI in pT1 CRC tissues using tissue clearing, immunofluorescence labeling, confocal microscopy, and 3D image reconstruction.

MATERIALS AND METHODS

Patients and tissue preparation

Two cohorts were assembled following approval by the Institutional Review Board with a waiver of patient consent (approval number: 2023-1417). Cohort A consisted of 34 surgically resected pT1 CRC, preserved as formalin-fixed, paraffin-embedded (FFPE) tissue blocks between 2010 and 2023 from patients with (9 cases) or without (25 cases) a prior history of endoscopic mucosal resection (EMR) or endoscopic submucosal dissection (ESD). For enrichment of inclusion of a possible VI, 34 pT1 CRC cases with definite or suspicious foci of lymphovascular invasion on surgical pathology reports were included. For the nine cases with a prior history of EMR or ESD (7 cases with EMR and 2 cases with ESD), surgically resected pT1 CRC tissues were used instead of EMR or ESD pT1 CRCs, as the thermal artifacts of the bases of EMR and ESD specimens hinder complete tissue clearing due to protein denaturation. In contrast, the thermal artifacts of the EMR and ESD scar were completely healed in nine surgical resection specimens, because surgical resections were performed about 3 months after EMR or ESD. One representative FFPE tissue block containing muscular VI foci was chosen from each of the 34 cases in cohort A. All histopathologic features, including the presence of lymphovascular invasion, were reassessed by three experienced gastrointestinal pathologists (J.S., J.K., and S.M.H.) to ensure reliability and consistency of the clinicopathologic data. Additionally, 27 fresh-frozen pT1 CRC tissue slabs (cohort B) were acquired from the institutional biobank, Bio-Resource Center, which is a member of the Korea Biobank Network, without knowledge of their VI status (approval number: 2023-24[275]). All 61 pT1 CRC cases were studied for 3D pathologic evaluation.

Elastic staining and desmin immunohistochemical labeling of 2D microscope slides

The modified elastica van Gieson technique was employed for elastic staining on tumor blocks from the 34 cancers in cohort A. Desmin immunohistochemical labeling (1:200, D33, Dako, Glostrup, Denmark) was performed in the immunohistochemistry laboratory of the Department of Pathology at Asan Medical Center. Briefly, tissue sections of 4 μm thickness were deparaffinized and rehydrated through serial immersions in xylene and graded ethanol solutions. Endogenous peroxidase activity was blocked by incubation in 3% H_2O_2 for 10 minutes, followed by heat-induced antigen retrieval. Immunohistochemical labeling was performed with an autostainer (Benchmark XT, Ventana Medical Systems, Tucson, AZ, USA) in accordance with the manufacturer's protocol. Sections were incubated at room temperature for 24 or 32 minutes with primary antibodies targeting desmin, followed by washing. Suspicious VI foci on H&E-stained slides were reassessed using elastic and desmin immunohistochemical labeling to enhance the identification of VI.

Sample preparation for 3D visualization

All FFPE (34 from cohort A) or fresh-frozen (27 from cohort B) tissue specimens underwent fixation in 10% buffered formalin and were maintained in a chilled solution of 0.02% sodium azide in phosphate-buffered saline (PBS). Tissues were dehydrated through a graded methanol series (50%, 80%, 90%, and three changes of 100%) at room temperature and incubated overnight at room temperature with a solution of 66% dichloromethane/33% MeOH. Tissue specimens were washed twice in

100% methanol to oxidize endogenous pigments and autofluorescent proteins, including red blood cells, and subsequently incubated at 4°C in a 5% hydrogen peroxide solution. The samples were rehydrated through serial dilutions of methanol and subsequently washed twice in PBS containing 0.2% Triton X-100 for 1 hour. Tissue samples were incubated at 37°C for 2 days in a solution of PBS/20% dimethyl sulfoxide/0.2% Triton X-100, and 0.3 mol/L glycine to enhance permeability.

Primary antibody binding for 3D visualization

CRC tissues were incubated at 37°C for 2 days in PBS containing 0.2% Triton X-100, 10% dimethyl sulfoxide, and 6% donkey serum to minimize nonspecific antigen-antibody interactions, followed by washing in PBS with 0.2% Tween-20 and 10 mg/mL heparin at 37°C for 1 hour. Heparin served to lower background labeling [12].

Primary antibodies used in this study included cytokeratin 19 (1:200, EP1580Y, rabbit monoclonal, Abcam, Cambridge, UK), desmin (goat polyclonal; 1:100, LifeSpan Biosciences, Shirley, MA, USA), CD31 (1:100, JC/70A, mouse monoclonal, Thermo Fisher Scientific, Waltham, MA, USA) and E-cadherin (1:150, M168, mouse monoclonal, Abcam). A maximum of three primary antibodies were applied simultaneously, and the antigen retrieval step was omitted. Following primary antibody labeling, tissue samples were washed five times for 1 hour each in PBS containing 0.2% Tween-20 and 10 mg/mL heparin. In CRCs, the dense desmoplastic stroma can function as a barrier that restricts antibody infiltration. Consequently, the following techniques were applied to enhance antibody penetration: (1) gradual increase of antibody concentration, (2) centrifugation, (3) use of pepsin-digested secondary antibody fragments, and (4) sonication.

Fluorescent labeling of antibodies for 3D visualization

Fragmented secondary antibodies, such as Alexa Fluor 488-conjugated AffiniPure F(ab')2 fragment donkey anti-rabbit IgG (Jackson Immuno Research, West Grove, PA, USA), DyLight 405-conjugated AffiniPure F(ab')2 fragment donkey anti-goat IgG (Jackson Immuno Research), and cyanine-3-conjugated AffiniPure F(ab')2 fragment donkey anti-mouse IgG were incubated at 37°C for 4 days in PBS containing 3% donkey serum, 0.2% Tween-20, and 10 mg/mL heparin, while being protected from light. The tissue samples were centrifuged at 400 ×g for 12 hours daily and sonicated for 1 hour and washed five times for 1 hour each in PBS/0.2% Tween-20 and 10 mg/mL heparin solutions at room temperature. All procedures were performed while shielded from light to preserve fluorescence.

Tissue clearing for 3D visualization

The tissues were gradually dehydrated in ascending concentrations of methanol (50%, 80%, and 100%) and incubated for 3 hours in a 66% dichloromethane/33% methanol mixture. They were then treated twice with 100% dichloromethane for 15 minutes. The samples were then immersed in dibenzyl ether (DBE) overnight. Representative images of pT1 CRC tissues before and after tissue clearing are shown in Fig. 1.

Visualization and 3D reconstruction

Immunolabeled cleared tissues were submerged in DBE within glass bottom culture dishes to match the refractive index between the glass, DBE, and tissue specimens. The specimens were imaged with an inverted confocal laser scanning microscope (LSM780, Carl Zeiss, Oberkochen, Germany). The signal of cytokeratin 19 conjugated to Alexa Fluor 488 was detected in both normal and malignant colorectal epithelial cells, using bandpass filter set 38 with an excitation range of 450/50 nm and emission range of 510/50 nm. The DyLight 405 signals indicate desmin expression in smooth muscle cells and were observed via a set of bandpass filters with an excitation range of 365 nm and an emission range of 445/50 nm. The Cyanine-3 signal of e-cadherin-labeled epithelial cells was observed using bandpass filter set 43 with an excitation range of 545/25 nm and an emission range of 605/70 nm. Despite treatment to reduce autofluorescence, residual signals persisted in the arterial elastic layers and collagen. This autofluorescence was useful for distinguishing arteries from veins. A z-stack image with a 2.5-μm interval was captured using a C-Apochromat 10×/0.45 W M27 objective lens, while a 1.5-μm interval z-stack image was obtained with a C Epiplan-Apochromat 20×/0.7 DIC M27 lens. The resulting continuous z-stack images were processed as single-layer images using Zen 2012 SP5 software (Carl Zeiss). Subsequently, the images were reconstructed into 3D images using IMARIS 9.8.0 software (Bitplane, Zurich, Switzerland) with each fluorescent signal rendered to distinctly visualize out-of-focus regions.

3D imaging and analysis

VI evaluation with 3D reconstruction for cohorts A and B was performed by two experienced gastrointestinal pathologists (J.S. and S.M.H.). In 3D analysis, VI was categorized into three phases: (1) intravasation, (2) intraluminal growth, and (3) ex-

https://doi.org/10.4132/jptm.2025.12.19

Fig. 1. Representative images of pT1 colorectal cancer tissues before (A) and after (B) tissue clearing.

travasation, as previously described [12]. Briefly, the differentiation between intravasation and extravasation is determined by the positioning of cancer cell foci in reference to the broader aggregation of cancer cells, either within or external to the muscular vein. The intravasation phase involves cancer cells forming small groups that extend into the vein's inner lining, while a considerably greater number of tumor cells are found beyond the muscular layer of the vein. Intraluminal growth refers to the accumulation of cancer cells inside the vein lumen, occurring without disruption to the muscular wall's structure. The extravasation phase refers to a limited number of cancer cells migrating beyond the muscular layer of the vein, while a greater population remains within the vein lumen.

Statistical analysis

Statistical analysis was performed using IBM SPSS software ver. 21 (IBM Corp., Armonk, NY, USA). Continuous variables were tested by the Student t-test and categorical data were evaluated by the chi-square test or Fisher's exact test. Statistical significance was defined as a p-value below .05.

RESULTS

Characteristics of the cases

The clinicopathologic features of the 61 patients in cohorts A and B with pT1 CRC are detailed in Table 1. Overall, the patients in cohorts A and B had a mean age of 62.1 ± 8.9 and 62.6 ± 11.3 years, respectively. Most CRCs were tubular adenocarcinomas (33 cases, 97.1% in cohort A; 26 cases, 96.3% in cohort B), except for one mucinous carcinoma in each group. Residual tubular adenocarcinomas were identified in all nine surgical resection specimens after previous EMR or ESD of cohort A. Because cohort A was selected with more cases of lymphovascular invasion for enrichment of inclusion of a possible VI, CRCs in cohort A had more lymphovascular invasion ($p < .001$), nodal metastasis ($p < .001$), and tumor budding ($p < .001$) than pT1 CRCs in cohort B. Patients in cohort A were followed for a median of 26 months (range, 1 to 38 months). Throughout the follow-up, lung metastasis was observed in one patient. The median follow-up time of cohort B could not be applied because specimens came from the Bio-Resource Center.

Tissue clearing of pT1 CRC tissues

Muscular veins were detected with desmin labeling. The distinction between veins and arteries relied on a combination of morphological features. Desmin immunolabeling of veins tended to be less pronounced than that of the arteries. The tunica media in muscular veins tended to exhibit reduced thickness relative to muscular arteries. A well-formed elastic lamina interna was observed in the arterial walls, appearing as autofluorescent concentric lines exhibiting a characteristic wavy pattern. As the assessment of VI is hindered by the normal expression of desmin in the muscularis mucosae, the current investigation concentrated on the VI of cancer cells within the submucosal layer.

Table 1. Clinicopathologic characteristics of cohort A (pT1 CRCs with enriched lymphovascular invasion) and cohort B (pT1 CRCs without knowing VI information) of pT1 CRC tissue

Characteristic	Total (n = 61)	Cohort A (n = 34)	Cohort B (n = 27)	p-value
Sex				
Male	33 (54.1)	22 (64.7)	11 (40.7)	.108
Female	28 (45.9)	12 (35.3)	16 (59.3)	
Age (yr)	62.3 ± 9.9	62.1 ± 8.9	62.6 ± 11.3	.835
Size (cm)	2.8 ± 1.5	1.9 ± 1.1	3.3 ± 1.3	<.001
Location				
Right colon	10 (16.4)	6 (17.6)	4 (14.8)	.958
Left colon	27 (44.3)	15 (44.1)	12 (44.4)	
Rectum	24 (39.3)	13 (38.2)	11 (40.7)	
Histologic subtype				
Tubular adenocarcinoma	59 (96.7)	33 (97.1)	26 (96.3)	>.99
Mucinous carcinoma	2 (3.3)	1 (2.9)	1 (3.7)	
Differentiation				
Well	20 (32.8)	6 (17.6)	14 (51.9)	.014
Moderate	36 (59.0)	26 (76.5)	10 (37.0)	
Poor	4 (6.6)	2 (5.9)	2 (7.4)	
NA	1 (1.6)	0	1 (3.7)	
pT category				
pT1	61 (100)	34 (100)	27 (100)	NA
pN category				
pN0	28 (45.9)	7 (20.6)	21 (77.8)	<.001
pN1	32 (52.5)	26 (76.5)	6 (22.2)	
pN2	1 (1.6)	1 (2.9)	0	
Lymphovascular invasion[a]				
Absent	23 (37.7)	5 (14.7)	18 (66.7)	<.001
Present	38 (62.3)	29 (85.3)	9 (33.3)	
Perineural invasion				
Absent	60 (98.4)	34 (100)	26 (96.3)	.443
Present	1 (1.6)	0	1 (3.7)	
Large vessel invasion				
Absent	59 (96.7)	32 (94.1)	27 (100)	.490
Present	2 (3.3)	2 (5.9)	0	
Tumor budding				
Absent	29 (47.5)	20 (58.8)	9 (33.3)	<.001
Present	18 (29.5)	14 (41.2)	4 (14.8)	
NA	14 (23.0)	0	14 (51.9)	

Values are presented as number (%) or mean ± SD.
CRC, colorectal cancer; NA, not applicable; SD, standard deviation.
[a]Based on the original surgical pathology report.

Comparison of VI detected in 2D (H&E, elastic, desmin) versus 3D

Evaluation of VI with 2D H&E only and a combination of H&E, elastic, and desmin staining was available only in cohort A. Subsequently, the prevalence of VI in cohort A was evaluated by H&E staining alone, combined H&E, elastic, and desmin staining, and 3D reconstruction. The prevalence of VI was 9/34 (26.5%) in H&E only, 14/34 (41.2%) in a combination of H&E, elastic, and desmin staining, and 17/34 (50.0%) in 3D evaluation (Table 2). The combination of H&E, elastic, and desmin

https://doi.org/10.4132/jptm.2025.12.19

Table 2. Frequency of venous invasion by H&E staining only, additional elastin and desmin staining and 3D evaluation

Evaluation	Cohort A	Cohort B	Cohort A + B	p-value
H&E only	9/34 (26.5)	Not applicable	9/34 (26.5)	
Combined H&E, elastic, and desmin	14/34 (41.2)	Not applicable	14/34 (41.2)	
3D reconstruction	17/34 (50.0)	10/27 (37.0)	27/61 (44.3)	.120

Values are presented as number (%).
3D, 3-dimensional.

Table 3. Comparison of LVI on surgical pathology report and re-evaluated venous invasion by H&E only, combined H&E, elastic, and desmin, and 3D reconstruction in cohort A

Evaluation	VI status	No. (%)		p-value
		LVI present	LVI absent	
H&E only	Present	8 (27.6)	1 (20.0)	.619
	Absent	21 (72.4)	4 (80.0)	
Combined H&E, elastic, and desmin	Present	13 (44.8)	1 (20.0)	.379
	Absent	16 (55.2)	4 (80.0)	
3D reconstruction	Present	15 (51.7)	2 (40.0)	.665
	Absent	14 (48.3)	3 (60.0)	

LVI, lymphovascular invasion; 3D, 3-dimensional; VI, venous invasion.

staining showed higher VI detection rates than in H&E slide evaluation alone; however, this difference did not reach statistical significance (p = .200). The difference in VI frequency between a combination of H&E, elastic, and desmin staining and 3D evaluation did not reach statistical significance (p = .465). However, 3D evaluation detected VI more frequently than in 2D H&E slide evaluation alone (p = .046). No significant difference in the prevalence of VI by 3D evaluation was observed between cohort A and cohort B (17/34, 50.0% vs. 10/27, 37.0%; p = .120) (Table 2).

Since lymphovascular invasion is composed of lymphatic invasion and VI, we compared the lymphovascular invasion status in the surgical pathology report with the reevaluated VI status using H&E only, combined H&E, elastic, and desmin staining, and 3D reconstruction (Table 3). The proportion of VI of the lymphovascular invasion in cohort A was gradually increased from 27.6% (8/29) evaluated by H&E only, 44.8% (13/29) by combined H&E, elastic, and desmin staining, to 51.7% (15/29) by 3D reconstruction.

Comparison of VI detected by 3D reconstruction and clinicopathologic characteristics

We compared VI detected by 3D reconstruction and clinicopathologic characteristics among pT1 CRCs in all cohorts A and B (Table 4). VI detected by 3D reconstruction was more commonly observed in CRCs with lymphovascular invasion (p < .001). There was a marginal significance between VI detected by 3D reconstruction and pN1 (p = .050). However, there was no significant association between VI detected by 3D reconstruction and other clinicopathologic characteristics.

3D pathologic evaluation of VI of pT1 CRCs

When cancer cells in the stroma are away from the muscular venous wall, they approach the vein to invade into blood vessels (Fig. 2). At this time, the cancer cells seem to extend projections toward the muscular veins, and small clusters are noted around the main projections.

In 27 out of 61 cases (44.3%) of thick tissue slabs from pT1 CRCs, 3D analysis revealed the presence of VI. We largely divided the process of VI into three phases: intravasation, intraluminal growth, and extravasation (Fig. 3).

Intravasation was observed in seven of the 27 cases (25.9%) characterized by cancer cells crossing the media of the involved veins. The presence of cancer cells in the media was commonly linked to damage to the smooth muscle layer of the muscular vein, which was indicated by a loss, reduction, or fragmentation of the desmin signal (Fig. 3A–C).

Intraluminal growth was observed in 22 of the 27 cases (81.5%). After entering the veins, cancer cells grow in a tube-like shape along the inner surface and line up next to the inner

Table 4. Comparison of VI detected by 3D reconstruction and clinicopathologic characteristics among pT1 colorectal cancers in all cohort

Characteristic	Total (n = 61)	3D VI + (n =27)	3D VI – (n = 34)	p-value
Sex				
Male	33 (54.1)	17 (63.0)	16 (47.1)	.209
Female	28 (45.9)	10 (37.0)	18 (52.9)	
Age (yr)	62.3 ± 9.9	64.1 ± 8.2	60.9 ± 11.1	.191
Size (cm)	2.8 ± 1.5	2.7 ± 1.6	2.4 ± 1.1	
Location				
Right colon	10 (16.4)	3 (11.1)	7 (20.6)	.068
Left colon	27 (44.3)	9 (33.3)	18 (52.9)	
Rectum	24 (39.3)	15 (55.6)	9 (26.5)	
Histologic subtype				
Tubular adenocarcinoma	59 (96.7)	26 (96.3)	33 (97.1)	>.99
Mucinous carcinoma	2 (3.3)	1 (3.7)	1 (2.9)	
Differentiation				
Well	20 (32.8)	6 (22.2)	14 (41.2)	.197
Moderate	36 (59.0)	17 (63.0)	19 (55.9)	
Poor	4 (6.6)	3 (11.1)	1 (2.9)	
NA	1 (1.6)	1 (3.7)	0	
pT category				
pT1	61 (100)	27 (100)	34 (100)	>.99
pN category				
pN0	28 (45.9)	8 (29.6)	20 (58.8)	.078
pN1	32 (52.5)	18 (66.7)	14 (41.2)	
pN2	1 (1.6)	1 (3.7)	0	
Lymphovascular invasion[a]				
Absent	23 (37.7)	3 (11.1)	20 (58.8)	<.001
Present	38 (62.3)	24 (88.9)	14 (41.2)	
Perineural invasion				
Absent	60 (98.4)	26 (96.3)	34 (100)	.490
Present	1 (1.6)	1 (3.7)	0	
Large vessel invasion				
Absent	59 (96.7)	26 (96.3)	33 (97.1)	>.99
Present	2 (3.3)	1 (3.7)	1 (2.9)	
Tumor budding				
Absent	29 (47.5)	12 (44.4)	17 (50.0)	<.001
Present	18 (29.5)	8 (29.6)	10 (29.4)	
NA	14 (23.0)	7 (25.9)	7 (20.6)	

Values are presented as number (%) or mean ± SD.
VI, venous invasion; 3D, 3-dimensional; NA, not applicable; SD, standard deviation.
[a]Based on the original surgical pathology report.

wall of the veins (Fig. 3D–F). In certain instances, small clusters of fragmented cancer cells appeared protruding from the main tube and subsequently separated into smaller groups or individual cells within the veins.

Of the 27 CRCs with VI, five (18.5%) had foci of extravasation. Although a greater number of extravasation foci were observed compared to intravasation, the difference did not reach statistical significance (p = .377). When cancer cells moved out of the muscle layer of the vein wall, substantial, cohesive aggregates of cancer cells transformed into individual, dispersed cells or small clusters, extending from the lumen beyond the muscular venous wall, suggesting infiltration of the venous wall (Fig. 3G–I).

https://doi.org/10.4132/jptm.2025.12.19

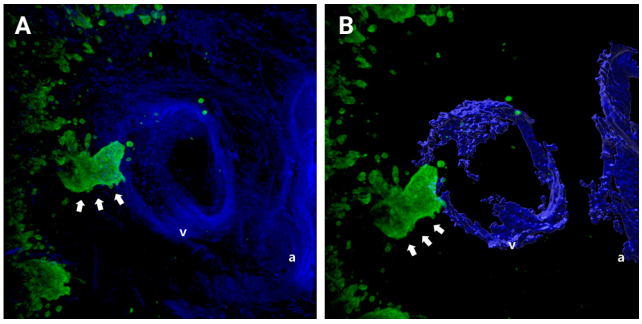

Fig. 2. Representative images of the approaching of cancer cell clusters (arrows) to the muscular venous wall. (A) Merged cytokeratin 19 and desmin image. (B) Rendered image of (A). Green labeling for cytokeratin 19 highlights cancer cells, blue labeling for desmin highlights the muscular layer of the muscular vein. a, artery; v, vein.

In addition to identifying each phase separately, we observed the co-occurrence of intravasation and intraluminal growth phases in three cases, and intraluminal growth with extravasation in five cases. All phases of intravasation, intraluminal growth, and extravasation were observed in one case (Fig. 4).

Among the three phases, intraluminal growth occurred at a significantly higher frequency compared to intravasation ($p < .001$) and extravasation ($p < .001$) (Fig. 5). While a greater number of intravasation foci were identified relative to extravasation, this difference lacked statistical significance ($p = .377$). When cancer cells infiltrated through the muscular layer toward the outer side of the veins, they initially organized into cord-like structures before detaching into individual cance r

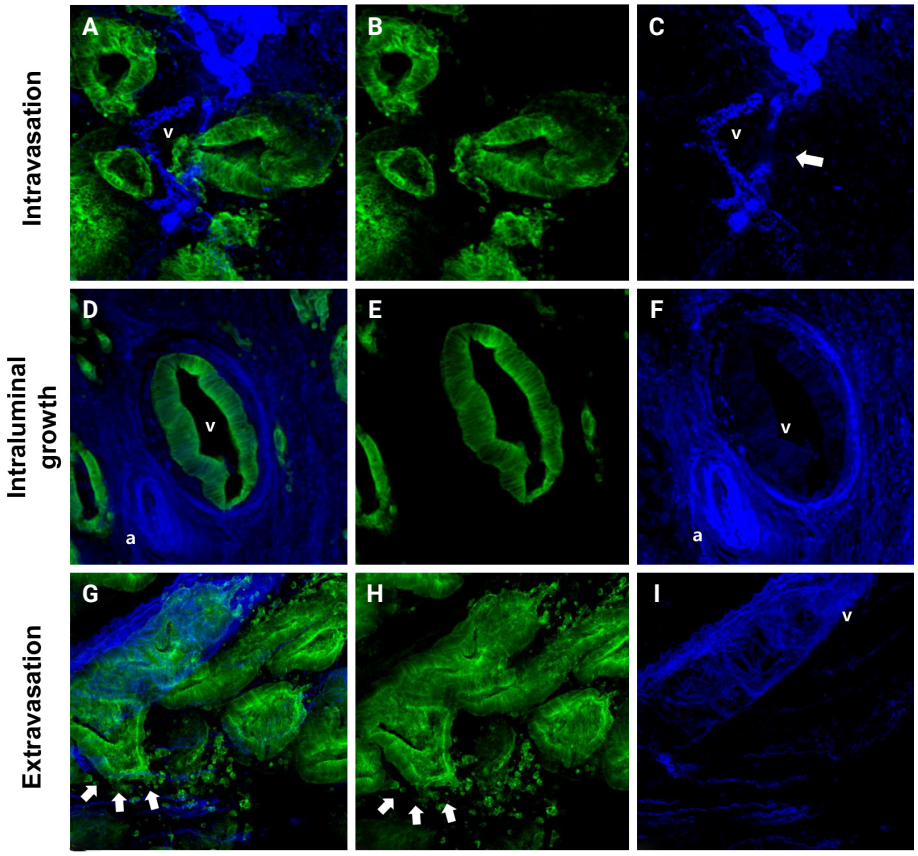

Fig. 3. Representative images of the intravasation (A–C), intraluminal growth (D–F), and extravasation (G–I) phases of venous invasion. The multicolor immunofluorescence labeling of colorectal cancer tissue demonstrates the intravasation, intraluminal growth, and extravasation phases of the muscular venous invasion. The green labeling for cytokeratin 19 highlights the cancer cells; the blue labeling for desmin highlights the muscular layer of the muscular vein. (A–C) Intravasation phase; cancer cells (green) are penetrating the walls (arrow) of blood vessels (blue). (D–F) Intraluminal growth phase; cancer cells (green) maintained their tubular shape within the muscular venous wall (blue). (G–I) Extravasation phase, cancer cells (arrows) penetrate out from the walls of the muscular vein. (A, D, G) Merged cytokeratin 19, desmin image. (B, E, H) Cytokeratin 19 single image. (C, F, I) Desmin single image. Arrows indicate destruction of smooth muscle of muscular vein. a, artery; v, vein.

cells or small clusters, following disruption of the muscular layer (extravasation) (Fig. 3G, H).

Comparison of VI between pT1 and pT2-T4 CRCs

We compared the prevalence of VI evaluated by 3D between the pT1 CRCs in this study and pT2–4 CRCs in a previous study that used similar techniques [12]. There was no significant difference (p = .258) in the prevalence of VI between pT1 CRCs in this study and pT2–4 CRCs in the previous study [12]. In addition, although there was more intravasation in pT1 CRCs and more extravasation in pT2–4 CRCs, the study found no significant difference in the prevalence of each phase of VI, including intravasation (p = .134), intraluminal growth (p = .186), and extravasation (p = .291) phases between pT1 CRCs in this study and pT2–4 CRCs in the previous study (Fig. 5).

Intraluminal growth was the most predominant phase of VI, occurring more frequently than other phases, such as intravasation and extravasation (p < .05).

Changes in E-cadherin expression throughout the VI process

E-cadherin plays an essential role in cellular adhesion, cell-to-cell recognition, and maintenance of epithelial polarity. Loss of E-cadherin expression serves as an important marker for epithelial-to-mesenchymal transition (EMT). E-cadherin expression varied across the phases of VI, with intact E-cadherin expression detected in the cancer cell clusters at the foci of muscular vein wall invasion. However, a tongue-like projection of small clusters (arrows in Fig. 6) within the lumen, originating from the primary cancer cells outside the muscular layer, or isolated cancer cells (arrows in Fig. 6) and small clusters that penetrated the muscular layer within a venous lumen, exhibited loss of E-cadherin expression (intravasation phase) (Fig. 6).

E-cadherin expressions altered as cancer cells formed tube-like formations and gathered along the inside of the vein wall. In the muscle layer of the vein wall, some cancer cells with tongue-like projections lost E-cadherin expression (intraluminal growth) (arrows in Fig. 7). Likewise, several cancer cells disassociated from the primary tubular structure at the leading edge and exhibited a reduction in E-cadherin expression.

When cancer cells left the muscle layer of the venous wall, large, cohesive clusters of cancer cells showed intact E-cadherin staining. Nonetheless, isolated neoplastic cells and small projec-

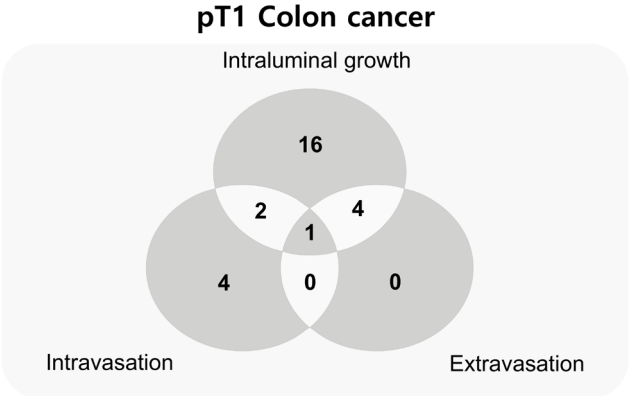

Fig. 4. Venn diagram of the number of cases at each phase and mixed phases of muscular venous invasion of pT1 colorectal cancers.

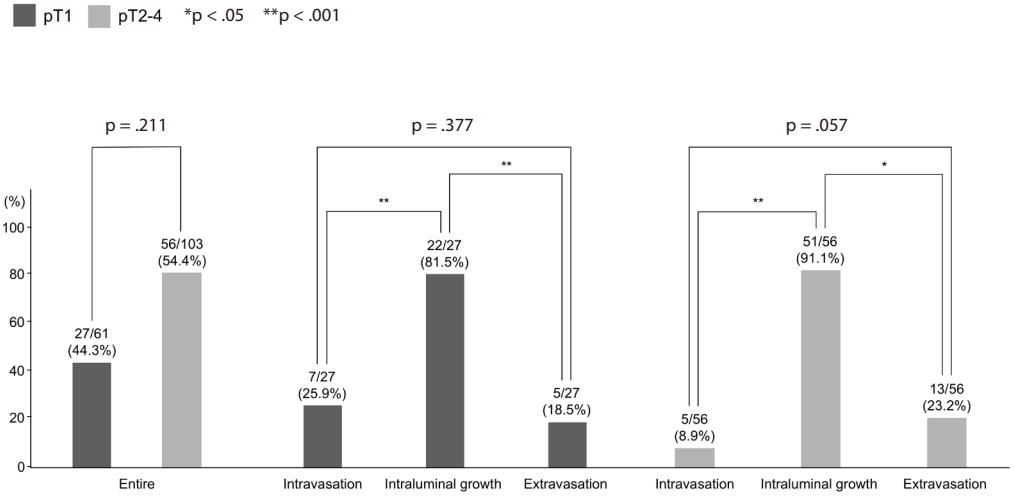

Fig. 5. Comparison of each phase of the venous invasion between pT1 and pT2–4 colorectal cancers.

https://doi.org/10.4132/jptm.2025.12.19

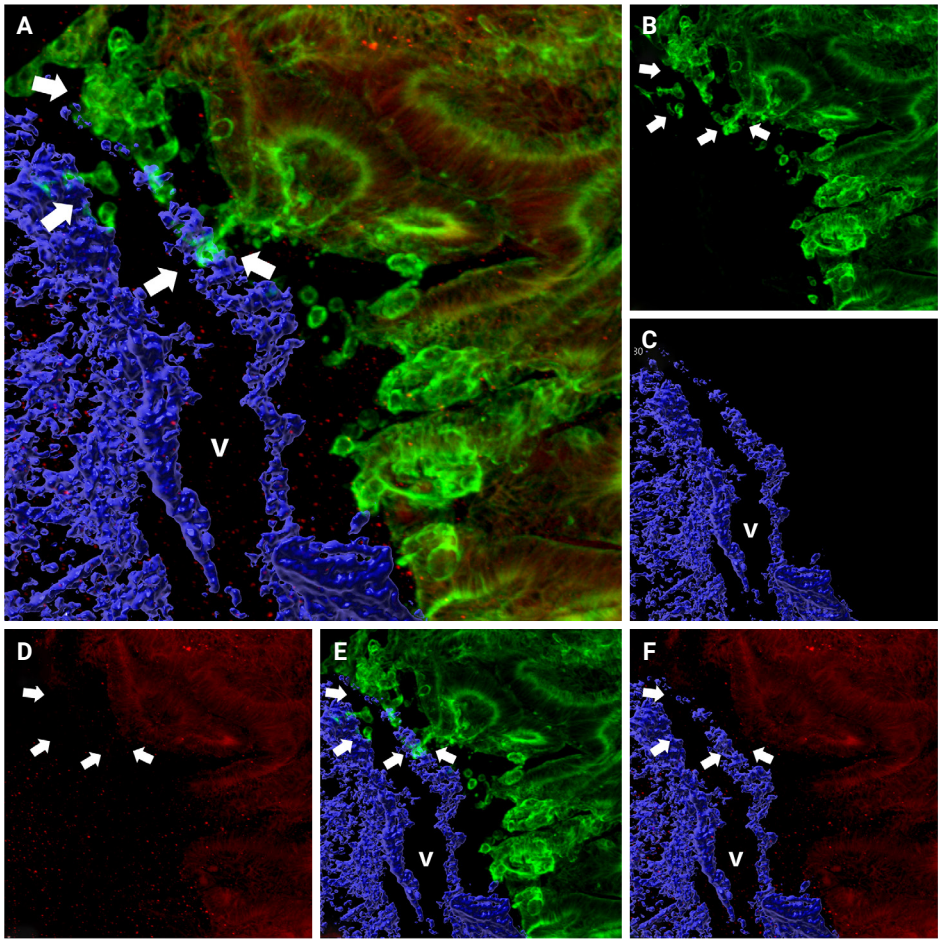

Fig. 6. Changes of E-cadherin expression during the intravasation phase. Intact E-cadherin expression was observed in the majority of cancer cell clusters outside the venous wall, but the loss of E-cadherin expression was observed in small numbers of cancer clusters (arrows) at the point of penetration and within the luminal portion of the muscular venous wall. (A) Merged cytokeratin 19, E-cadherin, and desmin image. Green labeling for cytokeratin 19 highlights cancer cells, red labeling indicates E-cadherin, and blue labeling for desmin highlights the muscular layer of muscular veins. (B) Cytokeratin 19 image. (C) Desmin image. (D) E-cadherin image. (E) Cytokeratin 19 and desmin image. (F) E-cadherin and desmin image. a, artery; v, vein.

tions within the stroma next to the venous wall demonstrated decreased E-cadherin expression (arrows in Fig. 8).

DISCUSSION

The present study investigated submucosal VI in pT1 CRCs by 3D image analysis. The high prevalence of VI identified (37.0%) underscores the significance of VI even at this early stage of CRCs and indicates the necessity for a comprehensive evaluation to provide accurate prognostic and therapeutic decision-making. Additionally, the results of the current study align with our previous investigation on pT2–4 CRCs [12], which showed similar phases of tumor spread in both the early and later stages of the CRCs. All three phases of VI, which are intravasation, intraluminal growth, and extravasation, were observed in pT1 CRCs. Mixed phases of VI—intravasation, intraluminal growth, and extravasation—were also observed. The present study shows that extravasation is an important final step in the metastatic process, indicating that even in pT1 CRCs, extravasation can happen, allowing cancer cells to leave the muscular veins and spread out to the surrounding tissues. The extravasation of neoplastic cells within the colon tissue indicates that cancer cells use the muscular vein as one of the routes to spread out, in other words, "intratumoral spreading."

Furthermore, both pT1 and pT2–4 CRCs exhibit similar patterns of E-cadherin expression changes across the phases

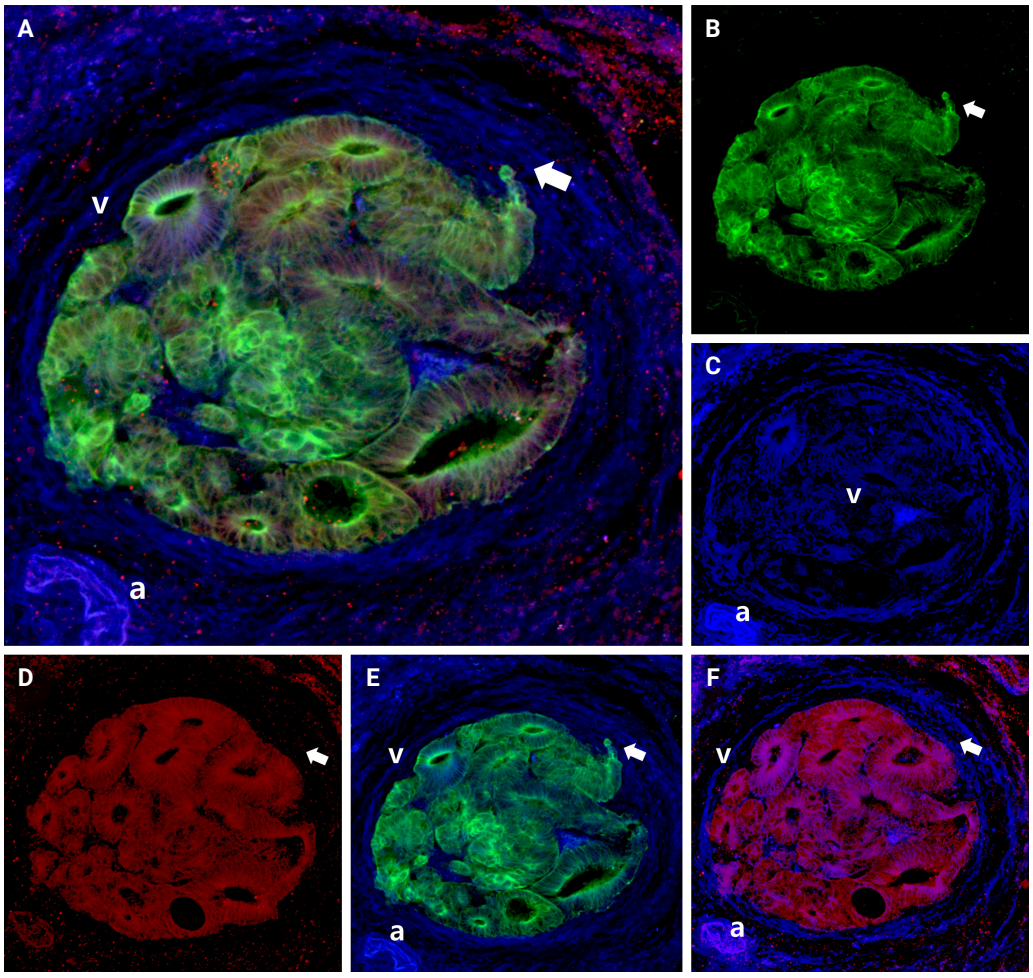

Fig. 7. Changes of E-cadherin expression during the intraluminal growth phase. Multicolor immunofluorescence labeling of colorectal cancer tissue showing the intraluminal growth phase of the muscular venous invasion. The majority of cancer cells forming well-oriented tubular structures show E-cadherin expression. However, a few cancer cells with tongue-like projections showed loss of E-cadherin expression (arrow). (A) Merged cytokeratin 19, E-cadherin, and desmin image. Green labeling for cytokeratin 19 highlights cancer cells, red labeling indicates E-cadherin, and blue labeling for desmin highlights the muscular layer of muscular veins. (B) Cytokeratin 19 image. (C) Desmin image. (D) E-cadherin image. (E) Cytokeratin 19 and desmin image. (F) E-cadherin and desmin image. a, artery; v, vein.

of VI. Neoplastic cells that invade the venous wall often lose E-cadherin expression in their projections. Notably, the present observations indicated that E-cadherin was re-expressed when neoplastic cells gained access to the vascular lumen and lined the venous wall on the luminal side, mirroring the behavior observed in pT2–4 CRCs. At the extravasated sites, neoplastic cells often appeared as single dispersed cells or small clusters exhibiting loss of E-cadherin expression. This observation was consistent with the results of the previous study and concluded that E-cadherin expression was continuously changed across VI both in pT1 and pT2–4 CRCs. Based on our observations, we propose a sequence and classification of the phases of muscular VI in pT1 CRC, as illustrated in Fig. 9.

Applying additional elastic staining detected more foci of VI compared to routine 2D H&E staining used in previous studies [24-26]. For example, Kim and colleagues assessed 418 patients with CRCs in stages I to III, and observed VI in 11% using conventional H&E staining. They noted VI in 35% of the CRC cases with the addition of elastic staining [25]. Similarly, Fei et al. [24] noted that 35% of 277 patients with stage I to IV CRCs had VI with routine H&E staining alone, whereas 56% of patients demonstrated VI when elastic staining was additionally employed [25]. Despite the differing cohorts in previous studies (stages I to III by Kim et al. [25] and stages I to IV by Fei et al.

https://doi.org/10.4132/jptm.2025.12.19

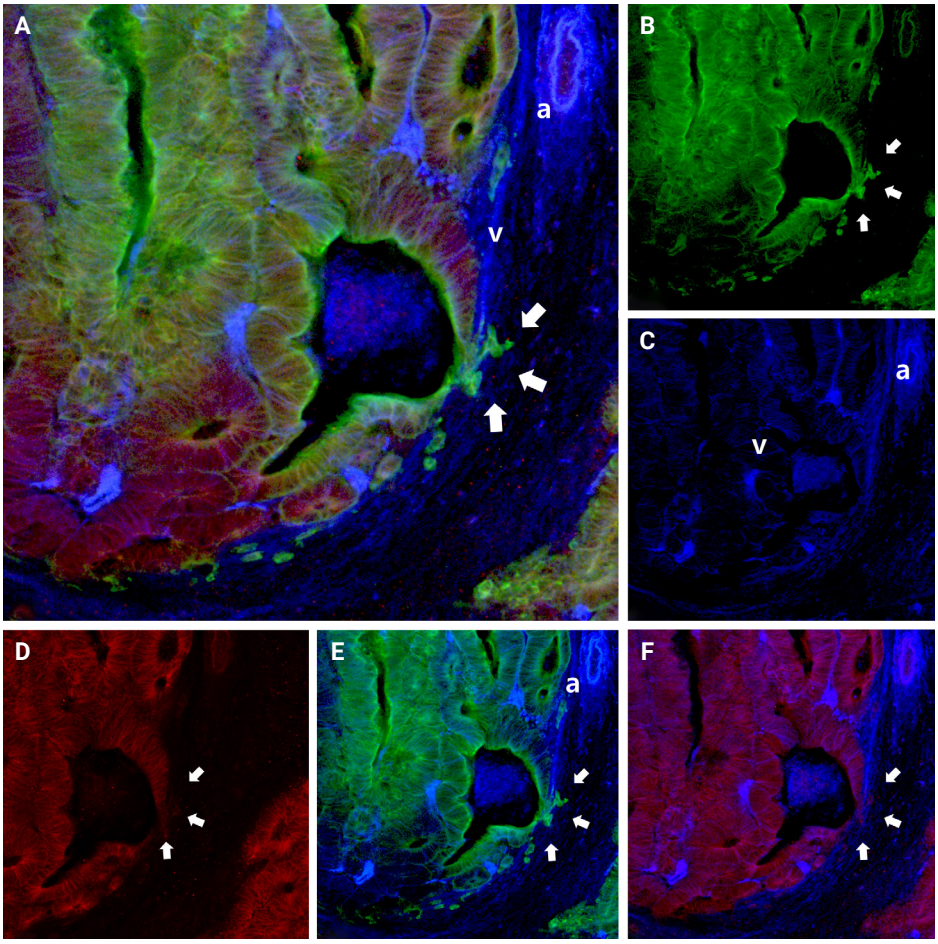

Fig. 8. Changes of E-cadherin expression during the extravasation phase. Multicolor immunofluorescence labeling of colorectal cancer tissue shows that the majority of cancer cells forming well-oriented tubular structures within the venous wall with E-cadherin expression. However, singly scattered cells and smaller numbers of cancer cells with tongue-like projections show a loss of E-cadherin expression (arrows). (A) A 3D reconstruction image of muscular venous invasion with a merged image of cytokeratin 19, E-cadherin, and desmin. Green labeling for cytokeratin 19 highlights cancer cells, red labeling indicates E-cadherin, and blue labeling for desmin highlights the muscular layer of muscular veins. (B) Cytokeratin 19 image. (C) Desmin image. (D) E-cadherin image. (E) Cytokeratin 19 and desmin image. (F) E-cadherin and desmin image. a, artery; v, vein.

[24]) compared to the present study (pT1), we observed an increased detection of VI with a combination of H&E, elastic, and desmin staining (41%) versus to H&E staining alone (Table 3). The findings of this study, in conjunction with previous research, suggest that additional elastic or desmin staining may identify additional foci of VI that are not discernible with H&E staining alone. The addition of elastic or desmin staining may be beneficial for detecting additional foci of VI when such foci are not clearly discernible on conventional H&E staining. In addition, 3D reconstruction detected more foci of VI, which were not noted by conventional 2D H&E staining nor by additional elastic staining and desmin immunolabeling (Fig. 10). The increased detection of VI in CRCs with 3D evaluation emphasizes its superiority in evaluating the complex architecture of CRCs with the presence of VI.

In one cohort of pT1 CRCs specimens analyzed in the present study, nine pT1 CRCs were previously subjected to EMR or ESD, nevertheless, residual tubular adenocarcinomas were observed in all nine resected specimens, and a significant incidence of VI was also identified. Based on the clinical protocols for managing pT1 CRCs, EMR or ESD of pT1 CRCs containing high-risk histopathologic features, such as CRCs with poor differentiation, presence of lymphovascular invasion, high tumor budding, and resection marginal involvement, necessitates further surgical re-

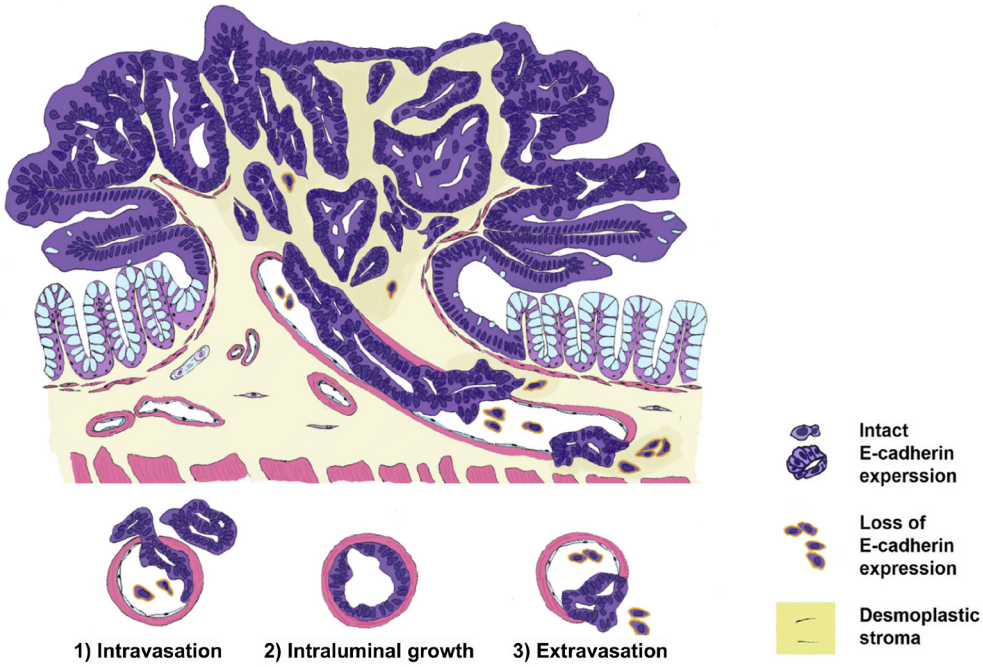

Fig. 9. Proposed sequence and phases of muscular venous invasion of pT1 colorectal cancers. The loss and re-expression of E-cadherin were observed in the following 3 phases: (1) intravasation, (2) intraluminal growth, and (3) extravasation.

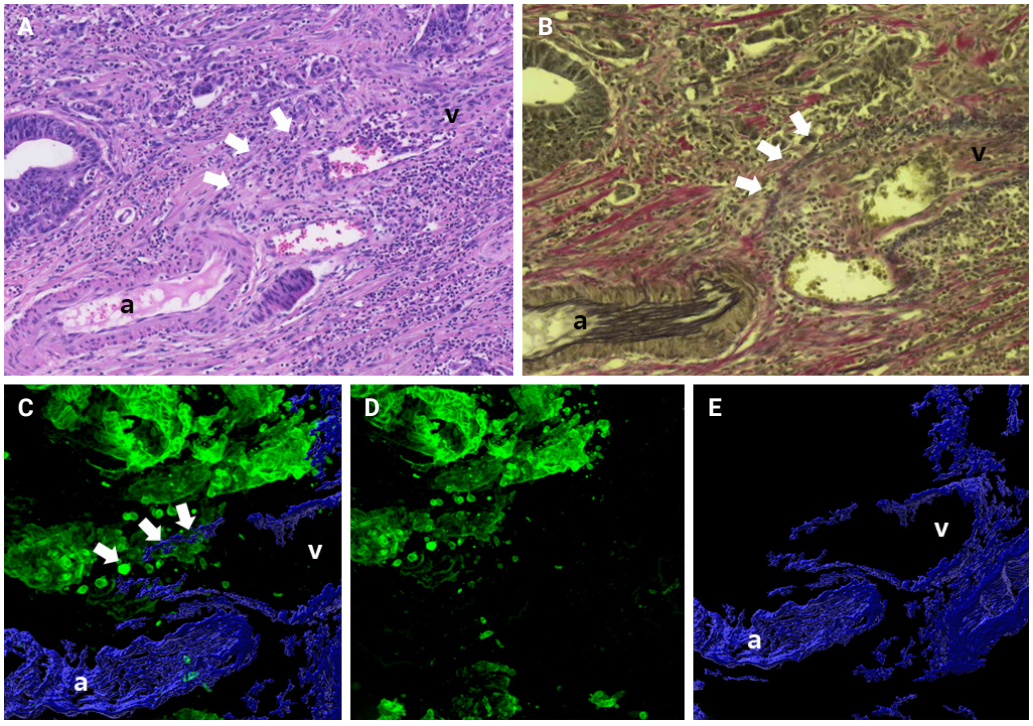

Fig. 10. Venous invasion (white arrows) is not detected by conventional 2-dimensional hematoxylin and eosin staining (A) or by additional elastic staining (B), but detected by 3-dimensional reconstruction (C–E). (C) Merged cytokeratin 19 and desmin image. Green labeling for cytokeratin 19 highlights cancer cells and blue labeling for desmin highlights the muscular layer of muscular veins. (D) Cytokeratin 19 image. (E) Desmin image. a, artery; v, vein.

https://doi.org/10.4132/jptm.2025.12.19

sections [27,28]. The high prevalence of muscular VI observed in the present study may indicate an increased possibility of distant metastasis of CRCs. During the follow-up period, we observed lung metastasis in one case. VI was detected on the 3D reconstruction and additional elastic and desmin staining evaluation, but not on conventional H&E slide evaluation.

In recent years, the examination of VI in CRCs has attracted considerable interest, especially regarding its effects on disease progression and patient outcomes. Table 5 summarizes that several prior studies have shown varying prevalence of VI, exhibiting significant discrepancies in recurrence rates and diagnostic criteria. The previous studies indicated up to 20% of VI in pT1 CRCs [29-31]. The incidence of VI detected by 2D H&E staining in the present study was 26.5% (9/34), which is comparable to the previous studies. The incidence of VI was higher when assessed using surgical resection specimens compared to EMR or ESD specimens in the previous study. These data may suggest varying inclusion criteria for the high risk of recurrence in surgical resection specimens.

Using additional elastic staining methods, such as Victoria Blue and Elastica van Gieson staining, has been shown to improve the detection rate of VI from 25% to 34% [32-35]. The rate of VI with additional elastic and desmin staining in the present study was 41.2% (14/34), slightly higher than in previous studies. Consistent with the previous studies, additional elastic staining revealed a higher number of VI foci in the assessment of pT1 CRCs compared to H&E alone.

To the best of our knowledge, this is the first study to investigate VI in pT1 CRCs using 3D pathologic evaluation. About half of the surgically resected pT1 CRCs contained VI. These findings highlight how important 3D histopathological reconstruction is for better understanding the structure of CRC and VI. The absence of 3D evaluations in earlier studies has under-evaluated VI in pT1 CRCs. Identifying muscular VI is important for the treatment of patients with CRCs before distant metastasis occurs. Some previous studies evaluated the metastatic rate of endoscopically or surgically resected pT1 CRCs, which ranged from 0.6% to 3% [28-31,34,35]. Distant lung metastasis was observed in one of the 34 cases (2.9%) with VI in pT1 CRCs in the present study, and these results align with those of the previous studies [28-31,34,35].

Despite providing valuable insights, this study has several limitations that should be acknowledged. First, the relatively small sample size of the cohort may have limited the statistical power of the study, potentially impacting the generalizability of the findings, as pT1 CRCs not so frequently require surgical intervention. Second, though various markers of EMT—such as ZEB1, ZEB2, TWIST1, vimentin, and N-cadherin—have been identified, this study focused solely on E-cadherin immunolabeling. This was necessitated by the constraint of using up to four antibodies simultaneously in 3D reconstruction. Future investigations incorporating E-cadherin together with additional

Table 5. Frequency of VI of pT1 colorectal cancers in the previous studies

Study	Frequency of VI (%)	Recurrence rates (%)	Classification	Treatment options	Evaluation
Ishii et al. (2009) [32]	34/136 (25.0)	-	-	LE + Surgery	2D (EVG)
Kobayashi et al. (2011) [29]	109/543 (20.1)	1.5	-	Surgery (no ER)	2D (H&E)
Tamaru et al. (2017) [30]	10/121 (8.3)	5		ER	2D (H&E)
	37/238 (15.6)	5.5	-	ER + Surgery	
	59/342 (17.3)	3.8		Surgery	
Mochizuki et al. (2020) [33]	216/776 (27.8)	-	Left	ER + Surgery	2D (H&E, VB)
	89/366 (24.3)	-	Right		
Nishimura et al. (2021) [34]	94/370 (25.4)	1.6	-	ER, ER + surgery	2D (VB, EVG)
Yamaoka et al. (2022) [35]	174/519 (33.5)	0.6	Low-risk T1b	Surgery	2D (EVG)
		3.4	High-risk T1b		
Johnstone et al. (2023) [31]	16/96 (16.7)	0	-	ER	2D (H&E)
Oka et al. (2024) [28]	81/1,257 (6.4)	1.7	-	LE alone	2D (VB, EVG)
	471/1,512 (31.2)	2.5		LE + Surgery	
Present study (2026)	17/34 (50.0)	3	Enriched LVI	ER + Surgery	2D (H&E, EVG), 3D
	10/27 (37.0)	0	Without knowing VI information		

VI, venous invasion; LE, local excision; 2D, 2-dimensional; EVG, Elastic van Gieson; ER, endoscopic resection; VB, Victoria Blue; LVI, lymphovascular invasion.; 3D, 3-dimensional.

EMT markers may enhance our understanding and further validate our conclusions. Furthermore, the proposed 3D-based VI detection approach was designed primarily for research purposes to explore its feasibility and potential value. Although the method demonstrated promising performance for detecting more foci of VI, the clinical application of 3D visualization is currently impractical due to the long experiment time of about 2 weeks for the experimental procedure. Developing the advanced 3D visualization with reduced experiment time of tissue clearing in the future may make this technique applicable for clinical diagnosis.

In conclusion, this study highlights the importance of 3D histopathological reconstruction for identifying VI in pT1 CRCs, showing that about 37% of pT1 CRCs have VI. All three phases of VI—intravasation, intraluminal growth, and extravasation—were detected. Notably, loss followed by re-expression of E-cadherin was frequently observed across the phases of VI, suggesting that EMT is not continuously maintained in the process of VI in pT1 CRCs. The present study also suggests that VI may serve as a pathway for intratumoral spreading in a subset of pT1 CRCs, which offers new insights into disease management and prognosis in patients with pT1 CRCs.

Ethics Statement

Institutional Review Board approval with a waiver of patient consent was obtained (approval number: 2023-1417). The biospecimen and data used in this study was provided Asan Bio-Resource Center, the institutional biobank, a member of the Korea Biobank Network (approval number: 2023-24[275]).

Availability of Data and Material

The datasets generated or analyzed during the study are available from the corresponding author on reasonable request.

Code Availability

Not applicable.

ORCID

Jihyun Park https://orcid.org/0009-0009-1166-9280
Mi-Ju Kim https://orcid.org/0000-0002-4296-3310
Yeon Wook Kim https://orcid.org/0009-0004-5843-7579
Byong-Wook Lee https://orcid.org/0009-0007-0585-0951
Junyoung Shin https://orcid.org/0000-0002-4833-9738
Jinho Shin https://orcid.org/0000-0003-0654-7392
Chan-Gi Pack https://orcid.org/0000-0002-6578-3099
Dong-Hoon Yang https://orcid.org/0000-0001-7756-2704
Jihun Kim https://orcid.org/0000-0002-8694-4365
In Ja Park https://orcid.org/0000-0001-5355-3969
Ralph H. Hruban https://orcid.org/0000-0003-4554-5672
Seung-Mo Hong https://orcid.org/0000-0002-8888-6007

Author Contributions

Conceptualization: JP, RH, SH. Formal analysis: JP, SH. Investigation: JP, MK, YK, BL, JS, JS. Funding acquisition: SH. Methodology: JP, RH, SH. Software: JP. Supervision: RH, SH. Writing—original draft: JP, SH. Writing—review & editing: JP, DY, CP, JK, RH, SH. Approval of final manuscript: all authors.

Conflicts of Interest

The authors declare that they have no potential conflicts of interest.

Funding Statement

This work was supported by the National Research Foundation of Korea (NRF) grant funded by the Korea goverment (MSIT) (No. RS-2023-NR077117) to SH.

Acknowledgments

This work was presented, in part, at the annual meeting of the Korean Society of Pathologists 2024, Seoul, Republic of Korea, October 31, 2024.
The biospecimen and data used in this study were were partly provided by the Asan Bio-Resource Center, Korea Biobank Network, which is supported by the National Institute of Health (NIH) research project: 2023-24 (275).

REFERENCES

1. Park EH, Jung KW, Park NJ, et al. Cancer statistics in Korea: incidence, mortality, survival, and prevalence in 2021. Cancer Res Treat 2024; 56: 357-71.
2. Siegel RL, Kratzer TB, Giaquinto AN, Sung H, Jemal A. Cancer statistics, 2025. CA Cancer J Clin 2025; 75: 10-45.
3. Kallini JR, Gabr A, Abouchaleh N, et al. New Developments in interventional oncology: liver metastases from colorectal cancer. Cancer J 2016; 22: 373-80.
4. Wang J, Li S, Liu Y, Zhang C, Li H, Lai B. Metastatic patterns and survival outcomes in patients with stage IV colon cancer: a population-based analysis. Cancer Med 2020; 9: 361-73.
5. Talbot IC, Ritchie S, Leighton M, Hughes AO, Bussey HJ, Morson

https://doi.org/10.4132/jptm.2025.12.19

BC. Invasion of veins by carcinoma of rectum: method of detection, histological features and significance. Histopathology 1981; 5: 141-63.
6. Braet F, Nagatsuma K, Saito M, Soon L, Wisse E, Matsuura T. The hepatic sinusoidal endothelial lining and colorectal liver metastases. World J Gastroenterol 2007; 13: 821-5.
7. Paschos KA, Majeed AW, Bird NC. Natural history of hepatic metastases from colorectal cancer: pathobiological pathways with clinical significance. World J Gastroenterol 2014; 20: 3719-37.
8. Talbot IC, Ritchie S, Leighton MH, Hughes AO, Bussey HJ, Morson BC. The clinical significance of invasion of veins by rectal cancer. Br J Surg 1980; 67: 439-42.
9. Howlett CJ, Tweedie EJ, Driman DK. Use of an elastic stain to show venous invasion in colorectal carcinoma: a simple technique for detection of an important prognostic factor. J Clin Pathol 2009; 62: 1021-5.
10. Kingston EF, Goulding H, Bateman AC. Vascular invasion is underrecognized in colorectal cancer using conventional hematoxylin and eosin staining. Dis Colon Rectum 2007; 50: 1867-72.
11. Vass DG, Ainsworth R, Anderson JH, Murray D, Foulis AK. The value of an elastic tissue stain in detecting venous invasion in colorectal cancer. J Clin Pathol 2004; 57: 769-72.
12. Jung D, Shin J, Park J, et al. Frequent intraluminal growth of large muscular veins in surgically resected colorectal cancer tissues: a 3-dimensional pathologic reconstruction study. Mod Pathol 2023; 36: 100082.
13. Norton EJ, Bateman AC. Risk assessment in pT1 colorectal cancer. J Clin Pathol 2024; 77: 225-32.
14. Benson AB, Venook AP, Al-Hawary MM, et al. Rectal cancer, version 2.2018, NCCN Clinical Practice Guidelines in Oncology. J Natl Compr Canc Netw 2018; 16: 874-901.
15. Benson AB 3rd, Venook AP, Cederquist L, et al. Colon cancer, version 1.2017, NCCN Clinical Practice Guidelines in Oncology. J Natl Compr Canc Netw 2017; 15: 370-98.
16. Glynne-Jones R, Wyrwicz L, Tiret E, et al. Rectal cancer: ESMO clinical practice guidelines for diagnosis, treatment and follow-up. Ann Oncol 2017; 28: iv22-40.
17. Hashiguchi Y, Muro K, Saito Y, et al. Japanese Society for Cancer of the Colon and Rectum (JSCCR) guidelines 2019 for the treatment of colorectal cancer. Int J Clin Oncol 2020; 25: 1-42.
18. Kaltenbach T, Anderson JC, Burke CA, et al. Endoscopic removal of colorectal lesions: recommendations by the US Multi-Society Task Force on Colorectal Cancer. Am J Gastroenterol 2020; 115: 435-64.
19. Labianca R, Nordlinger B, Beretta GD, et al. Early colon cancer: ESMO clinical practice guidelines for diagnosis, treatment and follow-up. Ann Oncol 2013; 24 Suppl 6: vi64-72.
20. Park CH, Yang DH, Kim JW, et al. Clinical practice guideline for endoscopic resection of early gastrointestinal cancer. Korean J Gastroenterol 2020; 75: 264-91.
21. Pimentel-Nunes P, Dinis-Ribeiro M, Ponchon T, et al. Endoscopic submucosal dissection: European Society of Gastrointestinal Endoscopy (ESGE) guideline. Endoscopy 2015; 47: 829-54.
22. Washington MK, Berlin J, Branton P, et al. Protocol for the examination of specimens from patients with primary carcinoma of the colon and rectum. Arch Pathol Lab Med 2009; 133: 1539-51.
23. Yoshida M, Suwa T, Shimada S, et al. Desmin immunostaining is effective for improving interobserver variability in the depth assessment of the submucosal invasion of colorectal cancers. Hum Pathol 2023; 141: 149-57.
24. Fei LY, Patel SV, Popa T, et al. Venous invasion detectable only by elastic stain shows weak prognostic value in colon cancer. Histopathology 2024; 84: 1038-46.
25. Kim HJ, Choi GS, Seo AN, et al. Prognostic value of venous invasion detected by elastin stain may surpass lymph node status in colon cancer. Dis Colon Rectum 2021; 64: 955-63.
26. Messenger DE, Driman DK, Kirsch R. Developments in the assessment of venous invasion in colorectal cancer: implications for future practice and patient outcome. Hum Pathol 2012; 43: 965-73.
27. Ito T, Eishi Y, Kobayashi D, Akashi T, Koike M, Ohashi K. A risk stratification for nodal metastasis in T1 colorectal cancer after successful therapeutic endoscopy. Gastrointest Endosc 2022; 96: 131-4.
28. Oka S, Tanaka S, Kajiwara Y, et al. Treatment decision for locally resected T1 colorectal carcinoma-verification of the Japanese guideline criteria for additional surgery based on long-term clinical outcomes. Am J Gastroenterol 2024; 119: 2019-27.
29. Kobayashi H, Mochizuki H, Morita T, et al. Characteristics of recurrence after curative resection for T1 colorectal cancer: Japanese multicenter study. J Gastroenterol 2011; 46: 203-11.
30. Tamaru Y, Oka S, Tanaka S, et al. Long-term outcomes after treatment for T1 colorectal carcinoma: a multicenter retrospective cohort study of Hiroshima GI Endoscopy Research Group. J Gastroenterol 2017; 52: 1169-79.
31. Johnstone MS, McSorley ST, McMahon AJ. Management of malignant T1 colorectal cancer polyps: results from a 10-year prospective observational study. Colorectal Dis 2023; 25: 1960-72.
32. Ishii M, Ota M, Saito S, Kinugasa Y, Akamoto S, Ito I. Lymphatic vessel invasion detected by monoclonal antibody D2-40 as a predictor of lymph node metastasis in T1 colorectal cancer. Int J

Colorectal Dis 2009; 24: 1069-74.
33. Mochizuki K, Kudo SE, Ichimasa K, et al. Left-sided location is a risk factor for lymph node metastasis of T1 colorectal cancer: a single-center retrospective study. Int J Colorectal Dis 2020; 35: 1911-9.
34. Nishimura T, Oka S, Tanaka S, et al. Clinical significance of immunohistochemical lymphovascular evaluation to determine additional surgery after endoscopic submucosal dissection for colorectal T1 carcinoma. Int J Colorectal Dis 2021; 36: 949-58.
35. Yamaoka Y, Shiomi A, Kagawa H, et al. Lymph node metastasis in T1 colorectal cancer with the only high-risk histology of submucosal invasion depth ≥ 1000 mum. Int J Colorectal Dis 2022; 37: 2387-95.

https://doi.org/10.4132/jptm.2025.12.19

JPTM

ORIGINAL ARTICLE

pISSN 2383-7837 · eISSN 2383-7845

Journal of Pathology and Translational Medicine 2026; 60: 263-279
https://doi.org/10.4132/jptm.2025.12.20

Progastrin, annexin A2, and tumor-associated macrophages in gastric adenocarcinoma

Konstantinos Christofidis[1], Rodanthi Fioretzaki[2], Stylianos Mavropoulos Papoudas[3], Nikolaos Charalampakis[4], Nikolaos Kavantzas[1], Dimitrios Schizas[5], Stratigoula Sakellariou[1]

[1]First Department of Pathology, School of Medicine, National and Kapodistrian University of Athens, Athens, Greece
[2]Department of Hematology, Laiko General Hospital of Athens, National and Kapodistrian University of Athens, Athens, Greece
[3]Independent Researcher, Athens, Greece
[4]Department of Medical Oncology, Metaxa Cancer Hospital of Piraeus, Piraeus, Greece
[5]First Department of Surgery, National and Kapodistrian University of Athens, Laiko General Hospital of Athens, Athens, Greece

Graphical abstract

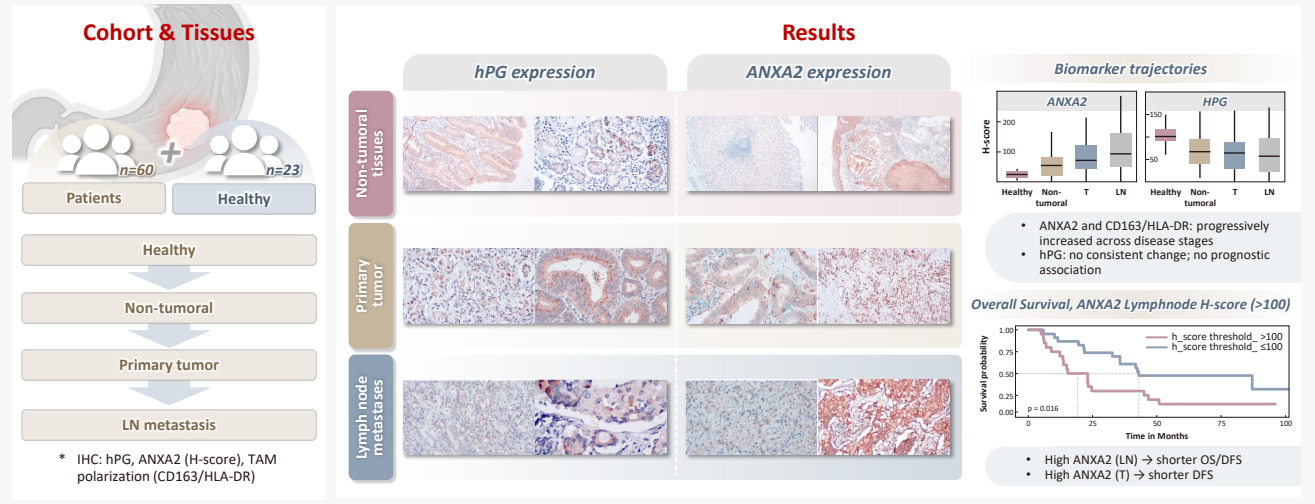

CONCLUSION This study is the first to demonstrate the adverse prognostic impact of ANXA2 overexpression in gastric adenocarcinoma tissues from Caucasian patients.ANXA2 expression increased from non-tumoral tissues to primary tumors and lymph node metastases and was associated with tumor-associated macrophage polarization. Our results support ANXA2's potential utility as a prognostic biomarker and therapeutic target, pending validation in larger cohorts.

Christofidis K et al. Journal of pathology and translational medicine

JPTM

ORIGINAL ARTICLE

pISSN 2383-7837 · eISSN 2383-7845

Journal of Pathology and Translational Medicine 2026; 60: 263-279
https://doi.org/10.4132/jptm.2025.12.20

Progastrin, annexin A2, and tumor-associated macrophages in gastric adenocarcinoma

Konstantinos Christofidis[1], Rodanthi Fioretzaki[2], Stylianos Mavropoulos Papoudas[3], Nikolaos Charalampakis[4], Nikolaos Kavantzas[1], Dimitrios Schizas[5], Stratigoula Sakellariou[1]

[1]First Department of Pathology, School of Medicine, National and Kapodistrian University of Athens, Athens, Greece
[2]Department of Hematology, Laiko General Hospital of Athens, National and Kapodistrian University of Athens, Athens, Greece
[3]Independent Researcher, Athens, Greece
[4]Department of Medical Oncology, Metaxa Cancer Hospital of Piraeus, Piraeus, Greece
[5]First Department of Surgery, National and Kapodistrian University of Athens, Laiko General Hospital of Athens, Athens, Greece

Background: Gastric adenocarcinoma is a major cause of cancer mortality worldwide, and reliable biomarkers remain insufficient. This study investigates the immunohistochemical expression of progastrin (hPG) and annexin A2 (ANXA2) and the polarization of tumor-associated macrophages in gastric adenocarcinoma to explore their potential prognostic and biological significance. **Methods:** A retrospective analysis was conducted on formalin-fixed, paraffin-embedded tissue samples from 60 patients with gastric adenocarcinoma (primary tumors, lymph node metastases, and non-tumoral gastric mucosa) and gastric biopsies from 23 healthy controls. The expression of hPG and ANXA2 was quantified using the H-score, and the CD163/human leukocyte antigen–DR (HLA-DR) ratio was used to represent macrophage polarization (M2/M1). Statistical analyses included non-parametric tests, Spearman correlations, Kaplan-Meier survival curves, and Cox proportional-hazards models. **Results:** ANXA2 expression was significantly elevated in cancer cells from primary tumors and lymph node metastases, compared with the non-tumoral gastric mucosa tissues and gastric mucosa tissues from healthy controls. ANXA2 expression increased with the tumor grade. High ANXA2 levels were associated with shorter overall and disease-free survival, but they did not have independent prognostic value. Although hPG expression correlated positively with ANXA2, it showed no significant prognostic association. The CD163/HLA-DR ratio increased with tumor progression and negatively correlated with ANXA2, but it did not influence survival outcomes. **Conclusions:** This study is the first to demonstrate the adverse prognostic impact of ANXA2 overexpression in gastric adenocarcinoma tissues from Caucasian patients. Our results suggest that ANXA2 might have utility as a prognostic biomarker and therapeutic target, if further large-scale studies validate and expand our findings.

Keywords: Progastrin (hPG); Annexin A2; Tumor-associated macrophages; Stomach neoplasms; Biomarkers

INTRODUCTION

Gastric cancer is the fifth most common cancer globally, with 968,350 new cases and 659,853 deaths annually. Its incidence rises with age, with an average age at diagnosis of 70 years. Gastric cancer is anatomically classified into cardia and non-cardia subtypes. Chronic *Helicobacter pylori* infection is the main cause of 90% of non-cardia gastric cancers, and additional risk factors include diet, alcohol, smoking, and Epstein-Barr virus infection. *H. pylori* eradication treatments, as well as improved nutrition and hygiene, have led to a decline in non-cardia gastric cancer incidence. Cardia cancers are less associated with *H. pylori* (20%) and often linked to obesity and gastroesophageal reflux. Their incidence tends to be high in a younger population than non-cardia gastric cancers [1-3]. A family history, particularly of hereditary diffuse gastric cancer caused by mutations in the cadherin 1 gene, accounts for less than 10% of cases [4,5].

Received: September 13, 2025 • **Revised:** December 8, 2025 • **Accepted:** December 19, 2025
Corresponding Author: Konstantinos Christofidis, MD
First Department of Pathology, School of Medicine, University of Athens, Building 10, 75 Mikras Asias Street, Goudi, 11527, Athens, Greece
Tel: +30-210746226, E-mail: konstantinos.christofidis@gmail.com

Gastric adenocarcinomas are histologically classified according to the WHO 2019 guidelines into tubular, poorly cohesive (including signet-ring cell carcinoma), and mixed adenocarcinomas. Rare subtypes include the papillary, mucinous, hepatoid, micropapillary and fundic-gland type adenocarcinomas, carcinoma with lymphoid stroma, and mucoepidermoid, Paneth cell, and parietal cell carcinomas [6]. Despite progress in medicine, gastric adenocarcinoma still lacks early detection methods, sensitive biomarkers, and effective therapies [7,8].

Progastrin (hPG), an 80-amino-acid precursor of amidated gastrin, is synthesized in gastric antral G cells [9,10]. Normally, non-amidated gastrin makes up <10% of secreted peptide forms. Elevated levels are seen in some pathological states, including cancer [11,12], due to *GAST* gene overexpression on chromosome 17q21 [11,13,14] and deficient processing enzymes in tumors [15-17]. hPG has been shown to promote cancer cell proliferation [18], resistance to apoptosis [19], and disruption of cell junctions [20] and support cancer stem cell properties [18,21] and angiogenesis [22]. It also suppresses M2 macrophage polarization and Wnt ligand secretion [23]. hPG acts via multiple pathways, including Wnt/β-catenin, KRAS, MEK-ERK, phosphoinositide 3-kinase/Akt, nuclear factor κB, and SMAD4 [24], and it is found in tumor cells and stroma [25]. Increased hPG levels have been found in patient samples from 11 different types of cancer, suggesting that it might have value as a biomarker [11]. Most studies have examined serum hPG levels [26–36]; only a few have researched its expression in tumor tissues [37-40]. Little research to date has examined the role of hPG in gastric adenocarcinomas, and what has been done has mainly used cell lines and mouse models [41-43]. The receptors for hPG are still unidentified, though annexin A2 (ANXA2) is a proposed candidate [44,45].

ANXA2 is a 36-kDa phospholipid-binding protein encoded on chromosome 15q22.2 [46-48]. It regulates multiple cellular functions and is implicated in tumorigenesis through pathways involving c-Myc, STAT3, SNAIL, TWIST, ARP3, MIEN1, LIMK, and CFL1 [49]. ANXA2 also seems to be critical for hPG's oncogenic action, at least in colon cancer cells [45,50]. ANXA2 is overexpressed in gastric cancer and localized mainly at tumor cell membranes, where it promotes the destabilization of epithelial junctions and increases the secretion of matrix metalloproteinases, thereby enhancing invasion and metastasis [51-55]. ANXA2 is also linked to *c-erbB-2* overexpression and poor patient outcomes [56]. Silencing ANXA2 can reduce tumor proliferation, reverse chemoresistance, and limit metastasis, underscoring its therapeutic relevance [57-60].

Tumor-associated macrophages (TAMs) are a critical component of the tumor microenvironment. Upon activation, macrophages polarize into multiple phenotypes with distinct roles. Activated macrophages are categorized as the M1 phenotype, which induces inflammation and shows microbicidal and tumor suppressive activity, and the M2 phenotype, which has immunoregulatory activity that contributes to both tissue healing and cancer development. Many more phenotypes exist between those two ends of the spectrum. M1 markers include human leukocyte antigen–DR (HLA-DR), CD86, inducible nitric oxide synthase, and pSTAT1, and M2 markers include CD163, CD204, and CD206 [61]. M1 polarization is induced by Toll-like receptor ligands, tumor necrosis factor α, interferon-α, and colony-stimulating factor 2. On the other hand, interleukin (IL) 4, IL10, IL13, transforming growth factor β (TGF-β), and prostaglandin E2 promote M2 differentiation [62]. A high M2/M1 TAM ratio is associated with worse prognosis in several cancers [63], including gastric cancer [64–68], and has been linked to some aspects of gastric adenocarcinoma oncogenesis [69-71]. As previously mentioned, hPG has been reported to suppress the differentiation of TAMs toward the M2 phenotype and reduce their expression of Wnt ligands [23]. It is also interesting that ANXA2 is expressed on the surfaces of macrophages, where it serves as a recognition element and mediates their activation [72].

In this study, we investigate the immunohistochemical expression of hPG and ANXA2 and the phenotypes of TAMs in gastric adenocarcinoma patients, with the hope of revealing possible interplay among them and any associations with prognostic factors and thus shed light on gastric cancer tumorigenesis and potentially propose new biomarkers.

MATERIALS AND METHODS

Patients and tissue samples

This retrospective study was carried out on gastrectomy specimens from 60 patients who underwent surgery for gastric adenocarcinomas at the First Department of Surgery of Laiko University Hospital, National and Kapodistrian University of Athens (NKUA), between 2014 and 2020. Clinical and pathological data, including demographics, surgical procedures, TNM classification, pre- and postoperative therapy, and follow-up information (recurrence, disease-free, and overall survival [OS]) were prospectively recorded. Selected clinicopatho-

https://doi.org/10.4132/jptm.2025.12.20

Table 1. Epidemiological and clinical characteristics of the patients

Parameter	Value
Age (yr)	67 (34–86)
Sex	
Male	35 (58.3)
Female	25 (41.7)
Location	
Non-cardia	42 (70.0)
Cardia	18 (30.0)
Surgical procedure	
Subtotal gastrectomy	33 (55.0)
Total gastrectomy	27 (45.0)
Chemotherapy	
No	51 (85.0)
Yes	9 (15.0)
Event	
Death of disease	37 (61.7)
Remission	3 (5.0)
Free of disease	20 (33.3)
Survival (day)	
Overall	1,374 (149–3,413)
Disease-free	984.5 (100–3,413)

Values are presented as median (range) or number (%).

logical characteristics are summarized in Table 1.

Formalin-fixed, paraffin-embedded tissue samples from those patients were retrieved from the archives of the Pathology Department of the same hospital. Sections from the primary gastric adenocarcinoma and any lymph node metastases were studied. Two control groups were included: non-tumoral gastric mucosa adjacent to the carcinomas derived from the same patients' surgical specimens and lesional-free gastric biopsies from 23 healthy, age- and sex-matched subjects without any history of gastric cancer. All cases were anonymized, with each sample assigned an alphanumeric code to protect the identity of the individuals. Permission for this scientific use of patient data was obtained from the Research Ethics and Deontology Committee, NKUA (492/18-07-2022). Individual consent was waived because the study was retrospective.

Immunohistochemical staining and evaluation

Immunohistochemistry (IHC) was performed according to standard procedures on 3–4 μm-thick tissue sections, which were stained with commercially available rabbit monoclonal IgG antibodies against HLA-DR (clone EP96 at 1:200 dilution, Bio SB, Santa Barbara, CA, USA), CD163 (clone D6U1J at 1:250–1:1,000 dilution, Cell Signaling Technology, Inc., Danvers, MA, USA), and ANXA2 (clone D11G2 at 1:200–1:800 dilution, Cell Signaling Technology, Inc.). No hPG antibodies are commercially available. A rabbit polyclonal antibody (1137 at 1:1,000 dilution) was kindly provided by Professor Arthur Shulkes and his research team at the University of Melbourne, Victoria, Australia.

An IHC evaluation to assess the expression of hPG, ANXA2, CD163, and HLA-DR at the protein level was performed by two surgical pathologists (K.C. and S.S.) who were blinded to clinicopathological information. The evaluation was performed by both pathologists simultaneously using a double-headed-microscope. At least 10 high-power fields (HPFs) were scanned for each IHC stain in every case. The scoring system for hPG (cytoplasmic staining) (Fig. 1) and ANXA2 (membranous staining) (Fig. 2) was set based on the percentage (0%–100%) of stained epithelial cells (gastric adenocarcinoma cells in neoplastic tissues and normal gastric mucosa epithelial cells in the controls) and the intensity of the immunostain (0, no staining; 1, weak; 2, moderate; 3, strong). We calculated the H-scores for these two stains using the following formula:

H-score = 1 × (% cells with weak staining) + 2 × (% cells with moderate staining) + 3 × (% cells with strong staining)

H-score values can range from 0 to 300. Based on the distribution of values, an H-score threshold of 100 was applied to compare survival groups. H-scores < 100 signify low expression, and H-scores ≥ 100 signify high expression for these stains.

When evaluating CD163 and HLA-DR, the total number of positive macrophages per 10 HPFs was calculated for each immunostain (Fig. 3). The ratio of CD163/HLA-DR was assessed, with values greater than 1 signifying a predominance of M2 macrophages over M1 macrophages.

Statistical analysis

All statistical analyses were performed using R version 4.1.2 (2021-11-01; R Foundation for Statistical Computing, Vienna, Austria). Data are expressed as frequencies, means with standard deviations, or medians with interquartile ranges, as appropriate. Quantitative variables were compared with Student's t test or the Mann-Whitney test for normally distributed and non-normally distributed variables, respectively. Qualitative variables were compared with the chi-squared test or Fisher's exact test, as appropriate. Relationships between parameters were assessed using Spearman's correlation coefficients.

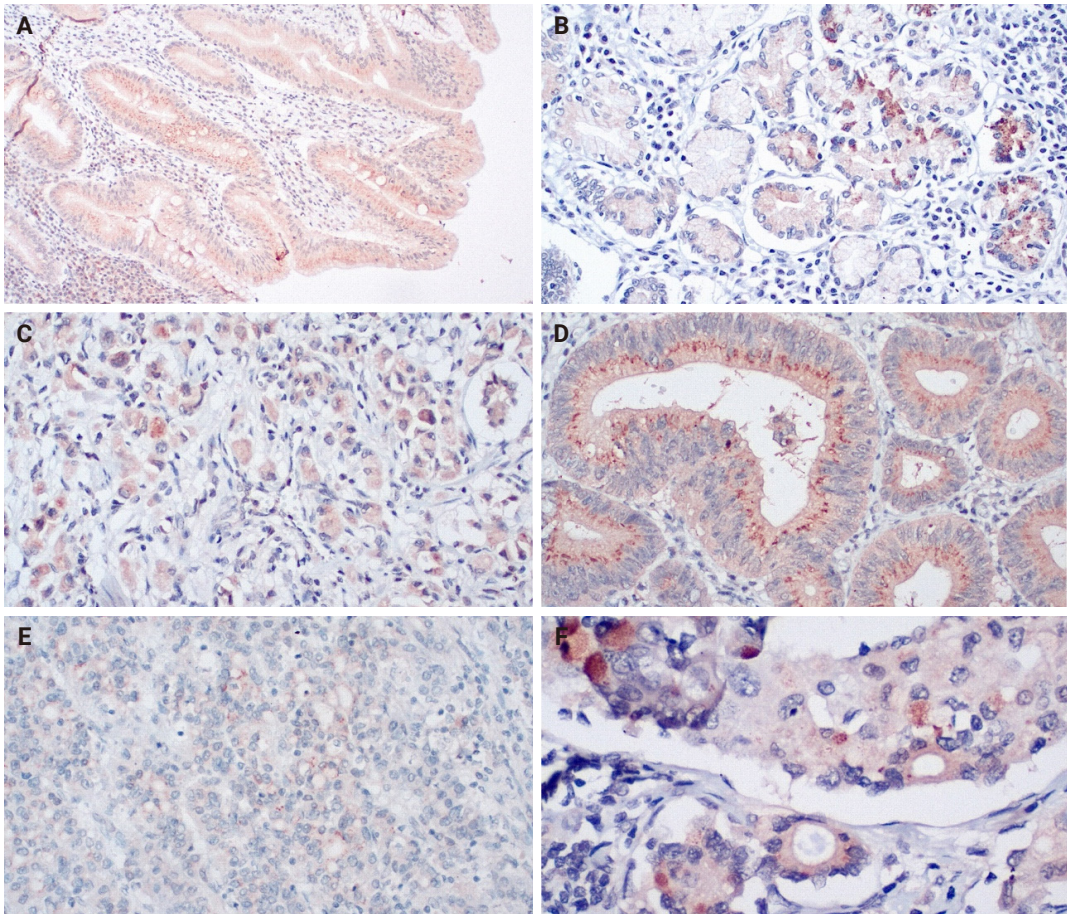

Fig. 1. Progastrin expression in non-tumoral tissues (A, B, moderate and strong expression), primary tumor tissues (C, D, weak and strong expression), and lymph node metastases (E, F, moderate and strong expression). Note the variety and heterogeneity of staining intensity, even among similar-looking cells from the same area.

To investigate IHC expression differences, we applied a non-parametric Wilcoxon test for paired samples, when dealing with samples from the same patient, or a non-parametric Wilcoxon test for unpaired samples, when the samples came from different patients. Correlations among the expressions of hPG and ANXA2 and the CD163/HLA-DR ratio in tumor or lymph node metastasis tissue were investigated by Spearman's rank correlation coefficients (ρ). A p-value was calculated to determine statistical significance. Relationships between the expression of hPG and ANXA2 and the CD163/HLA-DR ratio and patients' clinicopathological parameters (T, N, stage, grade, and histological subtype) were assessed using a Kruskal-Wallis ANOVA. The Dunn test was used to assess the ability of the Kruskal-Wallis ANOVA to differentiate among subgroups.

To investigate the different projected outcomes for OS and disease-free survival (DFS) according to the expressions of hPG and ANXA2 and the CD163/HLA-DR ratio in tumor and lymph node metastasis tissues, survival curves were estimated using the Kaplan-Meier method, and differences between groups were compared using the log-rank test to obtain a p-value. Cox proportional hazards analyses were performed to evaluate whether ANXA2 expression, dichotomized with an H-score threshold of 100, was associated with patient DFS and OS in both the primary tumors and lymph-node metastases. For each of these cases, a univariable model (ANXA2 alone) and a multivariable model (adjusted for sex, age, tumor histological subtype, location, grade, and stage) were compared using likelihood-ratio tests (LRTs) to evaluate the independent prognostic value of ANXA2. All p-values <0.05 were considered statistically significant.

https://doi.org/10.4132/jptm.2025.12.20

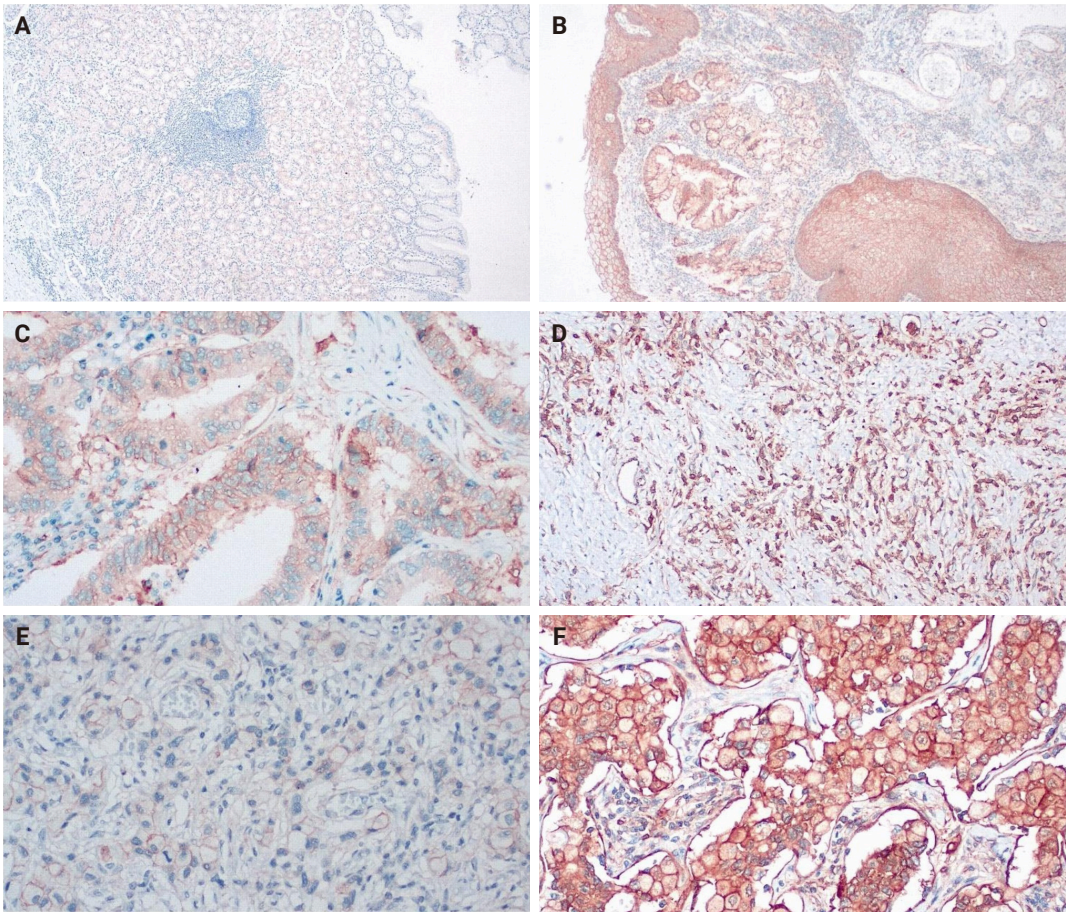

Fig. 2. Annexin A2 expression in non-tumoral tissues (A, B, weak and strong expression), primary tumor tissues (C, D, moderate and strong expression), and lymph node metastases (E, F, weak and strong expression).

RESULTS

Our IHC evaluation of hPG, ANXA2, CD163, and HLA-DR expression was feasible in all of the tumoral (primary gastric tumors [T] and lymph node metastases [LN]) and normal-looking tissues (non-tumoral gastric tissues from the same patients [non-tumoral] and healthy controls [healthy]). The staining pattern for hPG was cytoplasmic, indicative of the protein location. The H-scores ranged as follows: 0–159 in T samples, 0–166 in LN samples, 8–157 in patients' non-tumoral tissues, and 35–160 in the healthy controls. The staining pattern for ANXA2 was membranous, supportive of its role as a receptor. The H-scores ranged as follows: 0–242 in T samples, 0–285 in LN samples, 3–166 in patients' non-tumoral tissues, and 5–107 in the healthy controls. The CD163/HLA-DR ratio ranged as follows: 0.074–6.952 in T samples, 0.150–4.267 in LN samples, 0.195–3.310 in patients' non-tumoral tissues, and 0.116–1.055 in the healthy controls. Summary distributions of the hPG, ANXA2, and CD163/HLA-DR values in the various tissues examined are depicted in Supplementary Table S1.

Both ANXA2 and the CD163/HLA-DR ratio seem to rise from healthy to non-tumoral to T tissue to LN metastases, whereas hPG expression decreases (Fig. 4). The p-values in the figure indicate whether the corresponding pairs differ significantly (Supplementary Table S2), as will be explained in the next section.

Differential expression of hPG, ANXA2, and CD163/HLA-DR

As hinted by the summary distributions, the expressions of hPG and ANXA2 and the CD163/HLA-DR ratio differ between tumoral (T and LN) and healthy-looking tissues (non-tumoral and healthy). We continued our analysis by researching the statistical importance of the expression differences. All of our

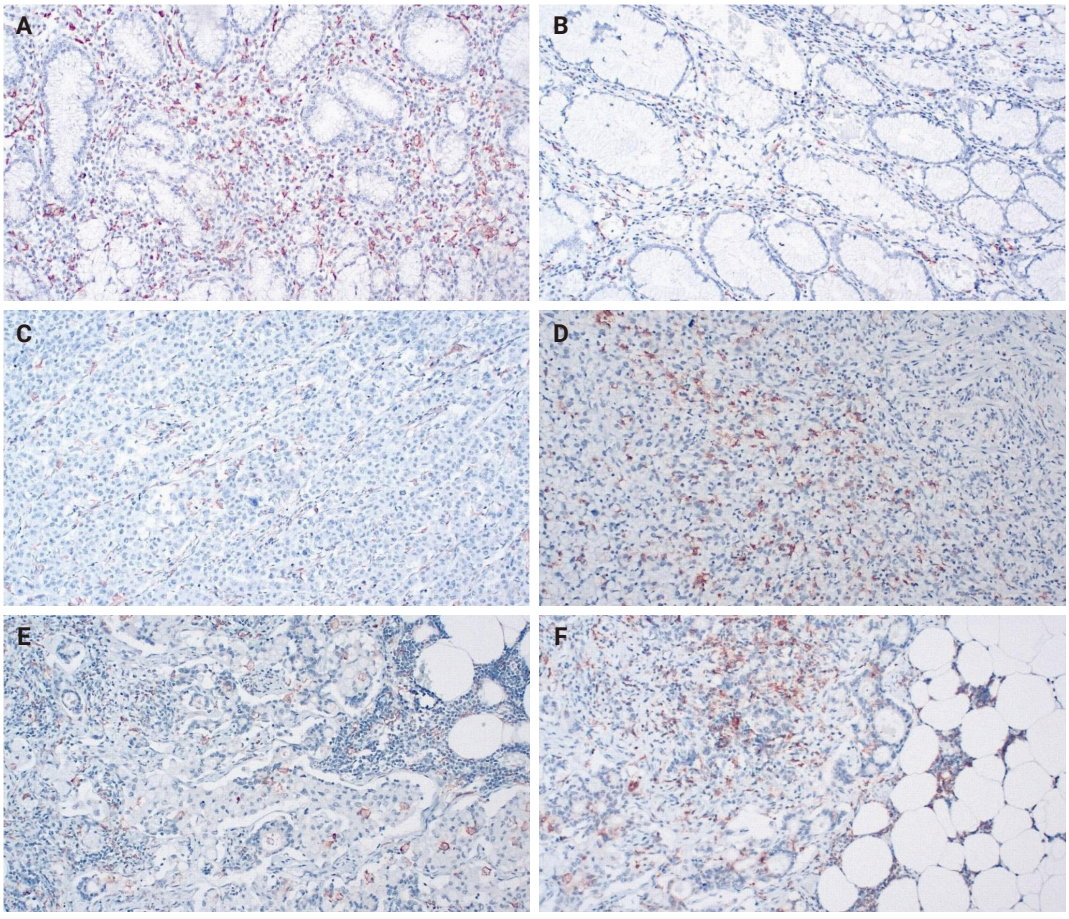

Fig. 3. Human leukocyte antigen–DR (A, C, E) and CD163 expression (B, D, F) in non-tumoral tissues (A, B), primary tumor tissues (C, D), and lymph node metastases (E, F).

tests showed statistically significant differential expression ($p < .001$), except for the one between hPG (T) or hPG (LN) and non-tumoral gastric tissues from the same gastrectomy specimen ($p = .344$ and $p = .957$, respectively).

We further tested the markers' differential expression between the two kinds of control tissues (non-tumoral and healthy). Those tests also highlighted statistically important differential expression ($p < .001$ and $p = .024$), except for the one comparing the CD163/HLA-DR ratio between the two types of control tissues ($p = .108$). These results are summarized in Supplementary Table S2.

Correlations among hPG and ANXA2 expression and the CD163/HLA-DR

We noticed that the expressions of hPG and ANXA2 and the CD163/HLA-DR ratio in the primary tumors are linked to each marker's value in the corresponding LN metastasis. More precisely, the values show a statistically significant ($p < .001$) positive correlation (rho = 0.597 and rho = 0.617), indicating that higher expression in the primary tumor correlates with higher expression in the LN metastasis. These expression correlations are summarized in Supplementary Table S3 and depicted in a scatterplot in Fig. 5 to visualize their direction and magnitude.

We also investigated the correlations among the different markers' expressions in both the primary tumors and LN metastases. A statistically significant ($p < .001$) positive correlation (rho = 0.437) between ANXA2 and hPG expression and a statistically significant ($p = .038$) negative correlation (rho = –0.269) between ANXA2 expression and the CD163/HLA-DR ratio were observed in the primary tumor tissues. No other expression correlation came to light in the rest of the tests performed. Supplementary Table S4 and the scatterplot in Fig. 5 present the results of these correlation tests.

https://doi.org/10.4132/jptm.2025.12.20

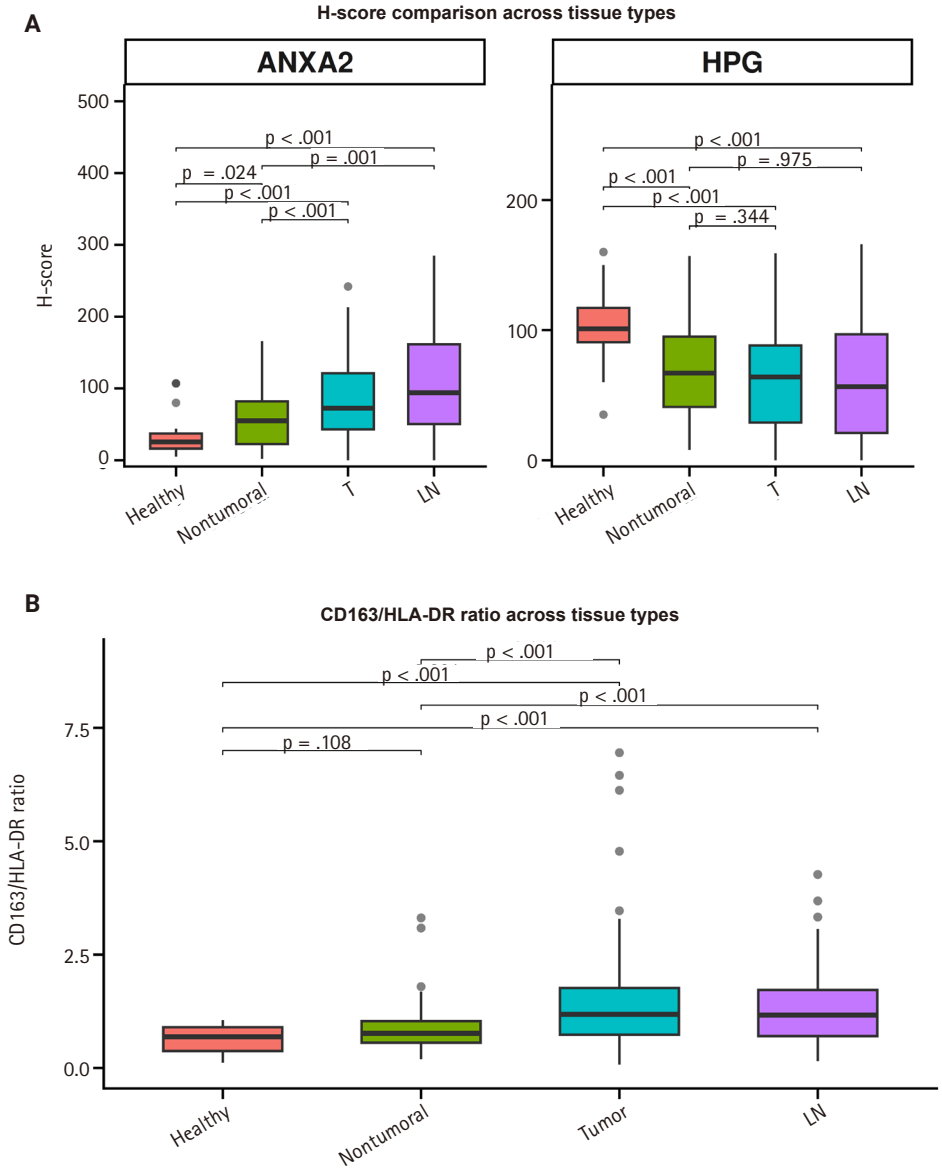

Fig. 4. Comparison of the progastrin (hPG) and annexin A2 (ANXA2) H-scores (A) and the CD163/human leukocyte antigen–DR (HLA-DR) ratio (B) values in gastric mucosa from healthy controls (healthy), patients' non-tumoral gastric mucosa (non-tumoral), primary tumors (T), and lymph node metastases (LN). The p-values over the brackets indicate whether the corresponding pairs differ significantly.

hPG and ANXA2 expression and CD163/HLA-DR in relation to clinicopathological parameters

hPG and ANXA2 expression, the hPG/ANXA2 ratio, and the CD163/HLA-DR ratio in T and LN tissues were studied in relation to common clinicopathological parameters (T and N, grade, stage, and histological subtype). All the parameters were distributed into their respective subcategories. A Kruskal-Wallis non-parametric ANOVA was performed to assess whether groups differed significantly. This investigation was expanded with Dunn's test with Bonferroni adjustment to ensure that the adjusted p-values retained their significance.

We found a statistically significant ANXA2 expression difference between tumor grades 2 and 3 (p = .016) in LN tissue. Moreover, a statistically significant difference between tumor grades 2 and 3 in the CD163/HLA-DR ratio in T and LN tissues also came to light (p = .041 and p = .023, respectively) (Table 2). ANXA2 expression in LN tissue seems to increase as the grade progresses from 2 to 3. On the other hand, the CD163/HLA-

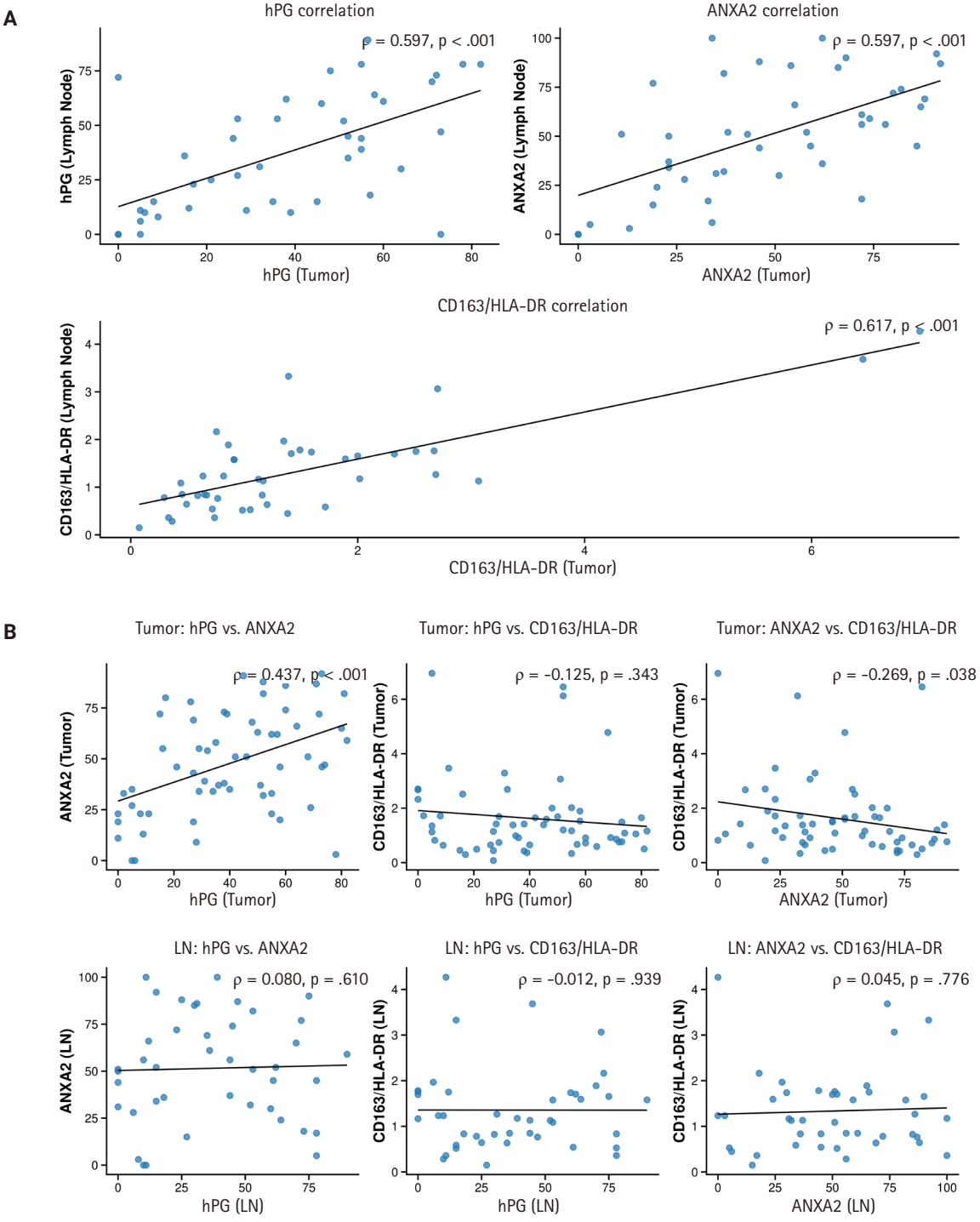

Fig. 5. (A) Correlations among progastrin (hPG) and annexin A2 (ANXA2) expression and the CD163/human leukocyte antigen–DR (HLA-DR) ratio in primary tumors (y-axis) versus lymph node metastases (x-axis). All the correlations depicted are statistically significant and positive. (B) Correlations among hPG and ANXA2 expression, hPG and the CD163/HLA-DR ratio, and ANXA2 and the CD163/HLA-DR ratio in primary tumors and lymph node metastases (LN). Notice the statistically significant positive correlation between ANXA2 and hPG expression and the negative correlation between ANXA2 expression and the CD163/HLA-DR ratio in primary tumor tissues. In the upper right corner of each subplot of the scatterplot is the rho (ρ) value, which indicates the direction and magnitude of each correlation, and the p-value, which represents the significance of the correlation.

https://doi.org/10.4132/jptm.2025.12.20

DR ratio in T and LN tissues appears to decrease as the tumor grade increases (Supplementary Table S5).

The significant p-values observed for hPG and ANXA2 expression differences between tumor stages in LN tissues did not retain their statistical significance after adjustment. These results indicate a failure to properly differentiate the values of these patients' clinicopathological parameters based on the expression of these antigens, so we discarded those correlations (Table 2).

Marker expression and projected patient survival outcomes

We investigated the different projected OS and DFS outcomes according to the expression of all the markers in tumoral tissues. The expression of ANXA2 in both the T and LN tissues produced survival curves that differed significantly, with worse survival outcomes associated with higher ANXA2 expression. As shown in Supplementary Table S6, both OS and DFS are severely affected when ANXA2 expression is high (p = .016–.035). Patients with high ANXA2 expression in their LN tissues showed the worst prognosis. The survival analysis results for ANXA2 are plotted in combined plots to compare the different survival groups (Fig. 6). As such, the population was divided into two distinct strata, patients with ANXA2 H-score values < 100 (low expression) and patients with ANXA2 H-score values ≥ 100 (high expression).

When we evaluated the effects of hPG levels on patient survival, higher expression seemed to coincide with better survival outcomes. However, as shown in Supplementary Table S6, all the tests have p-values higher than .05, making the trend non-significant. Consequently, patients' OS and DFS were not influenced by hPG expression. Likewise, we assessed the CD163/HLA-DR ratio for differences in survival using a threshold of 1, with values <1 showing a greater influence of HLA-DR, and values ≥1 indicating that CD163 is more influential. Although the ratio seemed to be higher in patients with better survival outcomes, the results were not statistically significant (p > .05).

In the next step of our analysis, we evaluated the independent prognostic value of ANXA2. First, we evaluated its expression's relationship with patient survival on its own in all conditions (univariable analyses). Then, we added common clinicopathological variables (sex, age, histological subtype, location, grade, stage) to the model to determine whether they significantly improved the model fit (multivariable analysis).

Table 2. Evaluation of the differential expression of hPG and ANXA2 and the CD163/HLA-DR ratio among groups

	No.	Kruskal–Wallis p-value
T		
T1/T2/T3/T4	9/6/22/23	
hPG (T)		.169
hPG (LN)		.378
ANXA2 (T)		.858
ANXA2 (LN)		.051
CD163/HLA-DR (T)		.222
CD163/HLA-DR (LN)		.225
N		
N0/N1/N2/N3	15/10/13/22	
hPG (T)		.222
hPG (LN)		.069
ANXA2 (T)		.545
ANXA2 (LN)		.125
CD163/HLA-DR (T)		.220
CD163/HLA-DR (LN)		.366
Grade		
1/2/3	0/17/43	
hPG (T)		.787
hPG (LN)		.259
ANXA2 (T)		.163
ANXA2 (LN)		.016[a]
CD163/HLA-DR (T)		.041[a]
CD163/HLA-DR (LN)		.023[a]
Stage		
I/II/III/IV	9/11/30/10	
hPG (T)		.080
hPG (LN)		<.001[b]
ANXA2 (T)		.723
ANXA2 (LN)		<.001[b]
CD163/HLA-DR (T)		.135
CD163/HLA-DR (LN)		.050
Histological subtype		
TB/PC/MIX/MUC	27/24/7/2	
hPG (T)		.355
hPG (LN)		.064
ANXA2 (T)		.071
ANXA2 (LN)		.381
CD163/HLA-DR (T)		.062
CD163/HLA-DR (LN)		.266

hPG, progastrin; ANXA2, annexin A2; HLA-DR, human leukocyte antigen–DR; TB, tubular; PC, poorly cohesive; MIX, mixed; MUC, mucinous. Dunn's test interpretation: [a]Significant; [b]Not significant.

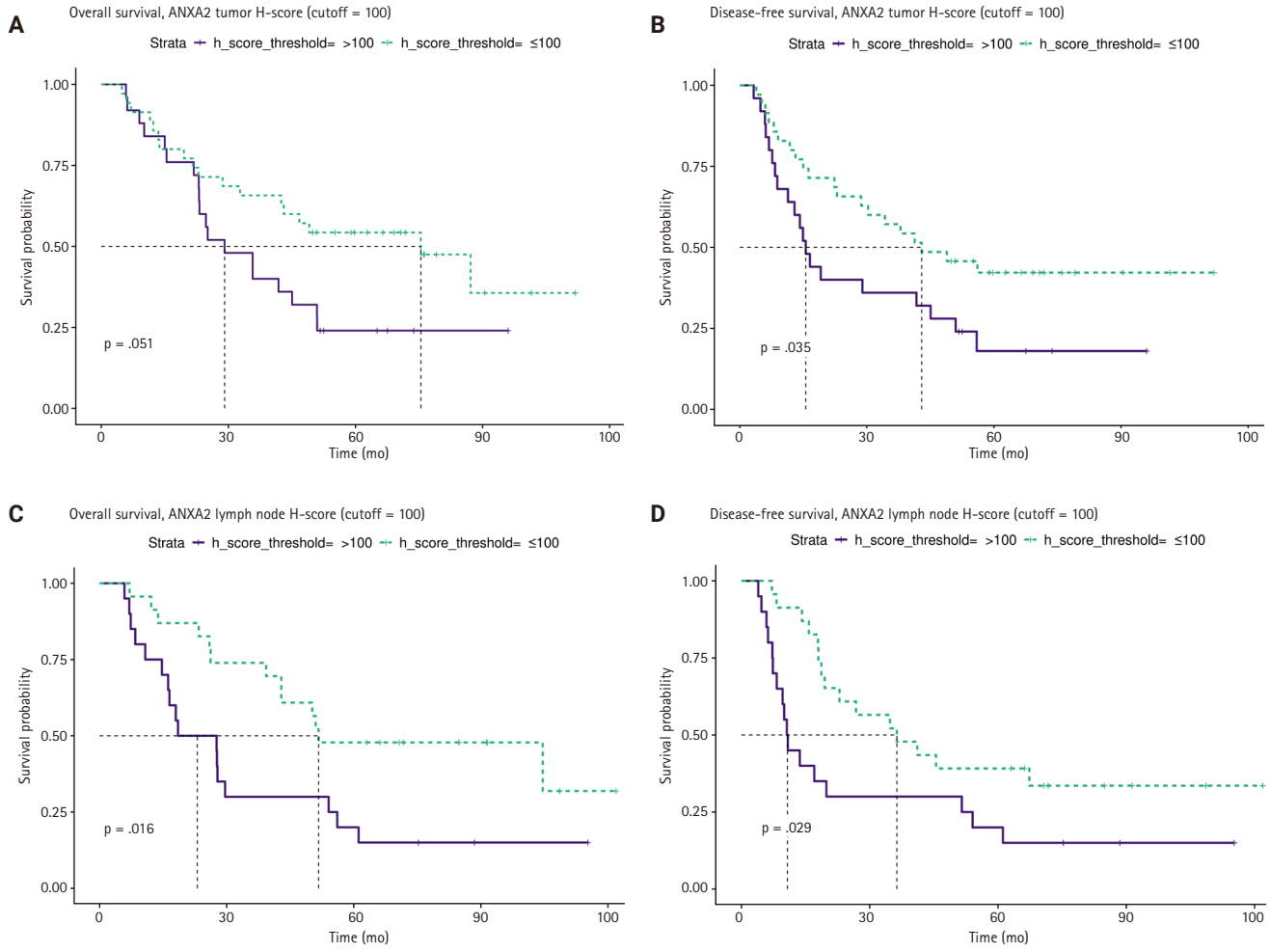

Fig. 6. Comparison of survival curves depicting patients' overall (A, C) and disease-free survival (B, D) stratified by high and low annexin A2 (ANXA2) expression in tumors and lymph node metastases. Survival is worse for patients with high ANXA2 expression.

In the univariable analysis of the primary tumors (T), low ANXA2 expression (H-score ≤ 100) showed a statistically significant association with longer DFS (hazard ratio [HR], 0.52; 95% confidence interval [CI], 0.28 to 0.97; p = .039) and a non-significant association with improved OS (HR, 0.53; 95% CI, 0.27 to 1.01; p = .054). However, in the multivariable analysis, those associations were attenuated and became non-significant (DFS: HR, 0.55; p = .110; OS: HR, 0.66; p = .310). Moreover, the LRTs were significant (DFS LRT p = .02; OS LRT p = .024), indicating that the block of clinical covariates provided significantly more prognostic information than the ANXA2-only model. Therefore, the prognostic effect of ANXA2 in T tissues is not independent and is largely explained by other clinicopathological variables.

In the univariable analysis of LN tissues, low ANXA2 expression (H-score ≤ 100) was associated with improved DFS (HR, 0.47; 95% CI, 0.23 to 0.94; p = .033) and OS (HR, 0.42; 95% CI, 0.20 to 0.87; p = .020). After the multivariable adjustment, the HRs for ANXA2 remained similar, but they lost their statistical significance (DFS: HR, 0.48; p = .096; OS: HR, 0.50; p = .130). In addition, the LRTs in this case were non-significant (DFS: p = .560; OS: p = .440), indicating that the added clinical variables did not significantly improve the model fit over the ANXA2-only model. Together, these findings indicate that although ANXA2 in LN tissues is a strong prognostic marker, it does not provide significant independent information because its effects are confounded by or overlap with those of the clinicopathological factors. A summary of these findings is displayed in Table 3.

https://doi.org/10.4132/jptm.2025.12.20

DISCUSSION

Gastric adenocarcinoma remains a major global health problem. Despite medical advances, the prognosis for advanced-stage gastric cancer remains poor. In this retrospective study, we studied hPG, ANXA2, and TAMs to determine their potential roles in gastric cancer progression and their prognostic significance. We investigated their expression in primary gastric adenocarcinomas (T) and their lymph node metastases (LN), in non-tumoral gastric tissue adjacent to the adenocarcinomas (non-tumoral), and in unremarkable gastric mucosa from healthy subjects (healthy). A thorough investigation was conducted to discern these markers' summary distributions, differential expressions, expression correlations, and relationships with patients' clinicopathological parameters and survival outcomes.

In our results, ANXA2 emerged as a protagonist in gastric adenocarcinoma oncogenesis. Its expression was significantly elevated in the neoplastic cells of T and LN tissues, compared with epithelial cells in the non-tumoral gastric mucosa adjacent to the adenocarcinomas and the gastric mucosa of healthy controls. The gradual increase in ANXA2 expression from healthy gastric tissues to non-tumoral mucosa in the vicinity of carcinoma to primary adenocarcinoma tissue and then lymph node metastases hints at its role in the development of gastric adenocarcinomas. In addition, we found that ANXA2 expression differed significantly between tumor grades, with higher ANXA2 levels in grade 3 tumors than grade 2 tumors, further supporting the notion that ANXA2 is linked to adverse tumor characteristics. Our results also indicate that higher levels of ANXA2 in T and LN tissues were associated with worse OS and DFS. Patients with higher ANXA2 expression in their LN tissues exhibited the poorest prognosis. These findings align with those of prior studies, which found that ANXA2 overexpression was associated with aggressive gastric cancer behavior and worse patient prognosis. Four studies conducted in Asian populations [51-53,56] and one in a South American population [54] showed that ANXA2 upregulation correlated with a higher tumor grade, increased size, venous invasion, lymph node and distal metastases, and an advanced stage. The association between ANXA2 expression and gastric cancer patient survival was previously evaluated in only two Asian cohorts, which reported poor survival rates in patients with ANXA2-overexpressing gastric cancer, though just one of them showed ANXA2 to be an independent prognostic factor in this setting [51]. To the best of our knowledge, this study is the first to highlight that poor prognosis is linked to ANXA2 protein overexpression in gastric adenocarcinoma in a Caucasian population, even though our data failed to demonstrate that it has independent prognostic value, probably because of the relatively small number of patients in our dataset.

Table 3. Summary of Cox proportional hazards models assessing the independent prognostic value of ANXA2 expression (dichotomized at an H-score of 100)

Tissue	Outcome	Model	HR (95% CI)	p-value	LRT p-value	Interpretation
Primary tumor (T)	DFS	ANXA2 alone	0.52 (0.28–0.97)	.039		Significant prognostic factor
		ANXA2 and clinicopathological covariates	0.55 (0.26–1.15)	.113	.021	Not an independent factor; effect is confounded
	OS	ANXA2 alone	0.53 (0.27–1.01)	.054		Nonsignificant prognostic factor
		ANXA2 and clinicopathological covariates	0.66 (0.30–1.47)	.310	.024	Not an independent factor; effect is confounded
Lymph-node metastases (LN)	DFS	ANXA2 alone	0.47 (0.23–0.94)	.033		Significant prognostic factor
		ANXA2 and clinicopathological covariates	0.48 (0.20–1.14)	.096	.559	Not an independent factor; effect overlaps with covariates
	OS	ANXA alone	0.42 (0.20–0.87)	.020		Significant prognostic factor
		ANXA2 and clinicopathological covariates	0.50 (0.21–1.23)	.133	.443	Not an independent factor; effect overlaps with covariates

Although low ANXA2 was a significant prognostic marker in the univariable analyses, it was not an independent prognostic factor. ANXA2 (T): the significant LRT p-values indicate that the clinicopathological covariates (sex, age, histological subtype, location, grade, stage) provide substantial additional prognostic information and explain the effect of ANXA2 on survival. ANXA2 (LN): the loss of statistical significance for ANXA2 after multivariable adjustment, combined with the non-significant LRTs, indicate that its effect overlaps with the prognostic information captured by the standard clinicopathological variables and is not independent.

ANXA2, annexin A2; HR, hazard ratio; CI, confidence interval; LRT, likelihood ratio test; DFS, disease-free survival; OS, overall survival.

Some data are available about the putative mechanism by which ANXA2 promotes gastric adenocarcinoma. First, in patient tissue studies, its upregulation was linked to reduced e-cadherin expression by Han et al. [52] and to *c-erbB-2* overexpression by Emoto et al. [56]. Second, Tas et al. [60] found high ANXA2 serum levels in chemotherapy-resistant patients. Research in human gastric cancer cell lines demonstrated that ANXA2 inhibition reduced tumor cell migration and matrix metalloproteinase secretion [53]. Moreover, Leal et al. [54] found that ANXA2 upregulation enhanced gastric cancer cell invasion, and Zhang et al. [57] showed that silencing it reversed tumor cell chemoresistance to cisplatin. Xie et al. [58] confirmed the role of ANXA2 in tumor cell proliferation and survival, as well as the therapeutic potential of its silencing, and Mao et al. [59] identified the EphA2–YES1–ANXA2 axis as a potential therapeutic target in gastric adenocarcinoma. Furthermore, *H. pylori* seems to be able to induce ANXA2 and S100A7 overexpression, thereby destabilizing epithelial junctions and promoting carcinogenesis [55].

Our study demonstrates the important role that ANXA2 plays in gastric cancer tumorigenesis and progression and suggests a threshold of expression (H-score = 100) above which patient survival is significantly compromised. Because IHC can easily detect protein overexpression in human tissues, the ANXA2 H-score could serve as a prognostic biomarker, if larger-scale studies further elucidate the extent of the negative effects on patient prognosis implied by our results. Furthermore, given that blocking its expression or disrupting its interactions with other proteins is feasible, ANXA2 emerges as a candidate therapeutic target for patients with ANXA2-overexpressing gastric adenocarcinomas. In this context, the H-score could serve as a marker predicting a therapeutic response.

hPG, a precursor form of gastrin, has been implicated in carcinogenesis due to its involvement in various signaling pathways that promote tumor growth and survival [24]. Studies using gastric cancer cell lines and mouse models have linked hPG upregulation to aggressive tumor characteristics. More specifically, antral cells that express the progastrin receptor cholecystokinin 2 receptor (CCK2R) have been shown to exhibit some traits of stem cells [41]. hPG increases Lgr5 expression and promotes organoid formation in CCK2R+/Lgr5– cells and differentiation into Lgr5+ stem cells [42].

Our study, which is, to our knowledge, the first to use IHC to investigate hPG expression in human gastric cancer tissues, shows some conflicting findings. On the one hand, hPG expression correlated positively with ANXA2 expression in the primary tumors, providing further support for the ligand (hPG)–receptor (ANXA2) relationship proposed in previous studies investigating hPG receptors [45,50]. On the other hand, tissue sections from primary tumors, lymph node metastases, and non-tumoral gastric mucosa from gastric cancer patients had significantly decreased hPG protein expression, compared with the levels in the healthy controls. Moreover, hPG expression showed no statistically significant differences between T and LN tissues and the adjacent non-tumoral gastric tissues. Importantly, our cohort did not show any significant correlation between hPG expression and the patients' clinicopathological parameters. Our findings are partly in contrast with the only other publication to have investigated how hPG levels in gastric cancer patients correlate with survival outcomes. In that recent study, Amjadi et al. [43] reported that increased serum hPG levels were found in patients with gastric cancer, compared with their gastric-cancer-free participants. However, similar to our findings, hPG levels were not statistically related to tumor prognostic features such as stage, grade, or metastatic potential [43]. Furthermore, in our dataset, we did not identify any statistically significant differences in survival outcomes according to the hPG expression level. Both OS and DFS were unaffected by the hPG levels in the primary tumors and lymph node metastases. It is interesting that an investigation of other human malignancies linked high hPG levels with worse clinical outcomes [11]. However, most previous research has focused on serum titers [28,30,32,33,36], rather than tissue [38] hPG expression levels. Therefore, the lack of prognostic significance in our study could imply that only the hPG serum concentration, as opposed to tissue protein expression, has prognostic value. However, taking all the data together, a more likely scenario is that hPG is not a reliable prognostic biomarker for gastric adenocarcinoma, indicating that the oncogenic development of this cancer relies on other molecular mechanisms and pathways. On the other hand, it is possible that our small sample was not adequate to reveal hPG's prognostic significance. Future research with a sizable set of patients might unmask any effects of hPG on gastric cancer prognosis. Another possible limitation of our study is that no antibody specific to hPG is commercially available, and the specificity of the one we used might not have been optimal and potentially shown some cross-reactivity. That possibility could also explain the lack of significant differential expression between the neoplastic and normal-looking tissues in this study because gastrin is normally expressed in gastric tissue.

https://doi.org/10.4132/jptm.2025.12.20

TAMs are key components of the tumor microenvironment that can adopt different phenotypes depending on the signals they receive from the tumor milieu. The M1 phenotype is typically associated with inflammation, microbicidal, and tumor suppressive activity, and the M2 phenotype is typically associated with tissue repair and tumor promotion [61,62]. The oncogenic role of the M2 macrophage phenotype and its association with aggressive tumor features, such as high grades, has been demonstrated by previous studies on human gastric cancer tissues, including two meta-analyses [64-68]. Moreover, M2 was found to be the main TAM phenotype in intraperitoneal metastases of advanced human gastric cancer [69], and high levels of M2 TAMs were shown to be linked to the epithelial–mesenchymal transition, and both of them had independent negative prognostic value and were possibly linked to the TGF-β signaling pathway [70]. In addition, a predominance of M2 over M1 TAMs in human gastric adenoma stroma was shown to increase the likelihood that it would transform into gastric adenocarcinoma [71].

In this study, we used the CD163/HLA-DR ratio to assess TAM polarization, with CD163 marking M2 macrophages, and HLA-DR marking M1 macrophages. The CD163/HLA-DR ratio increased significantly from healthy to non-tumoral tissues to primary gastric tumors to lymph node metastases, suggesting an increasing concentration of M2 macrophages as the disease progresses. This finding is in line with previous studies that showed an association between a shift in macrophages toward the M2 phenotype in lymph node metastatic disease and advanced TNM stage. It is of note that, in the present cohort, the CD163/HLA-DR ratio differed significantly between tumoral and normal-looking (non-tumoral and healthy) tissues, without a statistically significant difference between the non-tumoral and healthy tissues. This finding could imply that macrophage polarization toward an M2 phenotype in the tumor microenvironment is not an early event in gastric carcinogenesis but requires an accumulation of cancerous hits.

The literature supports an association between an increase in M2 TAMs and poor patient survival [64-68]. In this study, despite the observed changes in TAM polarization, the CD163/HLA-DR ratio showed no significant correlation with patient survival. In addition, the CD163/HLA-DR ratio in T and LN tissues decreased from tumor grade 2 to 3, in contrast to previous reports that demonstrated a link between a predominance of the M2 phenotype and poor histological differentiation [68]. Our findings are difficult to interpret and might be attributable to the small sample size of our cohort. Interestingly, we found a statistically significant negative correlation between ANXA2 expression and the CD163/HLA-DR ratio in tumor tissues, indicating that tumors with high ANXA2 expression might have a lower proportion of M2 TAMs. Although that result initially seems counterintuitive, given the known tumor-promoting roles of both ANXA2 and M2 macrophages, it is possible that ANXA2 overexpression triggers some compensatory mechanisms in the tumor microenvironment, including the induction of the M1 macrophage phenotype.

Although our study provides some valuable insights into the roles of hPG, ANXA2, and TAMs in gastric adenocarcinomas, several limitations should be acknowledged. First, our study was based on a relatively small sample, which might have prevented some statistical trends from coming to light. Studies with more patient samples are needed to validate our results and shed more light on the ways ANXA2 expression affects patient prognosis and explore the potential clinical applications of our findings in gastric cancer. Additionally, as already discussed, no specific hPG antibody was commercially available, and we have insufficient documentation about the specificity of the antibody we used. Furthermore, although we focused on the expression of hPG, ANXA2, and TAMs in primary gastric tumors and their lymph node metastases, future studies could investigate their role in circulating tumor cells and distant metastases to provide a more comprehensive understanding of their role in gastric adenocarcinoma. Moreover, although we demonstrated a significant negative correlation between the increased ANXA2 expression in neoplastic cells and patient survival, the molecular mechanisms underlying the oncogenic effects of ANXA2 in gastric cancer remain largely unclear. Future studies should focus on elucidating the signaling pathways activated by ANXA2 in gastric cancer cells and determining how those pathways interact with other molecules or components of the tumor microenvironment. Additionally, an exploration of the potential therapeutic utility of targeting ANXA2, either alone or in combination with other treatments, could open new avenues for the management of gastric cancer.

In conclusion, we are here the first to highlight the dismal prognosis associated with ANXA2 overexpression in a Caucasian population of gastric cancer patients. Additionally, our work, which is the first to use IHC to investigate hPG in human gastric cancer tissues, found no significant correlation between hPG expression and patients' clinicopathological parameters or survival outcomes. Finally, we verified the polarization of

the tumor microenvironment toward M2-like macrophages as gastric cancer progresses. Future research should aim to validate our findings in larger cohorts and explore the therapeutic potential of targeting ANXA2, as well as of modifying the TAM phenotype, in gastric adenocarcinoma patients.

Supplementary Information
The Data Supplement is available with this article at https://doi.org/10.4132/jptm.2025.12.20.

Ethics Statement
The study was conducted in accordance with the Declaration of Helsinki and approved by the Institutional Ethics Committee of Laiko General Hospital of Athens, Greece (492/18-07-2022). Individual consent was waived due to the nature of the study.

Availability of Data and Material
The data presented in this study are included in the article/supplementary material. Further inquiries can be directed at the corresponding author(s).

Code Availability
Not applicable.

ORCID
Konstantinos Christofidis https://orcid.org/0000-0002-8074-8419
Rodanthi Fioretzaki https://orcid.org/0000-0003-1219-8715
Nikolaos Charalampakis https://orcid.org/0000-0002-8756-9659
Dimitrios Schizas https://orcid.org/0000-0002-7046-0112
Stratigoula Sakellariou https://orcid.org/0000-0002-3639-6807

Author Contributions
Conceptualization: KC, NC, DS, SS. Formal analysis: KC, SMP. Investigation: KC. Methodology: KC, SS. Project administration: SS. Software: SMP. Supervision: NK, DS, SS. Validation: KC, SMP, RF, NC, NK, DS, SS. Visualization: KC, RF, NC, SS. Writing—original draft: KC. Writing—review and editing: KC, SMP, DS, SS. Approval of final manuscript: all authors.

Conflicts of Interest
The authors declare that they have no potential conflicts of interest.

Funding Statement
No funding to declare.

Acknowledgements
We would like to express our gratitude to Professor Arthur Shulkes and his team, including Chelsea Dumesny, for providing us with the progastrin antibody (1137).

REFERENCES

1. Bray F, Laversanne M, Sung H, et al. Global cancer statistics 2022: GLOBOCAN estimates of incidence and mortality worldwide for 36 cancers in 185 countries. CA Cancer J Clin 2024; 74: 229-63.
2. Machlowska J, Baj J, Sitarz M, Maciejewski R, Sitarz R. Gastric cancer: epidemiology, risk factors, classification, genomic characteristics and treatment strategies. Int J Mol Sci 2020; 21: 4012.
3. Kong X, Wang JL, Chen HM, Fang JY. Comparison of the clinicopathological characteristics of young and elderly patients with gastric carcinoma: a meta analysis. J Surg Oncol 2012; 106: 346-52.
4. Rawla P, Barsouk A. Epidemiology of gastric cancer: global trends, risk factors and prevention. Prz Gastroenterol 2019; 14: 26-38.
5. Taja-Chayeb L, Vidal-Millan S, Trejo-Becerril C, et al. Hereditary diffuse gastric cancer (HDGC). An overview. Clin Res Hepatol Gastroenterol 2022; 46: 101820.
6. Nagtegaal ID, Odze RD, Klimstra D, et al. The 2019 WHO classification of tumours of the digestive system. Histopathology 2020; 76: 182-8.
7. Japanese Gastric Cancer Association. Japanese gastric cancer treatment guidelines 2021 (6th edition). Gastric Cancer 2023; 26: 1-25.
8. Shen M, Wang H, Wei K, Zhang J, You C. Five common tumor biomarkers and CEA for diagnosing early gastric cancer: a protocol for a network meta-analysis of diagnostic test accuracy. Medicine (Baltimore) 2018; 97: e0577.
9. Dockray GJ, Varro A, Dimaline R, Wang T. The gastrins: their production and biological activities. Annu Rev Physiol 2001; 63: 119-39.
10. Rehfeld JF, Zhu X, Norrbom C, et al. Prohormone convertases 1/3 and 2 together orchestrate the site-specific cleavages of progastrin to release gastrin-34 and gastrin-17. Biochem J 2008; 415: 35-43.
11. You B, Mercier F, Assenat E, et al. The oncogenic and druggable hPG80 (progastrin) is overexpressed in multiple cancers and detected in the blood of patients. EBioMedicine 2020; 51: 102574.
12. Ferrand A, Wang TC. Gastrin and cancer: a review. Cancer Lett 2006; 238: 15-29.
13. Van Solinge WW, Nielsen FC, Friis-Hansen L, Falkmer UG, Re-

hfeld JF. Expression but incomplete maturation of progastrin in colorectal carcinomas. Gastroenterology 1993; 104: 1099-107.
14. Koh TJ, Bulitta CJ, Fleming JV, Dockray GJ, Varro A, Wang TC. Gastrin is a target of the beta-catenin/TCF-4 growth-signaling pathway in a model of intestinal polyposis. J Clin Invest 2000; 106: 533-9.
15. Kochman ML, DelValle J, Dickinson CJ, Boland CR. Post-translational processing of gastrin in neoplastic human colonic tissues. Biochem Biophys Res Commun 1992; 189: 1165-9.
16. Siddheshwar RK, Gray JC, Kelly SB. Plasma levels of progastrin but not amidated gastrin or glycine extended gastrin are elevated in patients with colorectal carcinoma. Gut 2001; 48: 47-52.
17. Prieur A, Cappellini M, Habif G, et al. Targeting the Wnt pathway and cancer stem cells with anti-progastrin humanized antibodies as a potential treatment for K-RAS-mutated colorectal cancer. Clin Cancer Res 2017; 23: 5267-80.
18. Giraud J, Failla LM, Pascussi JM, et al. Autocrine secretion of progastrin promotes the survival and self-renewal of colon cancer stem-like cells. Cancer Res 2016; 76: 3618-28.
19. Wu H, Owlia A, Singh P. Precursor peptide progastrin(1-80) reduces apoptosis of intestinal epithelial cells and upregulates cytochrome c oxidase Vb levels and synthesis of ATP. Am J Physiol Gastrointest Liver Physiol 2003; 285: G1097-110.
20. Hollande F, Lee DJ, Choquet A, Roche S, Baldwin GS. Adherens junctions and tight junctions are regulated via different pathways by progastrin in epithelial cells. J Cell Sci 2003; 116: 1187-97.
21. Jin G, Sakitani K, Wang H, et al. The G-protein coupled receptor 56, expressed in colonic stem and cancer cells, binds progastrin to promote proliferation and carcinogenesis. Oncotarget 2017; 8: 40606-19.
22. Najib S, Kowalski-Chauvel A, Do C, Roche S, Cohen-Jonathan-Moyal E, Seva C. Progastrin a new pro-angiogenic factor in colorectal cancer. Oncogene 2015; 34: 3120-30.
23. Hernandez C, Barrachina MD, Cosin-Roger J, et al. Progastrin represses the alternative activation of human macrophages and modulates their influence on colon cancer epithelial cells. PLoS One 2014; 9: e98458.
24. Fioretzaki R, Sarantis P, Charalampakis N, et al. Progastrin: an overview of its crucial role in the tumorigenesis of gastrointestinal cancers. Biomedicines 2024; 12: 885.
25. Aran D, Camarda R, Odegaard J, et al. Comprehensive analysis of normal adjacent to tumor transcriptomes. Nat Commun 2017; 8: 1077.
26. Prieur A, Mazard T, Assenat E, et al. Progastrin: a new specific early cancer screening biomarker. J Clin Oncol 2017; 35(15 Suppl): 11545.
27. You B, Kepenekian V, Prieur A, et al. 119P: Progastrin, a new blood biomarker for the diagnostic and therapeutic monitoring, in gastro-intestinal cancers: a BIG-RENAPE project. Ann Oncol 2018; 29(Suppl 8): VIII37.
28. Kohli M, Tan W, Vire B, et al. Prognostic value of plasma hPG(80) (circulating progastrin) in metastatic renal cell carcinoma. Cancers (Basel) 2021; 13: 375.
29. Chauhan A, Prieur A, Kolesar J, et al. Abstract 735: hPG80 (circulating progastrin), a novel blood-based biomarker for detection of poorly differentiated neuroendocrine carcinoma and well differentiated neuroendocrine tumors. Cancer Res 2021; 81(13 Suppl): 735.
30. Dupuy M, Iltache S, Riviere B, et al. Plasma hPG(80) (circulating progastrin) as a novel prognostic biomarker for hepatocellular carcinoma. Cancers (Basel) 2022; 14: 402.
31. Casile M, Passildas J, Vire B, Molnar I, Durando X. hPG(80) (circulating progastrin) as a blood biomarker for high-grade glial tumors: a pilot study. Front Neurol 2022; 13: 1073476.
32. Prieur A, Harper A, Khan M, et al. Plasma hPG(80) (circulating progastrin) as a novel prognostic biomarker for early-stage breast cancer in a breast cancer cohort. BMC Cancer 2023; 23: 305.
33. Doucet L, Cailleteau A, Vaugier L, et al. Association between post-operative hPG(80) (circulating progastrin) detectable level and worse prognosis in glioblastoma. ESMO Open 2023; 8: 101626.
34. Hofman P, Prieur A, Vire B, et al. hPG80 (circulating progastrin) is a new blood-based biomarker for diagnosis of early-stage non-small cell lung cancers. Ann Oncol 2023; 34(Suppl 2): S720.
35. Askar RS, Mahmoud HE, El-Gaaly SA, Hashem WM. Plasma Hpg80 (circulating progastrin) as a novel diagnostic biomarker for early and intermediate stages of HCC. QJM 2024; 117(Suppl 2): hcae175.459.
36. Azkona Uribelarrea E, Aurrekoetxea Oribe J, Mielgo Rubio X, et al. 296P: Circulating progastrin (hPG80): a versatile blood-based biomarker for all stages of non-small cell lung cancer management. J Thorac Oncol 2025; 20(3 Suppl 1): S180.
37. van Solinge WW, Odum L, Rehfeld JF. Ovarian cancers express and process progastrin. Cancer Res 1993; 53: 1823-8.
38. Westwood DA, Patel O, Christophi C, Shulkes A, Baldwin GS. Progastrin: a potential predictive marker of liver metastasis in colorectal cancer. Int J Colorectal Dis 2017; 32: 1061-4.
39. Caplin M, Savage K, Khan K, et al. Expression and processing of gastrin in pancreatic adenocarcinoma. Br J Surg 2000; 87: 1035-40.
40. Singh P, Lu X, Cobb S, et al. Progastrin1-80 stimulates growth of

intestinal epithelial cells in vitro via high-affinity binding sites. Am J Physiol Gastrointest Liver Physiol 2003; 284: G328-39.
41. Hayakawa Y, Jin G, Wang H, et al. CCK2R identifies and regulates gastric antral stem cell states and carcinogenesis. Gut 2015; 64: 544-53.
42. Berger H, Marques MS, Zietlow R, Meyer TF, Machado JC, Figueiredo C. Gastric cancer pathogenesis. Helicobacter 2016; 21 Suppl 1: 34-8.
43. Amjadi O, Alizadeh-Navaei R, Rezapour M, et al. Association between serum progastrin biomarker level and gastric cancer. Asian Pac J Cancer Prev 2022; 23: 3595-9.
44. Rengifo-Cam W, Singh P. Role of progastrins and gastrins and their receptors in GI and pancreatic cancers: targets for treatment. Curr Pharm Des 2004; 10: 2345-58.
45. Singh P, Wu H, Clark C, Owlia A. Annexin II binds progastrin and gastrin-like peptides, and mediates growth factor effects of autocrine and exogenous gastrins on colon cancer and intestinal epithelial cells. Oncogene 2007; 26: 425-40.
46. Gerke V, Moss SE. Annexins: from structure to function. Physiol Rev 2002; 82: 331-71.
47. Wang CY, Lin CF. Annexin A2: its molecular regulation and cellular expression in cancer development. Dis Markers 2014; 2014: 308976.
48. Sharma MC. Annexin A2 (ANX A2): an emerging biomarker and potential therapeutic target for aggressive cancers. Int J Cancer 2019; 144: 2074-81.
49. Christofidis K, Pergaris A, Fioretzaki R, et al. Annexin A2 in tumors of the gastrointestinal tract, liver, and pancreas. Cancers (Basel) 2024; 16: 3764.
50. Sarkar S, Kantara C, Singh P. Clathrin mediates endocytosis of progastrin and activates MAPKs: role of cell surface annexin A2. Am J Physiol Gastrointest Liver Physiol 2012; 302: G712-22.
51. Zhang Q, Ye Z, Yang Q, He X, Wang H, Zhao Z. Upregulated expression of annexin II is a prognostic marker for patients with gastric cancer. World J Surg Oncol 2012; 10: 103.
52. Han Y, Ye J, Dong Y, Xu Z, Du Q. Expression and significance of annexin A2 in patients with gastric adenocarcinoma and the association with E-cadherin. Exp Ther Med 2015; 10: 549-54.
53. Han F, Shrestha S, Huang H, et al. Expression of annexin II in gastric carcinoma and its role in gastric cancer metastasis. World J Gastroenterol 2017; 23: 7009-15.
54. Leal MF, Calcagno DQ, Chung J, et al. Deregulated expression of annexin-A2 and galectin-3 is associated with metastasis in gastric cancer patients. Clin Exp Med 2015; 15: 415-20.
55. Conlin VS, Curtis SB, Zhao Y, et al. Helicobacter pylori infection targets adherens junction regulatory proteins and results in increased rates of migration in human gastric epithelial cells. Infect Immun 2004; 72: 5181-92.
56. Emoto K, Sawada H, Yamada Y, et al. Annexin II overexpression is correlated with poor prognosis in human gastric carcinoma. Anticancer Res 2001; 21: 1339-45.
57. Zhang ZD, Li Y, Fan Q, Zhao B, Tan B, Zhao XF. Annexin A2 is implicated in multi-drug-resistance in gastric cancer through p38MAPK and AKT pathway. Neoplasma 2014; 61: 627-37.
58. Xie R, Liu J, Yu X, et al. ANXA2 silencing inhibits proliferation, invasion, and migration in gastric cancer cells. J Oncol 2019; 2019: 4035460.
59. Mao L, Yuan W, Cai K, et al. EphA2-YES1-ANXA2 pathway promotes gastric cancer progression and metastasis. Oncogene 2021; 40: 3610-23.
60. Tas F, Tilgen Yasasever C, Karabulut S, Tastekin D, Duranyildiz D. Circulating annexin A2 as a biomarker in gastric cancer patients: correlation with clinical variables. Biomed Pharmacother 2015; 69: 237-41.
61. van Dalen FJ, van Stevendaal MH, Fennemann FL, Verdoes M, Ilina O. Molecular repolarisation of tumour-associated macrophages. Molecules 2018; 24: 9.
62. Jayasingam SD, Citartan M, Thang TH, Mat Zin AA, Ang KC, Ch'ng ES. Evaluating the polarization of tumor-associated macrophages into M1 and M2 phenotypes in human cancer tissue: technicalities and challenges in routine clinical practice. Front Oncol 2019; 9: 1512.
63. Zhang Q, Liu L, Gong C, et al. Prognostic significance of tumor-associated macrophages in solid tumor: a meta-analysis of the literature. PLoS One 2012; 7: e50946.
64. Pantano F, Berti P, Guida FM, et al. The role of macrophages polarization in predicting prognosis of radically resected gastric cancer patients. J Cell Mol Med 2013; 17: 1415-21.
65. Zhang H, Wang X, Shen Z, Xu J, Qin J, Sun Y. Infiltration of diametrically polarized macrophages predicts overall survival of patients with gastric cancer after surgical resection. Gastric Cancer 2015; 18: 740-50.
66. Kim K, Wen X, Yang HK, Kim WH, Kang GH. Prognostic implication of M2 macrophages are determined by the proportional balance of tumor associated macrophages and tumor infiltrating lymphocytes in microsatellite-unstable gastric carcinoma. PLoS One 2015; 10: e0144192.
67. Yin S, Huang J, Li Z, et al. The Prognostic and clinicopathological significance of tumor-associated macrophages in patients with gastric cancer: a meta-analysis. PLoS One 2017; 12: e0170042.

https://doi.org/10.4132/jptm.2025.12.20

68. Yamaguchi T, Fushida S, Yamamoto Y, et al. Tumor-associated macrophages of the M2 phenotype contribute to progression in gastric cancer with peritoneal dissemination. Gastric Cancer 2016; 19: 1052-65.
69. Yan Y, Zhang J, Li J, et al. High tumor-associated macrophages infiltration is associated with poor prognosis and may contribute to the phenomenon of epithelial-mesenchymal transition in gastric cancer. Onco Targets Ther 2016; 9: 3975-83.
70. Taniyama D, Taniyama K, Kuraoka K, et al. Long-term follow-up study of gastric adenoma; tumor-associated macrophages are associated to carcinoma development in gastric adenoma. Gastric Cancer 2017; 20: 929-39.
71. Swisher JFA, Burton N, Bacot SM, Vogel SN, Feldman GM. Annexin A2 tetramer activates human and murine macrophages through TLR4. Blood 2010; 115: 549-58.
72. Swisher JF, Khatri U, Feldman GM. Annexin A2 is a soluble mediator of macrophage activation. J Leukoc Biol 2007; 82: 1174-84.

JPTM
Journal of Pathology and Translational Medicine 2026; 60: 280-283
https://doi.org/10.4132/jptm.2026.01.03

NEWSLETTER

pISSN 2383-7837 / eISSN 2383-7845

PathologyOutlines.com

What's new in molecular genetic pathology 2026: emerging biomarkers for personalized cancer therapies

Umberto Maccio

Department of Pathology and Molecular Pathology, University Hospital of Zurich, Switzerland

Received: November 24, 2025
Accepted: January 3, 2026

Corresponding Author:
Umberto Maccio, MD, MSc, MBA
Department of Pathology and Molecular Pathology, University Hospital of Zurich, Switzerland
E-mail: umberto.maccio@usz.ch

ORCID
Umberto Maccio
https://orcid.org/0000-0003-3253-3787

This article has been published jointly, with consent, in both Journal of Pathology and Translational Medicine and PathologyOutlines.com.

ABSTRACT

New and emerging biomarkers and current molecular assays for the most prevalent and lethal cancers worldwide—breast, lung, prostate, and colorectal cancer—are described. Notably, HER2-low breast cancer and HER2-mutated non-small cell lung cancer have recently been recognized as targetable entities. In addition, various tissue-based analyses are now available to assess prognosis and the risk of relapse in prostate cancer.

BREAST CANCER

Hormone receptors (estrogen and progesterone receptor), Ki67, and HER2 (per ASCO/CAP guidelines 2023) are assessed in newly diagnosed and relapsed breast cancer (BC). Emerging biomarkers and novel tumor categories are broadening access to targeted therapies.

- HER2-low
  - o HER2-low in BC is defined as HER2 immunohistochemical score of 1+ or 2+ without evidence of *HER2* gene amplification via in situ hybridization.
  - o Since 2022, the antibody-drug conjugate trastuzumab-deruxtecan has been approved for second line treatment in HER2-low BC.
- HER2-ultralow (or Her2 Score 0+)
  - o HER2-ultralow is an emerging category of BC defined as having faint immunohistochemical (IHC) membranous positivity in <10% of tumor cells (formal score 0 according to ASCO/CAP guidelines 2023).
  - o HER2-ultralow tumors may respond to trastuzumab-deruxtecan, but additional evidence is needed.
- Tumor infiltrating lymphocytes (TILs)
  - o TILs may be associated with a favorable prognosis in triple-negative BC.
  - o To maximize inter-observer reproducibility and optimize reporting, the International TILs working group has created a website (Home - International TILS Working Group) offering free training.
- Next generation sequencing (NGS)
  - o NGS can be used to analyze advanced BC under current therapies to identify gene mutations with prognostic significance or potential for targeted treatment (Table 1).

NON-SMALL CELL LUNG CANCER

In locally advanced or metastatic non-small cell lung cancer (NSCLC), comprehensive molecular profiling should include NGS panels covering actionable gene alterations, such as *EGFR*, *KRAS*, and *BRAF*, along with IHC assessment of ALK and PD-L1. An NGS panel that incorporates both DNA and RNA analysis enables the detection of gene mutations as well as gene translocations. Liquid biopsy is a minimally invasive procedure, typically performed on peripheral blood, that analyzes circulating tumor DNA (ctDNA) released by tumor cells, through various techniques (NGS, reverse transcriptase polymerase chain reaction [RT-PCR], etc.) with a very low limit of detection (LoD). It is now routinely used in cases of disease progression during targeted therapy to investigate resistance mutations. To ensure the liquid biopsy is representative, the original driver mutations (e.g., *EGFR* exon 19 deletion) must be detectable. Resistance mutations, if present (e.g., *EGFR* p.T790M), usually appear in conjunction with the original mutation. Emerging biomarkers and targetable alterations are detailed below.

Table 1. Summary of established and emerging biomarkers in most common solid tumors

Tumor type	Established Biomarkers/ analyses	Clinical Impact/Possible targeted therapies	Recommended testing method	Emerging biomarkers/analyses	Clinical Impact/Possible targeted therapies	Recommended testing method
Breast Cancer	Hormone receptors (ER/PR)	Antihormonal therapies in HR+ BC	IHC	TILs	Better prognosis, response to CT in TNBC	H&E
	HER2	HER2-targeted therapies in BC HER2+ and HER2-low	IHC, ISH for HER2 Score 2+	*NTRK*-fusions	Targeted therapies in secretory carcinoma (*NTRK3*::*ETV6* translocated) or in other BCs	IHC, NGS
	Gene expression test (e.g., OncoTypeDX®, MammaPrint®, EndoPredict®, Prosigna®)	Response to adjuvant CT in HR+ BC	RNA-based tissue analysis	MSI	Therapy with ICIs	IHC (MLH1, PMS2, MSH2, MSH6) or NGS
	PIK3CA mutations	Therapy with alpelisib–fulvestrant in HR+ HER2- BC	NGS	*AKT1*-mutations	Endocrine resistance, Capivasertib in 2nd line	NGS
	ESR1 mutations	Resistance against antihormonal therapy Elacestrant in 2nd line	NGS	HRD	Olaparib in BRCA1/2 mutations; possible response to PARP-inhibitors in other HRR-gene mutations (PALB2, CHECK2, etc.)	NGS
Lung cancer (NSCLC)	*EGFR* mutations	EGFR-targeted therapies	NGS	HER2-gene mutations	HER2-targeted therapies, TKIs	NGS
	KRAS mutation	Targeted therapy for KRAS p.G12C (sotorasib)	NGS	Tumor mutational burden (TMB)	If high cutoff varying depending on assay) may respond to ICIs	NGS
	ALK-translocations	ALK-inhibitors (e.g., alectinib)	IHC, NGS	*STK11*- and *KEAP1*-gene mutations	Frequently co-occur: poor survival, may predict resistance against ICIs	NGS
	BRAF mutations	BRAF/MEK-inhibitors for *BRAF* p.V600E	NGS	MTAP and p16	Loss (surrogate for deletion of chromosome 9p21) associated with poor survival; ongoing trials with PRMT5-inhibitors.	IHC
	NTRK-translocations	TKIs (e.g., Entrectinib/Larotrectinib/ Repotrectinib)	NGS	HRD	Trial with PARP-inhibitors ongoing	NGS
	RET-translocations	Selpercatinib	NGS			
	ROS1-translocations	ROS-inhibitors (e.g., crizotinib)	NGS			
	c-MET exon 14 skipping mutations	Tepotinib	NGS	n/a		
	PD-L1	Response to ICIs	IHC			
Prostate cancer	HRD	PARP-inhibitors	NGS	Oncotype DX Genomic Prostate Score (GPS)	Based on score can help in management/ follow-up	
	MMR	May predict response to ICIs	IHC (MLH1, PMS2, MSH2, MSH6) or NGS or PCR testing Bethesda pentaplex panel	ConfirmMDx	High NPV avoid unnecessary re-biopsy	epigenetic multiplex PCR
	TMB	If high (generally >10 mutations/megabase) may predict response to ICIs	NGS	Prolaris test	Based on score can help in management/ follow-up	Reverse transcriptase PCR
	Androgen Receptor Splice Variant 7 (AR-V7)	Aggressive disease; resistance to abiraterone and enzalutamide; Niclosamide and TAS3681 have been specifically designed to target and inhibit AR-V7, but their clinical use is still being investigated	NGS	Decipher Prostate Genomic Classifier	Based on score can help in management/ follow-up	Transcriptomics assay/RNA-based tissue analysis

(Continued on the next page)

Table 1. (Continued)

Tumor type	Established Biomarkers/ analyses	Clinical Impact/Possible targeted therapies	Recommended testing method	Emerging biomarkers/analyses	Clinical Impact/Possible targeted therapies	Recommended testing method
Colorectal cancer	MMR (MLH1, PMS2, MSH2, MSH6)	If deficient: Rule out Lynch syndrome; response to ICIs; if *BRAF* wt, screening for targetable gene fusions should be considered.	IHC for MLH1, PMS2, MSH2, MSH6; or NGS or PCR testing Bethesda pentaplex panel	*ALK/ROS1/NTRK* gene fusions	Potentially targetable	NGS (RNA-based fusion panel); break apart FISH for selected gene translocations
	BRAF/NRAS/KRAS	Activating mutations predict resistance to anti-EGFR therapy. *KRAS* p.G12C can respond to targeted therapy (sotorasib)	NGS			
	HER2	Amplification confer resistance to anti-EGFR therapy; Mutations in kinase-domain of ERBB2 may confer resistance to anti-HER2 therapy	IHC for screening; ISH for equivocal cases; NGS to assess mutations	n/a		
	POLE-/POLD1-mutations	Usually TMB>100 mut/Mb, demonstrate excellent response to ICIs	NGS			
Gastric cancer	*HER2*	Overexpression or amplification is predictive for response to trastuzumab and guides targeted therapy selection	IHC for screening; ISH for equivocal cases; NGS to assess mutations	Claudin 18.2	Expression in the tumor cells to select patients eligible for therapy with zolbetuximab	IHC
	PD-L1	Expression is used to select patients eligible for therapy with ICIs	IHC, expression assessed through CPS (Combined positive score)	n/a		
	MMR (MLH1, PMS2, MSH2, MSH6)	Indicates potential benefit from immunotherapy	IHC			

ER: Estrogen receptor; H&E: Hematoxylin and Eosin; HR: Hormone receptors; HRD: Homologous recombination deficiency; ICI: Immune-checkpoint inhibitor; IHC: Immunohistochemistry; MMR: Mismatch repair; MSI: Microsatellite instability; n/a: not available; NGS: Next generation sequencing; NSCLC: Non-small cell lung carcinoma; PR: Progesterone receptor; TILs: Tumor infiltrating lymphocytes.

- *HER2*-gene activating mutations
  - o NGS is the recommended test to detect *HER2* gene mutations in NSCLC, whereas no consensus on IHC testing exists.
  - o Trastuzumab-emtansine and trastuzumab-deruxtecan showed response rates in over 60% of *HER2*-mutant NSCLC patients.
- MTAP/p16
  - o Loss of MTAP (typically co-occurring with p16 loss) can be detected through IHC and is a surrogate marker for loss of chromosome 9p21 (Fig. 1).
  - o This is associated with poor prognosis and resistance against immunotherapy, with clinical trials evaluating response to PRMT5-inhibitors ongoing.

PROSTATE CANCER

Somatic tumor testing using NGS is performed on patients with metastatic castration-resistant prostate cancer (mCRPC) who have progressed on androgen receptor-directed therapy, irrespective of any prior treatment with docetaxel. The National Comprehensive Cancer Network (NCCN) guidelines recommend testing for homologous recombination repair mutations, microsatellite instability-high (MSI-H), deficient mismatch repair (dMMR) genes, and tumor mutational burden (Table 1). Moreover, several gene-expression-based tests have recently become available, enabling more refined risk stratification in localized prostate cancer. These tests are approved by NCCN and may be considered in men with NCCN low- or favorable intermediate-risk prostate cancer when additional risk stratification could influence management decisions, such as the choice between active surveillance and definitive therapy.

The most used gene-expression-based tests approved by NCCN are listed below.

- Oncotype DX Genomic Prostate Score
  - o Ranging from 0-100, it is designed for men with very low- and low-risk prostate cancer to predict the likelihood of organ-confined disease after surgery and has been validated in multiple cohorts.
  - o The assay analyzes expression of 12 cancer-related genes and 5 housekeeping genes via RT-PCR, focusing on pathways such as cell proliferation, stromal response, and androgen receptor signaling.
- Prolaris Prostate Cancer Prognostic Test
  - o Provides a score (0–6) to estimate 10-year prostate cancer-specific mortality and risk of

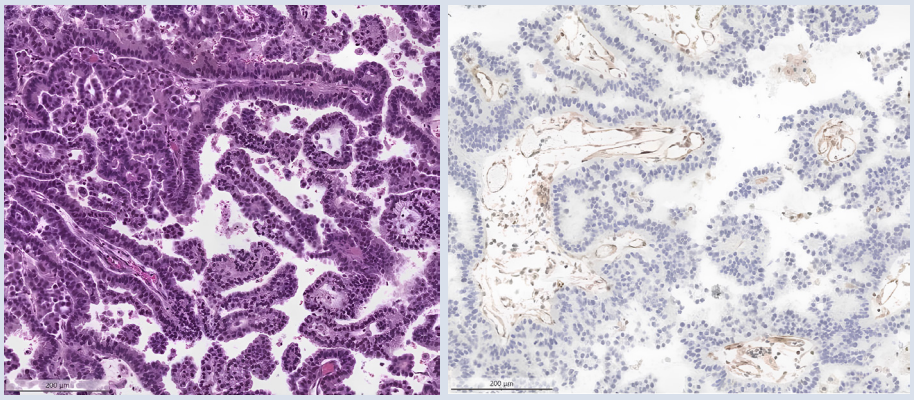

Fig. 1. Invasive non-mucinous lung adenocarcinoma with papillary pattern (H&E). Immunohistochemistry for MTAP shows a loss in neoplastic cells along with positive control in the endothelial cells.

biochemical recurrence after prostatectomy; it is applicable in both newly diagnosed and post-prostatectomy patients.
  - o It measures expression of 31 cell cycle genes via quantitative PCR (qPCR), is NCCN-recommended for a wide range of risk categories in patients with ≥10 years life expectancy, and supports decision-making between active surveillance and definitive treatment.
- Decipher Prostate Genomic Score
  - o Provides a score (0–1.0) to predict 5-year metastasis risk, 10-year prostate cancer-specific mortality, and likelihood of high-grade disease to guide the decision between surveillance and treatment in localized cancer, and informs post-prostatectomy management in high-risk cases.
  - o The assay analyzes expression of 22 genes via microarray, and is recommended by NCCN for patients with low- to intermediate-risk prostate cancer or adverse post-surgical features.
- MDx Genomic Prostate Score
  - o A 17-gene RT-PCR test analyzes prostate tumor tissue to produce a 0–100 aggressiveness score that predicts risks such as adverse pathology, recurrence, metastasis, and cancer-specific mortality, independent of standard clinical factors.
  - o Although extensively studied within NCCN risk groups and backed by strong clinical evidence, the assay is not formally validated or recommended in current NCCN guidelines.

COLORECTAL CANCER

NGS testing for detection of driver mutations in colorectal cancer (CRC) is recommended in the metastatic setting. Presence of activating mutations in *BRAF*, *KRAS*, or *NRAS* drives therapy choice in a metastatic setting (Table 1). HER2 amplification typically confers resistance against anti-EGFR therapies but represents a potentially targetable alteration. HER2 status should be assessed by IHC; cases with equivocal IHC results should be further evaluated by in situ hybridization. Of note, pathogenic mutations in the *POLE* or *POLD1* gene define a rare subset of CRC characterized by an ultra-mutated phenotype, similar to that seen in endometrial carcinoma. Ultra-mutated CRCs demonstrate an excellent response to immunotherapy.

Emerging targetable alterations are outlined below.

- Mismatch repair (MMR) proteins
  - o MMR proteins have been routinely assessed in newly diagnosed CRC.
  - o MLH1 loss with hypermethylation of *MLH1* gene promoter and/or *BRAF* mutation is typically associated with sporadic MMR-deficient CRC.
  - o Recently, a subgroup of microsatellite-instable CRC *BRAF*-wt with gene-fusions (*RET*, *ALK*, *ROS1*) have been described.
- New targetable genes
  - o *NTRK*, *ALK* and *ROS1* fusions represent emerging targetable alterations, but occur in a very small subset of colorectal cancers (generally <2%), most often in *RAS*/*BRAF* wild-type, right-sided, and frequently mismatch repair-deficient tumors.; therefore, an NGS panel that also evaluates these gene fusions alongside established biomarkers should be considered.
  - o *RET* fusions, while actionable in other malignancies (e.g., lung cancer), are not established as a targetable driver in colorectal cancer based on the current evidence. Existing medical literature does not support routine testing or targeting of RET in colorectal cancer.
  - o Incorporating these targets into routine NGS profiling could expand therapeutic opportunities beyond traditional markers.

GASTRIC CANCER

Established biomarkers used in gastric cancer include HER2, PD-L1 and MMR (Table 1). A new biomarker is claudin 18.2.

- Claudin-18 is normally expressed in gastric mucosa but is downregulated in gastric cancer, particularly at the invasive front, which correlates with increased proliferation and invasion.
- The *CLDN18*::*ARHGAP26* fusion is a known driver aberration in diffuse-type gastric cancer.
- Claudin 18.2 has emerged as a therapeutic target, with agents such as zolbetuximab demonstrating clinical benefit in claudin 18.2-positive advanced gastric cancer.
- Claudin 18.2 is evaluated on IHC by assessing membranous staining of tumor cells, most commonly using validated monoclonal antibodies such as the VENTANA CLDN18 (43-14A) clone. The evaluation is performed on formalin-fixed, paraffin-embedded tissue sections, and the staining is interpreted by a pathologist according to standardized scoring criteria.
- The most widely used scoring algorithm, particularly in the context of gastric and gastroesophageal adenocarcinomas, defines positive claudin 18.2 expression as moderate to strong (2+ or 3+) membranous staining in ≥75% of tumor cells.

Meet the Authors

Dr. Umberto Maccio has been an author and member of the board of reviewers of PathologyOutlines.com since 2024. He graduated from the Medical School in Turin, Italy, and completed thereafter a residency in Anatomical and Surgical Pathology and fellowship in Molecular Genetics at the University Hospital of Zurich, Switzerland, where he currently serves as an attending pathologist and deputy director of the Autopsy Division.